Development of a Time-Domain Modeling Platform for Hybrid Marine Propulsion Systems

by

Kevin Andersen
Bachelor of Engineering, University of Victoria, 2009

A Thesis Submitted in Partial Fulfillment
of the Requirements for the Degree of

MASTER OF APPLIED SCIENCE

in the Department of Mechanical Engineering

Supervisory Committee

Development of a Time-Domain Modeling Platform for Hybrid Marine Propulsion Systems

by

Kevin Andersen
Bachelor of Engineering, University of Victoria, 2009

Supervisory Committee

Dr. Zuomin Dong, Department of Mechanical Engineering
Supervisor

Dr. Bradley Buckham, Department of Mechanical Engineering
Co-Supervisor

Dr. Peter Oshkai, Department of Mechanical Engineering
Departmental Member

Abstract

Supervisory Committee
Dr. Zuomin Dong, Department of Mechanical Engineering
Supervisor
Dr. Bradley Buckham, Department of Mechanical Engineering
Co-Supervisor
Dr. Peter Oshkai, Department of Mechanical Engineering
Departmental Member

This thesis develops a time-domain integrated modeling approach for design of hybrid-electric marine propulsion systems that enables co-simulation of powertrain dynamics along with ship hydrodynamics. This work illustrates the model-based design and analysis methodology by performing a case study for an EV conversion of a short-cross ferry using the BC Ferries' M.V. Klitsa. A data acquisition study was performed to establish the typical mission cycle of the ship for its crossing route between Brentwood Bay and Mill Bay, across the Saanich Inlet near Victoria, BC Canada. The data provided by the data acquisition study serves as the primary means of validation for the model's ability to accurately predict powertrain loads over the vessel's standard crossing. This functionality enables model-based powertrain and propulsion system design optimization through simulation to intelligently deploy hybrid-electric propulsion architectures.

The ship dynamics model is developed using a Newton-Euler approach which incorporates hydrodynamic coefficient data produced by potential flow solvers. The radiation forces resulting from vessel motion are fit to continuous time-domain transfer functions for computational efficiency. The ship resistance drag matrix is parameterized using results from uRANS CFD studies that span the operating range of the vessel. A model of the existing well-mounted azimuthing propeller is developed to predict thrust production and mechanical torque for pseudo-second quadrant operation to represent all operating conditions seen in real operation. The propeller model is parameterized from the results of a series of uRANS CFD on the propeller geometry. A full battery-electric powertrain model is produced to study the accuracy of the model in predicting the drivetrain loads, as well as assessing the technological feasibility of an EV conversion for this particular vessel. A dual-polarization equivalent circuit model is created for a large-scale LTO battery pack. An average value model with MTPA control and dynamics loss model is developed for a commercially available electric drive system. Power loss models were developed for required converter topologies for computational efficiency. The model results for load prediction are compared to data acquired, and results indicate that the approach is effective for enabling the study of various powertrain architecture alternatives.

Table of Contents

List of Tables

List of Figures

Acknowledgments

I would like to extend a huge debt of gratitude to my supervisor Dr. Zuomin Dong with the supporting cast of Dr. Brad Buckham and Dr. Peter Oshkai for their guidance and support throughout my time at UVic. I would also like to acknowledge the tireless efforts of my colleague Mostafa Rahimpour who was instrumental in developing the necessary information for me to complete my work.

I would also like to acknowledge the extensive support that we have received from Bruce Paterson, Bob Kearney, Bambino Da Silva, and many other wonderful people at BC Ferries who made this project possible. Their contributions, along with those from many other industrial collaborators, were instrumental in supporting our research activities, in particular with the work presented here.

Financial support to UVic's Green Ship Hybrid Electric Propulsion System Modeling, Design, and Control Optimization Tools project was provided by Transport Canada under the Clean Transportation Initiative and the assistance from Ms. Marie-Chantal Ross, Development Officer, CEESAR of Transport Canada are gratefully acknowledged.

Dedication

This thesis is dedicated to my dear fiancé Samantha Wilde for her relentless patience and continuous support on the roller coaster of highs and lows that embodied this degree. Her unwavering encouragement is the primary reason that I was able to complete this thesis, for which I am eternally grateful.

I would also like to dedicate this to the loving memory of my late mother Diane Andersen and late grandmother Helen Boyce, two women whom I adored and whose love and strength inspired me to persevere in achieving my goals.

Glossary of Acronyms and Abbreviations

AC	-	Alternating Current
AC/DC	-	Alternating Current to Direct Current
AES	-	All Electric Ship
AVM	-	Average Value Model
BCF	-	BC Ferries
BEIPS	-	Battery Electric Integrated Power System
BEV	-	Battery Electric Vehicle
CAN	-	Controller Area Network
CC	-	Constant Current
CFD	-	Computational Fluid Dynamics
CV	-	Constant Voltage
DAQ	-	Data Acquisition
DC	-	Direct Current
DC/AC	-	Direct Current to Alternating Current
DC/DC	-	Direct Current to Direct Current
DoD	-	Depth of Discharge
DOF	-	Degree of Freedom
ECM	-	Engine Control Module
EMF	-	Electromotive Force
ESR	-	Equivalent Series Resistance
ESS	-	Energy Storage System
EV	-	Electric Vehicle
FCEV	-	Fuel Cell Electric Vehicle
FEM	-	Finite Element Modeling
GHG	-	Greenhouse Gas
GPS	-	Global Positioning System
HEV	-	Hybrid Electric Vehicle
HIL	-	Hardware-in-the-Loop
HPPC	-	Hybrid Pulsed Power Characterization

ICE	-	Internal Combustion Engine
IMO	-	International Maritime Organization
IPS	-	Integrated Power System
Li-ion	-	Lithium Ion
LNG	-	Liquefied Natural Gas
LTO	-	Lithium Titanate Oxide
MARPOL	-	Short for Marine Pollution (Regulation acronym from IMO)
MBD	-	Model Based Design
MSS	-	Marine System Simulator
MTPA	-	Maximum Torque Per Ampere
NED	-	North East Down (Coordinate System Reference)
OCV	-	Open Circuit Voltage
OpEx	-	Operating Expense
PID	-	Proportional Integral Derivative (Controller)
PMM	-	Planar Motion Mechanism
PMSM	-	Permanent Magnet Synchronous Machine
PSAT	-	Powertrain Systems Analysis Toolkit
PTI	-	Power Take-In
PTO	-	Power Take-Off
RC	-	Resistor/Capacitor
SIL	-	Software-in-the-Loop
SOC	-	State of Charge
SQP	-	Sequential Quadratic Programming
uRANS	-	Unsteady Reynolds Averaged Navier-Stokes
VERES	-	Software Program short for VEssel RESponse

Chapter 1 Introduction

1.1 Research Motivations

Marine transportation has been a cornerstone of the great human civilizations throughout history enabling expansion of trade, exploration of new territories, and transportation of goods. Over the years marine vessels have evolved to meet the growing demands of both trade and human transportation, driving the need for more efficient and effective propulsion solutions. With the emphasis on delivering fast, inexpensive, reliable, and safe marine transportation, propulsion systems has evolved drastically over the last 300 years from its humble beginnings using human or wind power. Wind powered sailing vessels were replaced by steamships, which enabled more reliable and faster operation. Steamships were eventually replaced by diesel engines in the early-20th century to minimize crew requirements, lower cost, and increase reliability in comparison to steam engines.

In general, the traditional diesel propulsion power plant has been the standard architecture for most vessels over the last 50 years; however, growing environmental concerns and new emissions regulations imposed by the IMO are causing a major shift in the industry's approach to propulsion system design. Recent history excluded, the escalating cost of oil provided the incentive to investigate more efficient and technologically advanced architectures to reduce operational expenses (OpEx). Though many diesel engine manufacturers are focusing their efforts on after-treatment systems to comply with the MARPOL emission regulations, the industry has collectively been exploring other opportunities for energy savings and emissions control which range from

burning cleaner fuels, such as LNG, to increasing the level of hybridization through more electrification.

Diesel-electric hybrid ships have long been deployed in special application where the vessel's mission cycles are dynamic. Diesel electric ships can offer increased operational efficiency when the power demand varies significantly. This performance gain is enabled by an array of diesel generators that can be systematically brought online to best match the generation to the active load, thus allowing generators to operate in higher efficiency ranges. However, the energy conversion losses of a diesel electric system can be significant as is shown in Figure 1, taken from MAN's diesel-electric propulsion manual [1]. It is essential to understand the system level conversion losses when comparing propulsions systems of different architectures.

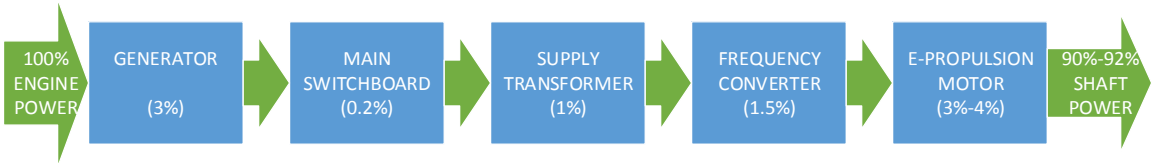

Figure 1: Typical Diesel-Electric Conversion Losses [1]

Diesel-electric and hybrid systems are not as advantageous in applications where a vessel spends the majority of its operational profile at steady output. When steady state in-transit operations dominate the load profile, the conversion losses in a diesel-electric system are likely greater than those of a traditional diesel system. For intelligent and optimal design of any propulsion system, it absolutely imperative that the designer understand the mission cycles and load profiles that make up a vessel's typical operation [2]. This can very challenging in practice because operational data is generally not available, and the expected mission cycles can vary significantly even between vessels of

the same class. There are no standardized drivecycles that can be applied to marine vessels, like those used in the automotive industry.

The ability to predict the ship's load profile in the design stage, and the capability to analyze the ship's performance through time-domain dynamic simulation provides the major motivating factors for this work. By creating a Model-in-the-Loop (MIL) platform that is capable of representing the integrated power system (IPS) dynamics, along with the hydrodynamics of thrust production and vessel motion, this work allows for advanced propulsion systems to be simulated and numerically optimized to produce the best possible system performance that meets the contract requirements. It also allows for execution of Model Based Design (MBD) for development of the main supervisory controller, enabling integrated controller synthesis for advanced energy management systems. By using Matlab/Simulink, the platform can seamlessly be extended to Software-in-the-Loop (SIL) and Hardware-in-the-Loop (HIL) to complete a vertically integrated suite of development tools.

The MBD approach is the state-of-the-art design process used by the automotive and aerospace industries, both industries realizing significant performance gains through increased levels of integration using embedded systems. Embedded systems have the ability to provide multi-variate and robust control for complex power systems, and are essential for modern "smart" energy management system deployment. The marine sector has, in many respects, lagged behind in adopting modern model-based design practices for propulsion system design; therefore, this work sought to not only develop the platform and methodology, but to also illustrate its effectiveness using a case study.

Lastly, there is a growing interest in introducing onboard energy storage and renewable technologies into the IPS, which inherently requires a higher level of sophistication and system integration. The MIL platform offers a method by which these technologies can be evaluated through simulation, and systematically implemented through MBD to lower risk and assist with economic projections.

1.2 Marine Hybridization and Electrification

The growth of the global fleet of electric and hybrid ships has outpaced traditional diesel installations by a factor of three over the last ten years [2]. Electric and hybrid propulsion offers more operational flexibility, and can achieve a significantly higher conversion efficiency in compared to traditional diesel. Generally speaking, electric drives achieve greater than 95% efficiency when operating between 5%-100% rated power output. Contrast that to diesel engines, whose efficiency is highest in the concentrated operating range of 85% - 90% rated power output [2]. When electric propulsion is employed, the electrical energy is provided by a set of diesel generators that can be brought online as needed to meet the load. By using multiple diesel generators rated at a fraction of the ship's maximum power demand, the energy conversion efficiency of the system can be increased by managing the number of generators online such that the internal combustion engine operates closer to peak efficiency.

The electric ship concept has proven to be highly effective in many commercial applications including icebreakers, cruise ships, ferries, specialty precision vessels, ocean service vessel, and drilling vessels [2]. Future trends in hybrid and electric propulsion systems are leading to more flexible and integrated systems that include,

- Parallel propeller drive systems that include PTO/PTI
- Inclusion of energy storage
- Moving from AC distribution to DC distribution grid
- Full battery-electric or zero emission operation

A full-electric battery powered ferry named the *Ampere*, with 120 car and 360 passenger capacity, has recently entered service in Norway's Sognefjord and has proven that battery technology can be the sole power source for larger vessels [3]. Hybridized vessels that include an energy storage system (ESS) enable several operational advantages which are discussed by Hansen and Wendt in [2]. First, energy storage provides a buffer bank that minimizes the requirements for spinning reserves; therefore, fewer diesel gensets are required to be online. The energy buffer also allows for peak shaving such that the generator equipment only services the average load. With sufficient capacity, the ship can be operated in zero emission mode while in the harbour, or quiet mode for noise sensitive applications.

Adoption of the DC grid allows for easier integration of alternative energy technologies such as ultracapacitors, batteries, and fuel cells. It also eliminates the need for fixed speed AC electricity generation. By removing the fixed-speed generator constraint required to regulate the AC electrical frequency, it allows for highly efficient variable-speed generation where the engine can now operate at its optimal torque-speed condition for a given load. This naturally opens more opportunities for real-time energy management.

From an equipment layout perspective, the All Electric Ship (AES) offers more flexibility in the placement of primary power plant equipment. When the internal combustion prime movers no longer need to be mechanically coupled to the propellers,

the main and auxiliary generators can be placed at more convenient locations in the ship allowing designers to better control noise emission and vibration. These are two areas that are becoming of increased environmental concern for both human passengers/crew and marine life [4].

The additional generators, electric motors, distribution systems, and converters may carry increased cost over conventional installations; however, this is typically recovered by fuel savings associated with the increased system efficiency [2], [4]. As mentioned previously, the total efficiency when accounting for electrical losses from prime mover to propulsor may be less than the traditional diesel system for certain applications [4]; therefore, it is of the utmost importance that the operating profiles be well understood in the design phase.

1.3 Hybrid Vehicle Powertrain Development in the Automotive Industry

Hybrid electric vehicles (HEVs) and other variants have achieved excellent commercial success in the automotive industry over the last ten years. Modern HEVs are highly integrated embedded systems designed for robust control and real-time energy management, even under highly dynamic operating profiles. Standard automotive drivecycles, created to represent normal drive usage patterns, provide a metric of comparison and a means of optimization for the vehicle in the design stage. The EPA uses a series of these drivecycles to provide a standard dynamometer test procedure for computing fuel economy ratings in consumer vehicles. An example of such a drivecycle is given by the EPA's Urban Dynamometer Driving Schedule (UDDS) shown in Figure 2. Typical drivecycles give the vehicle speed as a function of time, and a simple PI control-based driver algorithm is used as input to the vehicle model.

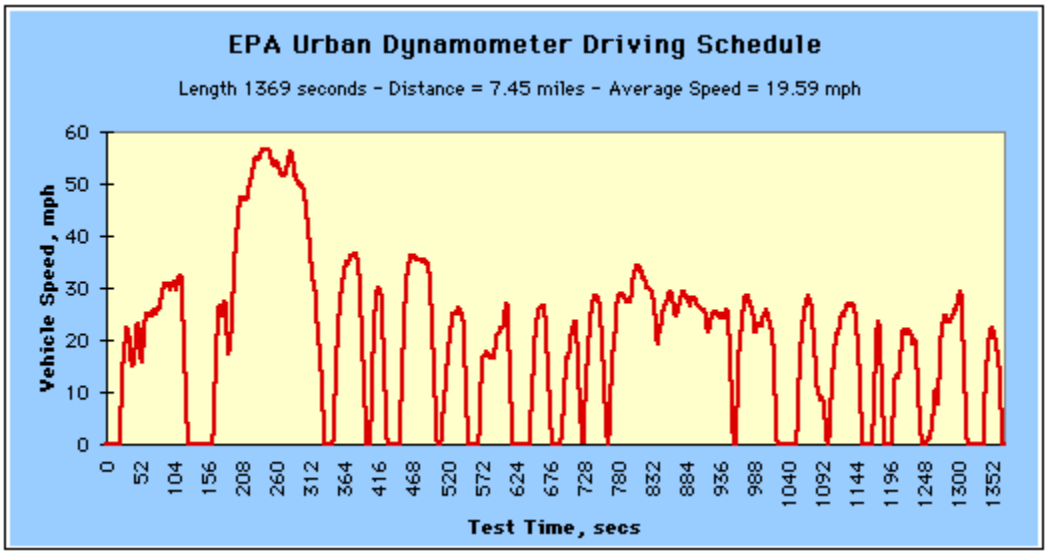

Figure 2: EPA Urban Dynamometer Driving Schedule [5]

Automotive powertrain development is performed using the MBD strategy, where time-domain models are systematically used throughout the design process to predict and validate the vehicle's performance. This approach generally includes,

1. Rapid numerical simulation of the vehicle's performance in the design stage using simplified power loss models for high level architectural studies
2. Detailed system simulation, analysis, optimization and validation using Software-in-the-Loop development
3. Seamless integration of controller hardware for Hardware-in-the-Loop testing using rapid prototyping and automatic code generation.

The MBD approach is executed using a vertically-integrated set of design tools whose workflow is best illustrated using the V-diagram shown in Figure 3. The process moves systematically around the "V", but always carrying a feedback path to earlier processes to ensure that design requirements are being met.

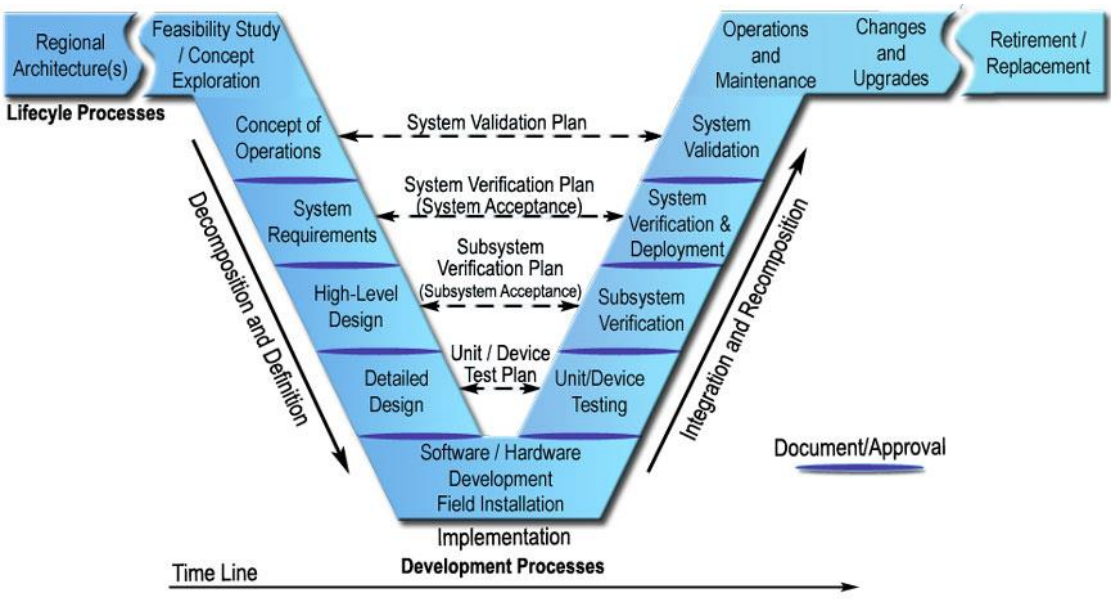

Figure 3: V-Diagram for Integrated System Development [6]

In this work, we are interested in developing a framework that can be applied to advanced hybrid electric marine propulsion using the V-diagram approach. Modeling is carried out using Matlab/Simulink as the base simulation software, and we develop a set of integrated tools and utilities that assemble the output from hydrodynamics codes and CFD solvers to parameterize generic ship models.

Referring back to the V-diagram, this work primarily addresses the "decomposition and definition" portion of the design process, though the framework presented provides the foundation for the remaining development steps. In this work, the major task is to first assemble a parametric set of reduced order multi-physics models for vessel motion, thrust production and power system dynamics. By leveraging modern computation fluid dynamics codes (CFD), this work creates an integrated set of utilities and a process workflow that is systematically executed and validated using a case study. The objective is to evaluate the effectiveness of the simulation approach against experimental data from an operational vessel, and demonstrate the effectiveness of the approach.

1.4 Case Study – BC Ferries M.V. Klitsa

With the merits of the MBD strategy and use of the V-diagram development strategy established, the objective now is to apply this methodology to hybrid electric marine propulsion with illustration through an example. As such, this thesis presents a case study of BC Ferries' (BCF) M.V. Klitsa for illustration of the model development process and simulation framework in order to assess its effectiveness in predicting system performance.

BCF has been investigating the technological feasibility of adopting battery electric "shuttle" ferries for their short-cross routes. As mentioned previously, this concept has already proven to be technologically feasible with the *Ampere* in Norway [3]; however, this ship has already encountered problems with the battery system as a result of insufficient cooling. The departure from the standard diesel or dual-fuel power plants carries a significant amount of technical risk, much of which can be mitigated using the modeling and development framework presented herein; consequently, this study will investigate the system performance of a battery electric conversion of the Klitsa, keeping the existing hull and propeller system.

Ferries are one of the few marine applications that have consistent and predictable load cycles. Well-defined load cycles allow for more refined system optimization to maximize the ship's overall performance under all loading conditions. In addition to these characteristics, the Klitsa provides an excellent test case for several reasons:

1. The Klitsa is similar in scale to heavy duty land-based transportation where electric technology has been successfully deployed commercially.
2. High efficiency electric motor drives can provide a straight replacement for the ship's existing diesel engines with direct drive.

3. Lots of space available and ballast opportunities for introduction of batteries.
4. The ship is operated in sheltered waters, and environmental variability is not a significant factor to consider.

The in-berth-to-travel time ratio is also very favorable for the new battery-electric architecture, with an approximate 2.5:1 ratio that allows for frequent charge cycles. With this operational characteristic, the battery system design can be approached in one of two ways:

1. Large capacity to meet the entire energy demand – deep charge overnight
2. Smaller capacity with frequent recharging

The use of rapid-charge, high cycle life batteries was a primary motivation for reducing capital costs of large capacity batteries, and has thus been selected for this study. The Klitsa operates between Brentwood Bay and Mill Bay in the Saanich Inlet on Vancouver Island, as illustrated below in Figure 4.

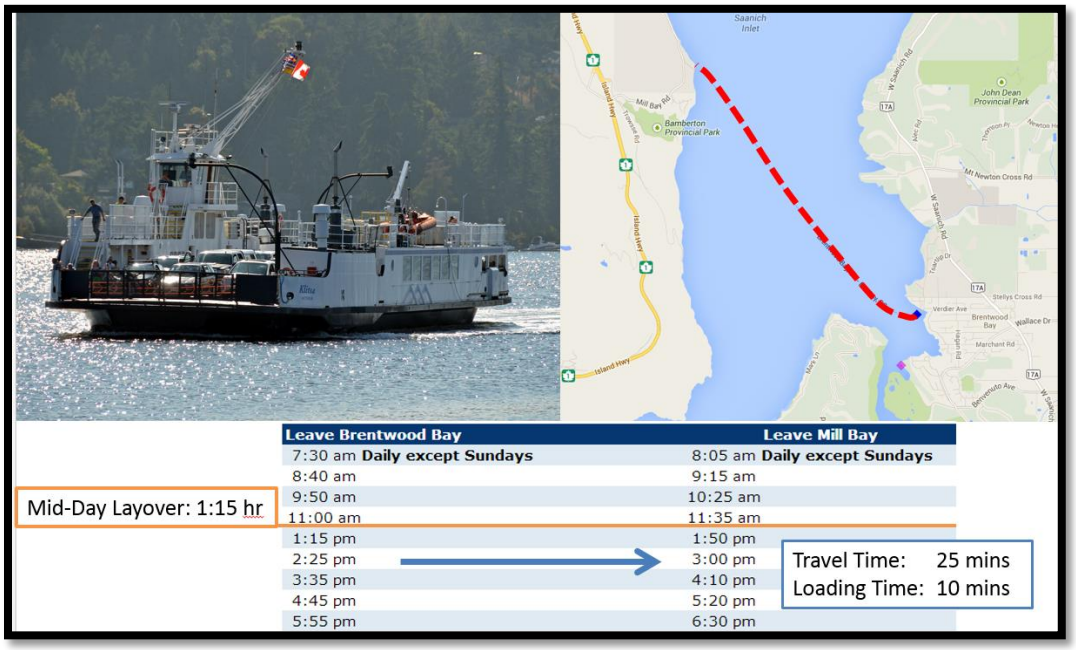

Figure 4: M.V. Klitsa Operating Route and Schedule

The ship makes eighteen crossings per day, with eight in the morning, and ten in the afternoon. The schedule also allows for a one hour mid-day layover where the ship is tied-up in Brentwood Bay. A breakdown of the charging availability as defined by current BC Ferries sailing schedule is provided below in Table 1.

Table 1: Charging Availability under Current Operating Schedule

Energy Storage Charge Type	Charge Time Availability (Hours)
Slow Charge Cycles	
Overnight Charging Time	12.5
Mid-Day Layover Time	1.15
Rapid Charge Cycles	
Loading/Unloading Charging Time	0.17
Number of Load/Unload Cycles	16
Total Rapid Charge Potential	2.67

The plant model of the Klitsa's existing propeller system and hull is systematically presented in Chapter 3, and 4 respectively. A comprehensive data acquisition study was also conducted as part of this project to provide a means of validation for the models. Details on the data acquisition experiment can be found in Appendix A.

The Klitsa is currently equipped with two 14L Series 60 Detroit Diesel engines, each coupled to a well-mounted azimuthing thruster system located at opposite ends of the ship. The azimuth angle is oriented using a PTO-based hydraulic system driven from the main driveshaft. Electrical power is provided by one of two auxiliary 50kW marine diesel generators. The main and auxiliary diesel engines provide the entire energy supply to the vessel during operation. Upon completing its daily schedule, the ship is connected to shore-power with all the engines and generators turned off.

For the purposes of this study, it will be assumed that the main engines are to be replaced with a commercially available electric drive system. The motor selected is a

high performance, low-speed PMSM traction drive system that has ideal torque/speed characteristic to replace the current propulsion engines. The study will also focus on full electrification though introduction of battery-based energy storage; therefore, the AC hotel loads currently provided by the auxiliary generators will be delivered via a DC/AC islanding converter. The IPS will be based on the DC Grid concept to facilitate the introduction of energy storage and minimize conversion losses. This is consistent with the approach of ABB and Siemens, both leading edge companies in advanced marine vessel propulsion. The new propulsive architecture that will be modeled is illustrated in Figure 5. The power plant depicted will referenced throughout this document as the battery electric integrated power system (BEIPS).

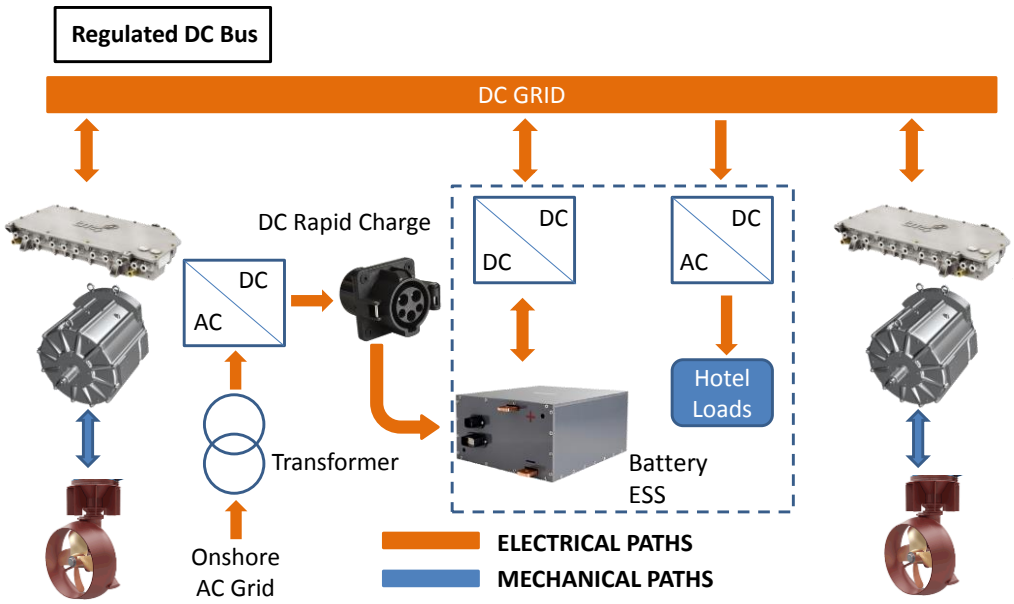

Figure 5: Proposed BEIPS Architecture

1.5 Related Work and Literature Review

The breadth of knowledge needed to develop hybrid-electric marine propulsion models is vast and multi-disciplinary in nature. Very few pieces of academic literature have attempted a fully integrated system modeling approach, though several excellent pieces

of work have focused on modeling and simulation of the IPS. On the vessel side, a large pool of literature can be found on predicting ship motion and motion control systems which forms a solid foundation for creating parametric vessel models. Models describing the mechanics and dynamics of thrust production for time-domain simulation provide the background for describing the energy conversion between power system and ship actuation. Finally, we can draw upon the extensive field of academic literature surrounding hybrid-electric vehicles in the automotive sphere and extend this knowledge to advanced marine propulsion. To summarize, the related research can be categorized as follows:

a) Marine vessel integrated power system modeling
b) Hybrid-electric vehicle technology
c) Mechanics and dynamics of thrust production
d) Ship motion and control

A brief review of related literature for each of these categories is presented in the following sections. Note that in this work, there is particular interest in developing a battery electric vehicle concept with rapid charging infrastructure; therefore, the literature pertaining to this architecture will be been emphasized.

1.5.1 Integrated Power System Modeling for Hybrid Marine Propulsion

With the trend towards further ship electrification, many bodies of work have focused on modeling, simulation, and control of integrated marine power systems. The models developed are typically used to study power system stability, reliability, fault recovery, and advanced energy management. Much of this work has been developed for military applications, though many recent studies have focused on commercial applications like

ocean service vessels. Comprehensive reviews of AES technology including subcomponents and distribution systems are provided by Thongam et al. [7], McCoy and Amy [8], and Tessarolo et al [9].

The most relevant literature related to this work is provided by a series of papers published by Zahedi, which develop a system-level model of an AES including fuel cell and batteries. First, Zahedi et al. [10] develop an average value model for an isolated bi-directional DC/DC converter for system-level simulation. Second, Zahedi et al. [11] develop a low voltage DC integrated power system model using an average value modeling approach for converters based on a *d*-*q* reference coordinate transformation. The authors illustrate the computational efficiency with this approach and its effectiveness for system-level studies. In a third paper [12], the authors develop a control framework for real-time energy management based on component efficiencies.

Some studies have attempted to couple the integrated power system simulation with the hydrodynamics of thrust production. Prempraneerach et al. [13] develop an integrated power system model for an AES with some propeller dynamics to simulate the effects of extreme events on the IPS, such as pulsed weaponry and propeller emergence. Extreme events are applied using a stochastic framework. Zahedi et al. [11] also incorporated propeller dynamics and deployed the Simulink-based Marine Systems Simluator (MSS) toolbox for the vessel model, though thrust production is simplified and details of the ship model are not given. Apsley et al. [14] also develop reduced order average value component models for the power system. Furthermore, the authors couple the propeller load to the ship forward speed while accounting for wake fraction effects.

Many other pieces of work have conducted simulation studies for AES performance in academic literature, for example, Ouroua et al [15], Weng et al. [16], or Jaster [17], each with a slightly different focus. Though these studies do make an attempt to incorporate the vessel and propeller dynamics to give a physical sense of the load, most studies assume that power system loads that are either,

a) assumed to be at steady state,

b) assumed to encounter arbitrary dynamic changes, or,

c) are studied while the ship is executing a single maneuver.

A comprehensive reference from Hansen et al. [18] discusses the mathematical modeling of individual system components, distribution systems, and thrust production to generate a state space representation of diesel-electric marine propulsion systems. Though the work referenced above provides an excellent starting point, very few studies present validation against real operational data to confirm the approach. The only exception is Ahmadi et al. [19] where small-scale bench testing was performed.

The work presented in this thesis is building towards development of real-time energy management and advanced control systems for marine vessels. Several excellent pieces of work have been developed in this area including Seenumani [20], Radan [21], Wei et al. [22], and Zahedi et al. [12]. Though these works are not explicitly used in this work, it will be seen that the underlying principle of system efficiency optimization will overlap with much of the discussion presented moving forward.

1.5.2 Hybrid Electric Vehicle Technology

Hybrid-electric vehicles have received a large amount of research attention over the past ten years, most of this work relating to energy management, optimal control, and

system design/optimization. Literature on the subject is indeed vast, but two comprehensive references in Husain [23] and Emadi [24] provide an excellent overview of the fundamentals of system/component modeling and HEV design process. Consumer automobiles are by far the most studied application of HEV technology. By comparison, consumer vehicles are relatively low-power when contrasted with marine vessels.

The case study of the Klitsa seeks to investigate a large-scale energy storage system with rapid charging infrastructure that forms the basis of the BEIPS architecture. The LTO battery chemistry has been selected for modeling as these batteries have already been successfully demonstrated in commercial rapid-charge transit bus applications. In the following sections, we focus on relevant literature to modeling the BEIPS components.

1.5.2.1 Converter Modeling and Averaging Techniques for System-Level Studies

Adoption of energy storage in hybrid electric marine propulsion applications requires the use of a DC/DC converter for interfacing with the DC distribution bus [2]. A full bridge isolated bi-directional DC/DC converter topology for shipboard applications of energy storage systems has been explored by Chung et al. [25] and Zahedi and Norum [26]. The converter integrates an active clamp on the current-fed side which is discussed in Yakushev et al. [27]. A similar unidirectional converter using zero voltage switching (ZVS) is presented in Prasanna and Rathore [28].

The objective is to develop a signal averaged model that is computationally efficient and suitable for system-level studies. A comprehensive review of averaging techniques is provided by Chiniforoosh et al. [29], and general discussion can be found in Erikson [30] and Rashid [31]. Zahedi et al. [26] explore the different averaging methods for a full

bridge bi-directional converter to evaluate the large and small signal performance versus computational efficiency. Further discussion on application of DC/DC converters to hybrid vehicle design can be found in Emadi [24] and Husain [23].

1.5.2.2 Permanent Magnet Synchronous Machine Modeling and Control

The electric propulsion system to be modeled in this work will be based off a commercially available PMSM drive package. A detailed derivation of the simulation model for a PMSM and voltage source inverter (VSI) drive systems is presented in Krause [32], and Krishnan [33]. Power loss models based on efficiency lookup tables, as well as simulation models are discussed in Husain [23] in the context of hybrid electric vehicle performance analysis. A discussion of steady state motor and inverter losses for PMSM-based drives systems using MTPA control are discussed by Chao, Chen and Diwoky [34] for predicting efficiency maps for traction drive system. This study includes both iron and copper losses for the motor, as well as semiconductor losses in the inverter. Sources of losses and loss minimization techniques for PMSMs are also discussed in Hassan and Wang [35].

The implementation of MTPA control strategies is discussed in Ahmed [36]. Zheng and Hongmei [37] discuss MTPA control and the effects of saturation and cross-coupling. The authors also discuss offline optimization techniques for building MTPA reference generators.

Two-level inverter bridges and modulations strategies are discussed in detail in Krause [32]. In this work, space vector pulsed width modulation (SVPWM) will be modeled to be consistent with the commercial drive system. Krause [32] presents the switching algorithm which will be implemented for performance comparison of the AVM model

with a detailed switching model. Chao, Mohr and Diwoky [34] use the semiconductor loss model for SVPWM presented in Bierhoff and Fuchs [38] to generate loss predictions for the inverter in steady state. Trzynadlowski and Legowski [39] discuss losses associated with vector PWM methods while Zhou and Wang [40] perform a comparative analysis between SVPWM and other three-phase carrier based PWM strategies.

1.5.2.3 Battery System Modeling with Thermal Effects

Battery models have been integrated into many of the AES and/or IPS modeling studies previously mentioned. A comprehensive overview of lithium battery systems and their electro-chemical governing equations is provided by Rahn [41]. More simplified equivalent circuit based models are discussed in Chen and Rincon-Mora [42], and the authors present a dual polarization model that has been applied to the LTO chemistry in Cleary et al. [43], Stroe et al. [44], Erdinc [45] to name few. The process of fitting equivalent circuit parameters to experimental data and constructing an equivalent circuit model is described Huria et al. [46]. Reduced order electrochemical models can also provide a good platform for system-level studies, though they require more intimate knowledge of the cell parameters. The single particle model for a lithium battery is discussed by Ahmed in [47] and [48], which illustrates the models effectiveness in adapting to degradation.

The work conducted by Cleary et al. [43] involved performance testing of a 9.2kWh battery pack comprised of LTO modules, and the experimental data was fit to a dual polarization type equivalent circuit approximation. The authors published a near-complete set of data for the equivalent circuit parameters that is used to create the large-scale pack model in this work. Further work on experimental testing of LTO modules is

provided by Lin et al. [49], while the LTO's experimental performance in fast-charging is discussed in Burke et al. [50].

The equivalent circuit model can also be coupled to a thermal model as is done in Erdinc et al. [45], Huria [46], and Clearly et al. [43]. This will constitute future work, and a wealth of additional references can be found in this area.

In this work, the focus is on development of a large-scale dual polarization equivalent circuit model that will be parameterized using the data offered by Cleary et al. [43]. When experimental data can be generated in-house, this model will later be replaced with the reduced order electrochemical model to provide a better framework for capturing degradation.

1.5.3 Thruster Dynamics Modeling

The field of literature relating to propeller performance is extensive. General references on the topic can be found in Carlton [51], Kerwin [52], and Breslin and Andersen [53], each providing a wide discussion on traditional topics relating to propeller geometry, design, performance, and analysis. Kerwin [52], along with subsequent papers from Epps [54] and Epps and Kimball [55] provide a comprehensive review of vortex-lattice lifting line (VLL) methods for analytical analysis and design of propellers in first quadrant operation. Though not explicitly used in this work, this computationally efficient propeller analysis code provides future opportunities for global system-level optimization within the MIL platform.

Modeling the dynamics of thrust production was initially studied for ROV/AUV applications, largely within the context of model based control synthesis. Initial work by Yoerger et al. [56] and Healey et al. [57] established a thrust dynamics model based on

momentum theory which was expanded upon by Blanke et al. [58], Bachmayer et al. [59] to include different mapping techniques for relating thrust and torque functions to state variables. Blanke et al. [58] provided a method of relating open water propeller coefficients to the dynamics model, but used linear approximations for open water curves. This work only investigated positive advance ratios (first quadrant) under normal incident flow conditions. Kim and Chung [60] extended this work to a quadratic framework over two quadrants in order to better represent typical open water curves; however, the dynamics of thrust production were ignored. The authors also studied the performance of a thruster in first and pseudo-second quadrant operation, and at various incident flow angles, providing insight into the thrust and torque curves for the rotatable azimuthing propellers. Note, the term pseudo-second quadrant has been coined in this term to differentiate between propeller reversing direction, and a 180° rotation of an azimuthing propeller. This will be explained further in Chapter 3.

1.5.4 Vessel Dynamics Modeling – Maneuvering and Seakeeping

The study of vessel motion in response to waves while traveling on a fixed course is termed seakeeping analysis. Seakeeping analysis can be performed in either the frequency or the time domain. Cummins [61] developed a mathematical relationship relating the dissipative radiation force that results from ship motion to the frequency dependent added mass and damping coefficients produced from inviscid theory. Faltinsen [62] and Fossen [63] provide comprehensive references that discuss the forces and response of vessels when subject to waves. McTaggart [64], [65] provides an excellent discussion of sea loads and the motion response of ships in the supporting documentation for ShipMo3D. Seakeeping modeling is conducted using hydrodynamic coefficients

computed from 2D strip-theory or 3D potential flow solvers. ShipMo3D is a 3D potential flow solver used in this work. The computation of hydrodynamic coefficients is discussed in Newman [66], McTaggart [67], and an example of a boundary element algorithm is given in Bertram [68].

Maneuvering models, in contrast, are concerned with the ship's motion and trajectory when executing a specific maneuver. Maneuvering models have not achieved the same level of accuracy as seakeeping methods [68], largely due to the complex fluid interactions that arise during the maneuver. The vessel experiences large displacements in six degrees of freedom (DOF) relative to its nominal cruise state which is difficult to represent with reduced order models. Abkowitz [69] presented a non-linear maneuvering model that has been extensively used in literature but requires coefficients from experimental planar motion mechanism (PMM) tests. In more recent years, researchers have been looking to generate these coefficients using uRANS CFD as is done in Simonsen et al. [70].

Fossen [63] discusses various maneuvering models including Ross el al. [71], where the authors develop a more physical model derived from low aspect ratio wing theory. Fossen [63] and McTaggart [65], [72] discuss a unified maneuvering/seakeeping approach for time-domain simulation that can be used for motion control system development. This unified approach, which blends seakeeping and maneuvering models has some limitations which are discussed in Chapter 4. Lastly, McTaggart [73], Ikeda et al. [74], [75] and Kato [76], [77] discuss the forces on appendages which has direct relevance to the case study of the Klitsa.

1.6 Thesis Roadmap

This thesis develops an integrated modeling framework and parameterization workflow, complete with tools and utilities, to enable model based development and simulation of advanced marine propulsion systems. This framework compiles the related research discussed in the previous section to create a computationally efficient system-level model that includes integrated power system, vessel motion, and thrust production dynamics.

The first objective is to develop a reduced order, multi-physics simulation framework that represents the M.V. Klitsa. The parameterization procedure and model structure is designed to be generic and applicable to any ship. The vessel dynamics model required by marine vessels is considerably more involved than that of a consumer automobile. The complex fluid phenomena governing the ship motion requires the use of hydrodynamic codes, uRANS CFD, and other types of hydrodynamic analyses to generate the necessary parametric data. The same is true for azimuthing propeller system. By deploying CFD through a series of well-defined experiments, parametric data can be generated to represent the full spectrum of operating conditions for the ship's hull and propeller models. This objective is addressed in Chapters 2, 3 and 4.

The second objective is to explore the use of battery-electric technology as part of the case study of the M.V. Klitsa. With the BEIPS concept having struck the interest of BCF, this thesis presents a preliminary design and parametric model of the BEIPS architecture to study its performance on the Brentwood Bay – Mill Bay crossing. This objective drives the work in Chapter 5.

The final objective is to compare the system-level model's performance against the ship's real-world operating data to assess the effectiveness of the approach in predicting

propulsive loads, and energy consumption. This objective is met by first defining a standard set of load profiles based on observation of the data collected, then comparing this data with the model's output when subjected to the same driver inputs. This work is presented in Chapters 6, and 7.

The multi-disciplinary scope required to assemble such a system-level model, which includes proper treatment of governing hydrodynamics coupled with hybrid electric power systems, is substantial; therefore, Chapter 2 compiles a review of relevant theory and fundamentals that will make up the overall model including,

1. Dynamical thrust production in multiple quadrants for development of an azimuthing propeller model that interfaces with powertrain mechanical loads
2. Unified maneuvering/seakeeping theory used for representing the vessel dynamics
3. Electric power system modeling with an emphasis on the BEIPS architecture

Once the necessary theory has been developed, Chapter 2 concludes with an overview of the model integration strategy, parameterization methodology, and general workflow. This approach is then systematically executed over the remaining chapters.

Chapter 3 develops a dynamical model of the existing well-mounted azimuthing thrusters for pseudo four-quadrant operation. This will enable a direct comparison of the model with real data collected from the ship. The model is developed using results produced by RANS CFD for on/off design conditions.

Chapter 4 develops a dynamical vessel model using a unified seakeeping/maneuvering approach with surge resistance parameterized from CFD studies. Hydrodynamic coefficients for the Klitsa's hull are generated by ShipMo3D, and interfacing utilities are

developed to make use of pre-defined blocks offered by the Marine Systems Simulator (MSS) toolbox for Simulink [78].

Chapter 5 develops a system-level BEIPS model aimed at computational efficiency, employing a combination of average value and power loss modeling. This chapter provides a preliminary system design based on commercially available components.

Validation of the overall system-level model is performed by comparative analysis using data collected from a comprehensive data acquisition experiment conducted as part of this work. This experiment developed a custom CAN-based data collection network that interfaced with onboard ship systems and standalone instrumentation. Details of the experiment have been excluded in the body of this document, but the key results are presented in Chapter 6. Here, three representative load cycles are developed to reflect the normal operational variability of the ship while in service.

Chapter 7 assembles all of the system components into a single simulation, and uses the load profiles of the data acquisition study to compare the powertrain load predictions produced by the model. Lastly, Chapter 8 provides a set of conclusions and highlights areas for future improvement.

1.7 Research Contributions

Though many propulsion modeling and simulation studies have been performed in literature, these modeling studies are often subjected to arbitrary or short-term load conditions aimed at illustrating the model's response to a specific event. In this work, the objective is slightly different in that we seek to develop an integrated system model that is capable of predicting energy demands of the ship over a mission cycle, such that different the performance of hybridized architectures can be compared. This functionality

allows for both control and system level optimization of the propulsion system in the design stage. To the author's knowledge, no other work has sought to create a modeling tool aimed at delivering this functionality.

This thesis provides the framework and methodology for high-level architectural analysis, mirroring the functionality offered by software such as Autonomie or PSAT used in the automotive industry. This approach allows for performance modeling using metrics of fuel consumption and system-level conversion efficiency, while also providing a foundation for Software-in-the-Loop and Hardware-in-the-Loop integrated development for IPS and motion control systems. Unlike most other studies, the modeling development process is validated using real-world data recorded from the operational ship.

By illustrating the process through a case study, this work has concurrently sought to assess the technological feasibility of a BEIPS propulsion architecture using rapid-charge technology for BCF's Brentwood Bay - Mill Bay crossing. This unique architecture is similar to that of the *Ampere*, though with a more demanding crossing schedule that resembles that of a transit bus. Summarizing, this thesis provides the following contributions:

1. Develops and publishes real-life operational drivecycles that can be used for further propulsion optimization studies.
2. Develops and validates an integrated modeling framework that allows for high level system propulsion analysis through simulation, specifically focusing on energy consumption, system efficiency, and emission reduction.

3. Develops a preliminary BEIPS power system design and system model based on commercially available components for assessing technical feasibility of battery electric ship with rapid-charge.
4. Creates software utilities for integration of the MSS toolbox with ShipMo3D and ProteusDS output files.
5. Develops an average value model for an electric machine with dynamic losses for predicting electric drive efficiency. Model is compared with actual published data from manufacturer.
6. Develops a realistic large-scale LTO battery dynamic model based on pack-level experimental data.
7. Provides a parameterized ship model for the M.V. Klitsa that can be used for further architectural studies, alternate route simulations, auto-pilot control system development, or Software-in-the-Loop integrated controller development.

Chapter 2 Ship Propulsion Modeling and Dynamics

Chapter 1 established the motivation for developing an integrated time-domain modeling platform for simulation of hybrid electric marine propulsion. With this type of analysis tool, the designer can simulate the overall performance of the ship under different operating conditions so to optimize the propulsion system architecture and power delivery. This is a significant departure from the traditional design approach used in naval architecture, which is largely a quasi-static design process optimized about particular operating points.

The traditional approach to ship propulsion design and its decomposition is an excellent starting point for the discussion. Thus, this chapter begins with a brief introduction on the subject matter to draw relevant information from the classical literature. This includes a brief overview of propulsive coefficients, hull-propeller interaction quantification, and propulsive efficiencies. The propulsion discussion provides a logical segue into propeller modeling theory, which forms the critical interface between the IPS and the vessel motion.

Next, the governing equations and simulation models for components making up the BEIPS architecture are presented individually. This is followed by a summary of unified seakeeping/maneuvering theory that will be used to develop the vessel motion dynamics model. Finally, this chapter concludes by presenting the overall model architecture and proposed parameterization methodology. This includes a strategy for systematic use of computational fluid dynamics and integration of hydrodynamic solvers.

2.1 Ship Propulsion – An Introduction

The design of a ship's propulsion system is a complex and often multiple objective optimization problem. The ship must be capable of safe operation under all anticipated conditions, and must meet all of the performance specifications issued in the design contract. At the fundamental level, the typical propulsion system consists of three components:

1. Prime mover – Responsible for converting chemical energy to mechanical energy
2. Transmission system – Responsible for transporting energy from prime mover to propulsor
3. Propulsor – Converts mechanical rotational energy into a thrust force [4].

Traditionally, the prime mover is a diesel engine or a gas turbine. The transmission system can be either electrical, or mechanical depending on the architecture. In recent years, the AES has been increasing in popularity. In this electrified configuration, the ship's hotel and propulsive demands are drawn from a common electrical supply.

The propulsion system produces a thrust force on the vessel which needs to overcome the hull resistance. In the absence of the propeller, the hull's resistance is comprised of three components:

- Frictional or viscous resistance, defined as the resistive force produced by tangential forces in the flow as a consequence of the boundary layer.
- Form or pressure resistance, defined as the resistive force from the pressure imbalance acting on the hull.
- Wave resistance, defined as the drag force associated with imparting energy into the wave system produced by the ship's motion.

A more thorough treatment of resistance is provided in an upcoming section as part of the vessel dynamics modeling. It is largely recognized that a good approximation for ship resistance with respect to the vessel's forward speed is given by,

$$F_R = c_1 {V_s}^2 \quad \textbf{(2-1)}$$

Here, F_R represents the total hull resistance, V_s is the ship forward speed, and c_1 represents the proportionality constant. The effective power required to tow the hull is given by,

$$P_E = F_R V_s \quad \textbf{(2-2)}$$

The effective power delivered by the propeller is characterized by the thrust force (T) multiplied by the advance speed of the propeller (V_a).

$$P_T = T V_a \quad \textbf{(2-3)}$$

The thrust produced by the propeller exceeds that of the hull's effective towing resistance. The process of accelerating flow along the hull by means of the propeller creates an increased pressure imbalance, adding to the resistive force. This effect is typically characterized using a thrust deduction factor defined as,

$$t = \frac{T - F_R}{T} \quad \textbf{(2-4)}$$

This relationship can be augmented in the event of k_p propellers on the vessel as follows:

$$t = \frac{k_p T - F_R}{k_p T} \qquad \text{or,} \qquad R = (1 - t) k_p T \quad \textbf{(2-5)}$$

The thrust deduction factor is typically determined experimentally with scale-model tow tank testing, though self-propelled CFD studies have been show to produce good approximations.

The advance velocity of the propeller differs from the forward speed of the ship. As the ship moves through the water, a boundary layer develops around the hull effectively slowing down the inflow velocity seen by the propeller(s) at the aft of the ship. The wake fraction *w* provides an empirical term to quantify this interaction and is defined by,

$$w = \frac{V_s - V_a}{V_s} \qquad \text{or,} \quad V_a = (1 - w)V_s \tag{2-6}$$

At the stern of the ship, the boundary layer has typically grown sufficiently thick that the propeller operates fully in this viscous region [4]. The corrected advanced velocity V_a is a somewhat fictitious term that is determined by analyzing the flow field at the propeller's location in relative to the hull. In actuality, the propeller is accelerating the flow and the velocity is significantly higher as will be discussed later. The total hull efficiency, as a measure of power input to the propeller versus effective power output that produces motion is given by,

$$\eta_H = \frac{P_E}{k_p P_T} = \frac{(F_R V_s)}{k_p (T V_a)} = \frac{1 - t}{1 - w} \tag{2-7}$$

2.1.1 Propeller Efficiency

The energy supplied to the propeller is provided by rotational mechanical energy. The performance characteristics of propellers are typically given for open water conditions, in absence of the hull. The open water propeller efficiency, η_O, is determined by the ratio of

effective thrust power produced versus the rotational mechanical power delivered to the propeller with torque Q, and angular speed ω_p.

$$\eta_O = \frac{P_T}{P_O} = \frac{T \cdot V_a}{Q \cdot \omega_p} = \frac{T \cdot V_a}{2\pi(Q \cdot n_p)} \quad \textbf{(2-8)}$$

Typical values for open water efficiency range from 0.3 to 0.7 depending on class of vessel [4]. When operating behind a ship's hull, the actual power delivered to the propeller is slightly different than its open-water value. This discrepancy is accounted for using the relative rotative efficiency defined by:

$$\eta_R = \frac{P_O}{P_P} = \frac{Q \cdot \omega_p}{M_P \cdot \omega_p} = \frac{2\pi(Q_O \cdot n_p)}{2\pi(M_P \cdot n_p)} = \frac{Q}{M_P} \quad \textbf{(2-9)}$$

Note M_P represents the mechanical input torque to the propeller while operating behind the hull, where Q represents the torque observed in open water conditions at the same advance ratio. This efficiency is typically close to unity, often ranging from 0.98 to 1.02. It encompasses the losses from non-uniform inflow conditions at the propeller [4].

2.1.2 Mechanical Transmission Chain

Traditional diesel, full-electric, and hybrid propulsion architectures have different losses associated with mechanical power transmission. Mechanical transmission losses occur in gearboxes, driveshafts, bearings, stuffing boxes, seals, and driveline couplings. When medium speed engines and/or electric speed drive systems are specified, a gearbox is required to reduce shaft speed, and increase output torque to drive the propeller as shown in Figure 6. The transmissive efficiency, which describes the low-speed mechanical power transmission linking the propeller to the gearboxes output shaft is expressed as,

$$\eta_s = \frac{P_P}{P_S} = \frac{M_P}{M_S} \quad \textbf{(2-10)}$$

$$P_S = M_S \cdot \omega_p = 2\pi \cdot M_S \cdot n_p \quad \textbf{(2-11)}$$

Here, M_S is the torque output of the gearbox and M_P is the torque delivered to the propeller. The subscript "S" denotes quantities at the output of the gearbox. The shaft loss efficiency typically lies between 0.5% and 1% of the nominal power and accounts for frictional losses in the stern tube and shaft bearings [4].

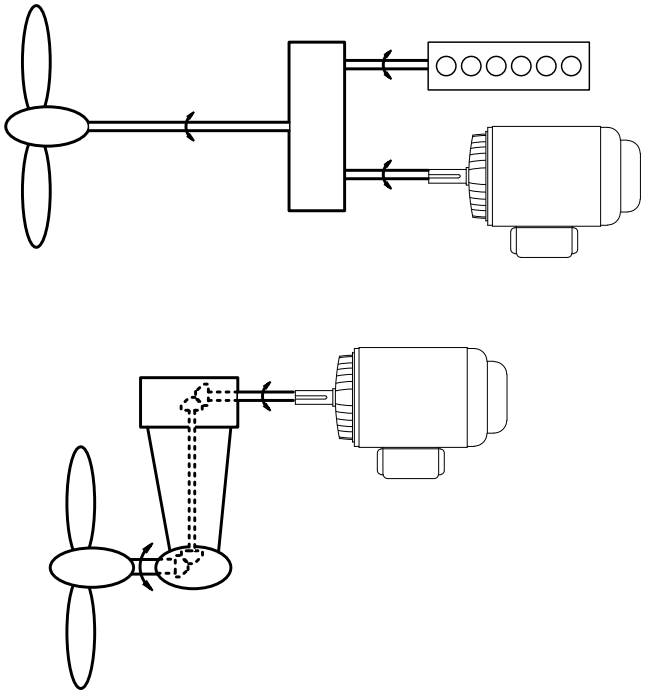

Figure 6: Illustration of Parallel Drive Gearbox (Top) and Right Angle Gearbox (Bottom) Configurations

The power delivered by the engine is described by the engine brake power, P_B, which is expressed by the basic mechanical rotational power relation,

$$P_B = M_B \cdot \omega_e = 2\pi \cdot M_B \cdot n_e \quad \textbf{(2-12)}$$

Denoting the gear reduction with the variable n_{GB}, the efficiency through the gearbox is expressed as,

$$\eta_{GB} = \frac{P_S}{k_e \cdot P_B} = \frac{M_S \cdot n_p}{k_e \cdot M_B \cdot n_e} = \frac{M_s}{k_e \cdot M_B} \cdot \frac{1}{n_{GB}} \quad \textbf{(2-13)}$$

where,

$$n_{GB} = \frac{n_e}{n_p} \quad \textbf{(2-14)}$$

Gearbox losses are typically 1-2% in a single-stage parallel shaft reduction, typically used with medium speed diesel engines. For multi-input parallel gearboxes and more complex multiple reduction systems, the losses are higher, generally 3-5% [4]. Right angle drive gearboxes, such as those used in azimuthing propellers, can have losses greater than 5%.

The total mechanical transmission efficiency is the product of mechanical drivetrain efficiencies,

$$\eta_{TRM} = \frac{P_P}{k_e \cdot P_B} = \frac{M_P}{k_e \cdot M_B} \cdot \frac{1}{n_{GB}} = \frac{M_P}{M_S} \cdot \frac{M_S}{k_e \cdot M_B} \cdot \frac{1}{n_{GB}} = \eta_S \eta_{GB} \quad \textbf{(2-15)}$$

The total propulsive efficiency is summarized by Figure 7. It's important to note that the propulsive efficiency will vary depending on the operating speed of the vessel. The previous discussion applies to efficiencies taken at design speed, when in reality the losses are a function of the vessel's operating point. For example, mechanical rotational losses are well described by damping function that includes of Coulomb, linear, and non-linear damping effects, see for example Pivano [79]. However, the preceding discussion helps in understanding sources of loss to be considered in the dynamic simulation models.

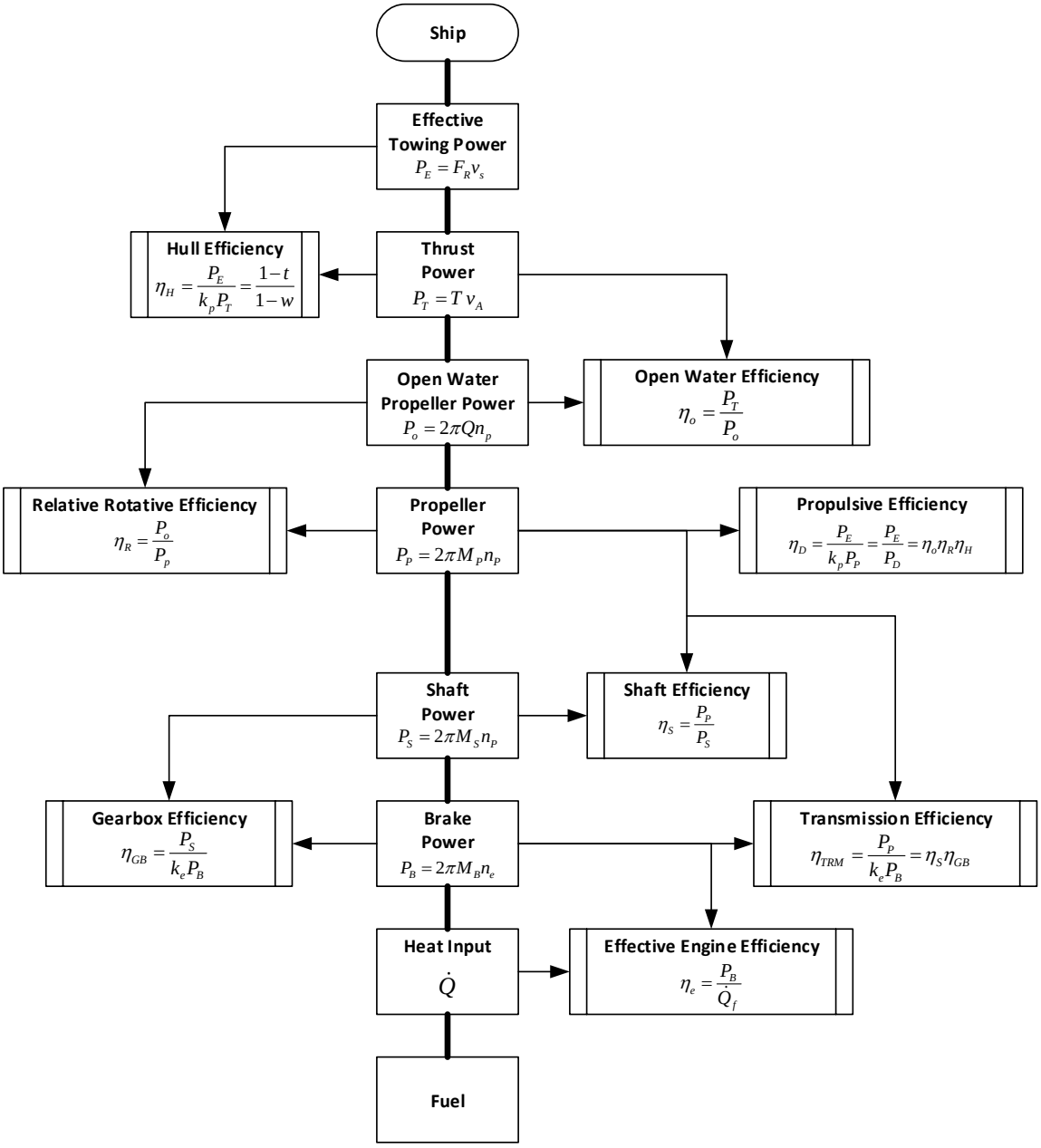

Figure 7: Propulsion Efficiency Breakdown for Traditional Diesel Propulsion [4]

2.1.3 Propeller Dynamics and Performance Modeling

The previous section provided an overall picture of the energy conversion process that makes up the propulsive efficiency of the ship, from prime mover through to vessel motion. Evidently one of the most crucial conversion processes is in transforming the mechanical rotational energy from the mover's output shaft, into a thrust force via the

propeller. The presence of the hull influences the inflow profile and operating conditions of the propeller, and other fluid-structure interactions can significantly impact on its performance. Literature on the subject is vast with the most comprehensive references presented by Carlton [51], Kerwin [52], and Breslin and Anderson [53].

In this work, the primary objective is to develop a model that can accurately predict powertrain loads from a freely maneuvering ship. During maneuvering, the ship's propellers will regularly encounter off-design conditions that can drastically change the load on the IPS. The Navier-Stokes equation defines the complex fluid mechanics governing thrust production, but is too computationally intensive to utilize in a system-level model; therefore, the standard propulsive coefficients provide a good starting point for reduced order model development.

The approach here draws on literature relating to model-based vessel motion control systems for surface vessels and AUVs/ROVs. Not only does the development of accurate propeller models allow for higher precision position and motion control, but it also enables opportunities for advanced IPS energy management and control.

Open-water propeller performance for both thrust and torque is typically plotted as non-dimensionalized coefficients K_T and K_Q versus the non-dimensionalized advance ratio J, where,

Advance Ratio	$J = \frac{V_a}{nD}$	**(2-16)**
Thrust Coefficient	$K_T = \frac{T}{\rho n^2 D^4}$	**(2-17)**
Torque Coefficient	$K_Q = \frac{Q}{\rho n^2 D^5}$	**(2-18)**

V_a: Advance Speed (m/s)
n: Propeller Speed (rev/s)
D: Propeller Diameter (m)
T: Thrust (N)
Q: Torque (Nm)

These coefficients represent steady state, first quadrant operation where the propeller is providing thrust to propel the vessel forward. When non-incident flow is encountered, or the propeller is not deeply submerged, the propeller performance characteristics will be different. Non-incident flow over the propeller will be encountered regularly during ship maneuvers, as well as in the presence ocean currents and waves. One problem with these standard definitions is that a discontinuity results when the propeller is at zero speed. This is problematic during dynamic simulation if the propeller stops, or reverses direction. Furthermore, these definitions are restricted to the first quadrant, and are don't extend conveniently into multiple quadrant operation. The quadrant of operation is traditionally defined by the rotational direction of the propeller and the direction of ship travel as described in Figure 8.

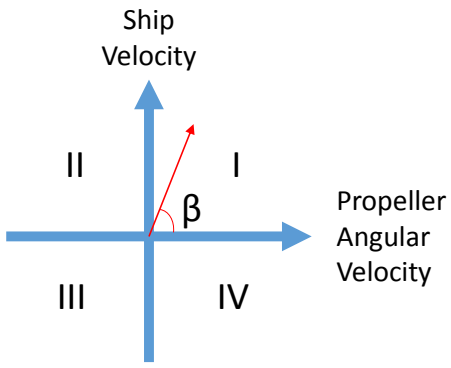

Figure 8: Traditional Definition of Propeller Quadrants

However, this definition needs to be expanded when referencing azimuthing propeller system because 2nd and 4th quadrant operation are achieved by reorienting the propeller by 180°. With this rotative functionality, another dimension can be added to Figure 8 to describe all possible quadrants of operation as seen in Figure 9.

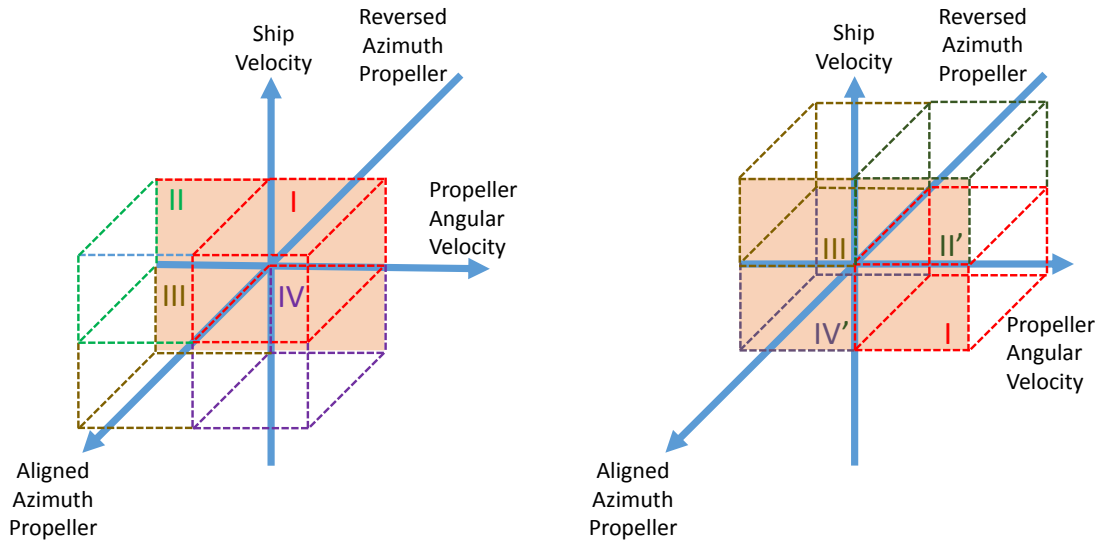

Figure 9: Expansion of 4-Quadrant Definition to Represent Azimuthing Propellers

An alternate formulation of the advance ratio that eliminates the discontinuity at zero speed is given by,

$$\beta = atan2\left(\frac{V_a}{0.7\pi nD}\right) \qquad \textbf{(2-19)}$$

The parameter β represents an angle that describes the quadrant of operation where,

$0 \leq \beta \leq 90^{\circ}$	First Quadrant
$90 < \beta \leq 180^{\circ}$	Second Quadrant
$180 < \beta \leq 270^{\circ}$	Third Quadrant
$270 \leq \beta < 360^{\circ}$	Fourth Quadrant

This definition is convenient for handling off-design propeller conditions. Standard non-dimensionalized propeller coefficients are limited in that they only represent steady state operating condition; therefore, a dynamic framework should be formulated to better accommodate time-domain simulation. Models for dynamic thrust production have been proposed by Yoerger et al. [56], Healey et al. [57], Bachmayer et al. [59], Blanke et al.

[58], and more recently Pivano [79]. The dynamics of thrust productions is anchored in fluid momentum theory. Healey et al. [57] presented a two-state model given by,

Mechanical Equation: $$J_{motor}\dot{\omega} + B_n\omega = Q_{motor} - Q_{prop} \quad \textbf{(2-20)}$$

Fluid Momentum Equation: $$m_f\dot{u}_p + B_f(u_p - u)|u_p - u| = T \quad \textbf{(2-21)}$$

Thrust Production: $$T = T(n, u_p) \quad \textbf{(2-22)}$$

Torque Production: $$Q = Q(n, u_p) \quad \textbf{(2-23)}$$

u_p: Axial flow velocity in disk

u: Surge speed of vessel

m_f: Mass of fluid in control volume

B_n: Linear mechanical viscous damping

B_f: Quadratic fluid damping coefficient

Various models have been suggested for mapping thrust and torque functions to the propeller speed and inflow velocity state variables. Some good results have been achieved using lift and drag curves derived from airfoil theory; however, in this work, it is more convenient to develop the torque/thrust relationship from the standard thrust and torque propeller coefficients. This approach allows for manufacturer data to be used directly.

The model developed by Blanke et al. [58] is based on standard propeller coefficients and uses a Bernoulli tube and actuator disk formulation for describing thrust production. Using a momentum balance in the streamtube passing the thruster's swept area, the authors show that the equation governing thrust production can be written as follows,

$$m_f \dot{u}_p + 2\rho A_p |u_p|(u_p - u_a) = T \quad \textbf{(2-24)}$$

Note, A_p represents the propeller disk area. Using published open water performance curves, the authors use a linear approximation to propeller curves described by the following relationships,

$$K_T = \alpha_0 + \alpha_1 J = \frac{T}{\rho n^2 D^4} \quad \textbf{(2-25)} \quad \Rightarrow \quad \begin{aligned} T &= \alpha_0 \rho n^2 D^4 + \alpha_1 \rho n^2 D^4 \left(\frac{u_a}{nD}\right) \\ &= T_{|n|n} n^2 + T_{|n|v} n u_a \end{aligned} \quad \textbf{(2-26)}$$

$$K_Q = \gamma_0 + \gamma_1 J = \frac{Q}{\rho n^2 D^5} \quad \textbf{(2-27)} \quad \Rightarrow \quad \begin{aligned} Q &= \gamma_0 \rho n^2 D^5 + \gamma_1 \rho n^2 D^5 \left(\frac{u_a}{nD}\right) \\ &= Q_{|n|n} n^2 + Q_{|n|v} n u_a \end{aligned} \quad \textbf{(2-28)}$$

where,

$$T_{|n|n} = \alpha_0 \rho D^4 \quad \textbf{(2-29)} \qquad Q_{|n|n} = \gamma_0 \rho D^5 \quad \textbf{(2-30)}$$

$$T_{|n|v} = \alpha_1 \rho D^3 \quad \textbf{(2-31)} \qquad Q_{|n|v} = \gamma_1 \rho D^4 \quad \textbf{(2-32)}$$

Here the coefficients α_i and γ_i are fitted parameters. It is important to distinguish between velocity parameters in these equations. The advance velocity V_a in the original definition needs to be re-evaluated within this dynamic framework. The ship's forward speed in surge is defined by the local frame velocity u. The ambient inflow conditions at the inlet of the Bernoulli tube is corrected using the wake fraction to account for the presence of the hull. The freestream velocity used to define propulsive coefficients represents the inflow velocity to the streamtube. The actual velocity through the propeller disk is higher as result of the flow acceleration, and this parameter is denoted by u_p. The inlet to the streamtube, denoted by u_a, is synonymous with advance velocity computed with the relationship,

$$u_a = (1 - w) \cdot u \quad \textbf{(2-33)}$$

Blanke et al. [58] provide a derivation of the forces acting on a propeller blade to generate an expression that relates flow velocity at the propeller to inflow condition,

$$a = \frac{u_p}{u_a} \quad \textbf{(2-34)}$$

Using this definition, each governing equations can be expressed as a function of the inflow velocity at the propeller. Blanke et al. [58] define the terms,

$$T^o_{|n|v} = \left(\frac{1}{1+a}\right) T_{|n|v} \quad \textbf{(2-35)} \qquad Q^o_{|n|v} = \left(\frac{1}{1+a}\right) Q_{|n|v} \quad \textbf{(2-36)}$$

The original Healey model is then modified to include the new mapping function of thrust and torque. With inclusion of the wake fraction and thrust deduction the basic surge equation of motion, the resulting set of equations is given by,

Mechanical Equation: $$J_{motor}\dot{n} = Q_{motor} - B_n n - Q_{|n|n}|n|n + Q^o_{|n|v}|n|u_p \quad \textbf{(2-37)}$$

Fluid Momentum Equation: $$m_f \dot{u}_p + 2\rho A_p |u_p|(u_p - u_a) = T_{|n|n}|n|n + T^o_{|n|v}|n|u_p \quad \textbf{(2-38)}$$

Surge Ship Motion Equation: $$m_s \dot{u} = R(u) + (1-t)\left(T_{|n|n}|n|n + T^o_{|n|v}|n|u_p\right) \quad \textbf{(2-39)}$$

Hull Interaction Equation: $$u_a = (1 - w) \cdot u \quad \textbf{(2-40)}$$

J_{motor}: Motor inertia (for integrated thruster with no gearbox)

$R(u)$: Surge resistance

w: Wake fraction

t: Thrust deduction factor

m_s: Mass of the ship

The preceding derivation was constructed using linear approximations to describe thrust and torque coefficients as a function of the advance ratio. Kim and Chung [60] expanded this approach to a quadratic framework which provides a significantly better fit for typical open water curves, especially at negative advance ratios. The authors develop a steady state framework using parabolic approximations and fit the coefficients to experimental data. They also investigate different flow regimes which are defined as equi-, vague-, and anti-directional where different sets of parabolic coefficients are utilized. This phenomena is discussed further in Chapter 3. Non-incident angular flow conditions are also experimentally tested in [60], though details are not provided.

The case study undertaken in this work is not a high precision motion control application. The majority of the time, the propellers are operating in normal first quadrant conditions; however, the azimuthing propellers frequently encounter off-design and opposing flow conditions while maneuvering in/out of berth. Recent experimental research by Buchanan [80] showed that the thrust develops on the order of 100ms, which is significantly faster than the dynamics of a ship; therefore, steady approximations are likely sufficient given the expressed objectives of the simulation platform.

The framework developed by Healey et al [57], Blanke et al. [58], and Kim and Chung [60] will provide the basis for the modeling equations governing the propeller, though this work will neglect the fluid momentum dynamics. Instead, a lookup surface-based method will be used to represent the plant dynamics, based on series of prescribed CFD experiments that capture the entire range of operating conditions that will be encountered by the propeller. The dynamics of fluid momentum will be negligible in comparison to ramp rate of the propeller, which is dictated by the integrated power system.

2.2 Hybrid-Electric Integrated Power Systems Modeling

Hybrid-electric technology has been deployed in marine vessels for many years, primarily through diesel-electric series-type architectures. Design of diesel-electric system is not trivial, especially with the AC grid backbone which requires reactive power control. In literature, the majority of the academic attention for hybrid electric vehicles has been spent on land-based transportation, most notably in consumer vehicles. The general terms used in the automotive sector such as Battery Electric Vehicle (BEV), Hybrid Electric Vehicle (HEV), Plug-In Hybrid Electric Vehicle (PHEV), Fuel Cell Electric Vehicle (FCEV), are not typically used in the context of marine systems. Fully electrified ships, where all propulsive devices are powered by electric machines, are generally referred to as All Electric Ships (AES). The supporting power system architecture is commonly referred to as the Integrated Power System (IPS).

By comparison, academic research relating to marine electrification and hybridization has been far less prevalent than for automotive applications. Modeling of the IPS is similar to modeling of a micro-grid, with multiple power producers and consumers attached onto a small-scale distribution network. That said, much of the automotive research on HEVs can be leveraged to assist in the development of the system-level simulation model for marine vessels.

The Battery-Electric Integrated Power System (BEIPS) that will be modeled in this work consists of the following components:

1. Battery Energy Storage System
2. Isolated Bi-Directional Buck/Boost Converter
3. Battery Charging System
4. Variable Speed PMSM Electric Drive Systems

5. DC/AC Islanding Converter

The task is to develop simulation models that capture the critical system dynamics but with sufficient order reduction to remain computationally efficient. It is also important to understand the different time constants associated with marine propulsion to determine which dynamics can be neglected. In a system-level model, high frequency dynamics associated with converters can be ignored and replaced with power loss models with very little impact on aggregate performance predictions. As an example, Apsley et al. [14] provide a table showing the variance in time constants associated with sub-components of an AES marine propulsion system.

Table 2: Time Constants of AES Ship Subsystems [14]

Source	Time
Semiconductor commutation	~1μs
Rotor time constant	50ms - 1s
PWM period	0.5 - 2ms
Propeller Run-Up Time	20 - 60s
Ship Run-Up Time	60 - 500s
Wave Disturbance	10 -100s

Component models must capture the critical system dynamics while accurately modeling the system losses. The use of power loss models, which are based on efficiency/fuel maps, can be used where appropriate; however, the use of steady state data for dynamic simulations will generally under predict losses during transient events. With highly dynamics profiles such as consumer vehicles, this can then lead to a significant discrepancy between actual and model predicted performance. With ships on the other hand, power output is relatively steady and aggregate error accumulation is likely small by comparison.

In the BEIPS architecture, the main components that will carry high transient losses are the ESS and the main propulsion drive motors. Consequently, these components will be developed in more detail by providing a physics-based model for losses. In contrast, the power converters can be sufficiently represented using power loss models in architectural studies. These can be replaced with average-value model in future for study of power system stability. The following sections provide a discussion on formulation of the simulation models for each component used in the case study.

2.2.1 Battery Energy Storage System Modeling

The electrical performance of batteries has been studied extensively in literature with applications ranging from portable electronics, to more relevant work relating to EVs, PHEVs, and BEVs. A comprehensive discussion of the fundamental electrochemical governing equations for different battery chemistries is presented by Rahn [41]. Rahn offers an in-depth reference that provides the basis for very detailed cell modeling such as FEM analysis. These models represent the underlying electrochemical physical processes of battery cells including the mechanics of diffusion, convection, ion transport, electrode kinetics, etc. These models require intimate knowledge of the cell's properties which are not generally shared by cell manufacturers.

The complexity of full physics-based models, combined with the scarcity of information available for their parametrization, have led to alternate approaches for approximating battery system dynamic response. Chen and Rincon-Mora [42] provide a review of mathematics-based and electric circuit-based modeling techniques that have been applied in literature. Mathematical-based models use empirical equations or abstracted methods to predict specific aspects of a battery's performance, such as

runtime. Though these can be useful in the design process, they do not allow for tracking of voltage and current trajectories in a time-domain simulation [42]. In contrast, electrical equivalent circuit-type models have been widely adopted for system-level studies, and the most commonly used method for HEVs.

The equivalent circuit representation allows for dynamical effects to be approximated using passive circuit elements such as inductors, capacitors, and resistors, while the electrochemical potential and electron transport is simplified to ideal voltage and current sources. This approach allows for co-simulation with electrical power systems. Electrical models can be classified into three categories [42]:

1. Thevenin-based (Figure 10)
2. Impedance-based (Figure 11)
3. Runtime-based

An example of a Thevenin-based circuit representation for a battery cell is provided in Figure 10. Transient effects are captured using parallel RC branches which are added in series with the DC series resistance, steady state internal cell resistance. Each passive component is implemented as a function of battery SOC, and cell temperature. A self-discharge parallel resistance may also be added depending on chemistry. The open circuit voltage (OCV) is modeled as an ideal voltage source that is again a function of SOC and temperature. Additional circuit configurations can be used to represent the response produced by different cells and chemistries.

Thevenin-based circuit parameters are numerically fit to experimental data produced by a Hybrid Pulsed Power Characterization (HPPC) cell testing [46]. Though this circuit is

effective in predicting transient performance, it cannot capture steady-state voltage variations that occur naturally in the electrochemical cell [42].

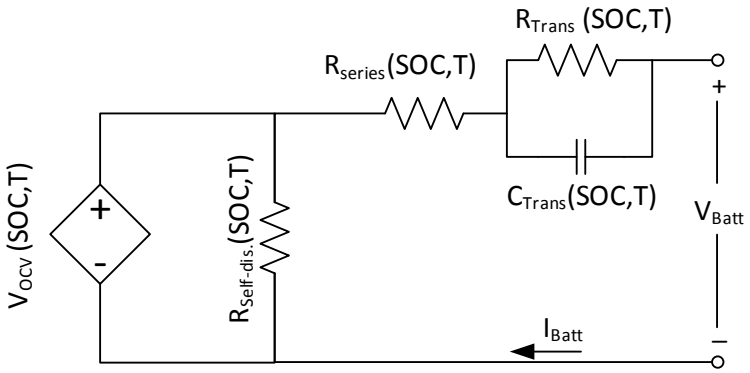

Figure 10: Thevenin-Based Electrical Battery Circuit

Figure 11 shows an example of an impedance-based battery equivalent circuit model. These models are parametrized using electrochemical impedance spectroscopy, a process whereby an AC signal is injected into the battery and the harmonic response is fit to a complex impedance network. This process can be cumbersome and limited to small ranges of SOC, but can provide a detailed insight into battery impedance if a signal has high AC content [42].

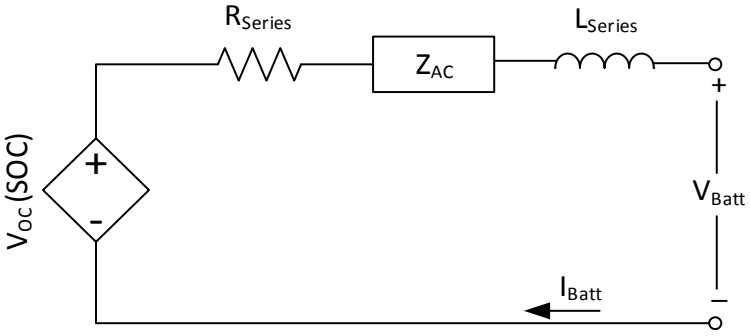

Figure 11: Impedance-Based Electrical Battery Circuit

The runtime-based model again uses electrical components, but is primarily intended to predict runtime at constant current, mainly for portable electronic applications and is not particularly relevant to this work.

The dual polarization Thevenin-based circuit has been shown to provide a good representation for the Lithium Titanate Oxide (LTO) chemistry selected for the case study [43]. Self-discharge can generally be neglected with this chemistry under normal conditions, and thus the parallel resistance can be eliminated from the circuit.

HPPC testing is most commonly performed at the cell level; therefore, pack level characteristics need to be scaled appropriately for the voltage and capacity requirements of the pack. The equivalent impedance of the R-RC-RC circuit is given by,

$$Z_{cell,eq} = Z_{Series} + Z_{RC1} + Z_{RC2} \quad \textbf{(2-41)}$$

Expanding the RC impedances we get,

$$Z_{cell,eq} = R_{S,cell} + \frac{1}{\frac{1}{R_{1,cell}} + j\omega C_{1,cell}} + \frac{1}{\frac{1}{R_{2,cell}} + j\omega C_{2,cell}} \quad \textbf{(2-42)}$$

$$Z_{pack,eq} = R_{S,pack} + \frac{1}{\frac{1}{R_{1,pack}} + j\omega C_{1,pack}} + \frac{1}{\frac{1}{R_{2,pack}} + j\omega C_{2,pack}} \quad \textbf{(2-43)}$$

For a pack consisting of n_s cells in series, the impedance of the pack can be analytically extrapolated using the following relationship,

$$Z_{pack,eq} = Z_{cell,eq} + Z_{cell,eq} + \cdots = n_s Z_{cell,eq} \quad \textbf{(2-44)}$$

The equivalent circuit parameters can be analytically related to pack level parameters as follows:

$$\frac{1}{\frac{1}{R_{1,pack}} + j\omega C_{1,pack}} = \frac{n_s}{\frac{1}{R_{1,cell}} + j\omega C_{1,cell}} = \frac{1}{\frac{1}{n_s R_{1,cell}} + j\omega \frac{C_{1,cell}}{n_s}} \quad \textbf{(2-45)}$$

Therefore,

$$R_{S,pack} = n_s R_{S,cell} \quad \textbf{(2-46)}$$

$$R_{i,pack} = n_s R_{i,cell} \quad \textbf{(2-47)}$$

$$C_{i,cell} = \frac{C_{i,cell}}{n_s} \quad \textbf{(2-48)}$$

An analytical expression can also be derived for cells in parallel. The impedance of equivalent cell circuits in parallel is given by,

$$\frac{1}{Z_{pack,eq}} = \frac{1}{Z_{cell,eq}} + \frac{1}{Z_{cell,eq}} + \cdots = \frac{n_s}{Z_{cell,eq}} \quad \textbf{(2-49)}$$

$$\begin{aligned} Z_{pack,eq} &= \frac{Z_{cell,eq}}{n_p} \\ &= \frac{1}{n_p}\left[R_{S,cell} + \frac{R_{1,cell}}{1 + j\omega R_{1,cell}C_{1,cell}} + \frac{R_{2,cell}}{1 + j\omega R_{2,cell}C_{2,cell}}\right] \end{aligned} \quad \textbf{(2-50)}$$

Therefore,

$$R_{S,pack} = \frac{R_{S,cell}}{n_p} \quad \textbf{(2-51)}$$

$$R_{i,pack} = \frac{R_{i,cell}}{n_p} \quad \textbf{(2-52)}$$

$$C_{i,cell} = n_p C_{i,cell} \quad \textbf{(2-53)}$$

Scaling of cell parameters to pack level provides an initial estimate, but is known to not be particularly accurate. This is because additional resistances from internal connections points, laser welds, and other contact resistances can have a significant impact on the overall impedance of the pack. Furthermore, pack internals can also produce additional

capacitive effects and/or inductive effects that are not captured in this model; therefore, pack level experimental data, combined with the above relations, will be used to develop the large-scale battery model as will be seen in Chapter 5.

2.2.2 Variable Speed PMSM Electric Drive System

Dynamic simulation models for permanent magnet synchronous machines (PMSM) are typically implemented using a *d-q* reference frame approach. From Faraday's law and Ohm's Law, the motor's stator voltage equations can be expressed in matrix form, and in the rotor reference frame as follows:

$$\boldsymbol{v}_{qd0s}^{r} = \boldsymbol{r}_s \boldsymbol{i}_{qd0s}^{r} + \omega_r \boldsymbol{\lambda}_{qds}^{r} + p\boldsymbol{\lambda}_{qd0s}^{r} \quad \textbf{(2-54)}$$

$$\left(\boldsymbol{\lambda}_{qds}^{r}\right)^{T} = [\lambda_{ds}^{r} \quad -\lambda_{qs}^{r} \quad 0] \quad \textbf{(2-55)}$$

$$\lambda_{qd0s}^{r} = \begin{bmatrix} L_{ls} + L_{mq} & 0 & 0 \\ 0 & L_{ls} + L_{mq} & 0 \\ 0 & 0 & L_{ls} \end{bmatrix} \begin{bmatrix} i_{qs}^{r} \\ i_{ds}^{r} \\ i_{0s}^{r} \end{bmatrix} + \lambda_{m}^{\prime r} \begin{bmatrix} 0 \\ 1 \\ 0 \end{bmatrix} \quad \textbf{(2-56)}$$

Note that the 'p' operator represents the time derivative operator. In expanded form, and with substitution of the flux linkages into the direct, quadrature, and zero sequence voltage expressions, we can write [32],

$$v_{qs}^{r} = \left(r_s + pL_q\right) i_{qs}^{r} + \omega_r L_d i_{ds}^{r} + \omega_r \lambda_{m}^{\prime r} \quad \textbf{(2-57)}$$

$$v_{ds}^{r} = (r_s + pL_d) i_{ds}^{r} - \omega_r L_q i_{qs}^{r} \quad \textbf{(2-58)}$$

$$v_{0s} = (r_s + pL_{sl}) i_{0s} \quad \textbf{(2-59)}$$

The power output is conserved regardless of the coordinate frame; therefore, the power equation for the electric machine can be expressed as,

$$P_{abcs} = P_{dq0} = \frac{3}{2}\left(v_{qs}i_{qs} + v_{ds}i_{ds} + 2v_{0s}i_{0s}\right) \quad \textbf{(2-60)}$$

Consequently, a simplified expression can be developed for torque generated by the machine using energy conservation,

$$P_{machine} = T_e\omega_r = T_e\left(\frac{2}{P_n}\right)\omega_e = \frac{3}{2}\left(v_{qs}i_{qs} + v_{ds}i_{ds} + 2v_{0s}i_{0s}\right) \quad \textbf{(2-61)}$$

Here P_n denotes the number of pole pairs which relates the electrical frequency to the mechanical rotor frequency. Substituting the stator equations into the power equation and grouping like terms, the losses can be decomposed as follows,

$$T_e\left(\frac{2}{P}\right)\omega_r = \overbrace{\frac{3}{2}r_s\left({i_{qs}^r}^2 + {i_{ds}^r}^2 + 2{i_{0s}}^2\right)}^{\text{Ohmic Losses}} + \overbrace{\frac{3}{2}\left(\lambda_{ds}^r i_{qs}^r - \lambda_{qs}^r i_{ds}^r\right)\omega_r}^{\text{Torque Production}} + \underbrace{\frac{3}{2}\left(i_{qs}^r p\lambda_{qs}^r + i_{ds}^r p\lambda_{ds}^r + 2i_{0s}p\lambda_{0s}\right)}_{\text{Stored Magnetic Energy}} \quad \textbf{(2-62)}$$

Ohmic losses and stored magnetic energy terms impact the mechanical output torque generated. The electromagnetic torque produced by the machine is given by,

$$T_e = \left(\frac{3}{2}\right)\left(\frac{P}{2}\right)\left(\lambda_{ds}^r i_{qs}^r - \lambda_{qs}^r i_{ds}^r\right) \quad \textbf{(2-63)}$$

The *d-q* flux linkages can be substituted to get an expression for torque production based on the input stator current,

$$T_e = \left(\frac{3}{2}\right)\left(\frac{P}{2}\right)\left((L_d i_{ds}^r + \lambda_m'^r) i_{qs}^r - \left(L_q i_{qs}^r\right) i_{ds}^r\right) = \left(\frac{3}{2}\right)\left(\frac{P}{2}\right)\left(\lambda_m'^r i_{qs}^r + \left(L_d - L_q\right) i_{qs}^r i_{ds}^r\right) \quad \textbf{(2-64)}$$

Note that $\lambda_m'^r$ represents the flux established by the permanent magnets. The PMSM model to this point has only considered copper losses through resistive dissipation in the stator coils. This model can be augmented to include other physical sources of energy dissipation including iron losses, and magnetic saturation effects. In this work, iron losses will be also be considered and the equivalent circuit type representation of the PMSM is shown in Figure 12.

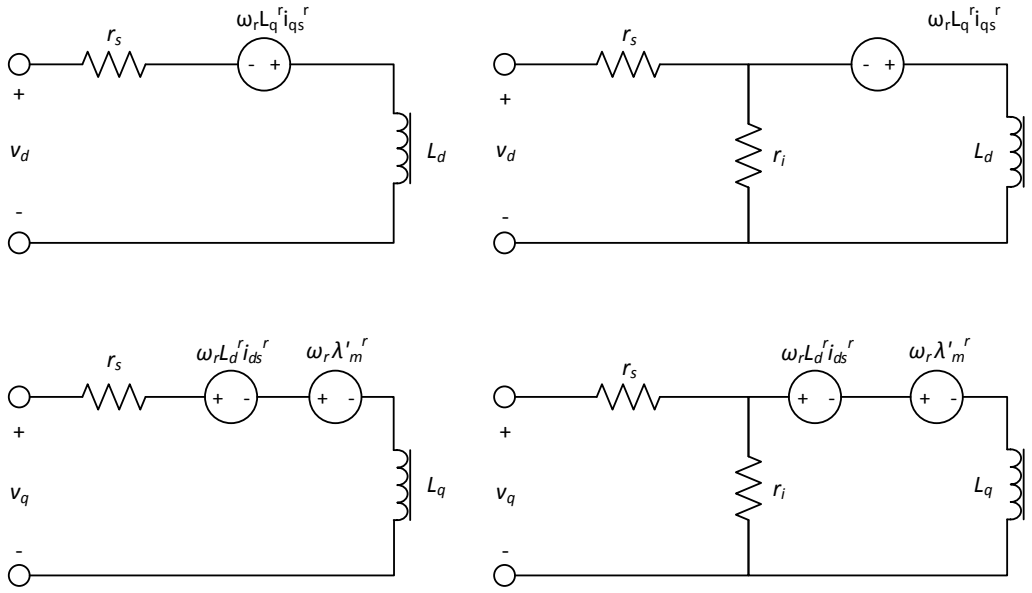

Figure 12: PMSM Equivalent Circuit including Iron Loss

The inclusion of iron losses reduces the amount of useful current delivered to the magnetic circuit. At steady state, the time derivative in the *d-q* stator voltage equations trend to zero and the equations reduce to [34],

$$v_{qs}^{r} = r_s i_{qs}^{r} + \left(1 + \frac{r_s}{r_i}\right)(\omega_r L_d i_{ds}^{r} + \omega_r \lambda_m'^{r}) \quad \textbf{(2-65)}$$

$$v_{ds}^{r} = r_s i_{ds}^{r} - \left(1 + \frac{r_s}{r_i}\right)\omega_r L_q i_{qs}^{r} \quad \textbf{(2-66)}$$

Because the three phases are balanced, the zero sequence equation equals zero. The inclusion of both iron and copper losses will provide two parameters that can help tune the model to represent the published performance data. The aggregate sum of these losses can be simulated to dynamically estimate electric machine efficiency when coupled with a motor drive.

2.2.2.1 Inverter and Drive System

A voltage source inverter (VSI) is one of the most commonly encountered switching converters used in traction drive applications. In an AES applications, VSI drives are often preferred because of their near unity power factor on the AC distribution system [2]. The alternate drive configuration for an AC motor is the current source inverter (CSI) whose details are not discussed here. The interested reader can find details on the CSI in Krause [32], Adnanes [81], and Hansen [2].

The commercial motor selected for the case study uses a VSI with Space Vector Pulse Width Modulation (SVPWM). In order to construct an average value model representation suitable for system-level simulation, a dynamic averaging technique must be implemented to eliminate the need to resolve switching devices, yet preserve the dominant converter dynamics. The PMSM motor and VSI drive circuit is presented in Figure 13.

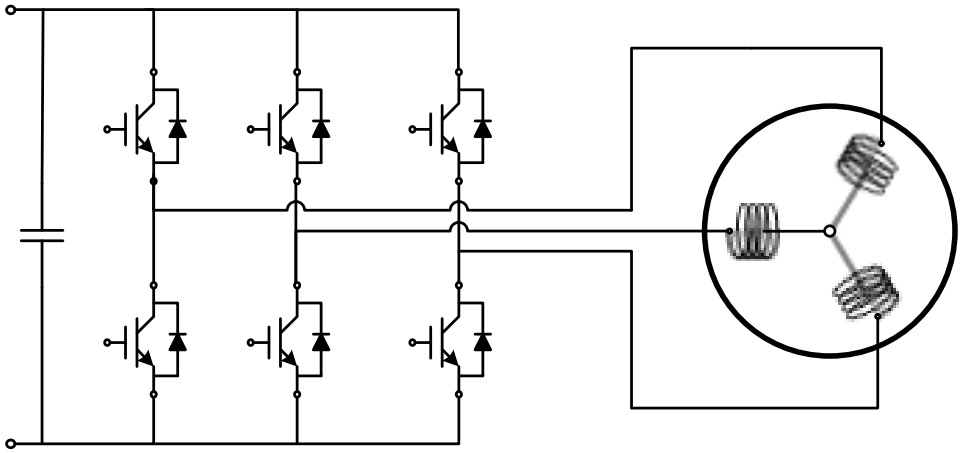

Figure 13: Inverter/Motor Topology

SVPWM is an advanced modulation technique for applying 3-phase voltage waveforms to the electric machine that are devoid of low frequency harmonics [32]. The switching algorithm is defined within the *d-q* transformation framework. The input voltage reference is sampled at the beginning of each switching cycle, then the algorithm computes the switching sequence and dwell time to achieve the voltage commanded [32]. The space vector modulation strategy is best explained in terms of the space vector diagram shown in Figure 14. The *d-q* modulator achieves the desired voltage using the eight discrete switching states defined by the inverter bridge switch permutations.

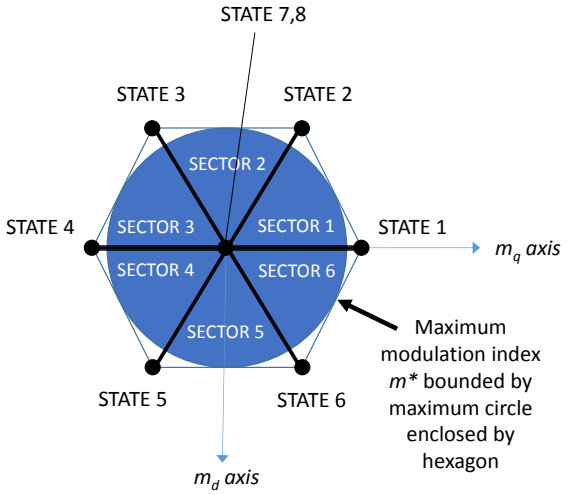

Figure 14: Space Vector Diagram

A more comprehensive treatment of the SVPWM strategy can be found in Krause [32]. Insight into the low-level switching behaviour is necessary for establishing a time-averaged simulation model as will be seen in the following section. Verification of any average value models must include comparison against a detailed simulation where the exact switching pattern of the inverter bridge based is modeled.

In control synthesis of VSI drives, the dynamics of the converter bridge can be modeled as a first order transfer function with a time constant equal to that of the switching frequency period Krishnan [33] or,

$$G_{conv}(s) = \frac{1}{\tau_s s + 1} \quad \textbf{(2-67)}$$

A time-averaged dynamic loss model for the semiconductors of the VSI can be developed with insight into the SVPWM switching cycles and current waveforms. In the work of Bierhoff and Fuchs [38], the authors develop an analytical expression for the total bridge losses associated with a SVPWM switching strategy. The total energy losses from the inverter bridge consists of switching losses in turn-on and turn-off, as well as conduction losses from switching devices and freewheel diodes. The total energy loss for a pair of switches is given by,

$$\dot{E}_{Inv,loss} = \dot{E}_{sl} + \dot{E}_{cl,I} + \dot{E}_{cl,D} \quad \textbf{(2-68)}$$

where,

Total Switching Loss:
$$\dot{E}_{sl} = \frac{f_s}{\pi}\left(E_{on,I} + E_{\mathrm{off},I} + E_{\mathrm{off},D}\right)\frac{V_{DC}}{V_{ref}} \cdot \frac{I_L}{I_{ref}} \quad \textbf{(2-69)}$$

IGBT Conduction Loss:
$$\dot{E}_{cl,I} = \frac{V_{CE,0} I_L}{2\pi}\left[1 + \frac{M\pi}{4}\cos(\delta)\right] + \frac{R_{CE} {I_L}^2}{2\pi}\left[\frac{\pi}{4} + \frac{2}{3} M\cos(\delta)\right] \quad \textbf{(2-70)}$$

Diode Conduction Loss:
$$\dot{E}_{cl,D} = \frac{V_{F,0} I_L}{2\pi}\left[1 - \frac{M\pi}{4}\cos(\delta)\right] + \frac{R_F {I_L}^2}{2\pi}\left[\frac{\pi}{4} - \frac{2}{3} M\cos(\delta)\right] \quad \textbf{(2-71)}$$

The parameters are given by,

V_{ref}	Reference voltage for switching energy loss
I_{ref}	Reference current for switching energy loss
f_s	Carrier switching frequency
V_{DC}	DC source voltage
I_L	Peak value of the AC line current (assumed sinusoidal)
$E_{on,I}$	IGBT turn-on switching energy losses
$E_{\mathrm{off},I}$	IGBT turn-off switching energy loss
$E_{\mathrm{off},D}$	Diode turn-off switching energy loss
M	Modulation index
$V_{CE,0}$	Threshold voltage across collector/emitter for IGBT in on-state
R_{CE}	Differential resistance of IGBT in on-state
$V_{F,0}$	Threshold voltage across collector/emitter for diode in on-state
R_F	Differential resistance of diode in on-state
δ	Displacement angle between fundamental voltage and load current

These equations were also used in Chao et al. [34] to develop efficiency maps for PMSM electric drive systems. We can therefore make an approximation for the energy losses in the inverter bridge as part of our simulation model using information contained within semiconductor datasheets with similar power ratings; however, the modulation index and displacement angle of the load must be computed as part of the AVM.

2.2.2.2 Electric Drive System Simulation

The previous sections presented the theoretical background governing the dynamics of a PMSM electric drive system. The *d-q* transformed governing equations are well suited for dynamic simulation; however, the inverter bridge requires signal averaging to reduce computational burden. The AVM of the total electric drive system, including both the machine and the VSI, must preserve the dominant converter dynamics, yet also needs to produce the modulation index and load angle δ for the dynamic loss model.

Krause [32] and Husain [23] discuss averaged simulation models for PMSM drive systems. Using conservation of energy and neglecting converter losses, the averaged DC current drawn by the inverter bridge can be expressed as,

$$\hat{\imath}_{dc} = \frac{3}{2}\frac{\hat{v}_{qs}^{r}\hat{\imath}_{qs}^{r} + \hat{v}_{ds}^{r}\hat{\imath}_{ds}^{r}}{\hat{v}_{dc}} \qquad \textbf{(2-72)}$$

Note that averaged values are expressed using the notation ($\hat{\cdot}$). The DC current is the input variable for motor/drive subsystem. It can be shown that the DC input current can be related to the modulation index and the converter angle ϕ_v as follows [32],

$$\hat{\imath}_{dc} = \frac{3}{2}M\left(\hat{\imath}_{qs}^{r}\cos\phi_v - \hat{\imath}_{ds}^{r}\sin\phi_v\right) \qquad \textbf{(2-73)}$$

This expression provides a simple relationship between modulation index and averaged input current. Now, the machine dynamics can be represented by average value expressions,

$$p\hat{\imath}_{qs}^{r} = \frac{\hat{v}_{qs}^{r} - r_s\hat{\imath}_{qs}^{r} - \omega_r L_d\hat{\imath}_{ds}^{r} - \omega_r\lambda_m'}{L_q} \quad \textbf{(2-74)}$$

$$p\hat{\imath}_{ds}^{r} = \frac{\hat{v}_{ds}^{r} - r_s\hat{\imath}_{ds}^{r} + \omega_r L_q\hat{\imath}_{qs}^{r}}{L_d} \quad \textbf{(2-75)}$$

The rotational frequency is assumed to be varying slowly as compared to the switching cycle; therefore, angular velocity can be considered constant over the averaging period. SVPWM provides a low-ripple torque output as a result of eliminating low frequency harmonics; therefore, the averaged torque can be written as,

$$\hat{T}_e = \frac{3}{2}\frac{P}{2}\left(\lambda_m'\hat{\imath}_{qs}^{r} + \left(L_d - L_q\right)\hat{\imath}_{qs}^{r}\hat{\imath}_{ds}^{r}\right) \quad \textbf{(2-76)}$$

Note, the preceding discussion also assumes that the DC bus voltage is constant or slowly varying as compared with switching frequency. This assumption is valid considering that the DC bus voltage is regulated. The overall simulation model information flow can be described by the block diagram in Figure 15.

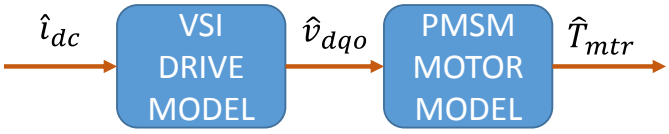

Figure 15: PMSM Drive AVM Block Diagram

2.2.3 Power Converter Modeling

AES architectures can consist of multiple types of power converters that convert between fixed frequency AC, variable frequency AC, and DC power supplies. Typical marine power converters are comprised of semiconductor devices including diodes, thyristors, SCRs, IGBTs, etc. depending on the application. A comprehensive overview of marine power electronic converters can be found in Adnanes [81], but detailed

treatment of this subject is beyond the scope of this work. A DC grid distribution system will be modeled for this case study, which inherently requires a power converter interface for all system components that attached to the bus. The interfacing converters are required for the several reasons:

- Control of harmonic content on DC distribution bus
- DC voltage regulation
- Fault mitigation and control
- Supervisory system control

Power converters are non-linear systems that require special attention. The previous section discussed average value modeling of a VSI converter in the context of developing a simulation model for the main propulsion motors. The switching dynamics of power converters are extremely fast relative to ship motion; therefore, much of the high frequency dynamics can be neglected for the present objectives. Moving forward into the SIL platform development, averaged value models for the other switching converters will be developed following the approach of Zahedi and Norum [26].

The BEIPS architecture requires a model for the main high power bi-directional DC/DC converter, which interfaces the battery-based energy storage system. In addition, a DC/AC islanding converter is required for servicing the AC hotel loads. For these converters, a simplified power loss modeling approach will be used to capture losses, but dynamics will be ignored. The efficiency is given as a function of the power requested as shown in Figure 16.

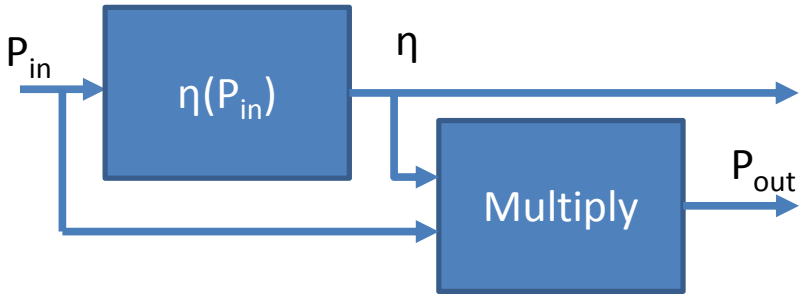

Figure 16: Power Loss Model for Converters

The islanding converter is unidirectional and its implementation is straightforward. The DC/DC converter is bi-directional; therefore, its implementation requires some additional functionality to account for losses when power flow is reversed. Unlike most AES applications that include energy storage, the DC/DC converter will be used to regulate the DC grid bus voltage in the absence of an electrical generation system. In this type of system, battery current is manipulated as the control variable in both buck and boost mode. The detailed implementation is discussed in Chapter 5.

2.2.4 Lithium-Ion Battery Rapid Charging

The BEIPS concept under investigation is intended to use frequent fast-charging cycles to replenish the energy consumed during a single crossing; therefore, a model of the charging infrastructure is required for inclusion in the simulation. The intent is to investigate the use of rapid-charging cycles during each load/unload periods, at both terminals. The charging process for lithium-ion batteries begins with a constant current (CC) supply which is held until the maximum rated battery voltage is reached. At this point, the charger switches to a constant voltage (CV) and the current gradually decays to zero. This is referred to a CC/CV charging cycle. The process is illustrated graphically in Figure 17.

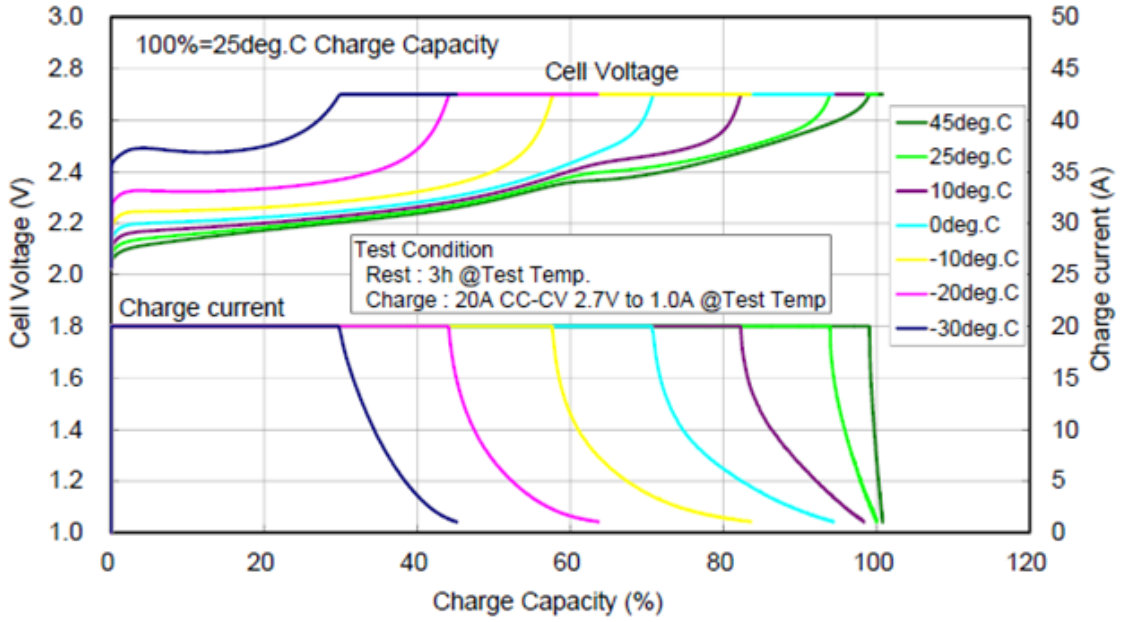

Figure 17: Cell Voltage as a Function of Charge Rate

During a rapid charge cycle, the CV portion of the charge may not be executed and the charge is stopped as soon as the maximum voltage is achieved. The SOC at which the maximum voltage is achieved is dependent upon the charge rate. Higher charge rates will cause the battery to reach its maximum voltage at a lower SOC in comparison to lower charge rates as seen in Figure 17. This process is also temperature sensitive.

The charging infrastructure must have sufficient capacity to deliver the energy required for a single-crossing with a reasonable safety factor to be conservative. Time constraints imposed by the sailing schedule dictate the charge rate. The design and assumptions of the charge system is presented in detail in Chapter 5. Recalling that the battery model's input variable is current and the output is voltage, the CC/CV charging system is implemented using two PID controllers that use the appropriate feedback variables depending on the charge mode.

2.3 Vessel Dynamics Modeling

2.3.1 Ship Dynamics Modeling

To this point we have addressed the background relating to modeling and simulation of the IPS components and thrust production. The last major remaining sub-section of the plant model is the representation of the ship motion dynamics in response to environmental and actuator forces. The detailed physics that govern vessel motion are represented by complex fluid mechanics, making the vehicle dynamics model for marine applications significantly more involved than in automotive studies; however, the dynamic response of ships has been studied extensively in classical marine literature through seakeeping and maneuvering analyses. This foundation provides the theoretical basis for development of parametric vessel model.

Seakeeping analysis is generally conducted to investigate the vessel's response to sinusoidal excitation while traveling at constant course and constant speed. This type of analysis is used primarily to predict the induced motion from wave excitation. Maneuvering theory, on the other hand, is conducted assuming no waves are present, and the focus lies in studying the vessel's trajectory and response when executing a prescribed maneuver.

In this work, the objective is to develop a holistic framework that can account for propulsive effects during both free motion at different sea states. Application of unified seakeeping/maneuvering theory discussed by Fossen [63] provides a foundational structure for developing the vessel's dynamic equations. This section provides a summary of the relevant theory relating to floating body dynamics, and introduces the Marine Systems Simulator (MSS) toolbox developed by Perez and Fossen [78] that will be used in the development.

2.3.2 Coordinate System Definitions and Notation

One of the major differences between the seakeeping and maneuvering analysis involves the choice of inertial coordinate system. We will define the global inertial frame using the North-East-Down convention. Displacements with respect to the inertial frame are represented by the position vector,

$$\boldsymbol{\eta} = [N \quad E \quad D \quad \phi \quad \theta \quad \psi]^T \qquad \textbf{(2-77)}$$

In both seakeeping and maneuvering studies, a body-fixed coordinate system is defined for convenience, largely because hydrodynamic coefficients are generally referenced to this frame. The instantaneous velocity of the ship in the body-fixed frame is denoted as,

$$\boldsymbol{\nu} = [u \quad v \quad w \quad p \quad q \quad r]^T \qquad \textbf{(2-78)}$$

where, u is velocity in surge
v is velocity in sway
w is velocity in heave
p is angular velocity of roll
q is angular velocity of pitch
r is angular velocity of yaw

In seakeeping analysis, another reference frame is defined to represent the equilibrium position of the ship traveling at a constant speed and at a constant course. This represents the equilibrium position of the ship in the absence of waves. For a given heading angle $\bar{\psi}$, the seakeeping frame is expressed in the NED inertial coordinates by,

$$\boldsymbol{v}_{s/n}^{n} = [U\cos\bar{\psi} \quad U\sin\bar{\psi} \quad 0]^T \qquad \textbf{(2-79)}$$

Motion and displacements relative to the equilibrium are defined using relative motion analysis. Perturbation coordinates are used to define relative displacement relative to the seakeeping frame.

$$\delta\boldsymbol{\eta} = \begin{bmatrix} \boldsymbol{r}^{\boldsymbol{s}}_{\boldsymbol{b/s}} \\ \boldsymbol{\Theta}_{\boldsymbol{sb}} \end{bmatrix} \quad \textbf{(2-80)}$$

$$\boldsymbol{r}^{\boldsymbol{s}}_{\boldsymbol{b/s}} = [\delta x \quad \delta y \quad \delta z]^T \quad \textbf{(2-81)}$$

$$\boldsymbol{\Theta}_{\boldsymbol{sb}} = [\delta\theta \quad \delta\phi \quad \delta\psi]^T \quad \textbf{(2-82)}$$

Velocity perturbations, expressed in body-fixed frame are defined as,

$$\delta\boldsymbol{\nu} = \begin{bmatrix} \delta\boldsymbol{\nu_1} \\ \delta\boldsymbol{\nu_2} \end{bmatrix} = \begin{bmatrix} [\delta u & \delta v & \delta w]^T \\ [\delta p & \delta q & \delta r]^T \end{bmatrix} \quad \textbf{(2-83)}$$

Coordinates in the body-fixed frame can be transformed into the seakeeping frame using a transformation defined by the Euler angle transformation matrix. It is critical to highlight a key distinction between seakeeping coordinates and generalized coordinates for maneuvering models. We define,

$\dot{\boldsymbol{\eta}} = \boldsymbol{J_\Theta}(\boldsymbol{\eta})\boldsymbol{\nu}$ **(2-84)** ⇒ Coordinate transformation from body-fixed frame to NED inertial frame

$\delta\dot{\boldsymbol{\eta}} = \boldsymbol{J_\Theta}(\delta\boldsymbol{\eta})\delta\boldsymbol{\nu}$ **(2-85)** ⇒ Coordinate transformation from body-fixed frame to seakeeping frame

A detailed explanation of the J_Θ transformation matrix can be found in [63] and is presented here without explanation. The objective now is to develop a linear transformation to allow for transition between seakeeping perturbations coordinates $(\delta\boldsymbol{\nu}, \delta\boldsymbol{\eta})$ to body fixed-NED coordinates $(\boldsymbol{\nu}, \boldsymbol{\eta})$. If we consider a ship moving at constant speed and constant course about its equilibrium position, the velocity of the ship in body-fixed frame is expressed as the sum of the average velocity and the perturbation velocity,

$$\boldsymbol{\nu_1} = \bar{\boldsymbol{\nu}}_{\boldsymbol{1}} + \delta\boldsymbol{\nu_1} \quad \textbf{(2-86)}$$

Using relative motion analysis and assuming small angular displacements, the average velocity $\bar{\boldsymbol{\nu}}_{\boldsymbol{1}}$ can be approximated by [63],

$$\bar{\boldsymbol{\nu}}_{\mathbf{1}} = U\begin{bmatrix} \cos\delta\psi\cos\delta\theta \\ -\sin\delta\psi\cos\delta\phi + \cos\delta\psi\sin\delta\theta\sin\delta\phi \\ \sin\delta\psi\sin\delta\phi + \cos\delta\psi\cos\delta\phi\sin\delta\theta \end{bmatrix} \approx U\begin{bmatrix} 1 \\ -\delta\psi \\ \delta\theta \end{bmatrix} \quad \textbf{(2-87)}$$

The average angular velocity in roll, pitch, and yaw is assumed to be zero; therefore, we can write,

$$\boldsymbol{\nu} = \bar{\boldsymbol{\nu}} + \delta\boldsymbol{\nu} \quad \textbf{(2-88)} \qquad \text{where, } \bar{\boldsymbol{\nu}} \approx U[1 \quad -\delta\psi \quad \delta\theta \quad 0 \quad 0 \quad 0]^T \quad \textbf{(2-89)}$$

By defining the vector $\boldsymbol{e_1}$ and matrix $\boldsymbol{L}$ as follows,

$$\boldsymbol{e_1} \equiv \begin{bmatrix} 1 \\ 0 \\ 0 \\ 0 \\ 0 \\ 0 \end{bmatrix} \quad \textbf{(2-90)} \qquad \text{and,} \qquad \boldsymbol{L} \equiv \begin{bmatrix} 0 & 0 & 0 & 0 & 0 & 0 \\ 0 & 0 & 0 & 0 & 0 & 1 \\ 0 & 0 & 0 & 0 & -1 & 0 \\ 0 & 0 & 0 & 0 & 0 & 0 \\ 0 & 0 & 0 & 0 & 0 & 0 \\ 0 & 0 & 0 & 0 & 0 & 0 \end{bmatrix} \quad \textbf{(2-91)}$$

Fossen [63] writes the velocity expressions given by Equation (2-88) and Equation (2-89) in matrix form,

$$\boldsymbol{\nu} \approx U(\boldsymbol{e_1} - L\delta\boldsymbol{\eta}) + \delta\boldsymbol{\nu} \quad \textbf{(2-92)}$$

From this expression, the perturbations velocities and accelerations expressed in body-fixed frame as [63],

$$\delta\boldsymbol{\nu} \approx \boldsymbol{\nu} + U(\boldsymbol{L}\delta\boldsymbol{\eta} - \boldsymbol{e_1}) \quad \textbf{(2-93)}$$

$$\delta\dot{\boldsymbol{\nu}} \approx \dot{\boldsymbol{\nu}} + U(\boldsymbol{L}\delta\boldsymbol{\nu}) = \dot{\boldsymbol{\nu}} + U\boldsymbol{L}\big(\boldsymbol{\nu} + U(\boldsymbol{L}\delta\boldsymbol{\eta} - \boldsymbol{e_1})\big) \quad \textbf{(2-94)}$$

The Euler angles relating the seakeeping perturbations coordinates $(\delta\boldsymbol{\nu}, \delta\boldsymbol{\eta})$ to NED coordinates is given by,

$$\begin{bmatrix}\phi\\ \theta\\ \psi\end{bmatrix} = \begin{bmatrix}0\\ 0\\ \bar{\psi}\end{bmatrix} + \begin{bmatrix}\delta\phi\\ \delta\theta\\ \delta\psi\end{bmatrix} \quad \textbf{(2-95)}$$

This is an important result for unifying maneuvering and seakeeping theory into a single model; however, there is a range of applicability for this type of formulation. The above relationships assume perturbations about a cruise velocity U which works well for in-transit analysis; however, this definition can breakdown with large scale perturbations or significant changes in forward speed.

2.3.3 Seakeeping Analysis and the Classical Frequency-Domain Model

Seakeeping analysis is typically conducted in the frequency domain assuming harmonic excitation. In classical hydrodynamic literature, the formulation of the equations of motion are constructed within a linear framework under the assumption that forces can be summed using superposition. It is often convenient for notational simplicity to replace perturbation notation with a change of variable for time domain equations,

$$\boldsymbol{\xi} = \delta\boldsymbol{\eta} \quad \textbf{(2-96)}$$

The equations of motion governing a floating structure undergoing forced oscillations are expressed as follows,

$$\boldsymbol{M}_{RB}\ddot{\boldsymbol{\xi}} = \boldsymbol{M}_{RB}\delta\dot{\boldsymbol{\nu}} = \delta\boldsymbol{\tau}_{\boldsymbol{RB}} \quad \textbf{(2-97)}$$

$$\text{where,} \quad \dot{\boldsymbol{\xi}} = \delta\boldsymbol{\nu} \quad \textbf{(2-98)}$$

$$\boldsymbol{M}_{RB} = \begin{bmatrix} m & 0 & 0 & 0 & 0 & 0\\ 0 & m & 0 & 0 & 0 & 0\\ 0 & 0 & m & 0 & 0 & 0\\ 0 & 0 & 0 & I_{xx} & I_{xy} & I_{xz}\\ 0 & 0 & 0 & I_{yx} & I_{yy} & I_{yz}\\ 0 & 0 & 0 & I_{zx} & I_{zy} & I_{zz} \end{bmatrix} \quad \textbf{(2-99)}$$

The sum of forces acting on the body is decomposed into three components,

$$\boldsymbol{\tau}_{RB} = \boldsymbol{\tau}_{hyd} + \boldsymbol{\tau}_{hs} + \boldsymbol{\tau}_{exc} \quad \textbf{(2-100)}$$

The excitation forces imposed on the body are captured by $\boldsymbol{\tau}_{exc}$. The hydrostatic forces from the vessel's displacement is encompassed in the vector $\boldsymbol{\tau}_{hs}$. Lastly, the hydrodynamic forces imposed by the fluid as result of the motion are represented by $\boldsymbol{\tau}_{hyd}$. Cummins [61] showed that the hydrodynamic radiation forces acting on a body subjected to forced oscillation in an inviscid fluid can be expressed by,

$$\boldsymbol{\tau}_{rad} = -\boldsymbol{A}_{\infty}\ddot{\boldsymbol{\xi}} + \int_0^t \boldsymbol{K}\,(t-\kappa)\dot{\boldsymbol{\xi}}(t)d\kappa \quad \textbf{(2-101)}$$

The term $\boldsymbol{A}_{\infty}$ represents the added mass at infinite frequency. The term $\boldsymbol{K}(t)$ is a matrix of retardation functions that capture the time-history of impulse forces arising from the disturbed water surface as a result of ship motion [61]. Using an inverse Fourier transform, the retardation function can be defined as a function of frequency-dependent damping coefficients [61],

$$\boldsymbol{K}(t) = \frac{2}{\pi}\int_0^{\infty} \boldsymbol{B}(\omega)\cos(\omega t)d\omega \quad \textbf{(2-102)}$$

Hydrodynamic solvers compute added mass and damping coefficients as function of frequency. This can in turn be used to numerically solve for $\boldsymbol{K}(t)$; however, the coming sections will illustrate an alternate approach using state space transfer function fitting for increased computational efficiency.

Substituting the expressions for hydrodynamic and hydrostatic forces into the Equation (2-97), the linear time-domain equation of motion for forced oscillation is,

$$[\boldsymbol{M}_{RB} + \boldsymbol{A}_{\infty}]\ddot{\boldsymbol{\xi}}(t) + \int_0^t \boldsymbol{K}(t-\kappa)\dot{\boldsymbol{\xi}}(t)d\kappa + \boldsymbol{C}\boldsymbol{\xi}(t) = \boldsymbol{\tau}_{exc} \quad \textbf{(2-103)}$$

The matrix $\boldsymbol{C}$ represents the hydrostatic forces resulting from displacement of the body. When the excitation forces are considered to be sinusoidal and at a constant frequency, the time-domain equation can be transformed into frequency-domain [63], [66], [62].

$$(-\omega^2[\boldsymbol{M} + \boldsymbol{A}(\omega)] - j\omega\boldsymbol{B}(\omega) + \boldsymbol{C})\tilde{\boldsymbol{\xi}}(j\omega) = \tilde{\boldsymbol{\tau}}_{exc}(j\omega) \quad \textbf{(2-104)}$$

Hydrodynamic codes employ 3D potential flow solvers or 2D strip theory to compute the added mass coefficients $\boldsymbol{A}(\omega)$ and damping coefficients $\boldsymbol{B}(\omega)$ for the linear equation of motion at a specified vector of discrete frequencies. It is essential to note that the damping coefficients from the hydrodynamic code only represent potential damping, and do not consider viscous effects that are present in a real fluid. Additional resistive terms are added to account for these effects as discussed in section 2.3.5.

The classical frequency domain equation derived uses perturbation coordinates from the inertial seakeeping frame. As we move towards development of a unified seakeeping/maneuvering model, it is more convenient to express equations in the body-fixed frame. Substituting equations (2-93) and (2-94) into the time domain equation of motion (2-103) [63],

$$[\boldsymbol{M}_{RB} + \boldsymbol{A}_{\infty}](\dot{\boldsymbol{\nu}} + U\boldsymbol{L}\boldsymbol{\nu}) + \int_0^t \boldsymbol{K}(t-\kappa)[\boldsymbol{\nu} - U\boldsymbol{e}_1]d\kappa + \boldsymbol{C}\boldsymbol{\eta} = \boldsymbol{\tau}_{ext} \quad \textbf{(2-105)}$$

Note that the Ogilvie formulation for the retardation function, which provides greater stability for numerical evaluation, has not been applied because the retardation function will be estimated using a transfer function fitting approach. The reader is directed to [82]

and [63] for details. Finally, it is convenient to expand the first term and lump like terms for further simplification to reach the time domain seakeeping equation,

$$\boldsymbol{M}\dot{\boldsymbol{\nu}} + \boldsymbol{C}^{*}\boldsymbol{\nu} + \int_{0}^{t} \boldsymbol{K}(t-\tau)[\boldsymbol{\nu} - U\boldsymbol{e}_1]d\tau + \boldsymbol{G}\boldsymbol{\eta} = \boldsymbol{\tau}_{external} \qquad \textbf{(2-106)}$$

$$\text{where,} \quad \boldsymbol{M} = \boldsymbol{M}_{\boldsymbol{RB}} + \boldsymbol{A}_{\infty} \qquad \textbf{(2-107)}$$

$$\boldsymbol{C}^{*} = \boldsymbol{C}^{*}_{\boldsymbol{RB}} + \boldsymbol{C}^{*}_{\boldsymbol{A}} = (U\boldsymbol{M}_{\boldsymbol{RB}}\boldsymbol{L} + U\boldsymbol{A}_{\infty}\boldsymbol{L}) \qquad \textbf{(2-108)}$$

Note that the hydrostatic stiffness matrix variable has been replaced to differentiate between Coriolis matrix terms. This linearized model does not consider the forward speed ship resistance, and assumes negligible perturbations in surge; therefore, a forward-speed resistive force model must be developed in matrix form to account for these effects. Treatment of forward speed effects is best done in the context of maneuvering.

2.3.4 Unified Seakeeping/Maneuvering Analyses for Vessel Dynamics Model

To this point, the matrix formulation of the equations of motion have only considered perturbation about an equilibrium point moving at constant speed and constant course. The resistive forces required to achieve the forward speed of the seakeeping frame are unaccounted for, thus this framework must be augmented to include the ship's forward speed resistance. Furthermore, the objective is to develop a model that can predict induced powertrain loads for a freely maneuvering ship; therefore, a maneuvering model must be selected to account for non-linear drag effects.

Though maneuvering models have been studied extensively in academic literature, these models have not demonstrated a high level accuracy. Bertram [68] discusses the

maturity levels of traditional maneuvering models and their limited success in comparison to seakeeping models and other vessel motion analysis techniques.

The selection of the maneuvering model depends on the design problem at hand. Three degree of freedom (DOF) surge-sway-yaw- models are the most common and widely used for simple maneuvering studies [63]; however, more accurate models have been developed to include the influence of roll [71]. Auto-pilot models can be as simple as a single DOF system, such as the second order yaw Nomoto system [83]. Referring back to the case study, the Klitsa is equipped with azimuthing propellers in a unique and highly maneuverable configuration, eliminating the classic rudder arrangement upon which maneuvering theory is generally founded. The barge-type hull is highly stable, so the roll subsystem will have minimal impact on its maneuvering characteristics; therefore, a 3-DOF model is appropriate for capturing the dominant dynamics.

One of the most widely used maneuvering models is the non-linear model of Abkowitz [69] which uses a 3rd order truncated Taylor series expansion of the maneuvering coefficients in the surge-sway-yaw systems. Bertram presents a set of non-dimensionalized maneuvering coefficients for various vessel classes for parameterization of the Abkowtiz non-linear model [68]. The Abkowitz model was developed primarily for ships with the following characteristics:

- Defined bow and stern
- Propeller(s) at the stern
- Rudder steering system

Many other maneuvering models have been developed over the years including work by Fedyaevsky and Sobolev [84], Norrbin [85], Nomoto [83], Ross [71], and more, which

require experimental model data for parameterization. In this work, the 3-DOF model based on surge resistance and cross-flow drag discussed in Fossen [63], has been selected for its ease of implementation in the absence of maneuvering coefficient data.

Returning back to Equation (2-106), the system is augmented to include the unaccounted resistive terms using a linear damping matrix $\boldsymbol{D_L}$, and non-linear damping matrix $\boldsymbol{D_N}$.

$$\boldsymbol{M\dot{\nu}} + \boldsymbol{C^*\nu} + \boldsymbol{D_L\nu} + \boldsymbol{D_N}(\boldsymbol{\nu}) + \int_0^t \boldsymbol{K}(t-\kappa)[\boldsymbol{\nu} - U\boldsymbol{e}_1]d\kappa + \boldsymbol{G\eta} = \boldsymbol{\tau}_{external} \qquad \textbf{(2-109)}$$

where,

$$\boldsymbol{D_L} = \begin{bmatrix} -X_u & 0 & 0 & 0 & 0 & 0 \\ 0 & -Y_v & 0 & 0 & 0 & -Y_r \\ 0 & 0 & 0 & 0 & 0 & 0 \\ 0 & 0 & 0 & 0 & 0 & 0 \\ 0 & 0 & 0 & 0 & 0 & 0 \\ 0 & -N_v & 0 & 0 & 0 & -N_r \end{bmatrix} \qquad \textbf{(2-110)}$$

$$\boldsymbol{D_N} = \begin{bmatrix} 1/2\,\rho S(1+k)C_f^{new}(u)\cdot|u|u \\ \frac{1}{2}\rho\int_{-L_{pp}/2}^{L_{pp}/2} T(x)C_d^{2D}(x)|v+xr|(v+xr)dx \\ 0 \\ 0 \\ 0 \\ \frac{1}{2}\rho\int_{-L_{pp}/2}^{L_{pp}/2} T(x)C_d^{2D}(x)x|v+xr|(v+xr)dx \end{bmatrix} \qquad \textbf{(2-111)}$$

With the addition of damping terms, this linearized integro-differential equation now includes both seakeeping terms and a 3-DOF non-linear maneuvering model to summarize the vessel dynamics. A discussion of parameterization and a detailed explanation of the viscous components of resistance are provided in the following section.

2.3.5 Formulation of Ship Resistance

Quantifying total ship resistance in dynamic conditions presents one of the major challenges in this reduced order modeling framework. Ship resistance calculations are typically computed at steady state assuming calm sea conditions. The underlying physics of fluid flow around the hull governing resistance is well beyond the scope of this document and will not be discussed in detail. The interested reader is directed to the comprehensive work of Larsson [86]. The decomposition of ship resistance in calm water is illustrated in Figure 18.

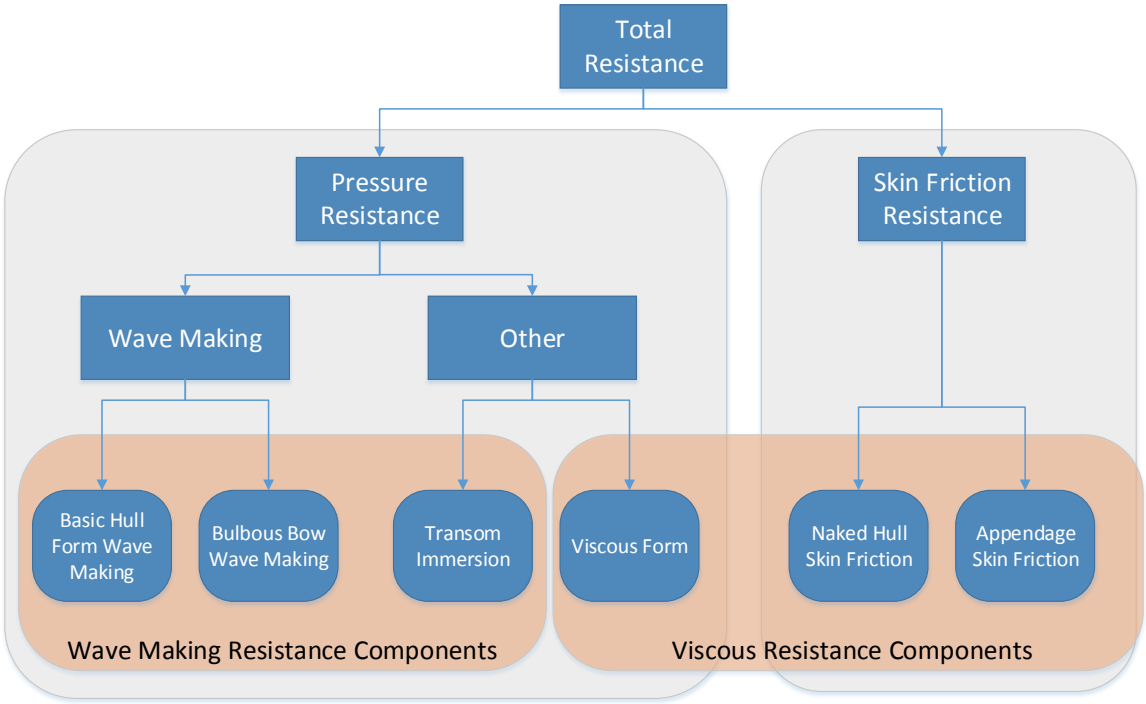

Figure 18: Traditional Ship Resistance Decomposition in Calm Water [51]

Additional forces arise from environmental factors such as wind and waves that contribute to the overall resistance. In practice, it is not effective to separate these effects into different analytical expressions. Rather, the ITTC78 standard describes the non-dimensionalized resistance coefficient as the sum of sub-coefficients that include skin friction, residual resistance, roughness allowance, and air resistance [87],

$$C_T = \underbrace{(1+k)C_F}_{\substack{Viscous\\ Friction\\ Coefficient}} + \underbrace{C_R}_{\substack{Residual\\ Resistance}} + \underbrace{\Delta C_F}_{\substack{Roughness\\ Allowance}} + \underbrace{C_{AA}}_{\substack{Air\\ Resistance}} \quad \textbf{(2-112)}$$

The hull's frictional coefficient C_f is defined as the equivalent friction of a flat plate with equal area to that of the hull's wetted surface, and is given by,

$$C_F = \frac{0.075}{(\log_{10} R_n - 2)^2} \quad \textbf{(2-113)}$$

The total viscous resistance is computed by multiplying flat plate friction by a hull form factor *k* to account for viscous dissipation in the fluid resulting from the hull's physical shape. The residual resistance coefficient is a lumped term that accounts for all other sources of resistance, including pressure resistance and wave-making resistance.

Wave-making resistance represents the losses associated with the energy imparted into the wave-pattern produced by ship motion. The addition of a bulbous bow can provide destructive interference in the wave system at predesigned operating speeds; thereby reducing the amount of energy that is lost in the wave system. Pressure drag accounts for a significant portion of the overall resistive force. As the viscous flow detaches from the ship, it produces a lower pressure at the stern which acts to resist the motion. Transom immersion, sink, and trim can also contribute to excess pressure-based drag. For a more comprehensive of the topic, see Carton [51] or Larsson [86].

The roughness coefficient accounts for the increased hull surface roughness that will naturally occur during operation as result of biofouling. A service allowance can be considered in the design stage to ensure that the propulsion system can meet the contract speed even after multiple years of operation. Finally, the air resistance coefficient

represents the resistive force from displacing air while the ship is moving at forward speed. This coefficient is dependent upon the surface area of the ship above the waterline.

The Klitsa is an open-deck low profile ferry where the air resistance will be negligible compared to other sources. This analysis will also assume no surface roughness effects; therefore, Equation (2-112) reduces to two coefficients: skin friction and residuals.

In traditional literature, the drag force acting on a floating body is typically decomposed into linear and non-linear components, see for example Fossen [63] or Faltinsen [62]. The equation of motion developed in the previous section established a linear damping matrix $\boldsymbol{D_L}$ and the non-linear drag matrix $\boldsymbol{D_N}$. The linear damping matrix can be further decomposed into potential and viscous damping terms [63],

$$\boldsymbol{D_L = D_P + D_V} \qquad \textbf{(2-114)}$$

As is customary for most ship analysis application, the surge subsystem will be decoupled from the remaining degrees of freedom. The potential damping associated with surge, sway, and yaw subsystems can be considered to be negligible compared to dominant viscous forces; however, potential damping will be significant impact on resistive forces in heave, pitch and roll [63]. Fossen [63] presents a method to estimate the potential damping in heave, roll, and pitch based on a spring-mass-damper system discussed in Chapter 4. Each DOF will contain viscous damping components, and the resulting linear damping matrix with SNAME notation is given by [63],

$$\boldsymbol{D_L} = -\begin{bmatrix} X_u & 0 & 0 & 0 & 0 & 0 \\ 0 & Y_v & 0 & Y_p & 0 & Y_r \\ 0 & 0 & Z_w & 0 & Z_q & 0 \\ 0 & K_v & 0 & K_p & 0 & K_r \\ 0 & 0 & M_w & 0 & M_q & 0 \\ 0 & N_v & 0 & N_p & 0 & N_r \end{bmatrix} \quad \textbf{(2-115)}$$

Where,

$$-X_u = B_{11v} \quad \textbf{(2-116)}$$

$$-Y_v = B_{22v} \quad \textbf{(2-117)}$$

$$-Z_w = B_{33v} + B_{33}(\omega_{heave}) \quad \textbf{(2-118)}$$

$$-K_p = B_{44v} + B_{44}(\omega_{roll}) \quad \textbf{(2-119)}$$

$$-M_q = B_{55v} + B_{55}(\omega_{pitch}) \quad \textbf{(2-120)}$$

$$-N_r = B_{66v} \quad \textbf{(2-121)}$$

Here, the potential damping matrix components B_{ij} represent the potential damping coefficients at the natural frequency of the second order spring-mass-damper systems. The coefficients B_{ijv} represent the linear viscous terms.

The non-linear damping for a ship in surge can be modeled by,

$$X = -\underbrace{\frac{1}{2}\rho S C_T(u_r)}_{X_{|u|u}} |u_r| u_r \quad \textbf{(2-122)}$$

S is the wetted surface area, and C_T is the total resistance coefficient from the ITTC definition of resistance in Equation (2-112). Neglecting air resistance and roughness allowance, and substituting the definition of frictional coefficient given by (2-113) into equation (2-112) we get,

$$C_T = \underbrace{\frac{0.075}{(\log_{10} R_n - 2)^2}}_{C_F}(1+k) + C_R \qquad \textbf{(2-123)}$$

Here R_n is the Reynold's number, which is of course dependent on the ship`s length L_{pp} and forward speed u_r.

$$R_n = \frac{u_r L_{pp}}{\upsilon} \qquad \textbf{(2-124)}$$

This linear/non-linear decomposition of resistance has been known to under predict surge resistance at low speed [63]. To address this shortcoming, Fossen [63] presents an exponential equation for adjusting the resistance as a function of forward speed,

$$C_T{}^{new}(u_r) = C_T(u_r{}^{max}) + \left(\frac{A_x}{S}C_X - C_T(u_r{}^{max})\right)\exp(-\alpha u_r{}^2) \qquad \textbf{(2-125)}$$

$$\text{where,} \quad C_X = \frac{S}{A_x}C_T \qquad \textbf{(2-126)}$$

Note that A_x represents the projected frontal area. The new surge damping coefficient can then be written as,

$$\begin{aligned} X &= -\frac{1}{2}\rho S C_T |u_r| u_r \\ &= -\frac{1}{2}\rho S |u_r| u_r \cdot \\ &\quad \left[C_T(u_r{}^{max}) + \left(\frac{A_x}{S}C_X - C_T(u_r{}^{max})\right)\exp(-\alpha u_r{}^2)\right] \end{aligned} \qquad \textbf{(2-127)}$$

An analytical expression is now available for computing non-linear surge resistance. To complete the 3-DOF maneuvering model based on cross-flow drag, we now require a method for predicting non-linear drag associated with coupled sway and yaw motions. The computation of non-linear cross-flow drag is performed by integrating the quadratic

drag equation across the waterline length of the vessel in both sway and yaw, respectively.

$$Y = -\frac{1}{2}\rho \int_{-\frac{L_{pp}}{2}}^{\frac{L_{pp}}{2}} T(x) {C_d}^{2D}(x) |v_r + xr| (v_r + xr)\, dx \qquad \textbf{(2-128)}$$

$$N = -\frac{1}{2}\rho \int_{-\frac{L_{pp}}{2}}^{\frac{L_{pp}}{2}} T(x) {C_d}^{2D}(x) x |v_r + xr| (v_r + xr)\, dx \qquad \textbf{(2-129)}$$

Here *T(x)* represents the ship's draft as function of longitudinal position *x*, and ${C_d}^{2D}$ is the 2-dimensional drag coefficient for ship's transverse cross-section as a function of position. The drag coefficients are predicted using data from Hoerner [88] which has been assembled into a Matlab function by Perez and Fossen [78] in the MSS toolbox.

2.3.6 Evaluation of the Fluid-Memory Effects

There is one remaining term to complete the integro-differential equation of motion for the ship dynamics model. The convolution term, which represents fluid memory effects associated with the radiation force, is not convenient for simulation in its current form. The convolution can be evaluated numerically at each timestep using hydrodynamic coefficient data; however, this can lead to increased simulation time as result of the increased computational burden. The convolution term also poses problems for motion control system synthesis [82].

Because the convolution integral is a linear operator, it can be represented by a set of linear time-invariant differential equations for the six degrees of freedom [82]. The fluid memory effects can be approximated by an accumulator-type state space system that summarizes the force history described in the convolution term. State space

representation exhibits the Markovian characteristic; whereby, at any instant in time, the instantaneous value contained within the state vector embodies the history of the system's response [82]. Here, the intermediate state variables are non-physical parameters, but whose differential equations are computed using system identification in the frequency-domain using hydrodynamic coefficient data.

The system identification process can be conducted in the time-domain or in the frequency domain as discussed by Perez and Fossen [82]. The intent is to replace the convolution with a system of the form,

$$\boldsymbol{\mu} = \int_0^t \boldsymbol{K}(t-\tau)\delta\boldsymbol{\nu}(\tau)d\tau \quad \Rightarrow \quad \begin{aligned} \dot{\boldsymbol{x}} &= \boldsymbol{A_r x} + \boldsymbol{B_r}\delta\boldsymbol{\nu} \\ \boldsymbol{\mu} &= \boldsymbol{C_r x} \end{aligned}$$

An algorithm can numerically fit the system response data to a transfer function by manipulating the structure, order, and coefficients of transfer functions to minimize the error between hydrodynamic data points and the fitted function. This is typically formulated as a least-squares error minimization problem. Potential flow solvers provide a discrete set of hydrodynamic data that is used for the fitting algorithm. The fitting process can be conducted in the time-domain, but the aggregate error that compounds from the discrete Fourier transformation and subsequent conversion to continuous time can be problematic. The error from each transformation propagates through the fitting procedure and can cause inaccuracies in the state space representation. Perez and Fossen [82] and Taghipour et al. [89] provide a comprehensive discussion of response curve fitting methods in both the time and frequency domain.

Perez and Fossen [82] conclude that frequency domain fitted systems are easier to implement and lead to superior representations of the convolution term in comparison to

time-domain fitting methods. Unnecessary errors are avoided by using hydrodynamic data directly.

In the work of Taghipour et al. [89], the authors implement this state-space approximation technique in Simulink and illustrate the computational benefits of this approach under different simulation timesteps. It was shown that as the timestep decreases, the simulation speed of the state space system has a stark advantage, being over 80 times faster than direct numerical computation. This advantage erodes away slightly when larger timesteps are used (>0.01s) [89]. Evidently there is a clear advantage to this approach, especially as timesteps are decreased to accommodate switching power converter components.

In this work, ShipMo3D is used to generate the hydrodynamic coefficient data for the Klitsa. This code is a 3D potential flow solver that can produce the infinite frequency added mass term numerically. The availability of the infinite frequency added mass term has implication on the fitting procedure; therefore, the following section presents a brief background on the frequency domain fitting process.

2.3.6.1 Frequency Domain System Identification

Hydrodynamic codes use either a 3D potential flow solver, or 2D strip theory to compute hydrodynamic coefficients as a function of frequency. Using Fourier analysis, the retardation function describing the fluid-memory effects can be expressed as,

$$\boldsymbol{K}(t) = \frac{2}{\pi}\int_0^\infty \boldsymbol{B}(\omega)\cos(\omega t)d\omega \qquad \textbf{(2-130)}$$

Taking the Fourier transform of the retardation function, the frequency-domain representation can be computed directly from the hydrodynamic coefficients [82],

$$\boldsymbol{K}(j\omega) = \int_0^{\infty} \boldsymbol{K}(t)e^{-j\omega t}d\omega \quad \textbf{(2-131)}$$

$$= \boldsymbol{B}(\omega) + j\omega[\boldsymbol{A}(\omega) - \boldsymbol{A}_{\infty}] \quad \textbf{(2-132)}$$

The curve-fitting procedure has been coded into the *FDIRadMod* function provided by the MSS toolbox [78]. This problem is formulated into a least-squares error minimization problem. The approximating transfer function is denoted by $\widehat{\boldsymbol{K}}_{ik}(j\omega)$ given by,

$$\widehat{\boldsymbol{K}}_{\boldsymbol{ik}}(s,\boldsymbol{\theta}) = \frac{P(s,\boldsymbol{\theta})}{Q(s,\boldsymbol{\theta})} = \frac{p_m s^m + p_{m-1}s^{m-1} + \cdots + p_0}{s^n + q_{n-1}s^{n-1} + \cdots + q_0} \quad \textbf{(2-133)}$$

The parameter $\boldsymbol{\theta}$ is a vector containing the transfer function coefficients and the indices *i,k* denote the degree of freedom being evaluated.

$$\boldsymbol{\theta} = [p_m, p_{m-1}, \dots, p_0, q_{n-1}, q_{n-2}, \dots, q_0]^T \quad \textbf{(2-134)}$$

Thus, the minimization problem can be written as follows,

$$\theta_{ik}{}^{*} = \arg\min_{\theta} \sum_{l} w_l \left|\boldsymbol{K}_{ik}(j\omega_l) - \widehat{\boldsymbol{K}}_{ik}(j\omega_l,\boldsymbol{\theta})\right|^2 \quad \textbf{(2-135)}$$

Note that w_l is a weighting function that can be included to allow more emphasis on specific frequencies if desired.

Computation of the retardation functions from equation (2-132)(2-31) requires the infinite frequency added mass. Only 3D solvers possess this functionality; consequently, 2D solvers require an estimation procedure to approximate this term. Instead, Perez and Fossen [82] assemble the work of Damaren [90] and Kaasen and Mo [91] to restructure this expression to be a function of damping coefficients only, thereby eliminating the need for the infinite frequency added mass terms. For specific details on this method, the reader is directed to Perez and Fossen [82] and Kaasen and Mo [91].

The fitting process can manipulate both the model order, and the transfer function coefficients to get the optimal fit. Certain characteristics of the transfer function can be gleaned by investigating zero and infinite frequency limits. Table 3 shows a list of properties that hold true for the retardation functions [82].

Table 3: Retardation Function Characteristics for Transfer Function Fitting

Mathematical Property		*Implications for transfer function approximation* K(s)
$\lim_{\omega \to 0} \boldsymbol{K}(j\omega) = \boldsymbol{0}$	$\Rightarrow$	Minimum of one zero at s = 0
$\lim_{\omega \to \infty} \boldsymbol{K}(j\omega) = \boldsymbol{0}$	$\Rightarrow$	Strictly proper
$\lim_{t \to 0^+} \boldsymbol{K}(t) \neq \boldsymbol{0}$	$\Rightarrow$	Relative degree 1
$\lim_{t \to \infty} \boldsymbol{K}(t) = \boldsymbol{0}$	$\Rightarrow$	BIBO stable

It also can be shown that the mapping between the perturbation vector $\dot{\boldsymbol{\xi}}$ is passively coupled to the memory effect force $\boldsymbol{\mu}$. This implies that the diagonal entries $\boldsymbol{K}_{ii}(j\omega)$ of the approximating transfer functions are positive real [82].

Using the above characteristics, the *FDIRadMod* function uses a Gauss-Newton algorithm that can be linearized and solved iteratively for each DOF to achieve a 6x6 matrix of state space systems that represent the convolution integral term $\boldsymbol{\mu}$.

$$\widehat{\boldsymbol{K}}(s) = \begin{bmatrix} \frac{P_{11}(s)}{Q_{11}(s)} & \cdots & \frac{P_{16}(s)}{Q_{16}(s)} \\ \vdots & \ddots & \vdots \\ \frac{P_{61}(s)}{Q_{61}(s)} & \cdots & \frac{P_{66}(s)}{Q_{66}(s)} \end{bmatrix} \quad \textbf{(2-136)}$$

2.3.7 Integration of ShipMo3D with Marine Systems Simulation Toolbox

The MSS toolbox can import data directly from two hydrodynamic codes: WAMIT, and VERES. WAMIT is a 3D code potential flow solver that computes hydrodynamic coefficients at zero forward speed. VERES is a 2D forward speed code based on strip theory that is well established in the naval architecture community. The MSS toolbox contains utilities to extract the necessary data from WAMIT and VERES output files in order to parameterize pre-defined blocksets and models.

ShipMo3D is a hydrodynamic code that has been developed by the Canadian Defense Research Council. This code has been experimentally validated against Canadian naval ships, and has been adopted by several Canadian naval architecture firms. SM3D is a 3D potential flow solver that also includes forward speed effects. It also possesses utilities for exporting to ProteusDS, which can be linked to Simulink for coupled dynamic simulation and visualization.

SM3D has been selected as the hydrodynamic solver to be used in this work, and a data extraction utility script has been created to parse the data into the necessary format for compatibility with the MSS toolbox.

2.4 Integrated Modeling – Assembling the Pieces for Study of Hybrid Electric Propulsion

This chapter has provided a detailed overview of the various sub-systems that must be integrated together to develop the general modeling framework for ship propulsion analysis. The task is now to develop the parametrization strategy for this set of models, and define the interaction between sub-systems.

The MBD approach to development enables both plant and controller be created within the same simulation environment. This development platform is also capable of

automated code generation to allow for seamless control hardware implementation without a separate programming effort. The process allows for rapid-prototyping and extensive testing in a lab environment before the system is deployed on a real vessel.

MBD has become the state-of-the-art development process in the automotive industry, and has proven to be an especially effective approach in developing hybrid electric vehicles which require complex real-time control. When extending this design approach to the marine industry, the complex physical flow characteristics governing hull resistance, thrust production, and their dynamic interactions must be simplified for computational efficiency. This will allow for rapid simulations and real-time system development. The previous sections have developed the theoretical background for implementation of the plant dynamics; however, these equations are parametric and require ship-specific data from either experimental model tests or analyses using computational fluid dynamics (CFD).

Hydrodynamic codes provide the necessary data for quantifying the hydrodynamic forces acting on the body in response to excitation. The hydrodynamic coefficients are also required for approximating the fluid memory effects with a state space representation that will improve computational efficiency of the simulation. SM3D shall be used because of its immediate availability at UVic, as well as its strategic value for seamless integration with ProteusDS in advanced motion control analysis with the Simulink-based powertrain platform.

A script was written to extract the relevant information from SM3D's output files and the ProteusDS hydrodynamic database that SM3D generates. This script also performs a coordinate system transformation to switch to the NED coordinate system used by the

MSS toolbox, as well as an origin location change to CO. The new origin lies at midships with z origin located on the waterplane. All force and moment data produced by SM3D is transformed to the new coordinate system. Note that ProteusDS uses a z-down coordinate system; therefore, data extracted from the hydrodynamic database only required a vertical shift from the center of gravity. Finally, the script also includes a mirroring algorithm to produce a complete set of data for seas ranging from 0-360 degrees.

Unsteady RANS CFD analyses can be used to develop estimates for ship resistance. CFD can also be used for generating propeller thrust and torque coefficients over multiple quadrants of operation. The data produced from CFD hull resistance studies allow for parameterization of the decoupled surge subsystem entries of the drag matrices. The results are decomposed into the standard linear and non-linear framework.

Thrust and torque coefficients are assembled into lookup surfaces which are functions of quadrant angle β defined by Equation (2-19), and relative flow angle α. The ship's instantaneous velocity vector and the azimuth angle define the relative flow angle seen by the propeller. The thrust production and torque models are also influenced by the presence of the hull which is accounted for using the standard wake fraction.

Wake fraction estimates can be generated as a function of forward speed by averaging the x-direction velocity component over the propeller's swept area in CFD resistance studies. This correction to incoming flow velocity is applied to the body-fixed forward speed vector u the get a more accurate representation of the propeller's inflow conditions.

The powertrain model consists of the IPS and all drivetrain components that deliver the mechanical rotation energy to the propeller's input shaft. The powertrain model can include any propulsion architecture from traditional diesel, AES, or hybridized systems.

The data for parameterizing the simulation models is sourced from manufacturers and component datasheets.

The model is actuated via a driver model, which can be implemented in various ways. The MSS toolbox has predefined autopilot blocks that can be used to maneuver the model between waypoints and with specified speed information; however, this work will use real-world driver inputs recorded from the data collection experiment on the M.V. Klitsa. The load cycle information is presented in Chapter 6.

The basic integration methodology and parameterization strategy is summarized in Figure 19.

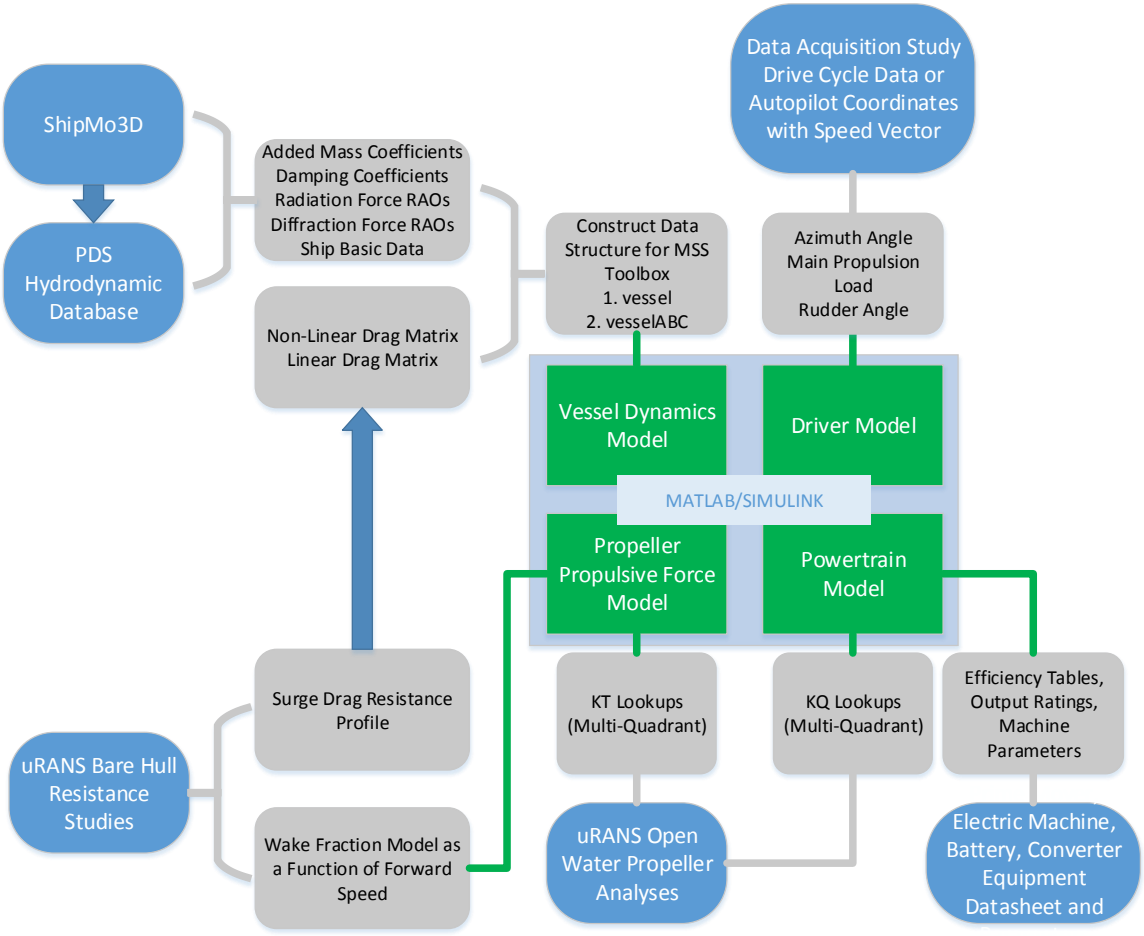

Figure 19: Simulation Platform Integration Methodology and Parameterization Strategy

The next chapters will develop these models in detail, illustrating the process using the M.V. Klitsa as an example. The process of model development is intended to be relatively parametric, and applicable to any other ship.

Chapter 3 Development of an Azimuthing Propeller Model for Integrated Powertrain Simulations

3.1 Model Development Methodology

Chapter 2 presented an overview of dynamic models that can be used for thrust and torque prediction, primarily in the context of model-based control development. The development of accurate thrust models is particularly important in high precision applications such as dynamic position, but it also provides a method of predicting power system loads during dynamic simulation, allowing aggregate performance to be analyzed over different mission cycles. For the case study of the Klitsa, the task is to develop a computationally efficient model of an azimuthing propeller, which will frequently encounter off-design propeller conditions when traveling in-and-out of berth.

First quadrant data is generally quite easy to obtain from the propeller manufacturer; however, acquiring data for beyond the first quadrant is often difficult. As a result, RANS CFD has been systematically deployed to perform parameter sweeps aimed at generating the necessary dataset to capture all realistic operating conditions. This dataset will create 2D lookup surfaces to estimate the load torque load acting on the IPS, as well as the actuation forces for the vessel in the time-domain.

Lookup table based performance models are common practice in automotive power system models, as they provide an excellent method of distilling down complex physics into a computationally efficient empirical models. Over time, and as the marine industry evolves to adopt MBD in practice, manufactures will likely begin to provide simulation models during the initial design phase as is done in the automotive industry.

This chapter systematically develops the simulation model for the azimuthing thrusters currently installed on the M.V. Klitsa. The work required to parameterize the equations

was a collaborative effort between Rahimpour and Andersen [92]. The CAD model generation, design of CFD experiment, and implementation of CFD results into the reduced order simulation model was conducted by the author of this work. The configuration and execution of CFD studies was conducted by Rahimpour with some support from Andersen. This chapter will systematically present the development process including,

a) The propeller's geometry generation and assumptions
b) Definition of quadrants and model layout
c) CFD results and validation
d) Simulink-based propeller model implementation

3.1.1 Thruster Geometry

The M.V. Klitsa is equipped with two well-mounted azimuthing propellers to enable a high degree of maneuverability. These units are designed for single-direction operation, as is typical when coupled to a diesel engine. The azimuthing tower enables thrust to be directed in any direction within the horizontal plane, regardless of the ship's direction of travel.

The first quadrant propeller coefficient curves were acquired from the manufacturer to serve as a validation tool for both the CFD analyses and the dynamic simulation model. A 3D geometry of the propeller was not provided by the manufacturer. Instead, the geometry was created from an electronic 2D drawing illustrating the propeller blade section geometry as function of radius. The drawing did not provide pitch distribution explicitly; however, the preliminary design documentation provided to BC Ferries from provided some pitch information that was leveraged to complete the 3D CAD model.

With the available information, the 3D geometry was approximated by tracing the 2D blade sections in CAD using Draftsight. The section profile data points were then imported into a 2D sketch within NX with the sketch plane tangent to a cylindrical surface of the respective radial sections. The 2D points were aligned using the pitch distribution data. Using the point of intersection between the directrix and the cylindrical blade section surface as the locating datum point, the 2D profile was wrapped to the cylindrical surface to create the blade section profile curve. This was repeated systematically until the full set of 3D profile curves were in place, thus allowing for surfaces to be built. The process of geometry creation is illustrated in Figure 20 through Figure 23.

This procedure, though somewhat crude, produced a plausible geometry that provided excellent results when compared to the manufacturer data, as will be seen section 3.3.1.1. The thruster also contains a standard 19A duct whose geometry is presented in Carlton [51]. The hub diameter and cone angle were approximated, and the blending of the blade was created using a surface extension tool in NX. The geometry has been removed of all fillets and edge breaks for import into StarCCM+ for RANS analysis.

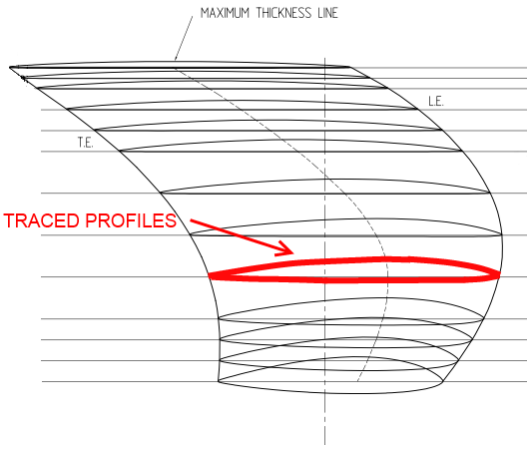

Figure 20: 2D Blade Profiles

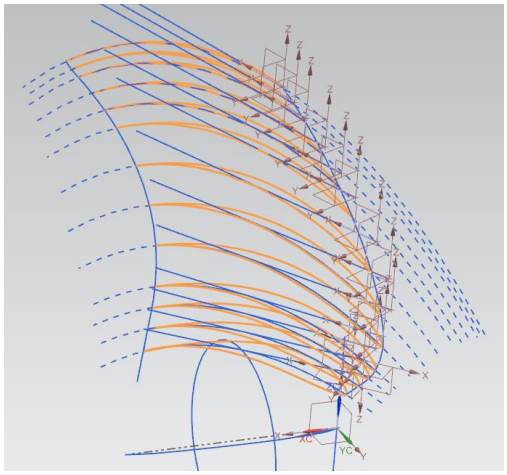

Figure 21: 3D Wrapping of 2D sections

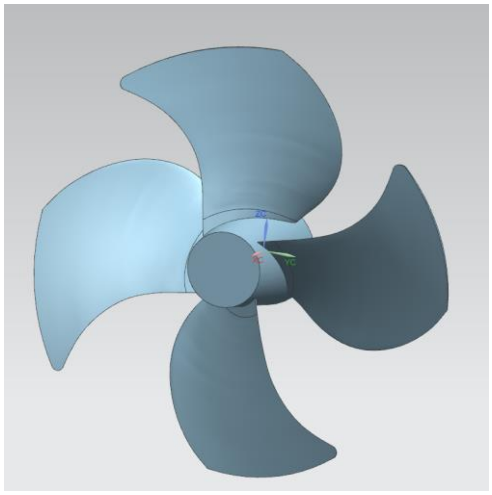

Figure 22: 3D Propeller Geometry

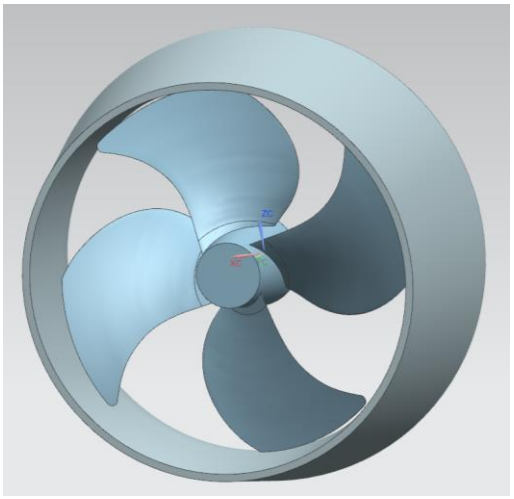

Figure 23: Propeller and 19A Duct

3.2 Quadrants of Operation and Off-Design Conditions

The operating conditions for a propeller in uniform flow is often characterized by a system of four quadrants that describes the relative direction of incoming flow and the propeller's direction of rotation. Referring back to Figure 8 and Figure 9 from Chapter 2, the first quadrant represents the normal operating condition with the ship traveling forward being propelled by the thrust developed by the propeller. The traditional second quadrant defines the "crash back" condition, where the propeller's direction of rotation is

reversed while the ship is still travelling forward to acting to brake the ship. The third quadrant represents the situation where the ship is moving backward with the propellers rotating in the reverse direction, thus propelling the ship in reverse. The fourth quadrant represents the "crash ahead" situation where the propeller rotation is positive but the ship is moving backwards.

As was seen in section 2.1.3, this definition needs to be extended with a third dimension to capture the extra degree of freedom from azimuth rotation. In the case of the Klitsa, the input shaft rotation is uni-directional; therefore, only the 1st and 4th quadrants of operation are possible with the traditional definition. However, we know that braking thrust can be generated by rotating the azimuthing propeller by 180°, enabling 2nd and 4th quadrant operation as illustrated Figure 24.

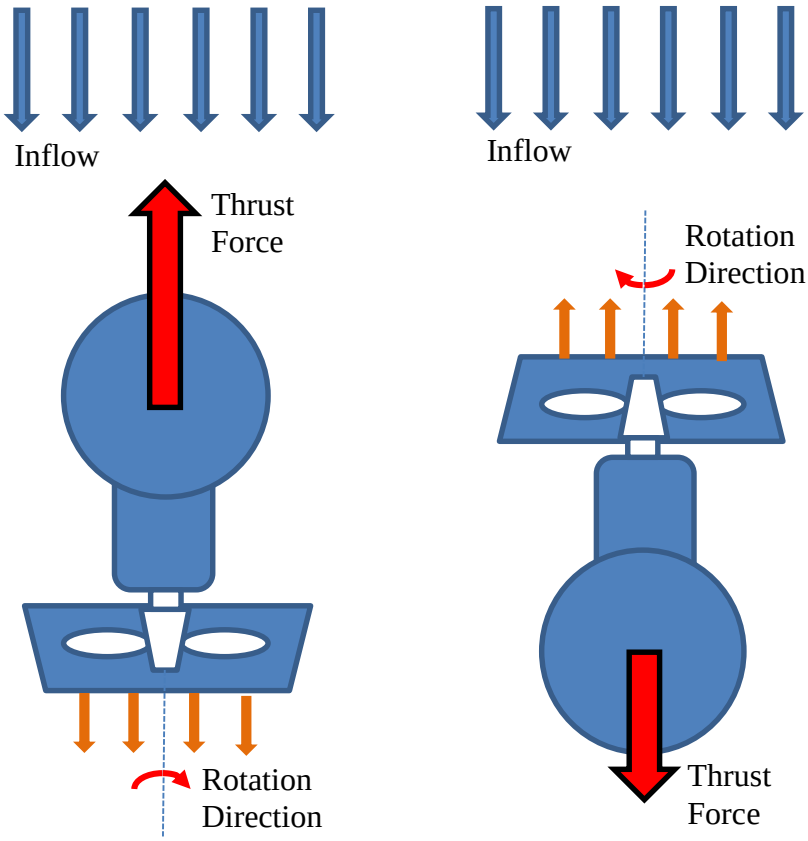

Figure 24: Azimuth Propeller 1st Quadrant (left) and Pseudo 2nd Quadrant (right)

If the propeller were able to reverse direction, this would give a 3-dimensional cube that describes 8 possible operating conditions. In this work, the propeller's rotation will remain uni-directional, and the model has been created using lookup tables based on quadrant angle β, and the relative flow angle α,

$$\beta = \text{atan2}\left(\frac{V_a}{0.7\pi nD}\right) \quad \textbf{(3-1)}$$

$$\alpha \equiv \alpha_{azi} - \alpha_{RF} \quad \textbf{(3-2)}$$

This quadrant angle definition replaces the standard advance ratio term to eliminate the discontinuity at zero propeller speed, making it more robust for simulation. The quadrant angle combined with incident flow angle define the relative direction of propeller thrust relative to the ship's motion. The relative angle of flow α is given by the angle between incoming flow seen by the propeller and azimuth angle. An illustration of the relative flow angle is provided in section 3.4.1 in the context of actuation forces for the true thruster configuration. The top-level block diagram of the lookup-based model is shown in Figure 25.

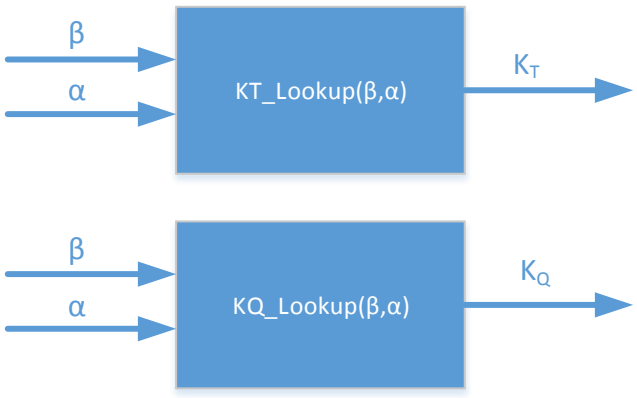

Figure 25: Top-level Lookup Table Block Diagram

3.3 CFD Design of Experiment and Lookup Table Generation

3.3.1.1 First Quadrant Analysis and Geometry Validation

A brief summary of the CFD results is presented in this section. These analyses were performed using StarCCM+ using steady and unsteady Reynolds Averaged Navier Stokes (uRANS) with k-ω SST turbulence model as recommended by best practices. Using the 3D model developed in the previous section, the geometry was first validated by comparing first quadrant CFD analysis results with the published open-water performance curves. The results are compared graphically in Figure 26. It can be seen that results are in very close alignment; therefore, the geometry produced must be sufficiently close to the real propeller.

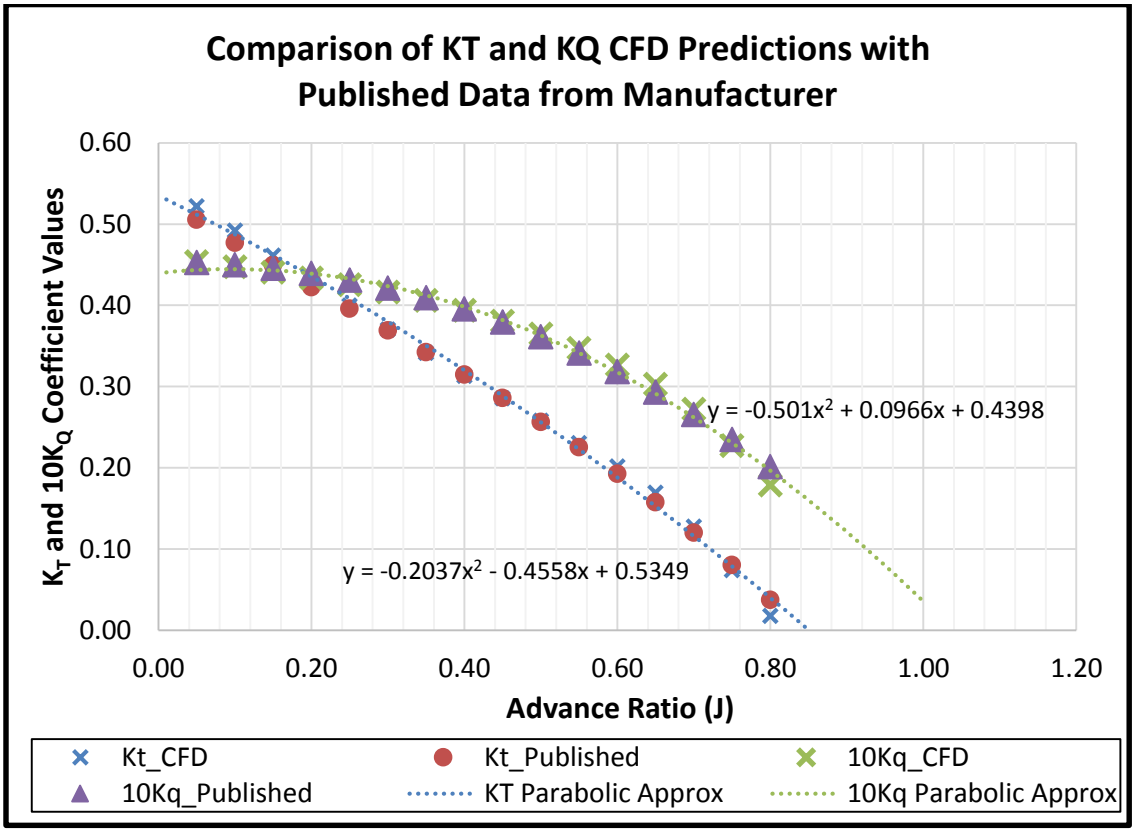

Figure 26: Comparison of K_T and K_Q CFD Predictions with Open-Water Published Data

Both the thrust coefficients and torque coefficients show excellent agreement. Note that the torque coefficient has been scaled by a factor of 10 for clarity, as is customary. A parabolic approximation trendline has been fit to both K_T and K_Q results. The application of a parabolic approximation is an agreement with the results presented by Kim and Chung [60]. An image of the 1st quadrant solution produced by StarCCM+ is provided in Figure 27. This plot illustrates the velocity magnitude for a cross-sectional plane through the domain. The velocity profile is intuitive and flow field is physical.

The advance ratio for CFD parameter sweeps is bounded by the ratings of the propeller and the maximum ship speed. The maximum attainable speed for the hull is approximately 10 knots. The propeller's maximum operating speed is 464rpm, and the minimum is set by the engine idle speed of approximately 650rpm. This implies that the maximum realizable advance ratio can be calculated by,

$$J_{max} = \frac{V_a}{nD} = \frac{(10knots)\frac{0.5144\ m/s}{knot}}{\left(\frac{650/3.882rpm}{60s/min}\right)1.135m} \approx 1.6 \qquad \textbf{(3-3)}$$

If the results from the Figure 26 are extrapolated, it can be seen that the thrust and torque coefficient will actually become negative at an advance ratio of 1.6. This implies that the propeller will become overdriven and will act similar to a turbine. The thrust force would transform into an additional resistive drag force, and mechanical power will be added to the powertrain system rather than being consumed. The overdriven situation is a short-term transient, and will last only momentarily when engines are initially ramped back after traveling at full speed. Operators are aware of this phenomenon and generally reduce engines gradually. For the purposes of this study, the propeller model will be limited in the first quadrant to positive values of thrust and torque coefficients.

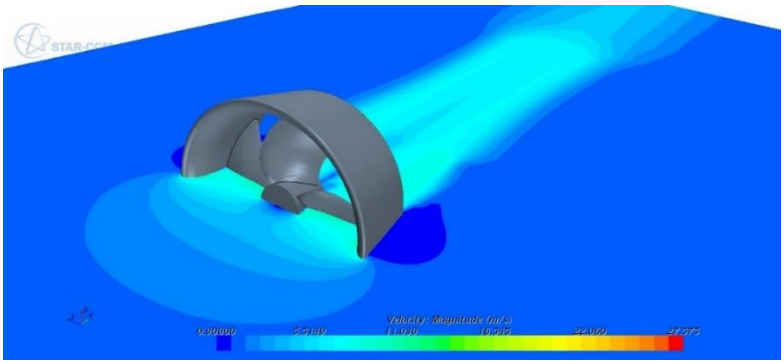

Figure 27: CFD Image Showing Velocity Magnitude Profile in 1st Quadrant

3.3.1.2 Anti-Directional and Vague-Directional Operation

The first quadrant CFD results agreed very well with published data; however, data was not available for the propeller at non-incident inflow conditions. As will be seen in Chapter 6, the ferry often uses a full 180° rotation of the thrust for braking while approaching berth; therefore, the CFD experiment sought to provide a complete set of data with sufficient resolution to properly model the opposing directional state. In the work of Kim and Chung [60], the authors experimentally studied the steady state thrust and torque production of an ROV thruster in the first quadrant, as well as in the opposing directional pseudo-second quadrant. The term pseudo-second quadrant has been coined in this work to differentiate between the reversal of the propeller's direction, as is defined in traditional literature, with the effect of rotating of a propeller by 180° with an azimuthing mechanism. Note that if the propeller is symmetric and no duct is present, the performance would be approximately equivalent for true second quadrant, and pseudo-second quadrant conditions.

Kim and Chung [60] observed that this pseudo-second quadrant operating regime exhibited two distinctly different flow fields separated by an inflection point termed the Critical Advance Ratio (CAR). This was also observed in the CFD results as is shown in Figure 28 through Figure 31.

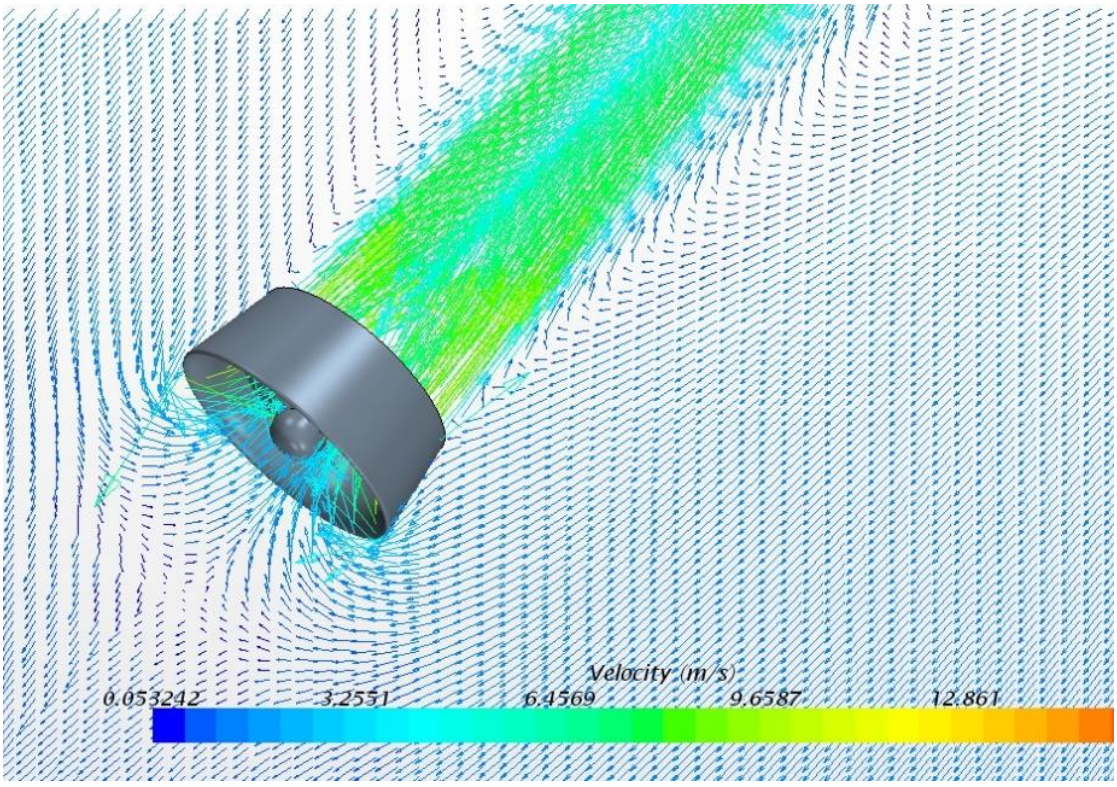

Figure 28: Anti-Directional Flow Field from CFD

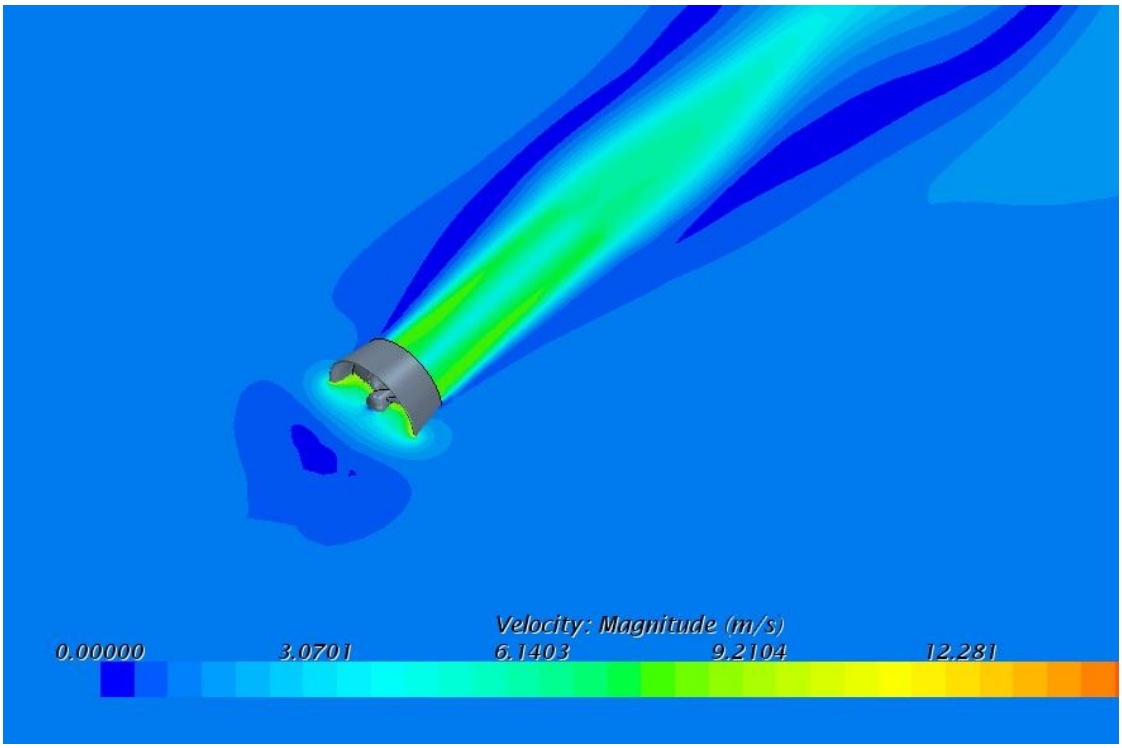

Figure 29: Anti-Directional Velocity Magnitude from CFD

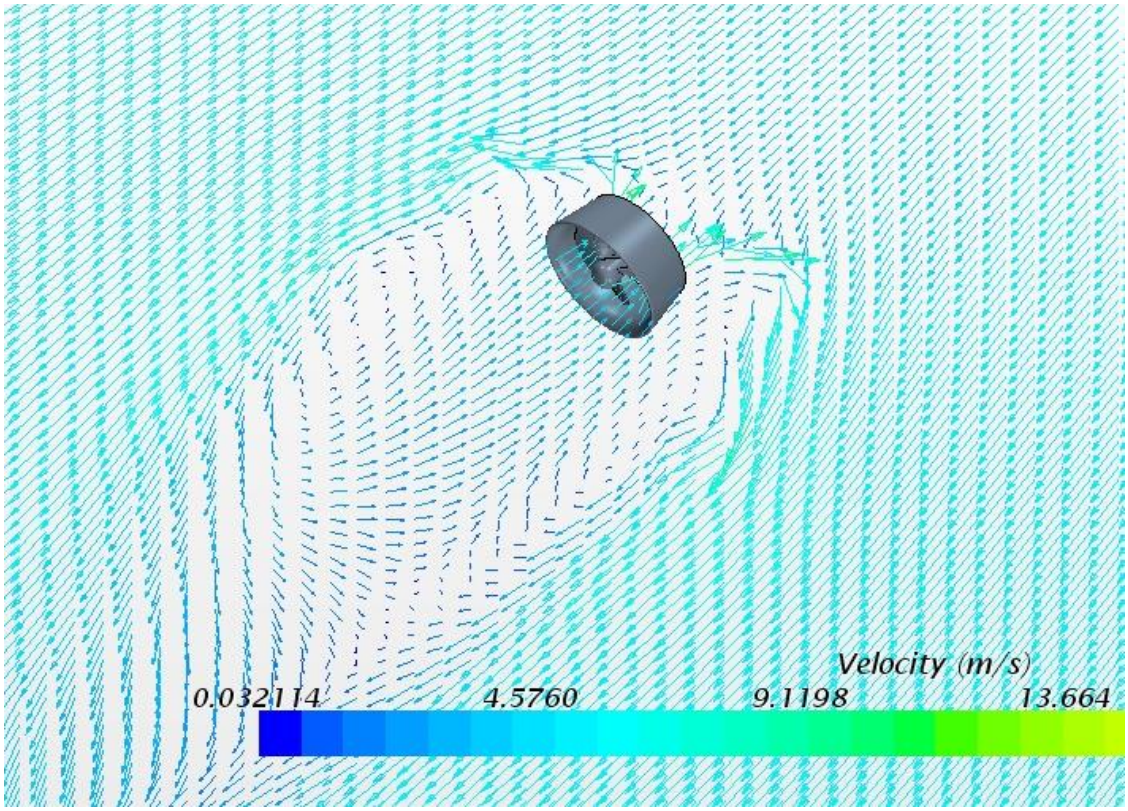

Figure 30: Vague-Directional Flow Field from CFD

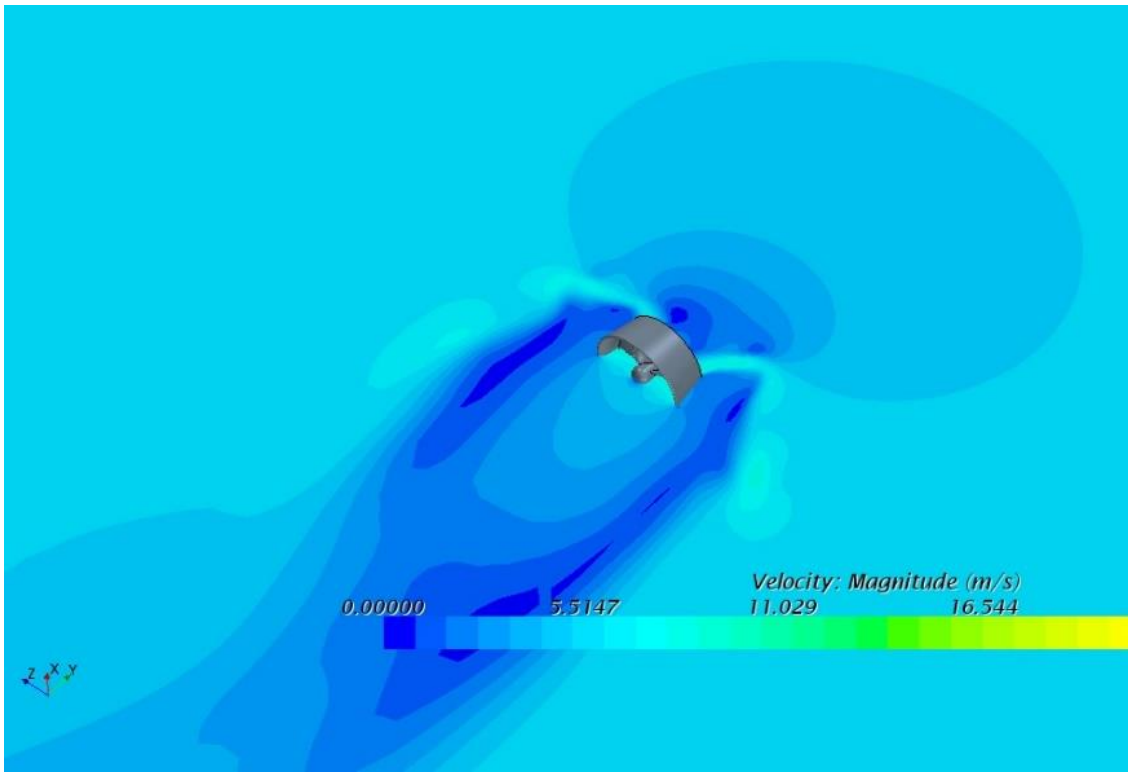

Figure 31: Vague-Directional Velocity Magnitude from CFD

Kim and Chung describes the these two flow patterns as,

a) Anti-directional

b) Vague-directional

The anti-directional state represents the situation where the propeller delivers sufficient momentum to the flow to effectively counter the momentum of the incoming freestream fluid. A contracting thrust tube develops upstream, in the direction opposing flow, as can be seen in Figure 28 and Figure 29. This situation occurs when the rotational speed of the propeller is relatively high in comparison to the flow velocity, or at small advance ratios.

The vague-directional state occurs when the incoming freestream velocity momentum dominates, and the propeller cannot impart sufficient momentum to overcome the incoming flow. With sufficient incoming freestream velocity, the flow through the propeller will actually reverse. Interestingly, this situation produces an increase in thrust force. This is not entirely unexpected when we recognize that the maximum thrust of a propeller is produced in the bollard pull condition; therefore, if the net force balance between thrust production and inflow momentum produces close to net zero velocity inlet, then the propeller may be acting in a state similar to bollard pull.

There is a point where the vague directional relationship will ultimately breakdown, but this occurs outside the physical operating conditions of this application. For example, extensive tests have been conducted at MARIN using standard series propellers to plot complete sets of four quadrant data, see Carlton [51]. The vague-directional state is shown in Figure 30 and Figure 31.

The results from the CFD studies performed by Rahimpour and Andersen [92] on the thruster in opposing flow conditions are illustrated in Figure 32. An inflection point is observed at an advance ratio around -0.3, which is consistent with the CAR seen by Kim and Chung [60]. A parabolic trendline fit also illustrates that thrust prediction models based on parabolic approximations provide a reasonable approximation for both flow regimes.

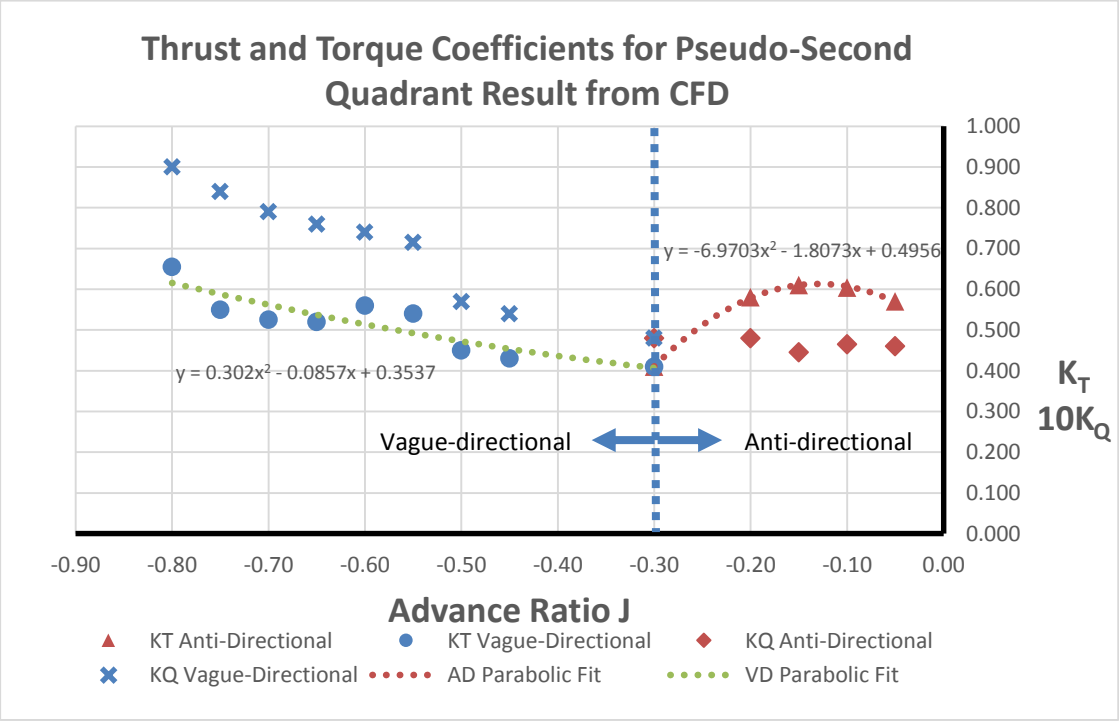

Figure 32: Thrust and Torque Coefficient for Pseudo-Second Quadrant Results from CFD

No clear inflection point was observed for the torque coefficient, which remained somewhat flat in the anti-directional regime, then increased in the vague-directional regime. To further validate the CFD process, a similar experiment was conducted on the well the Kaplan Ka4-70 propeller with 19A duct whose complete set of four quadrant data is published in Carlton [51]. The results for pseudo 2nd quadrant, or opposing flow conditions, matched the published data thereby validating the CFD analysis procedure and analysis configuration.

3.3.1.3 Oblique Flow and Angled Operation of Azimuthing Thrusters

The final portion of the CFD experiment involved an investigation of non-incident or oblique flow over the propeller. The azimuthing thrusters on the Klitsa allow for thrust to be directed in any direction within the horizontal plane, regardless of the vessel's travel direction. During maneuvers in-and-out of berth, the relative angle between the propeller's inflow field and its azimuth orientation will regularly be non-zero. This non-incident flow condition will impact both thrust production, as well as powertrain loading. When approaching berth, the operator will rotate the propellers to 180° in preparation for braking. They will also tailor the direction of rotation to utilize the transient thrust production to direct the bow or stern as desired.

Due to the large transient forces associated with rotation of the propeller, this process is generally performed at reduced ship speed and at low propeller speed to minimize the mechanical stress. A sharp torsional transient occurs on the powertrain system when these rotations are performed. By analyzing the operational data collected on the Klitsa, we can define a series of CFD analyses aimed at quantifying the impact of oblique flow on thrust and torque production at different relative flow angles under real operating conditions.

Based on observation of the data, the propeller rotation is typically performed just above the engine's idle speed so to maintain clutch engagement, yet not overload the engine with the torque transient. Consequently, the design of experiment was limited to the single propeller speed, but with six different forward speed operating points to provide reasonable resolution. For each of these six operating conditions, CFD analyses were conducted to produce the propeller's thrust and torque coefficients by sweeping the incident flow angle in increments of 30°.

Table 4: Operating Points used for Oblique Flow CFD Analyses

Propeller Speed (rpm)	Ship Speed (knots)						
167	1	2.5	4	5.5	7	8.5	10

The operating points used in the analyses are presented in Table 4. The results from the angular CFD studies are tabulated in grid form in Table 5. The advance ratio is computed using the parameters in Table 4.

Table 5: CFD Results for Angled Flow

KT Parameter Sweep with Angled Flow					
J \ α	30°	60°	90°	120°	150°
0.163	0.24	0.24	0.24	0.25	0.28
0.407	0.21	0.23	0.30	0.32	0.27
0.651	0.13	0.23	0.31	0.36	0.62
0.896	0.03	0.22	0.35	0.58	0.84
1.140	0.11	0.19	0.39	-	0.98
1.384	-0.30	0.10	0.46	1.03	1.24
1.628	-0.57	-0.01	0.52	1.12	1.42
KQ Parameter Sweep with Angled Flow					
J \ α	30°	60°	90°	120°	150°
0.163	0.042	0.042	0.042	0.043	0.049
0.407	0.038	0.040	0.049	0.053	0.050
0.651	0.027	0.040	0.051	0.057	0.089
0.896	0.012	0.038	0.055	0.079	0.116
1.140	0.006	0.034	0.056	-	0.134
1.384	-0.033	0.023	0.065	0.140	0.173
1.628	-0.070	0.008	0.075	0.153	0.197

A steady flow solver was used for angular positions up to 90 degrees with good results. Beyond this, unsteady solvers were required due to the complex flow pattern that develops with opposing flow. The analysis at 120° with advance ratio of 1.14 failed to converge, so this data point has been neglected.

3.4 Development of Simulink-Based Thrust Model and Validation

The CFD analyses established a dataset for the spectrum of potential operating points that the propeller will encounter in real-world operation. This data represents quasi-steady state thrust and torque characteristics of the propeller. The objective now is compile this data to generate a lookup surface that can be implemented into the simulation model. In the case of the Klitsa, it is convenient to lump the right-angle gearbox and driveline into the azimuthing propeller model. Both thrust and torque coefficients are computed using "2D Lookup Table" Simulink block with advance angle β, and relative flow angle α as signal inputs. The output is then scaled based on Equations (2-17) and (2-18) and to produce the dimensionalized values.

The mechanical drivetrain system was originally implemented using Simscape to provide a more physical representation of the system; however, it was found that simulation times increased drastically with this approach and the model was reverted back to a basic Simulink model. The magnitude of the thrust force produced by the propeller is decomposed into directional components to build the thrust force actuation vector $\boldsymbol{\tau}_{prop}$, expressed in body-fixed coordinates. The top level layout of the model is presented in Figure 33.

Because the ramp rate of the propellers is relatively low due to the large forces and inertias at play, the dynamics of thrust production from the fluid momentum equation were assumed to be negligible; therefore, quasi steady-state data has been assumed. As will be seen in Chapter 7, this approximation produces satisfactory results for extracting powertrain loads. Future work should investigate the dynamic effects of thrust development to verify this assumption.

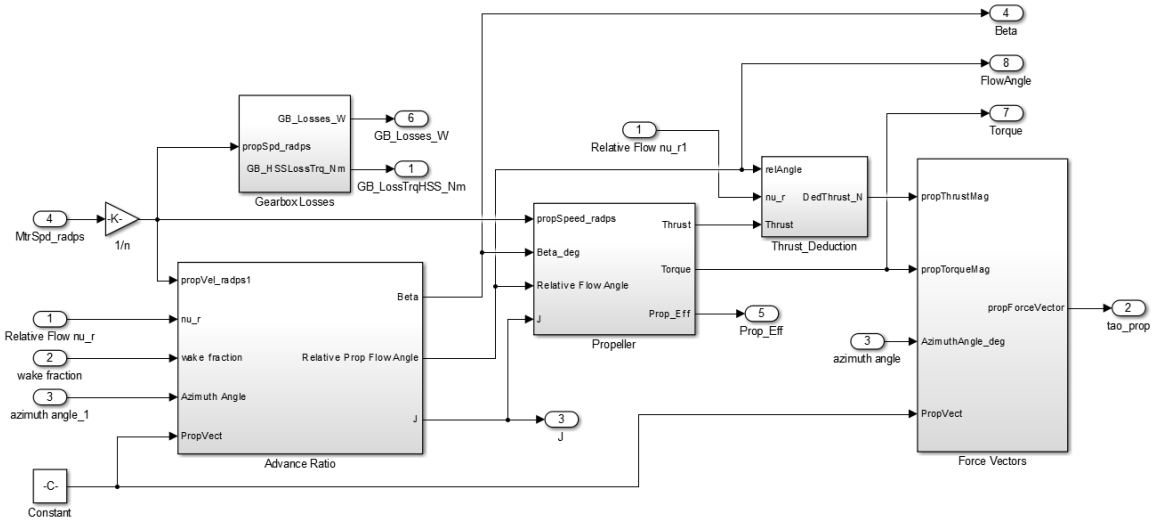

Figure 33: Top-Level Propeller Model Implementation in Simulink

One of the major implementation challenges when using a lookup table approach in a dynamic simulation is proper handling of the 0-360° angle wrapping. For example, when the azimuth position crosses zero from 0.5° to 359.5° in one time step, the propeller has only rotated by 1°; however, the lookup table will see this as a 359° rotation and erroneously interpolate between these two numbers during intermediate calculations. The lookup map must provide a continuous surface that properly interpolates in this scenario.

The results produced by CFD were extended to -720° to 720° to properly track the azimuth angle position data collected from the ship, thereby, eliminating the interpolation problem. This solution was effective for the present study, but should be improved to increase robustness in future work. The resulting lookup surfaces for both thrust and torque coefficients are shown in Figure 34 and Figure 35, respectively.

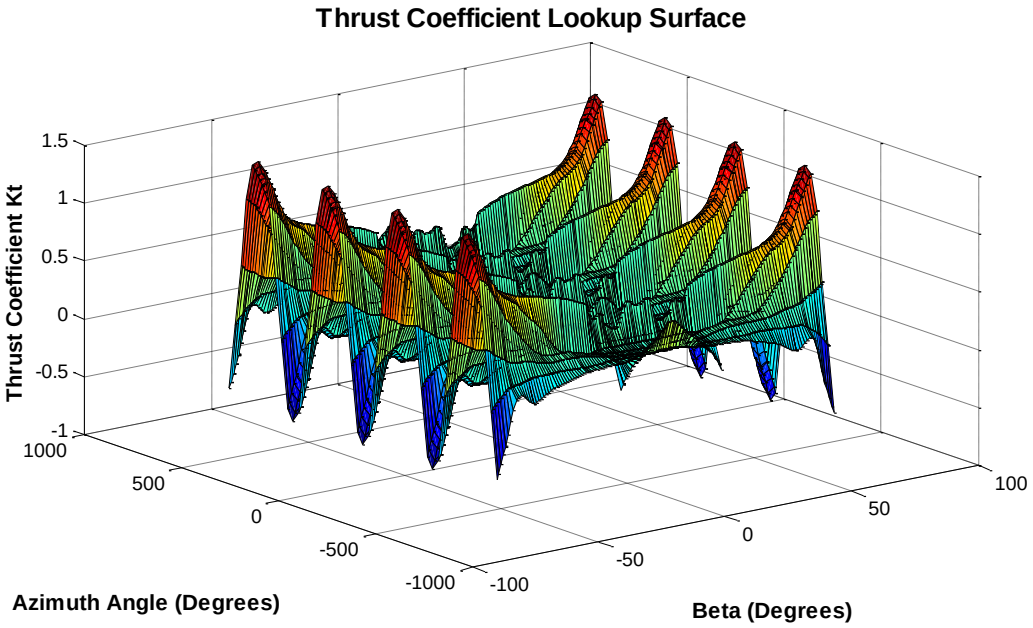

Figure 34: Thrust Coefficient Lookup Surface (Produced by CFD)

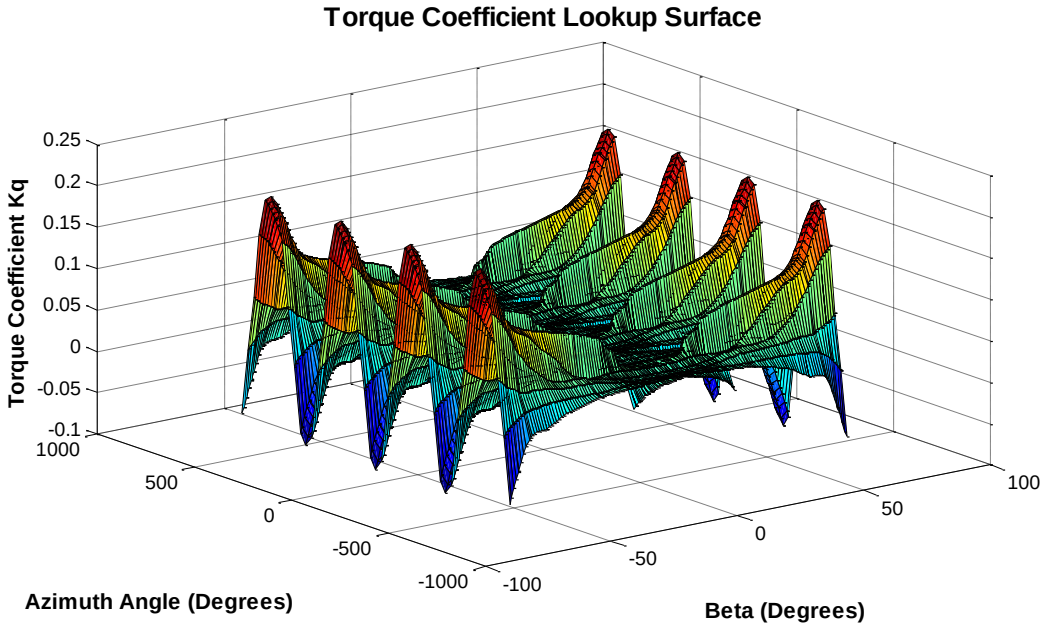

Figure 35: Torque Coefficient Lookup Surface (Produced by CFD)

The well-mounted propeller has inertial and loss parameters as listed Table 6. These parameters have been assembled from the design documentation provided by the manufacturer. The manufacturer estimated 15% losses in the propeller's mechanical drivetrain, which includes PTO from the hydraulic system. This loss estimate was

assumed to be at maximum rated power output and rated speed. A linear torsional damping term was implemented to account for dynamic losses, with the damping coefficient calculated to produce 15% power loss at rated conditions. The resulting resistive torque was implemented on the high speed side of the gearbox to be included in the electric drive's rotational equation of motion.

Table 6: Summary of Propeller System Model Parameters

PROPELLER PROPERTIES	VALUE	UNIT
PROPELLER ROTATIONAL INERTIA	11.6	kg-m^2
PROPELLER GB REDUCTION	3.882	
GB/SHAFT LOSSES	0.85	
TORQUE DAMPING COEFFICIENT (LSS)	16.6	Nm/rad/s
PROPELLER DENSITY	7650	kg/m^3

3.4.1 Thruster Configuration and Vessel Actuation Forces for M.V. Klitsa

The M.V. Klitsa's thruster configuration differs from most conventional vessels in that the units are not symmetric about the ship's longitudinal centreline. Because the ferry is double-ended, a single thruster has been placed on opposite ends of the ship to enable a high degree of maneuverability. The thrust production from each thruster will not be equal as a result of the wake fraction effect. The thruster configuration is illustrated in Figure 36.

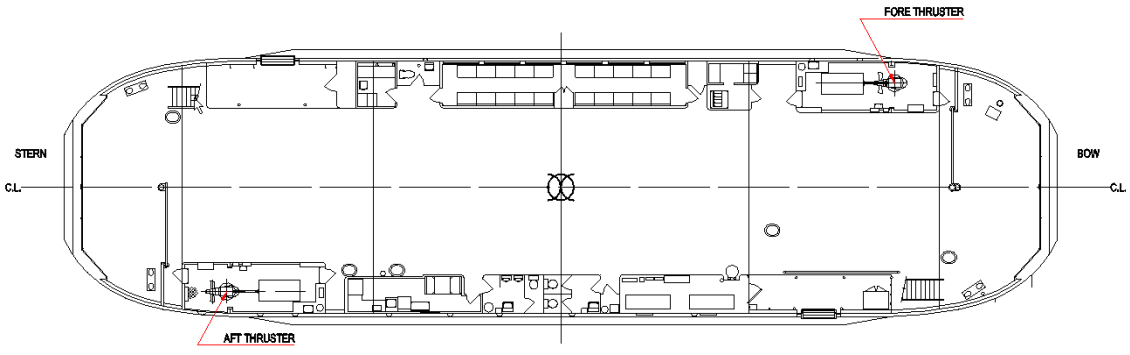

Figure 36: Thruster Configuration on the M.V. Klitsa

The relative angle of incident flow over each propeller is a function of the commanded azimuth propeller angle position, as well as the relative movement of the vessel. If we consider only velocities in the horizontal plane, an expression can be developed for relative flow induced over the propeller as a result of the vessel's motion expressed in body-fixed coordinates.

Consider the sketch shown in Figure 37 that illustrates the thrust force vectors and relative flow vectors produced by vessel motion. For positive surge, sway, and yaw velocities *u*, *v*, and *r*, the resultant flow vector is found by vector addition the velocity vectors. Note that the flow direction produced by yaw is dependent on the propeller's installed location as measured from the origin CO. Velocities in surge and sway are seen as an incoming flow whose vectors are equal in magnitude but opposite direction to the ship's velocity. A positive yaw produces an incoming flow that is tangential to the propeller's position vector relative to the origin. With the angular definitions defined below, a 0° relative flow angle represents first quadrant, fully incident operation.

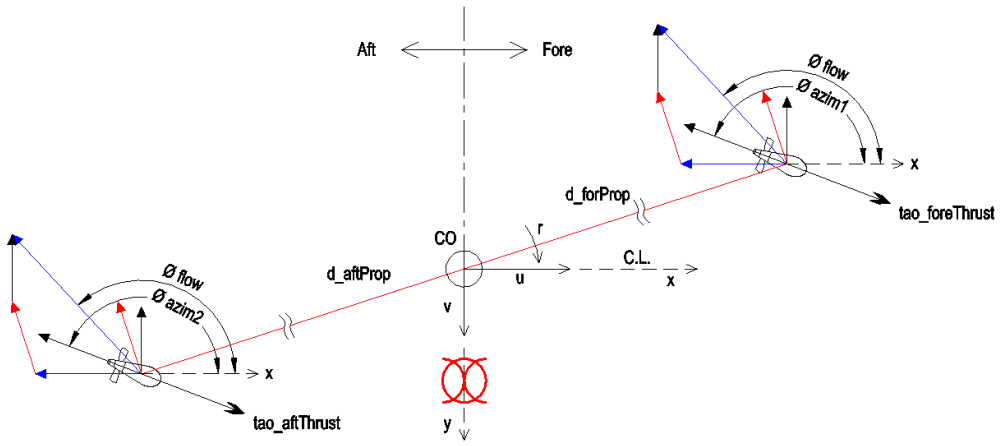

Figure 37: Thruster Inflow Conditions Resulting From Vessel Motions

The fore and aft thrusters produce opposing yaw moments when subjected to the same displacement angle; therefore, the yaw moment direction is corrected based on a parameter that is dependent on the propeller's location in the ship.

Chapter 4 Development of a Time-Domain Dynamics Model for a Barge-Type Ferry Hull

4.1 Development of Ship Inertial Model

The M.V. Klitsa was constructed in 1952 with the original drawings completed by hand. Though 2D CAD drawings were available from BC Ferries illustrating the structural plans, the primary source of information for the ship's buoyancy and trim properties is given in the ship's trim and stability book [93]. This document provides hydrostatic stability information along with estimates for the ship's centre of gravity (CG) and buoyancy centre for different operating conditions. Though the stability book offers insight into hydrostatic properties, it does not offer much insight into the inertial properties beyond vessel mass.

An accurate approximation of the ship's inertial properties is imperative to achieving good modeling results for vessel motion. To estimate the moments of inertia governing the roll-pitch-yaw subsystem, a simplified 3D CAD representation was created to estimate mass properties numerically. The 3D hull representation is also required for import into ShipMo3D for computation of hydrodynamic coefficients. Using the information contained within the stability book, the 3D CAD was systematically detailed to achieve the vessel mass and CG positions published in the document.

Two excerpt from the blueprints showing the primary structural layout of the hull are illustrated in Figure 38 and Figure 39. Using these drawings, the hull sections were modeled systematically in CAD to produce a realistic mass distribution for the steel structure. Most of the girder, plate, and flange dimensions and material thicknesses were provided on the drawing. Anything not labeled was assumed to be ¼" thick mild steel plate.

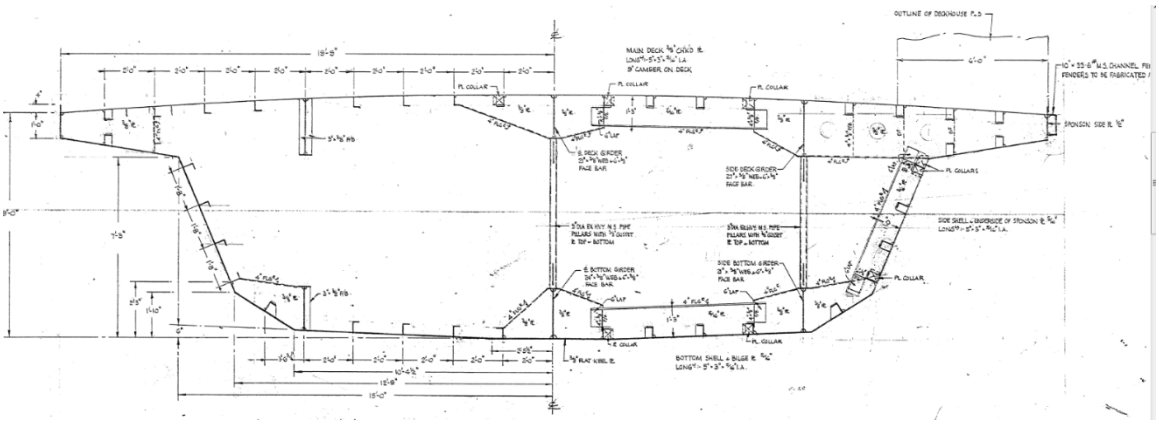

Figure 38: Cross-Sectional View Illustrating Transverse Support Structure

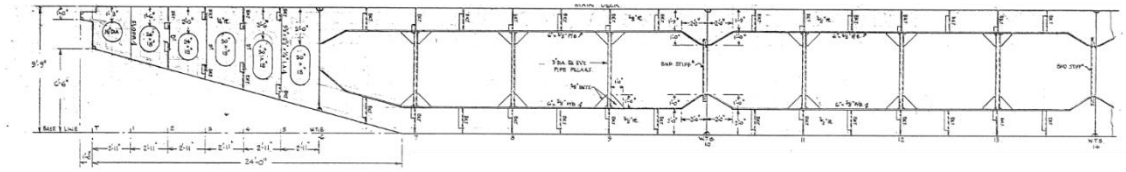

Figure 39: Crossing Sectional View Illustrating Longitudinal Support Structure

The mass of the hull structure alone was computed by the CAD software to be 270 tonnes. The lightship displacement of the Klitsa, according to the stability book, is given to be 334.5 tonnes leaving around 64 tonnes unaccounted for.

The next step was to estimate the dead weight of the permanent equipment and fixtures onboard. Approximations for the main equipment were estimated from datasheets, and information found on similar products. The decks also include auxiliary equipment, tools, fixtures, safety systems, and additional structural elements. Modeling of all individual components is clearly unfeasible; therefore, the passenger and crew areas were intuitively separated into different regions where a uniform distributed load could be applied. This approach is similar to that applied in building construction. For this inertial model, the normal human occupied spaces were broken out as follows:

a) Office/Kitchen Space

b) Industrial Space

c) Passenger Space

The assumed values for distributed uniform loads for each section have been taken from building code to approximate the additional mass for onboard equipment to reconcile the lightship discrepancy. A static block of mass was created for each of these regions to represent the assumed distributed load, and placed 0.5m above the floor to approximate the height of the centre of gravity.

The “Normal Departure” condition was selected from the stability book as the primary means of comparison and validation. Normal departure implies that all fuel, oil, and lube tanks are topped up before departure. The fresh water tanks are full, but sewage tanks are empty. These additional fluid masses were accounted for using the specific gravity of each fluid listed in [94] and placing a mass at the volumetric centre of each tank.

Table 7 shows a summary of the stability book hydrostatic parameters and assumed vessel loading for the ship model. This table also compares the CG location predicted by the CAD model versus that published in the stability book. Note that the datum for measurements of the longitudinal centre of gravity (LCG), transverse centre of gravity (TCG), and vertical centre of gravity (VCG) is located on the baseline at midships, an the longitudinal centreline of the ship.

The CG location prediction of the CAD model is in good agreement with that of the stability book, and the mass distribution should produce a good estimate for the inertial properties.

Table 7: Normal Departure Parameters from the Stability Book [94] and Comparison with CAD Model Estimate

	Mass (kg)	LCG (m)	Dir	TCG (m)	Dir	VCG (m)
Light Ship	355077	0.098	f	0.030	p	2.7
Crew	396	0		0		4.6
Vehicles	46758	0		0.15	s	4.2
Passengers	14621	0		0		3.8
Tanks	18543	3.4	a	4.6	p	1.6
Totals	**435395**	**0.067**	**a**	**0.0091**	**p**	**2.9**

	Mass (kg)	LCG (m)	Dir	TCG (m)	Dir	VCG (m)
Stability Book	435395	0.067	a	0.0091	p	2.9
CAD Model	434953	0.18	a	0.084	p	2.9

An image of the final CAD model used for approximating the inertias is illustrated in Figure 40. Here, the blocks shown on-deck represent vehicles with the prescribed VCG, TCG, LCG and mass properties consistent with the stability book.

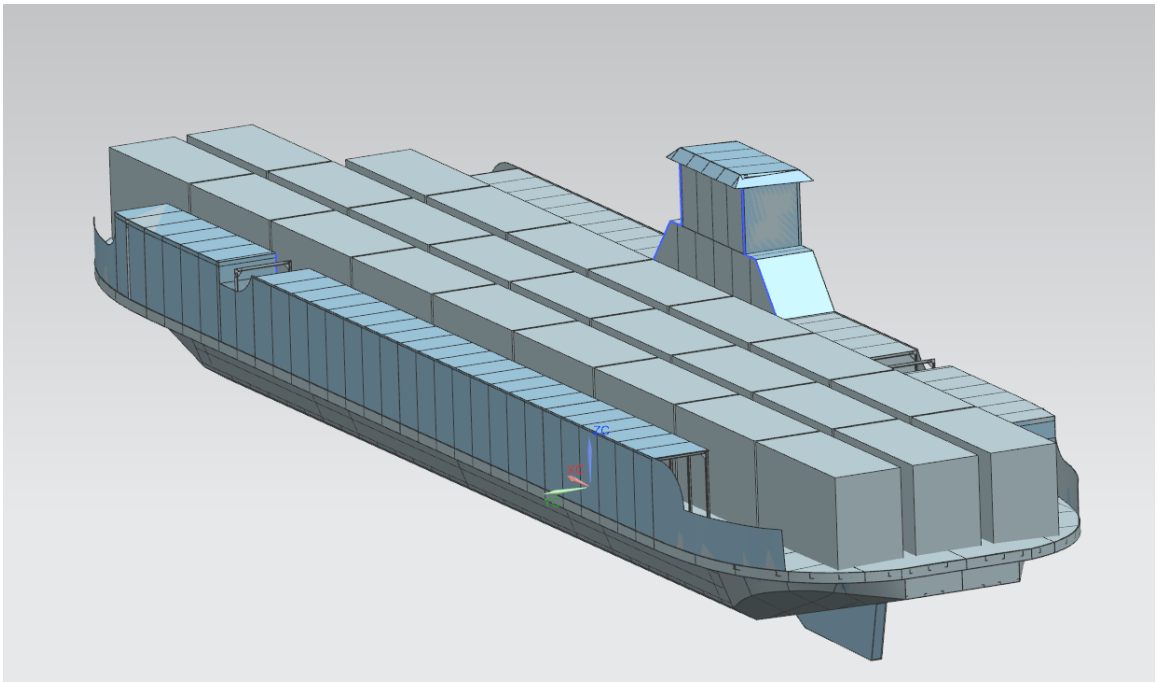

Figure 40: 3D CAD Image of the Klitsa Used to Determine Inertial Properties

The operating conditions assumed in the integrated Simulink environment for the Klitsa are described in Table 8. The computed ship inertial properties and assumed draft is summarized in Table 9. The effects of trim have neglected in this analysis, but can be added in future if the application dictates.

Table 8: Assumed Parameters for Centre of Gravity Location and Vessel Draft

Weight		VCG		Draft of Props		Vertical Distance Baseline to Deepest Draft on Props	Draft of Baseline at Midships
Long Tons	Tonnes	feet	m	feet	m	m	m
428.53	435.41	9.42	2.87	7.33	2.23	0.74	1.49

Table 9: Inertial Data for Hydrodynamic Coefficient Generation

Principal Moments of Inertia		
I_{xx}	7.70E+06	kg-m2
I_{xy}	5.83E+07	kg-m2
I_{xz}	6.00E+07	kg-m2
Products of Inertia		
I_{xy}	2.55E+06	kg-m2
I_{yz}	-3.28E+04	kg-m2
I_{xz}	-5.75E+04	kg-m2
Radius of Gyration		
R_x	5.09E+00	m
R_y	1.16E+01	m
R_z	1.17E+01	m

4.1.1 Generation of Hydrodynamic Coefficients Data

The inertial data, operational parameters, and hull geometry form the basic inputs needed to generate hydrodynamic coefficients with SM3D. The hydrodynamic coefficients produced by this code are directly imported into Matlab for use with the MSS toolbox.

Unfortunately SM3D uses a Z-Up coordinate system with origin located at the centre of gravity. This is inconsistent with the coordinate system required by the MSS toolbox which is Z-Down, and with origin CO located on the waterline at midships. The hydrodynamic coefficient data is more conveniently accessed by creating a ProteusDS (PDS) hydrodynamic database file. PDS uses a Z-down coordinate system, with origin at the centre of gravity. The routine for exporting to PDS already performs the coordinate transformation to Z-down; therefore, all of the force data contained in the hydrodynamic database file is shifted to CO with the *shipMo2Vessel* utility created in this work.

The pre-existing Simulink blocks available in the MSS toolbox require a prescribed Matlab data structure that parses ship information and hydrodynamic coefficients into a compatible format for the MSS toolbox. The workflow required to generate SM3D hydrodynamic coefficients for use with the MSS toolbox is illustrated in Figure 41.

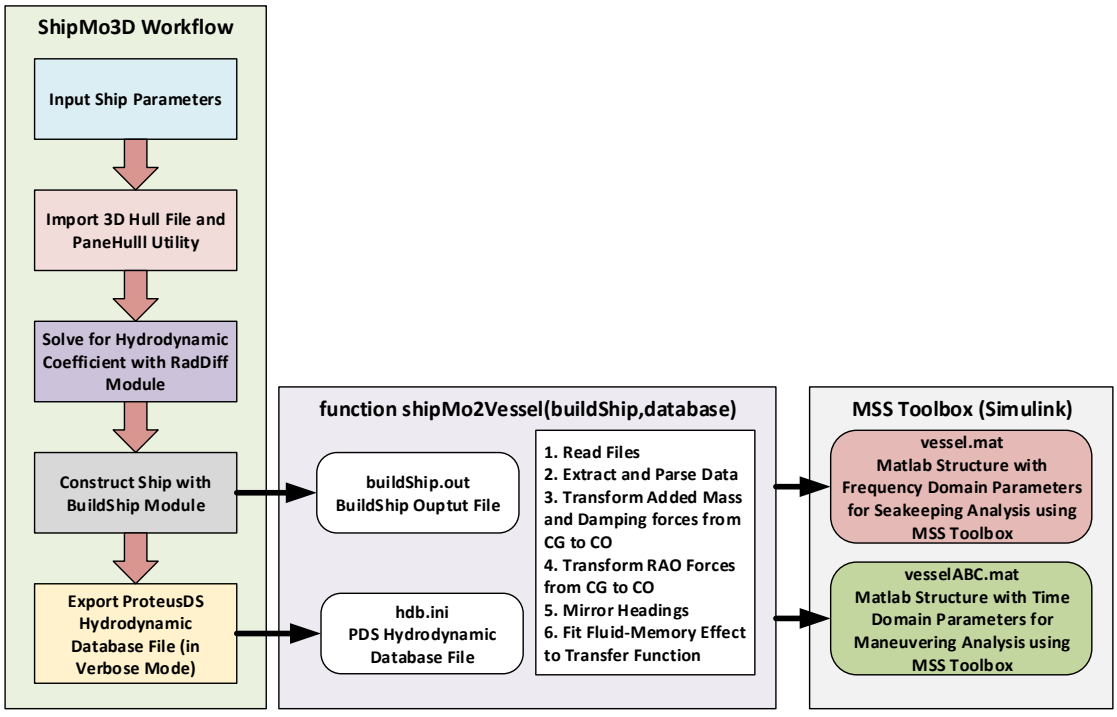

Figure 41: Workflow for Parameterization of Vessel Models in the MSS Toolbox

SM3D offers a simple graphical user interface for configuring the hydrodynamic analysis, and provides a 3D geometry import tool to facilitate construction of the hull geometry. The panelled hull used for the analysis is shown in Figure 42.

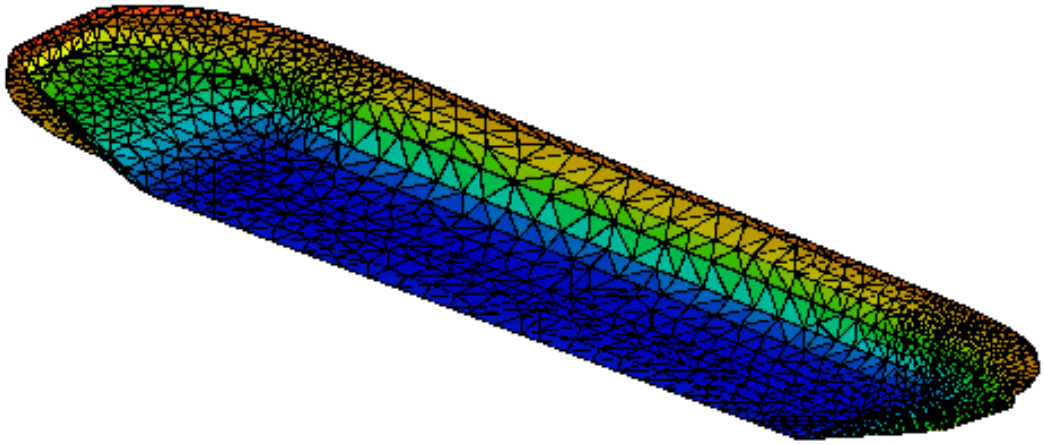

Figure 42: Panelled Hull in ShipMo3D

The computed added mass and damping coefficients are presented in Figure 43. The results are fairly well behaved, although some oscillations and ripple are present in the plots indicating some numerical inconsistencies. As expected, the damping coefficients trend to zero as the frequency increases; however, these results only illustrate the diagonal elements of the added mass and damping force matrices. It will be seen in section 4.1.4.1 that SM3D produced numerical errors when computing off-diagonal coefficients.

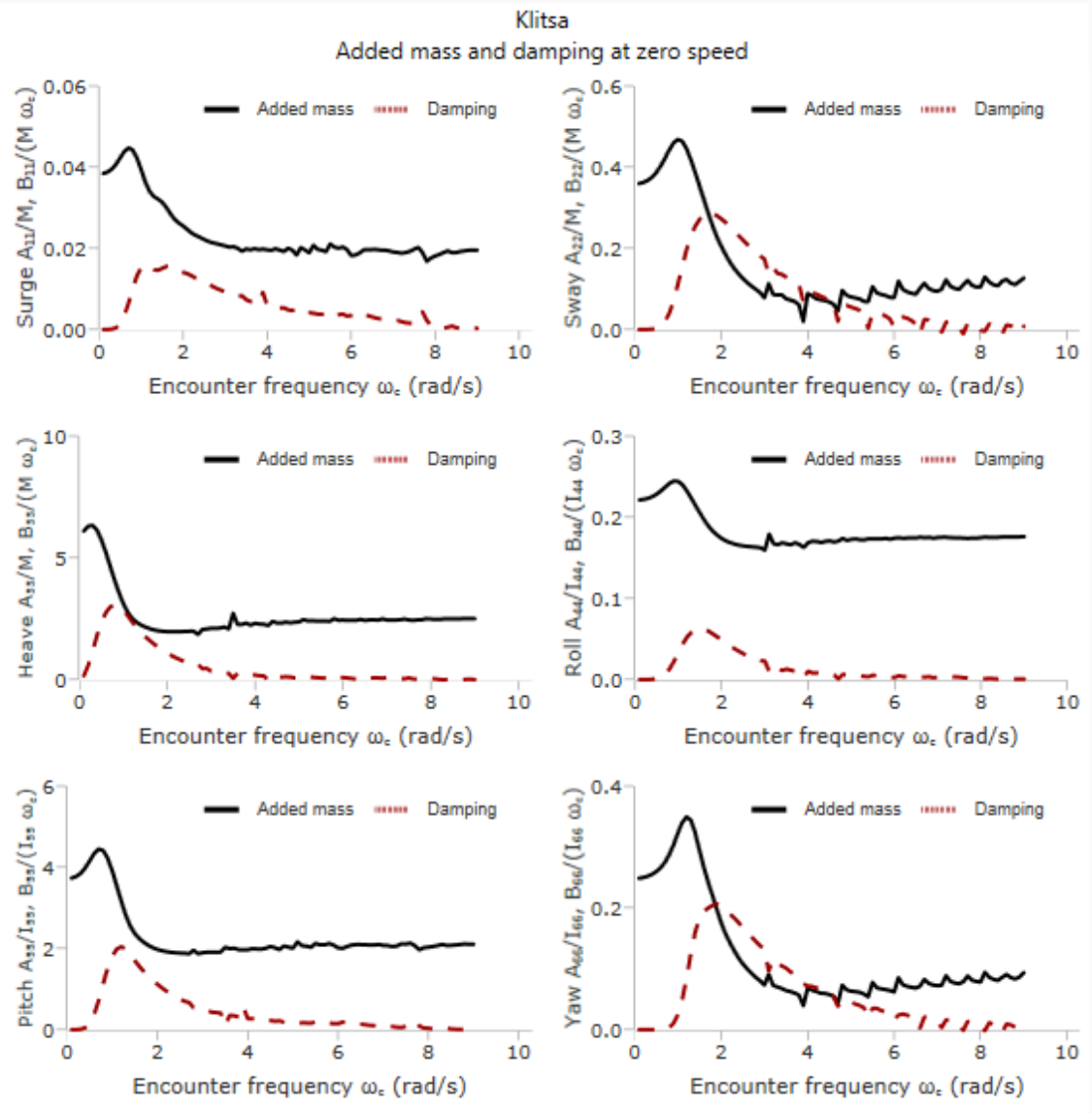

Figure 43: Non-Dimensionalized Added Mass and Damping Coefficients Computed using SM3D

The maximum value of encounter frequency was selected based on a simple analysis of historic data recorded by a wave buoy located in the Saanich Inlet. The dataset obtained from [95] dates back to February 19, 2001 and extends to the access date of March 1st, 2015. Using the historical wave spectrum peak period, and with consideration for the water depth, the maximum encounter frequency was found to be approximately 8.3 rad/s with a forward speed of 10 knots. The significant wave height as reported by the buoy

was also investigated to better understand the environmental conditions in the Saanich Inlet. This body of water is quite sheltered and the wave loads induced on this ship should be relatively small. First order wave force approximations are appropriate given that the historical significant wave height tops out around 0.9m as shown in Figure 44.

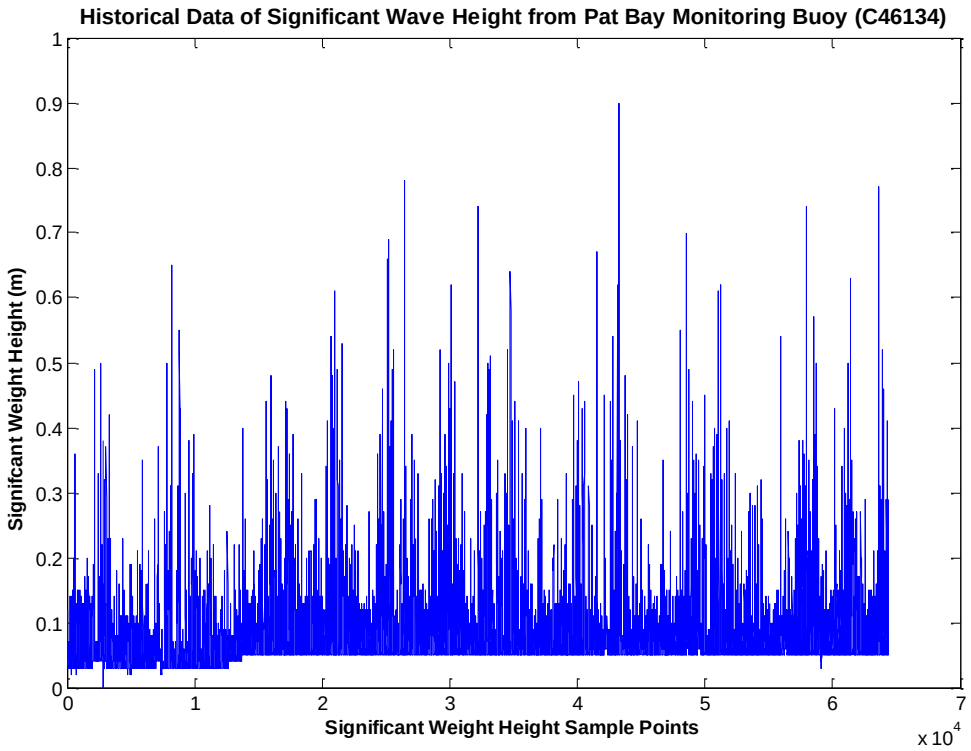

Figure 44: Historical Data of Significant Wave Height from Pat Bay Monitoring Buoy (C46134) [95]

The PDS hydrodynamic database file can be exported upon completion of the BuildShip utility in SM3D. In this module, the user can add skegs, propellers, and other hull features to the analysis. SM3D does not allow for non-symmetric appendage and thruster configurations; therefore, the actual propeller and skeg configuration onboard the Klitsa cannot be exactly replicated. On the real ship, the skegs are offset from the centreline and positioned at 2° relative to longitudinal axis of the ship. In light of these constraints, the BuildShip utility was constructed as accurate as possible with

longitudinally parallel skegs along the centreline, and propellers symmetrically distributed at midships. The final representation of the wetted hull is shown in Figure 45.

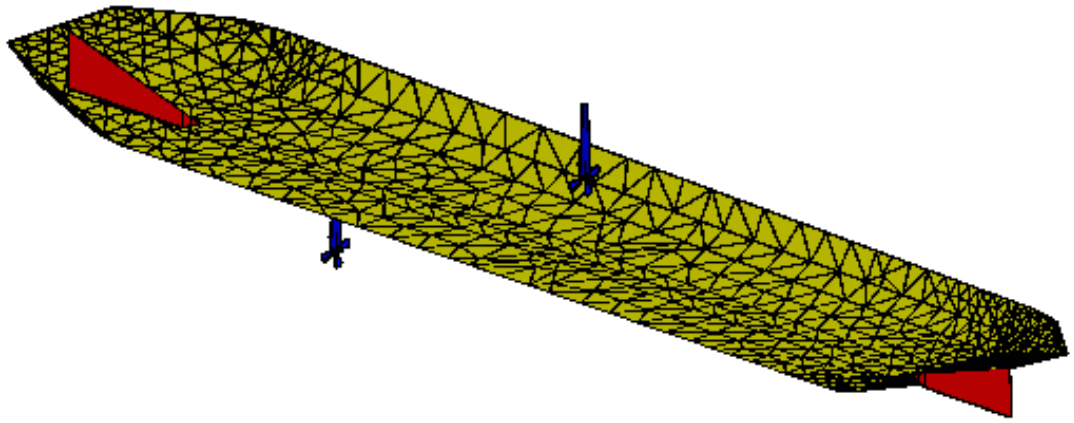

Figure 45: Final BuildShip Configuration for Computing Ship Hydrodynamic Coefficients

4.1.2 Vessel Dynamics Model

The MSS toolbox contains a pre-configured block which implemented the unified maneuvering/seakeeping Newton-Euler vessel equations of motion described in Chapter 2. This is a linearized model based about an equilibrium transit speed, which can be used directly for this study. The linearizing approximation works quite well while the ship is in transit and not making significant course changes. Yaw rate will be relatively small, and the Klitsa's barge-like hull is stable and does not typically yield much roll and pitch action in Saanich Inlet crossing. The unified seakeeping/maneuvering equation of motion developed with Chapter 2 with expansion of external forces is given by,

$$(\boldsymbol{M_{RB}} + \boldsymbol{A}_{\infty})\dot{\boldsymbol{\nu}}_{\boldsymbol{r}} + (\boldsymbol{C}^{*}_{\boldsymbol{RB}} + \boldsymbol{C}^{*}_{\boldsymbol{A}})\boldsymbol{\nu}_{\boldsymbol{r}} + \boldsymbol{D_L}\boldsymbol{\nu}_{\boldsymbol{r}} + \boldsymbol{D_N}(\boldsymbol{\nu}_{\boldsymbol{r}})$$

$$+ \underbrace{\int_0^t \boldsymbol{K}(t-\tau)[\boldsymbol{\nu} - U\boldsymbol{e}_1]d\tau}_{\boldsymbol{\mu}} + \boldsymbol{G\eta} \qquad \textbf{(4-1)}$$

$$= \boldsymbol{\tau}_{wave} + \boldsymbol{\tau}_{wind} + \boldsymbol{\tau}_{foreSkeg} + \boldsymbol{\tau}_{aftSkeg} + \boldsymbol{\tau}_{prop}$$

In this equation, the external forces acting on the body have been separated based on the configuration of the Klitsa. Recall that this equation is represented in body fixed coordinates, and the transformation matrix $\boldsymbol{J_\Theta}$ in Equation (2-84) will convert to inertial coordinates. The implementation of this matrix equation in the MSS toolbox is shown in Figure 46. The model also includes the 3-DOF non-linear maneuvering model for the surge-sway-yaw subsystems and allows for a linear viscous matrix $\boldsymbol{D_L}$ to be specified.

The hydrodynamic coefficients from SM3D produce the added mass and potential damping data for the matrix equation above. Now, the viscous and non-linear drag matrices need to be systematically developed using CFD and empirical data coefficients to fully define damping matrix $\boldsymbol{D}$. Lastly, the fluid memory effects need to be incorporated into the equation using the state space approximation technique described in section 2.3.6.

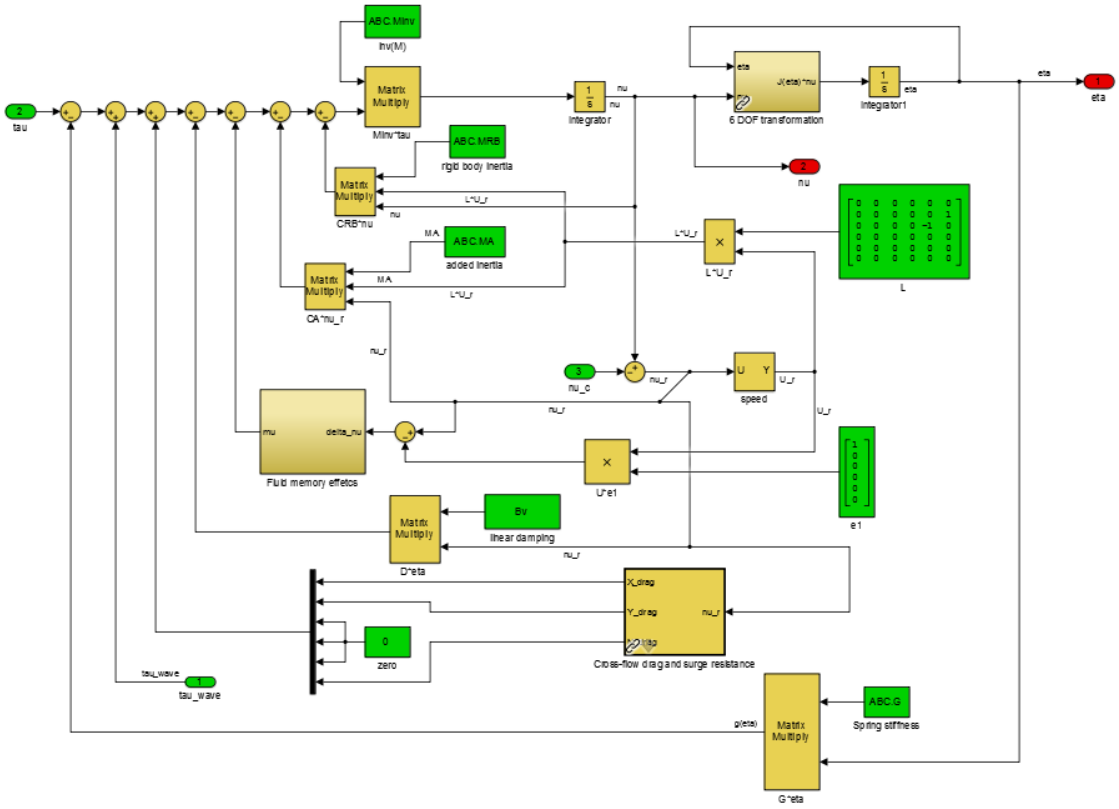

Figure 46: Implementation of the Unified Seakeeping/Maneuvering Model [78]

4.1.3 Construction of Drag Matrix

From Chapter 2, it was shown that the drag matrix for the ship is traditionally decomposed into linear and non-linear components. This drag decomposition into linear and non-linear components is somewhat cumbersome, and care must be taken to properly account for all aspects of the resistive forces. CFD analyses were performed to establish the bare hull resistance characteristics of the hull as function of forward speed. This data will serve as the primary means of validation for the linear/non-linear decomposition of the surge subsystem. The CFD analyses were performed by Rahimpour [96] with specifications provided by Andersen.

The CFD data set for total hull resistance, as function of vessel forward speed, is presented in Figure 47. From Chapter 2, recall that the surge damping force can be considered decoupled from the remaining degrees of freedom; therefore, the total drag force can be written as,

$$F_{drag} = \underbrace{X_u u_r}_{\substack{Linear \\ Force}} + \underbrace{\frac{1}{2}\rho S C_T{}^*(u_r)|u_r|u_r}_{\substack{Non-Linear \\ Force}} \quad \textbf{(4-2)}$$

The hull form factor was computed in accordance with ITTC1978, whereby, this parameter was computed using the CFD results with low ship speed, i.e. where Froude number is small. This was done in Rahimpour [96]. The frictional coefficient is computed using equation (2-125). The term $C_T(u_r{}^{max})$ is taken directly from the CFD results at maximum speed of ten knots.

The parameters α, C_D, and X_u can be fit to the CFD data points using the *lsqcurvefit* function in Matlab to produce the best parameterization for the linear/non-linear decomposition. The fitted results are also illustrated below in Figure 47.

There is a small discrepancy in the treatment of the hull form factor presented in Fossen [63] and the ITTC78 guidelines. In order to explore this discrepancy, two parameter fitting optimization routines were executed, one allowing the parameter *k* to be manipulated, and the other that fixed at this value produced by ITTC78 recommendations as performed in Rahimpour [96]. Both results are illustrated in the plot. The more accurate model drag model is achieved by allowing modification to the hull form factor *k.* The final parameters produced from both optimization routines are shown in Table 10.

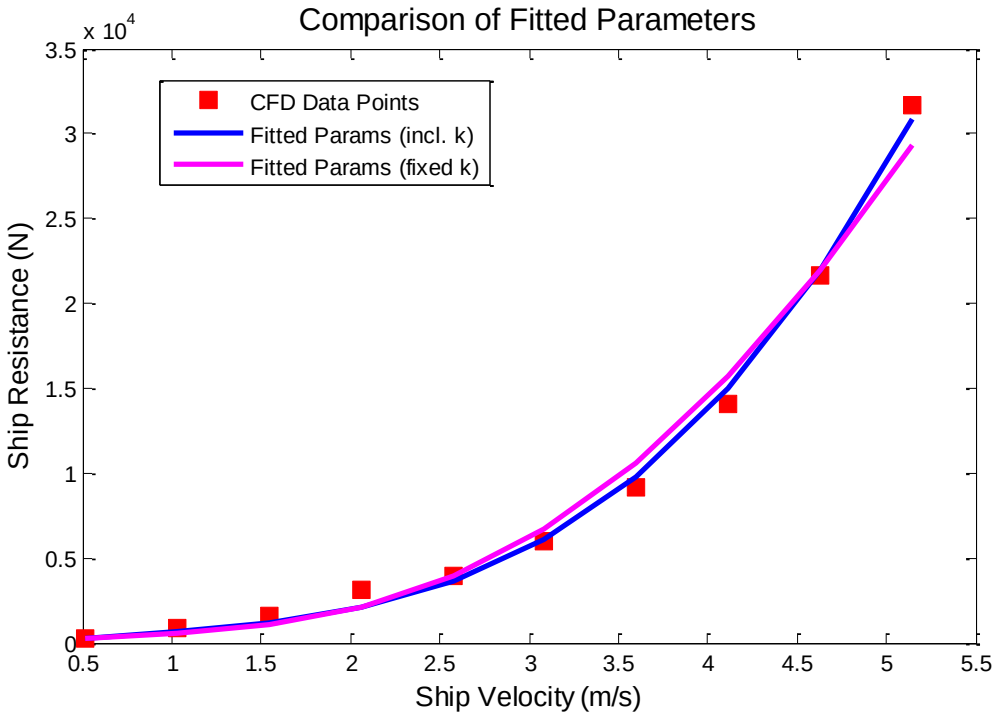

Figure 47: Comparison of Surge System Fitted Parameters

Table 10: Fitted Parameters using Least Squared Fitting with Genetic Algorithm

	X_u	CX	α	k
Fitted Parameters (incl. k)	547.7	0.001	0.0224	0.9992
Fitted Parameters (k from ITTC78)	420.4	0.001	0.0598	0.093

With the surge system now parameterized, the remaining coupled DOF subsystems must now be investigated. The following formulation follows the approach presented in Fossen [63] and uses functionality built into the MSS toolbox. The linear damping matrix is decomposed as follows,

$$\boldsymbol{D_L} = \begin{bmatrix} 0 & 0 & 0 & 0 & 0 & 0 \\ 0 & 0 & 0 & 0 & 0 & 0 \\ 0 & 0 & B_{33}(\omega_{n,heave}) & 0 & 0 & 0 \\ 0 & 0 & 0 & B_{44}(\omega_{n,roll}) & 0 & 0 \\ 0 & 0 & 0 & 0 & B_{55}(\omega_{n,pitch}) & 0 \\ 0 & 0 & 0 & 0 & 0 & 0 \end{bmatrix} + \begin{bmatrix} X_u & 0 & 0 & 0 & 0 & 0 \\ 0 & B_{22v} & 0 & 0 & 0 & 0 \\ 0 & 0 & B_{33v} & 0 & 0 & 0 \\ 0 & 0 & 0 & B_{44v} & 0 & 0 \\ 0 & 0 & 0 & 0 & B_{55v} & 0 \\ 0 & 0 & 0 & 0 & 0 & B_{66v} \end{bmatrix} \quad \textbf{(4-3)}$$

The potential damping is only considered significant in heave, roll, and pitch. By formulating a set of spring-mass-damper equations for the diagonal entries of $\boldsymbol{D_P}$, the natural frequency of each subsystem can be found numerically using the added mass and damping coefficients computed by ShipMo3D. The MSS toolbox contains an iterative numerical solver function *natfrequencies* that returns the natural frequency of the spring-mass-damper system from hydrodynamic data. The potential damping coefficient at the natural frequency is selected as the entry into the potential damping matrix. The reader is directed to Fossen [63] for further details.

Selection of the linear viscous terms is a bit more ambiguous, but these terms can provide a good means of tuning the model if accurate response data is available. Fossen [63] offers a derivation for the linear viscous terms using the closed loop response of a vessel under PD control. There appears to be errors in the Fossen's equation derivation. Furthermore, the author's formulae use zero frequency added mass coefficients which aren't physical. Instead, these equations will use the infinite frequency values and viscous damping terms are estimated by,

$$B_{22v} = \frac{m + A_{22}(\infty)}{T_{sway}} \quad \textbf{(4-4)}$$

$$B_{33v} = 2\Delta\zeta_{heave}\omega_{n,heave}\left[m + A_{33}\left(\omega_{n,heave}\right)\right] \quad \textbf{(4-5)}$$

$$B_{44v} = 2\Delta\zeta_{roll}\omega_{n,roll}\left[I_x + A_{44}\left(\omega_{n,roll}\right)\right] \quad \textbf{(4-6)}$$

$$B_{55v} = 2\Delta\zeta_{pitch}\omega_{n,pitch}\left[I_y + A_{55}\left(\omega_{n,pitch}\right)\right] \quad \textbf{(4-7)}$$

$$B_{66v} = \frac{I_z + A_{66}(\infty)}{T_{yaw}} \quad \textbf{(4-8)}$$

Fossen provides typical values ranges for the time constants and damping ratios in the above set of equations. These terms are generally determined experimentally, but could be assessed using CFD. In this work, the assumptions for these parameters are presented in Table 11. These factors are not have significant impact on this particular study with the simplifying 1DOF assumption used in Chapter 7, but these values will be refined later when full 6 DOF motion is considered.

Table 11: Assumed Parameters for Viscous Damping Matrix Coefficients

Parameter	Assumed Value
T_{sway}	250s
T_{yaw}	250s
$\Delta\zeta_{heave}$	0
$\Delta\zeta_{roll}$	0.05
$\Delta\zeta_{pitch}$	0

With these assumptions, the linear drag matrix is now completely parameterized. The remaining set of matrix entries are the coupled sub-systems in the non-linear drag matrix. The cross-flow force *Y* and yaw moment *N* are computed by numerical integration of equation (2-128) and equation (2-129).

The 2D drag coefficient is computed using data published in [88] that has been implemented into the Matlab function *Hoerner* as part of the MSS toolbox [78]. This function takes the basic hull characteristics of beam *B* and draft *T* as inputs in order to compute the drag coefficient at discretized longitudinal sections of the hull. Numerical integration is performed at each time-step in the simulation. The numerical integration algorithm is already built into the pre-defined unified seakeeping/maneuvering block. The geometric parameters of the ship used for estimating the transverse drag coefficients are presented in Table 12.

Table 12: Parameters for Numerical Integration of Non-Linear Drag Forces in Sway and Yaw

Integration Parameters		
Ship Length	L_{pp}	43.7 m
3D Drag Coefficient	C_X	0.001
2D Transverse Drag Coefficient*	CY_2D	0.59
Frontal Project Area	Axc	11.2 m^2
Transverse Project Area	Ayc	58.9 m^2

**** From Hoerner(B,T) Function***

4.1.4 Radiation and Diffraction Forces and Wave Excitation

Thus far, the generalized Newton-Euler formulation of the motion equations have been presented without addressing the convolution term that arises from the radiation force described by the Cummins equation (2-101). Chapter 2 illustrated how the fluid memory effect can be represented using a state space transfer function to speed up the simulation. In traditional literature, the motion response of a ship when subjected to waves is decomposed into two problems [62]:

1. Calculation of resultant forces/moments on the body when it is forced to oscillate harmonically at a specific frequency. This process determines the added mass and damping forces which are used to calculate the radiation force.
2. Calculation of resultant forces/moments on the body when it is fully restrained and exposed to harmonic excitation from waves. This is commonly referred to as wave excitation loads. The forces induced arise from the Froude-Kriloff and the diffraction forces/moments.

In addition to the added mass and potential damping terms, the hydrodynamic database file generated for PDS contains the Froude-Kriloff and diffraction forces resulting from wave excitation. These additional forces are compiled into the *vessel* structure as separate variables when the *shipMo2Vessel* script is executed. This data is contained within the *vessel* structure, and contains the response amplitude operator (RAO) data as a function of frequency and forward speed.

The MSS toolbox contains blocks that can generate different wave spectrums for inclusion in the simulation. The wave field generation block also interfaces directly with a wave loading block that computes the external force acting on the hull. This functionality is readily available, but will be neglected for the present simulations.

4.1.4.1 Curve Fitting of the Fluid-Memory Effects and Comparison with ShipMo3D

Chapter 2 provided the motivation and mathematical background for representing the fluid memory force associated with the Cummins equation using a state space accumulator system. Using a curve fitting algorithm in the frequency domain, a set of continuous-time transfer functions can be generated and compared to direct numerical integration of hydrodynamic coefficient data for validation. The fitting algorithm is

provided in the *FDIRadMod* function within the MSS toolbox [78]. Each entry of the 6x6 matrix must be evaluated separately, and this function has been lumped into the *shipMo2Vessel* utility function as a loop to compute all entries. An example of the curve fitting routine's output in the surge-surge system is shown in Figure 48. The fitted transfer function is of order 6, and produces good accuracy with the hydrodynamic data points.

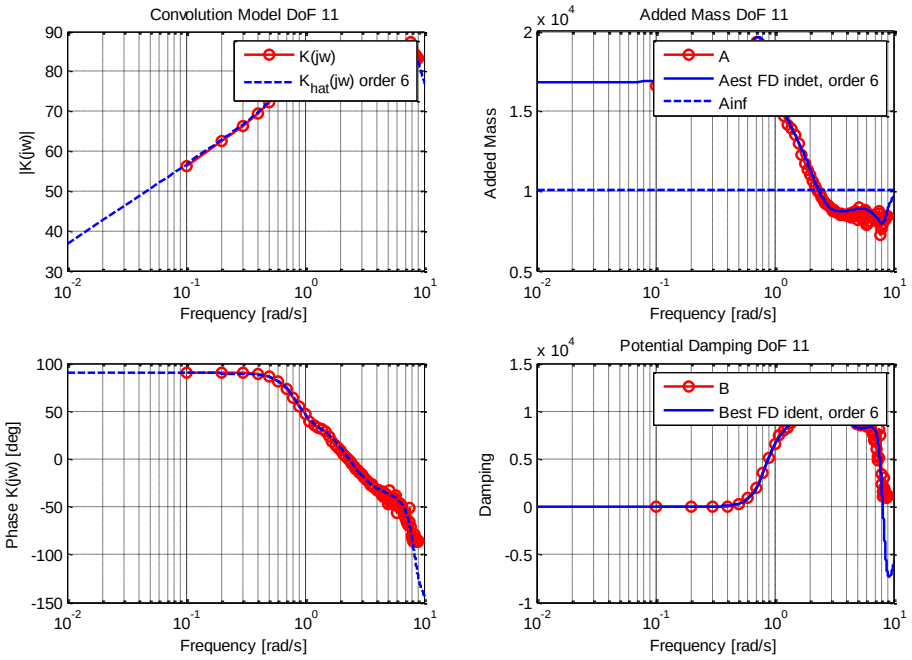

Figure 48: Example of Transfer Function Fitting to Hydrodynamic Data in DOF (1,1)

The *FDIRadMod* function contains two algorithms that differ based on the availability of infinite frequency added mass terms. Though ShipMo3D computes the infinite frequency added mass terms, it was found that the fitting algorithm often failed when using these values in for off-diagonal entries. When the fitting routine failed, the infinite frequency produced by SM3D was ignored, and the algorithm was configured to approximate the infinite frequency added mass [82].

A comparison of the transfer function approximation for the retardation functions $\widehat{\boldsymbol{K}}_{ik}(t)$ compared to numerical results produced by SM3D are presented in Figure 49 through Figure 54. These figures illustrate the impulse response of the state space transfer function shown in blue, and the numerically computed retardation functions computed by SM3D in red.

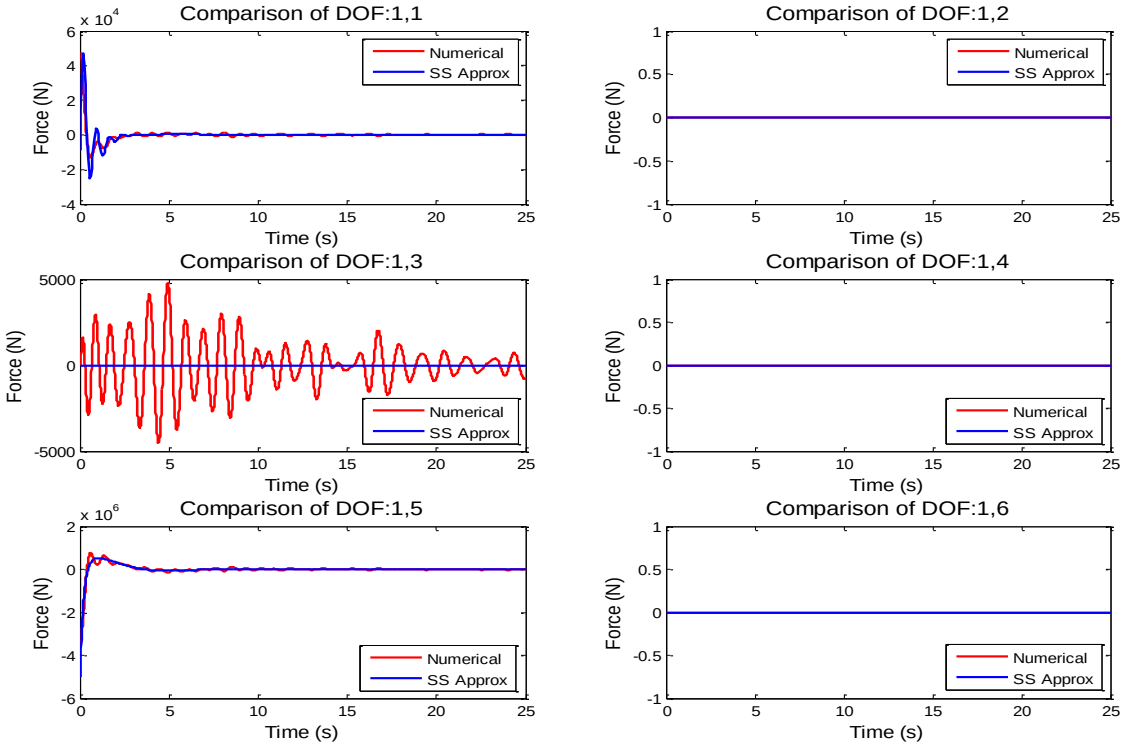

Figure 49: Comparison of Kernel Function with Impulse Response of SS System (Surge)

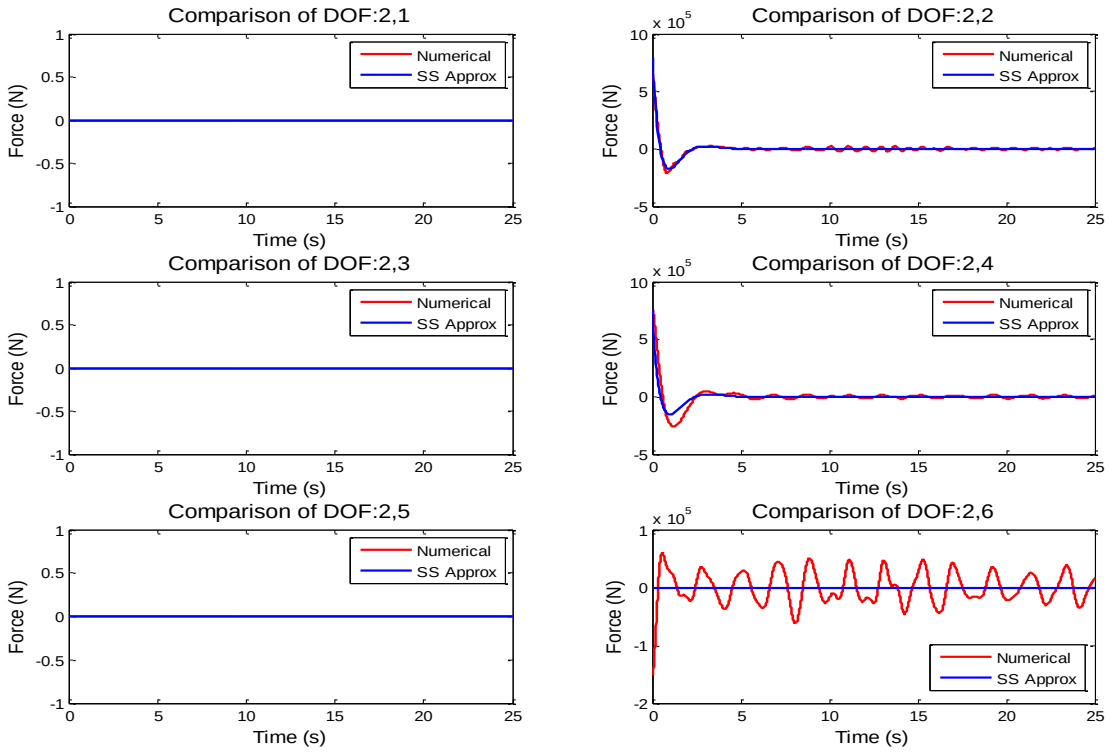

Figure 50: Comparison of Kernel Function with Impulse Response of SS System (Sway)

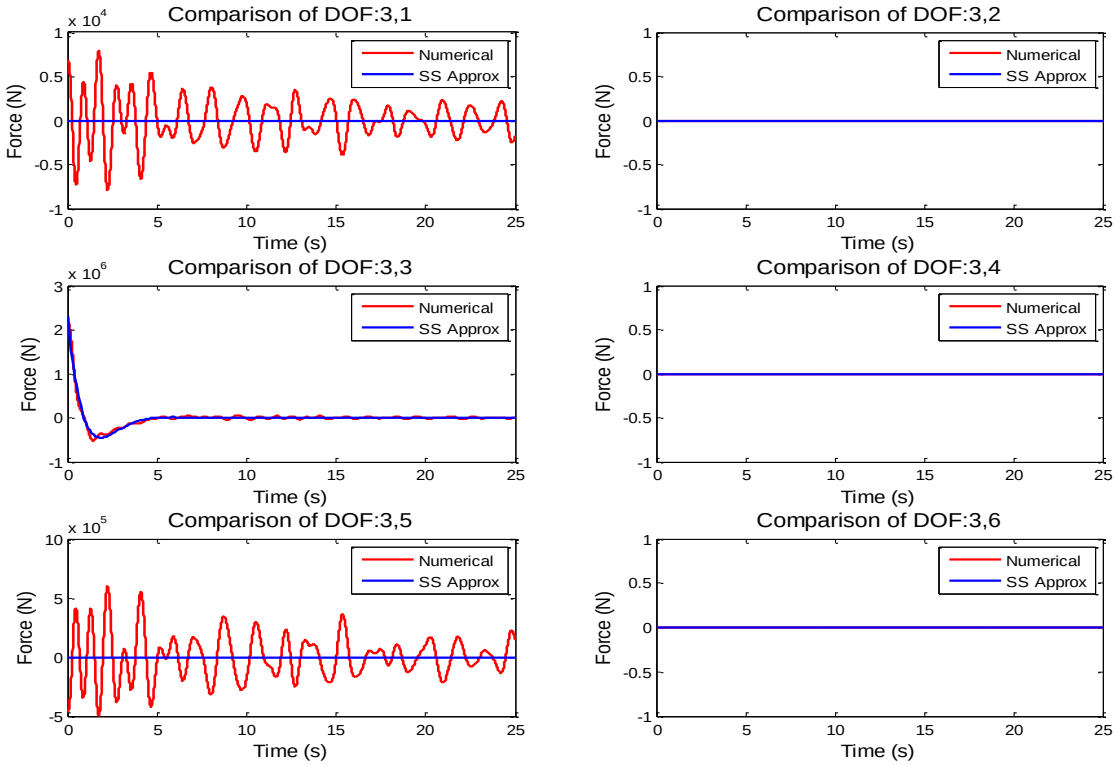

Figure 51: Comparison of Kernel Function with Impulse Response of SS System (Heave)

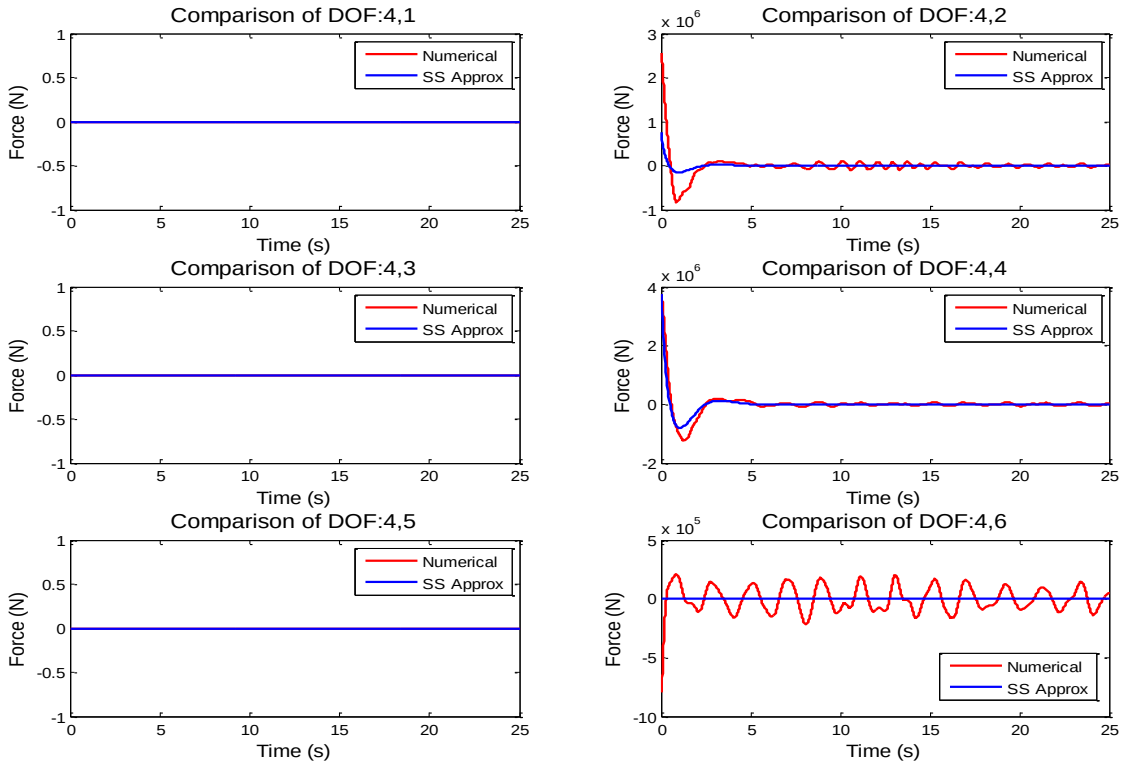

Figure 52: Comparison of Kernel Function with Impulse Response of SS System (Roll)

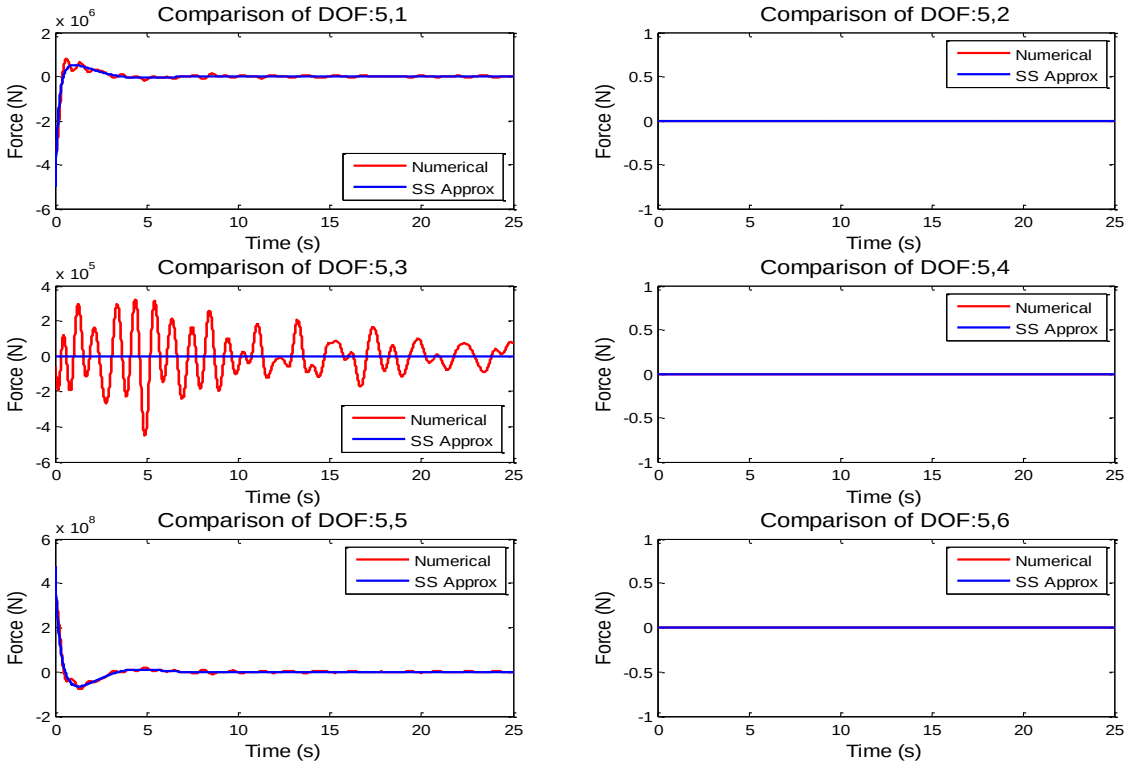

Figure 53: Comparison of Kernel Function with Impulse Response of SS System (Pitch)

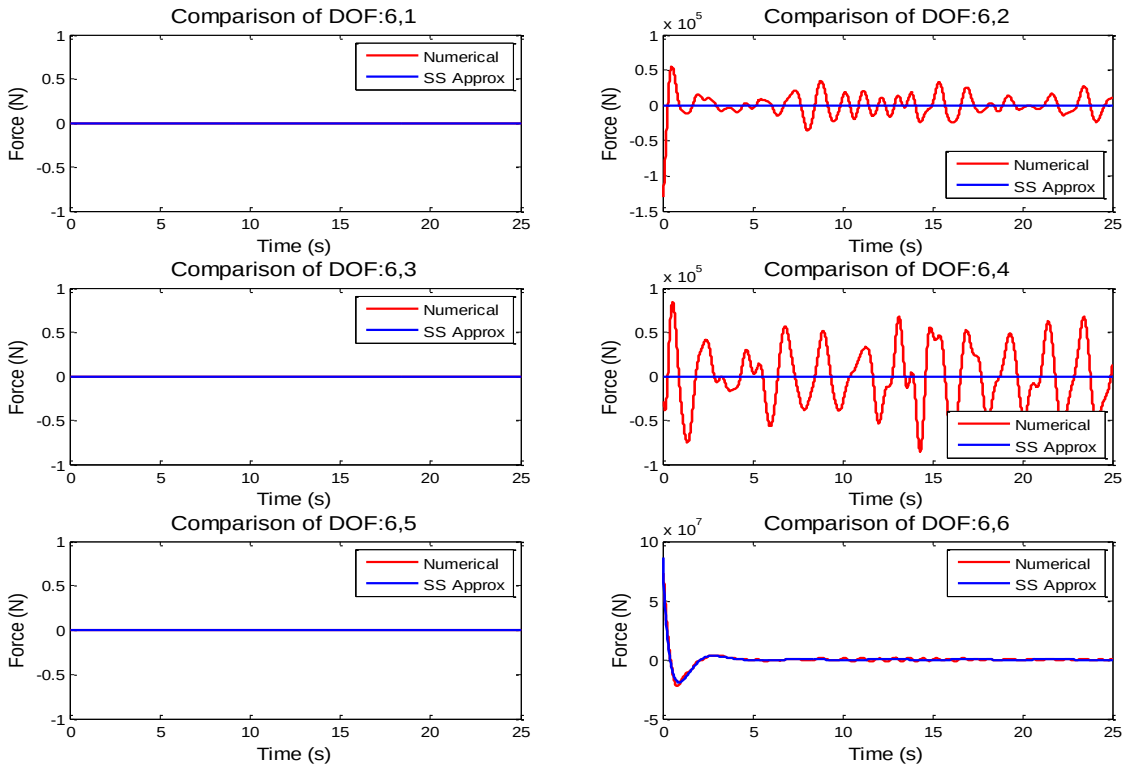

Figure 54: Comparison of Kernel Function with Impulse Response of SS System (Yaw)

The transfer function approximations for most of the matrix entries are generally in good agreement with the results of SM3D; however, the hydrodynamic coefficients produced by SM3D in several of the off-diagonal entries were non-physical, and the transfer fitting process failed.

Multiple analysis attempts were performed in SM3D focusing on refining the geometry in hopes to create better results; however, the problem could not be resolved. The problematic entries are not particularly important to the study at hand; therefore, the results above were accepted as-is. Moving forward, the analysis will be repeated using a different solver in hopes to resolve the issue, especially in the heave-pitch sub-system.

4.1.5 Wake Fraction and Thrust Deduction Factors

The wake fraction and thrust deduction factors can have a significant impact on the overall performance of the vessel. Reduction in the ambient flow entering the propeller typically leads to an increase in thrust production and greater propeller load on the mechanical powertrain. Similarly, the thrust deduction factor accounts for the added hull resistance that occurs during self-propulsion as a result of the increased pressure drag produced by acceleration of the flow via the propeller.

These factors play a critical role in defining the performance of the propulsion system and are typically determined experimentally using model tests. In this work, the wake fraction was computed by placing a series of flow probes in the CFD solution at both propeller locations relative to the hull. The volume mesh was developed such that it produced a refined and symmetric spatial distribution at the location where the propeller would be operating. The averaged x-direction velocity across the isosurface was then computed at each forward speed. The results are presented in Figure 55.

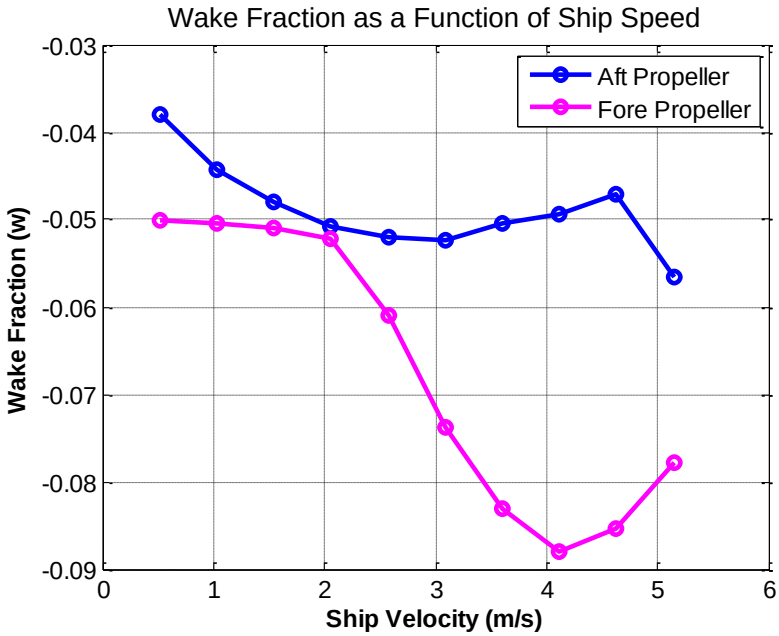

Figure 55: Plot of Wake Fraction as Function of Ship Speed

Interestingly, the wake fraction is negative for both propellers indicating that the flow is being accelerated. Based on the placement of the thrusters, and assuming inviscid theory, this result may intuitively makes sense because the propellers are approximately located at the fore and aft shoulders of the hull. At these positions, the velocity has increased and pressure has decreased. Interestingly, the original design documentation for the Klitsa's propulsion analysis assumed a wake fraction of 0.283, which is in stark disagreement with the results observed with CFD.

The effect of the wake fraction is implemented using a simple lookup table that will adjust the incoming surge velocity seen by the propeller. Depending on the direction of travel, the fore and aft thruster effects are switched accordingly using a case-switch subsystem.

The thrust deduction factor was slightly more difficult to resolve. The initial plan was to perform a series of self-propulsion tests using CFD; however, complications and time constraints did not allow. Instead, the operational data collected from the data acquisition study was used to estimate the thrust deduction factor. Two computation methods were used, the first using the wake fraction results directly from CFD, and the second by averaging the wake fraction data across all the operating points as a means of comparison. The results are tabulated in Table 13. The major issue with this approach is the large discrepancy observed between the computed results. Environmental factors and instrumentation error will naturally produce some variance in the predictions, making it hard to be definitive.

Table 13: Computation of Thrust Deduction Factor from Operational Data

Test Case	Operating Data Points			Computed Parameters												
	Prop1 Speed (rpm)	Prop 2 Speed (rpm)	Ship Speed (m/s)	Wake Fraction (Fore)	Wake Fraction (Aft)	Adv. Speed Prop 1 (m/s)	Adv. Speed Prop 2 (m/s)	Adv. Ratio Prop 1	Adv. Ratio Prop 2	Thrust Coef. Prop 1	Thrust Coef. Prop 2	Thrust Force Prop 1 (kN)	Thrust Force Prop 2 (kN)	Total Thrust (kN)	Bare Hull Res. (kN)	Eff. Res. (kN)	Thrust Ded. Factor
1	332.3	332.3	3.77	-0.08	-0.05	4.09	3.96	0.65	0.63	0.17	0.18	8.83	9.53	18.35	10.81	18.35	**0.41**
2	412.2	412.2	4.70	-0.08	-0.05	5.10	4.93	0.65	0.63	0.17	0.18	13.38	14.55	27.92	23.01	27.92	**0.18**
3	395.4	395.4	4.15	-0.09	-0.05	4.51	4.35	0.60	0.58	0.20	0.21	14.73	15.66	30.39	14.59	30.39	**0.52**
4	386.4	386.4	4.31	-0.09	-0.05	4.69	4.52	0.64	0.62	0.18	0.19	12.37	13.40	25.77	16.96	25.77	**0.34**
5	325.3	327.4	3.69	-0.08	-0.05	4.00	3.87	0.65	0.63	0.17	0.19	8.49	9.27	17.76	10.03	17.76	**0.44**
6	433.0	433.8	4.80	-0.08	-0.05	5.20	5.05	0.64	0.61	0.18	0.19	15.87	17.02	32.89	25.04	32.89	**0.24**
7	394.1	396.7	4.44	-0.09	-0.05	4.83	4.66	0.65	0.62	0.17	0.17	12.56	12.76	25.32	18.92	25.32	**0.25**
1	332.3	332.3	3.77	-0.09	-0.05	4.09	3.96	0.65	0.63	0.17	0.18	8.83	9.53	18.35	10.81	18.35	**0.41**
2	412.2	412.2	4.70	-0.09	-0.05	5.10	4.93	0.65	0.63	0.17	0.18	13.38	14.55	27.92	23.01	27.92	**0.18**
3	395.4	395.4	4.15	-0.09	-0.05	4.50	4.35	0.60	0.58	0.20	0.21	14.73	15.66	30.39	14.59	30.39	**0.52**
4	386.4	386.4	4.31	-0.09	-0.05	4.68	4.52	0.64	0.62	0.18	0.19	12.37	13.40	25.77	16.96	25.77	**0.34**
5	325.3	327.4	3.69	-0.09	-0.05	4.00	3.87	0.65	0.62	0.17	0.19	8.49	9.27	17.76	10.03	17.76	**0.44**
6	433.0	433.8	4.80	-0.09	-0.05	5.21	5.04	0.64	0.61	0.18	0.19	15.87	17.02	32.89	25.04	32.89	**0.24**
7	394.1	396.7	4.44	-0.09	-0.05	4.82	4.66	0.65	0.62	0.17	0.17	12.56	12.76	25.32	18.92	25.32	**0.25**

In an effort to reconcile the thrust deduction variance, the data was plotted against forward speed as shown in Figure 56. A decreasing trend is observed with increased forward speed, which is somewhat intuitive being that the propeller's ability to maintain flow acceleration will reduce as the ship speed increases. Less flow acceleration will produce less pressure imbalance; however, it is unlikely that this effect would trend to zero. When the ship is stationary, the added resistance is not applicable and the dynamic model for thrust deduction factor should converge to zero.

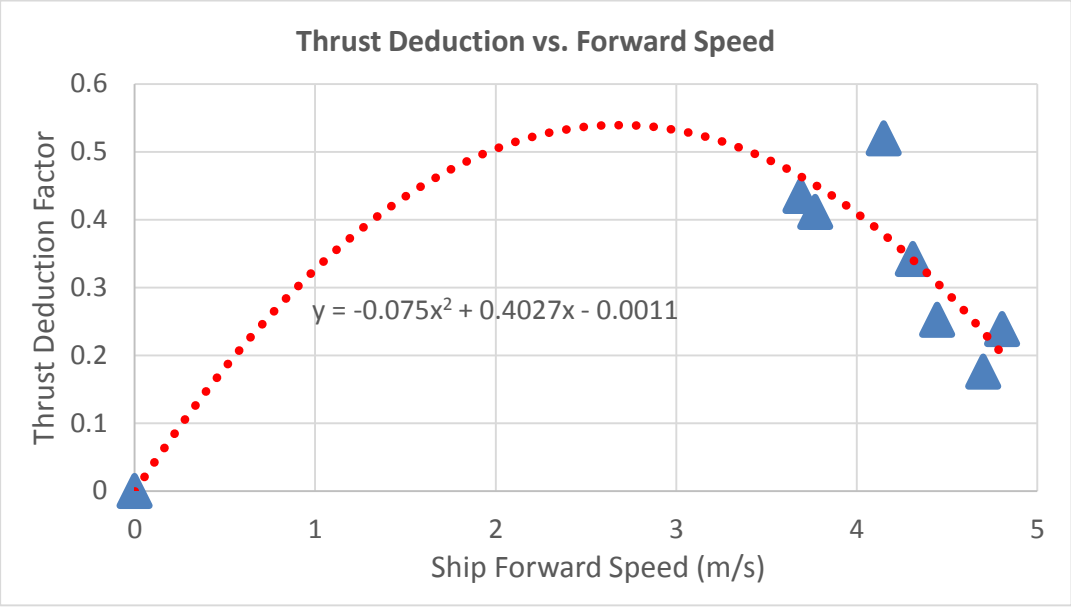

Figure 56: Plot of Thrust Deduction versus Forward Speed

As a first-pass assumption, a parabolic trendline was produced to serve as the basis for the thrust deduction model. The equation of the trendline as a function of forward speed was implemented in Simulink to capture the increase resistance associated with self-propelled case. The peak of this curve is significant, above 0.5 which is thought to be unrealistic; therefore, the dynamic model used a dynamic saturation block to constrain the output depending on forward speed. Above 1 meter per second, the function is contained within 0.25 and 0.5 which is reasonable based on the results of Table 13. The implementation is shown in Figure 57.

The thrust deduction has only been applied to the decoupled surge system; however, it should be noted the thrust deduction factor will also impact the sway and yaw forces when azimuth propeller is rotated. The effects of thrust deduction have not been explored on these subsystems in this work. When the propeller operates at non-incident flow conditions, the model has been implemented to scale the thrust deduction factor using a cosine distribution as a function of relative inflow angle α. The scaled thrust deduction is then fully applied to the surge subsystem, but only when the propeller is operating in the 1st quadrant.

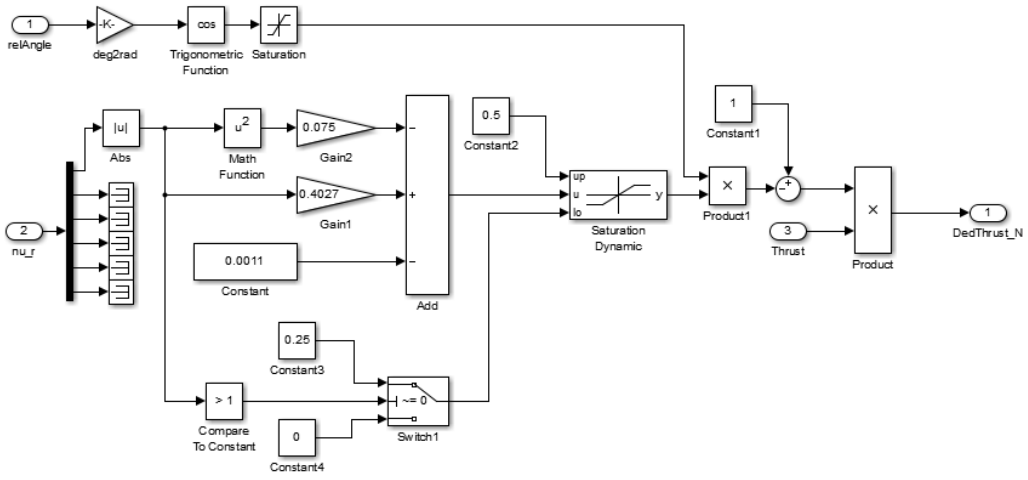

Figure 57: Thrust Deduction Dynamic Model Implementation

Chapter 5 Modeling of AES Power System

5.1 Model Fidelity of Hybrid Power Systems

The process of modeling hybrid power systems is a balance between capturing the dynamic response and loss characteristics of the power system while maintaining a reasonable simulation time. The level of complexity and model order for any given study varies depending on the analysis objectives. For system level-studies of hybrid power systems, the dominant dynamics of each sub-component need to be well represented to ensure that the interaction between components are fully captured. In many cases, high frequency dynamics from power converters can be neglected with minimal impact on the overall result.

Hybrid vehicle modeling and control optimization research often reduces powertrain components to power loss models for rapid execution of simulations when a large design space is being explored. The automotive powertrain analysis program PSAT, and its predecessor Autonomie, use this approach to enable the user to rapidly assess high-level vehicle performance for different powertrain architectures. The principle of power loss modeling is to account for energy conversion losses, from source to consumer, throughout a dynamic cycle. Loss models for individual powertrain components are based on steady state efficiency maps or performance lookup tables. Components are then assembled into a system configuration, and power flows from source to load, through each component reducing the useful power output at each stage.

Though power loss models are invaluable to early hybrid power system sizing and analysis, this type of modeling does not account for system dynamics and transient losses. Recent research by Prescott [97] showed that real-time controller tuning based on simplified power loss models may produce poor performance when deployed on a

detailed plant model; however, system control optimization tuning algorithms in HEVs cannot be performed efficiently using detailed simulation models. This highlights the importance of developing a suitable model order reduction strategy for the application. Similarly, Jaster [17] developed a detailed power system model using SimPowerSystems for a hybrid ship that was extremely computationally intensive, and required use of a parallel real-time computing cluster to execute in reasonable amount of time. Even with parallel computing, the small time-step required to resolve the switching inverters led to unacceptable simulation times making this an unfeasible approach for any commercial design application.

In this work, the objective is to develop a BEIPS simulation model that balances accuracy with computational efficiency. Power loss models are used where appropriate and more detailed models are created for components whose transient dynamics have a large impact on overall energy consumption, thus bridging the gap between lookup table based representation and physical system based representation. This chapter develops and validates the individual power system component models that will be simulated as a system in Chapter 7.

5.2 Proposed Architecture

To capitalize on British Columbia's clean and relatively inexpensive supply of hydro-electricity, the proposed architecture will be similar to that of a BEV. In actuality, a real implementation would likely have backup diesel generation on-board, making this similar architecture similar to an EREV system in automotive applications. All of the ship's energy needs must be supplied by the battery system. This includes delivery of AC electrical power to service hotel loads from onboard equipment and lighting.

The battery provides a DC source of energy that is converted to a stable bus voltage using a bi-directional DC/DC converter. The DC distribution grid delivers electrical energy to the primary electric propulsion machines, while also supplying power to a DC/AC islanding converter which produces the ship's AC supply. Trends in ship electrification are moving towards DC grid systems because of its advantages in [2],

1. Reducing conversion losses,
2. Flexibility in introducing energy storage, fuel cell, and solar technology,
3. Enabling of variable-speed generation,
4. Flexibility in equipment location.

The typical DC grid AES uses ICE-based electrical generation for supplying the electrical power to the IPS. In the BEIPS architecture, these power producing elements are completely replaced by the battery-based energy storage system. One key assumption in this case study to note is that all existing auxiliary equipment, which includes electrically driven pumps, fans, compressors, will remain as AC-supplied components serviced by the DC/AC islanding converters for simplicity. Therefore, the BEIPS is comprised of the following major components:

1. Two main electric propulsion motors
2. Bi-directional DC/DC converter
3. DC/AC islanding converter
4. Energy storage system

For reference, the architecture was illustrated back in Chapter 1 in Figure 5. The following sections provide a detailed formulation of the simulation models created for each of these components. The battery system requires some initial design assumptions

which are advised by an energy consumption analysis based on the experimental data collected as part of the data acquisition study. The remaining components have been developed to maintain the capacity and power requirements of the existing ship. The capacities are summarized in the table below.

Table 14: Installed Capacity of Primary Equipment Onboard M.V. Klitsa

Component	Rated Power Output	Qty. In Operation
Diesel Generator (AC Supply)	50kW/62.5kVA	1
Diesel Propulsion Engine	261kW@1800rpm	2

5.2.1 Battery Modeling

The dual polarization equivalent circuit model, shown in Figure 58, has been selected for representation of the LTO battery pack. The fitting process for the equivalent circuit parameters are discussed in Huria et al. [46]. In Cleary et al. [43], the authors conduct pack-level testing then perform equivalent circuit parameter fitting based on [46] to generate parameters for a 9.2kWh LTO battery pack. The pack consisted of eight 50Ah modules assembled in series. The parameters are given as a function of temperature and SOC; however, the data set is incomplete and does not cover all possible SOC and temperature conditions. As a result, the data had to be extrapolated to complete the battery simulation model.

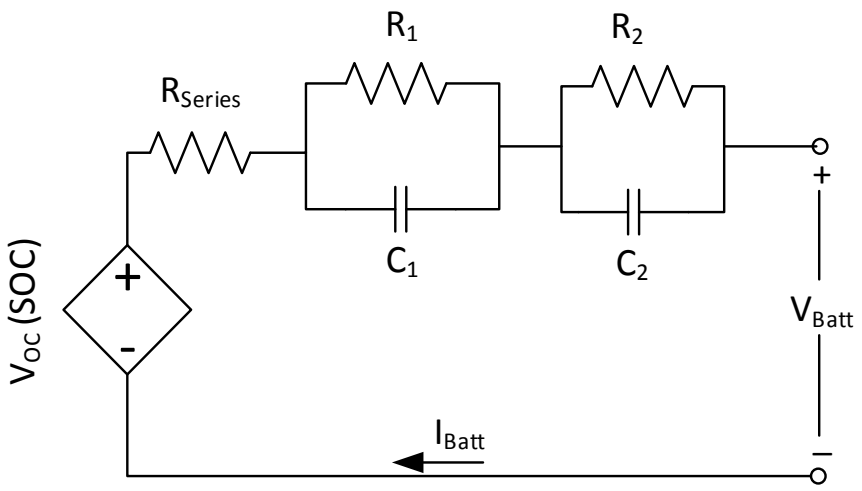

Figure 58: Dual Polarization Circuit

The most complete set of data offered in [43] is given at 40°C, where resistance and capacitance terms are provided over the largest SOC range. The original goal of this work was to construct a thermal-electric battery model that was capable of capturing transient thermal effects; however, due to the limited data availability, temperature will be assumed to be constant at 40°C. This is likely a reasonable approximation being that a 12°C cooling source from seawater can be used for thermal management.

In contrast to research focused on testing and parameter identification at the cell-level, the study in [43] provides pack-level results which are rare in the public sphere. Pack-scale performance data is much more accurate than scaling from cell level data. Scaling by way of series/parallel impedance extrapolation from cell-level equivalent circuit parameters does not properly account for all the additional impedances that arise from the module assembly. In this work, we look to extend the results from [43] into a large scale battery packs suitable for an electric ferry.

The published equivalent circuit parameters were implemented into a dual polarization equivalent circuit model using Simscape, as done in Huria et al. [46]. The large-scale battery pack is then constructed by first creating a 9.2kWh module (from [43]), then

adding modules in series and parallel to achieve the desired voltage level and capacity. Figure 59 illustrates the large-scale battery assembly process. By using Simscape, the model can be constructed as it would be done in real-life using physical network approach.

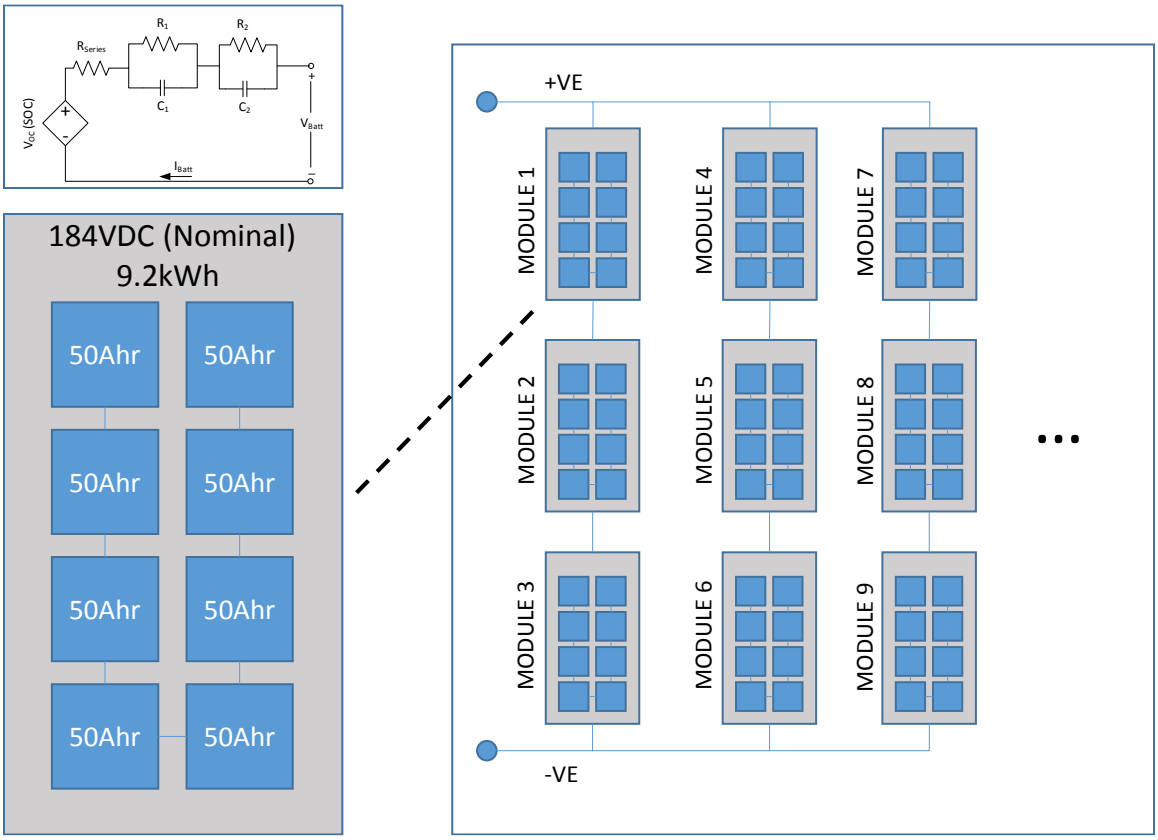

Figure 59: Construction of Large-Scale Battery Model Using Module Test Data

The implementation in Simscape allows for the dynamic response of the entire pack to be investigated. Recall from Chapter 2 that scaling formulae were developed for adding equivalent circuits together in series/parallel, but the Simscape formulation offers a more physical representation of the system, while also allowing thermal effects to be added in the same environment in future. It also enable for variation of initial SOCs for each module to study imbalance situation and BMS system control.

The physical system approach allows for script-based automatic model generation, which is a huge benefit when looking towards future in battery capacity optimization studies. The main drawback of large-scale battery model implementation in Simscape is the increased simulation times that can occur when co-simulating with complex systems, especially those implemented in basic Simulink. Highly dynamic load profiles can drastically slow down the simulation as will be discussed in section 5.2.1.2.

The equivalent circuit parameters at 40°C, published in [43], are summarized in Table 15. Interestingly, the authors did not include the OCV as a function of SOC in their report. The data for series resistance R_{ESR} was given a function of OCV, yet no immediate data was provided to correlate the series resistance with SOC. As a result, the OCV versus SOC parameters had to be estimated from datasheets of a similar LTO cell. This allowed the ESR to be estimated as a function of SOC for equivalent circuit model. This process produced low resolution in some regions, especially at SOCs greater than 90%. Parameters that have been estimated based using the above technique are italicized in Table 15. It should be noted that the ESR values have been averaged between their charge and discharge values for simplicity. The original Simscape model included individual lookup tables for charge and discharge ESR; however, this was found to cause a numerical instability which slowed down the simulation drastically.

Table 15: Summary of Equivalent Circuit Parameters for 9.2kWh Module

SOC	OCV (V)	R_{ESR} (Ω)	R_1 (Ω)	C_1 (F)	R_2 (Ω)	C_2 (F)
0.132	*169.3*	*0.05714*	0.0246	109.8	0.058811	7203
0.232	*174.6*	*0.05692*	0.0242	207.89	0.042464	12199
0.333	*179.5*	*0.05627*	0.0205	235.4	0.03255	11025
0.434	*182.2*	*0.05574*	0.0142	296.02	0.022281	4205.2
0.534	*183.4*	*0.05297*	0.014	309.54	0.011296	3158.6
0.635	*185.0*	*0.04831*	0.0113	354.31	0.010301	2645.8
0.736	*187.7*	*0.04834*	0.0099	436.17	0.010394	2446.6
0.837	*191.0*	*0.04779*	0.0102	437.13	0.010403	2456.5
0.937	*200.5*	*0.04779*	0.0101	468.56	0.008193	2146.6

As mentioned previously, one of the major gaps in the data published in [43] relates to the OCV versus SOC relationship. The OCV is typically calculated at a very small C-rate (1/25C), whereas the OCV plots provided by the authors are given at 1C. The authors appear to have confused terminal voltage with OCV in these plots in the context of the equivalent circuit parameters. Instead of using the OCV data provided in the report, the curves from another LTO cell provider were used as a basis for the model. Figure 60 shows a 1C discharge capacity test comparison between the 9.2kWh module presented in Cleary et al. [43], with the model developed in Simulink. The results are within reasonable agreement, though resolution has been lost due to the incomplete dataset.

The major benefit of the equivalent circuit model is its ability to quantify the dynamic response of the battery system when a dynamic load profile is applied. Unfortunately, the published information doesn't provide a good means for direct validation for the model's dynamic response; however, the response can be qualitatively evaluated using an HPPC test on the large-scale pack model once it has been designed. The following section presents the pack specifications and the preliminary design, then the dynamic performance is investigated using the HPPC test in section 5.2.1.2.

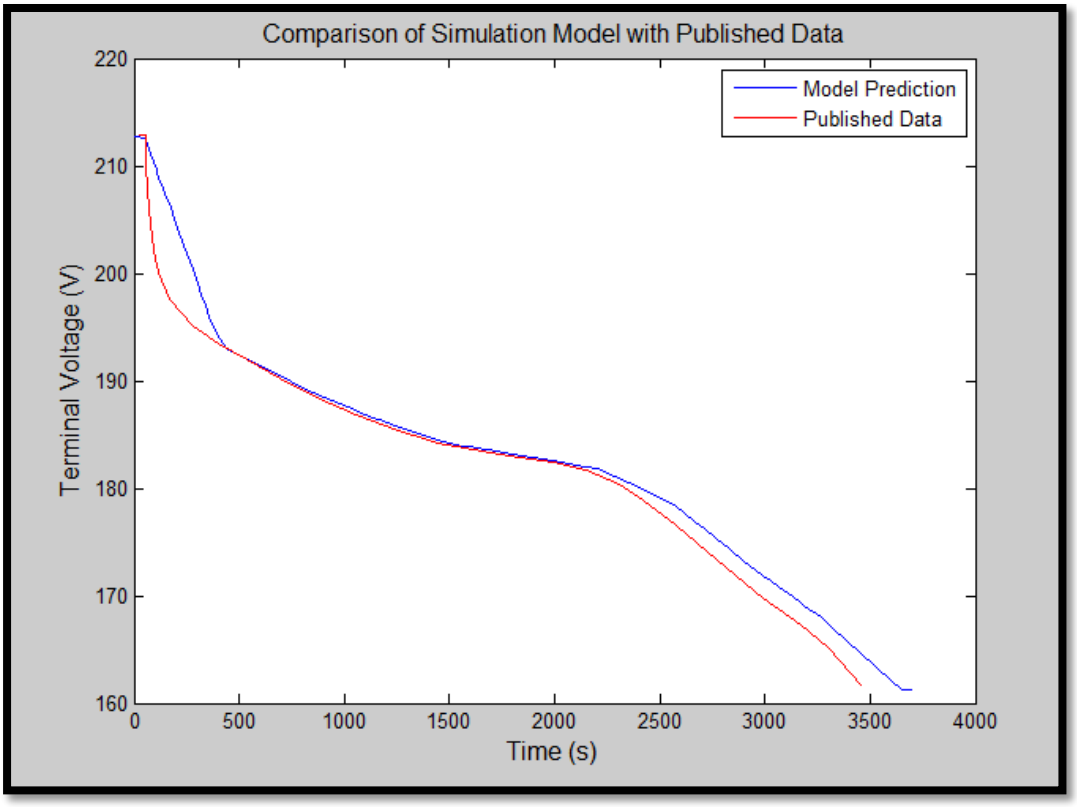

Figure 60: Comparison of Battery Model and Results from [43]

5.2.1.1 M.V. Klitsa Battery Capacity Sizing and Design

Now that the 9.2kWh equivalent circuit model has been established, the large-scale pack must be designed to meet the energy needs of the M.V. Klitsa. The load profiles collected in the data acquisition experiment are discussed in the next chapter, but the energy requirements can be conservatively estimated using the installed capacities and the schedule information for the ship.

Beginning with a conservative design approach that assumes full power demand from all consumers including propulsive and hotel loads, while also including a contingency reserve, the instantaneous peak power demand can be computed by summing all of the rated capacities from the existing equipment. With the rated capacities listed in Table 16 and the expected operational durations provided in Table 17, the energy storage capacity

requirements can then be calculated based on a worst case scenario. Note that this approach does not explicitly include an allowance for battery degradation.

Table 16: First-Pass Design Requirements for Power Output

Electric Drive 1	260kW
Electric Drive 2	260kW
Maximum Hotel Load	50kW
Contingency Allowance	30kW
Total Maximum Power Demand	**600kW**

Table 17: First-Pass Design for ESS Capacity Estimation

One-Way travel time	0.42h
Return Total Travel Time	0.833h
Max Energy Consumption (Return)	**500kWh**

From these requirements, the 9.2kWh modules were combined into series and parallel to achieve the desired energy capacity. The high voltage DC bus is to remain constant at 750VDC to maximize the efficiency of the electric drive motors. The bi-directional DC/DC converter will operate in boost-mode to regulate the DC grid voltage from the battery terminals; consequently, the number of modules in series is selected such that the maximum voltage is less than the high voltage DC bus at maximum pack voltage. This is consistent with the commercially available the bi-directional converters such as [98].

Lastly, the expected life can be extrapolated empirically based on cycling data available for the LTO cells. If the mean C-Rate is kept to below 3C, then data exists for providing a preliminary pass on expected degradation. The final configuration for achieving the desired capacity and meeting the converter constraints are given in Table 19.

Table 18: Single 9.2kWh Module Technical Specifications

Module Information		
Nominal Voltage	184.00	V
Maximum Voltage	210.00	V
Minimum Voltage	160.00	V
Capacity (Ah)	50.00	Ah
Capacity (kWh)	9.20	Kwh

Table 19: Battery Pack Configuration and Specifications

Pack Information		
Branch Series Modules	3	unit
Parallel Branches	20	unit
Total Modules	60	unit
Pack Nominal Voltage	552	V
Pack Maximum Voltage	630	V
Pack Minimum Voltage	480	V
Capacity Per Branch	9.2	kWh
Total Pack Capacity	552	kWh
Total Pack Capacity (Ah)	1000	Ah
Expected Load	275	kW
Expected Current	498.2	A
1C Current	1000	A
Expected C-rate	0.5	C
Maximum C-rate	3.00	C

5.2.1.2 Large-Scale Battery Pack Modeling and Simulation

A custom Simscape library block was created by assembling individual module blocks into the 3S20P module configuration as dictated by the Klitsa's energy requirements. The resulting Simscape model, looking under the mask, is illustrated in Figure 18. The library block tracks each module's SOC individually, which can be averaged to get the global SOC state. The battery pack model block also returns the total power dissipation across all energy modules for calculating losses and estimating system efficiency. A capacity test using the battery pack block is shown in Figure 62. The model executed sufficiently fast, even with 60 modules simulating simultaneously, but only when current draw was

constant. Dynamic simulation drastically increased simulation time. For the 1C discharge capacity test, the execution was completed in 88 seconds using the *tic/toc* functions within Matlab which includes compiling time. The actual simulation time required for 3660s of simulation time was found to be 25s, giving 146:1 ratio in faster than real-time. A plot of the SOC, terminal voltage, and current profile for the static discharge capacity test is provided in Figure 62.

Figure 61: Construction of Battery Pack from Module Blocks in Simulink using Simscape

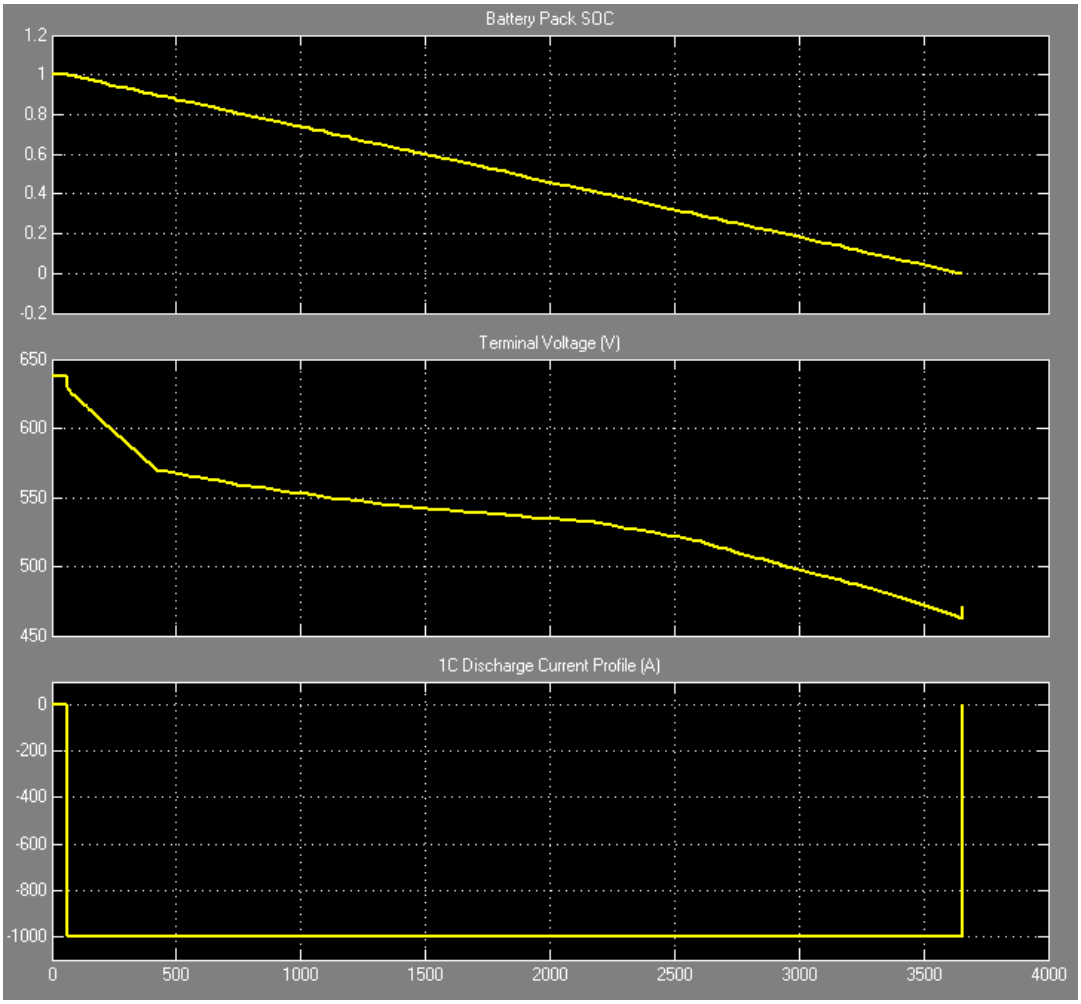

Figure 62: 1C Discharge Test for 3S60P Module Battery Pack to Confirm Capacity

Though the large-scale pack model implementation in Simscape provided reasonable simulation times in isolation, it caused significant problems during the system-level model simulation. The increased simulation time was unacceptable for the objectives of this work; therefore, this Simscape pack model was subjected to an HPPC simulation in order to provide dynamic response data. Using this data, the large-scale battery pack performance was fit to a reduced order equivalent circuit model using the method presented in Huria et al. [46]. This drastically reduced the number of states in the model, and the implementation could be performed in regular Simulink blocks for computational efficiency.

The parameter fitting process was executed using the Matlab's Parameter Estimation utility. The results of the HPPC dynamic response test for the Simscape model and the fitted model are shown in Figure 63 and Figure 64. Again, the fitted parameters have been restricted to a single temperature 40°C in this work, but can be expanded in future. The response is well represented by the equivalent circuit approximation, and the dynamic response is consistent with other published research.

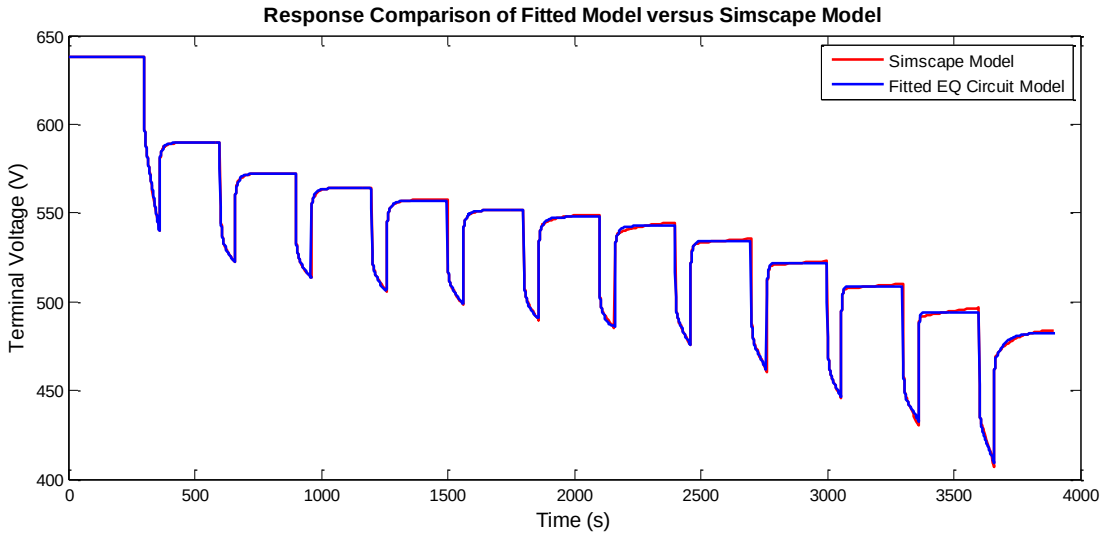

Figure 63: Response Comparison of Fitted Simulink Model versus Simscape Model

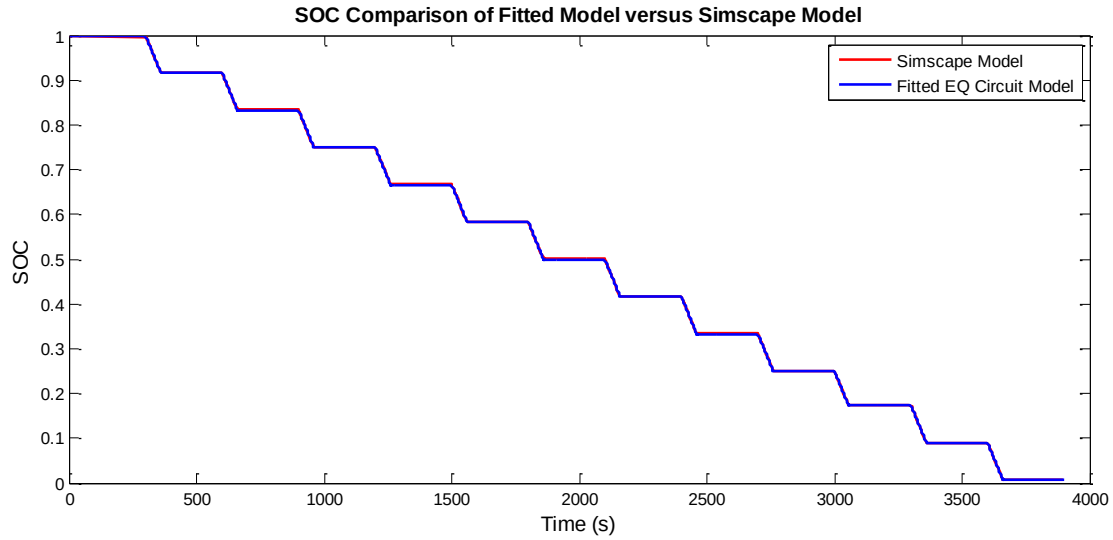

Figure 64: SOC Comparison of Fitted Simulink Model versus Simscape Model

5.2.2 Bi-Directional DC/DC Converter Modeling

Unlike most automotive HEVs, shipboard DC installations require a fixed DC bus voltage to control power quality and ensure full performance of all sub-system components. The harmonics induced in the electrical system as a result of switching power converters must be managed to minimize losses and ensure reliable operation. Because the battery voltage will drop as it is discharged, a DC/DC converter is required to boost the battery output to maintain a stable DC distribution voltage. In traditional ships, the AC voltage is regulated using field control in the synchronous generators [81]. In DC grid-based AES applications, the voltage is also regulated by the electrical generation system through controlled rectification or field excitation control in the generator. The BEIPS system in this work differs slightly in that onboard electricity generation has been completely replaced with stored electrical energy in the battery. As a result, the DC/DC converter must be perform the task of voltage regulation on the distribution DC bus.

Battery voltages are typically lower than those required by electrical drive components; therefore, the converter operates in boost mode when supplying energy to the grid. The system must also be capable of absorbing power in the battery; therefore, the converter must be able to operate in buck-mode when the power flow is reversed.

Several academic papers have studied the converter topology shown in Figure 65 for use in shipboard applications with energy storage. This converter has the advantage of being electrically isolated as a result of the voltage transformer. This feature is critical in the context of fault control and safety. As can be seen in circuit diagram, the converter's topology also includes an active-clamp system to enable zero voltage switching (ZVS) for minimization of switching losses.

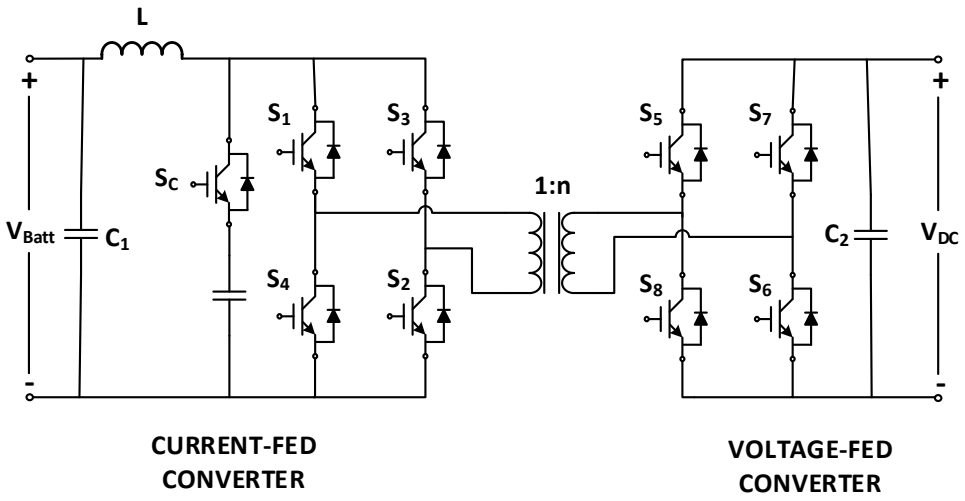

Figure 65: Bi-Directional Buck-Boost Converter Topology for Ship Applications

The detailed analysis of this converter is beyond the scope of this thesis. Furthermore, the converter's switching dynamics are orders of magnitude faster than those of the ship dynamics, so they can ultimately be neglected and replaced with averaged models. The work of Zahedi et al. [26] and Chung et al. [25] analyzed this converter topology using an AVM small-signal approach in shipboard hybrid power systems applications; however, in these studies the converter uses a different control law than that required in this work. Their architecture assumes that the high voltage is regulated elsewhere in the system; therefore, current control is used on the high voltage side in boost mode to manipulate power output. In buck mode, the converter uses voltage control on the battery side.

In this work the control law in slightly different because the converter must regulate the distribution voltage in both buck and boost modes. In the event that the electric machines become overdriven and begin producing power, the bus voltage will begin to climb unless power can be absorbed in the system. The converter must take action to apply load via the batteries, switching its operation to buck mode. Current is exported to the batteries to maintain the DC voltage; however, the current delivered to the batteries must be

regulated so to not exceed maximum C-rate. Furthermore, the maximum battery voltage cannot be exceeded. A real application may require the use of a DC chopper for safety, but this is unlikely to be a problem with LTO chemistry and the large capacity battery. The current control law for the converter is described in Table 20.

Table 20: Desired Control Law BEIPS

	BUCK MODE (BATTERY CHARGE)	BOOST MODEL (BATTERY DISCHARGE)
CONTROL INPUT	Duty Cycle (d)	Duty Cycle (d)
SYSTEM OUTPUT	Voltage (V_{DC})	Voltage (V_{DC})
DISTURBANCE	Input Current ($_{DC}$), Battery Resistance (R_{Batt})	Low Voltage (V_{Batt}), Load Impedance (R_2)
STATES	Inductor Current (i_L), LV Capacitor Voltage (v_{C1})	Inductor Current (i_L), LV Capacitor Voltage (v_{C2})

Because power system stability is not being investigated in this work, this converter can be reduced to a power losses for simplicity; however, the next logical improvement to the power system model is to upgrade the DC/DC converter to include the average value dynamics. As a first step, it is important to verify that the desired control law is achievable. Chung et al. [25] derive the average value and small-signal approximations for the converter used for controller synthesis. Here, a similar analysis is performed to verify the desired control law.

The equations governing the converter can be expressed in average value terms, denoted by $\langle\cdot\rangle$, where the averaged signal value is defined by,

$$\langle x_s \rangle = \frac{1}{T_S} \int_{t}^{t+T_s} x_s(\tau) d\tau \qquad \textbf{(5-1)}$$

Here, T_s denotes the period of the switching frequency, and x_s is a general placeholder for a signal variable. The duty cycle D and switching pattern for this converter in boost mode is illustrated below in Figure 66.

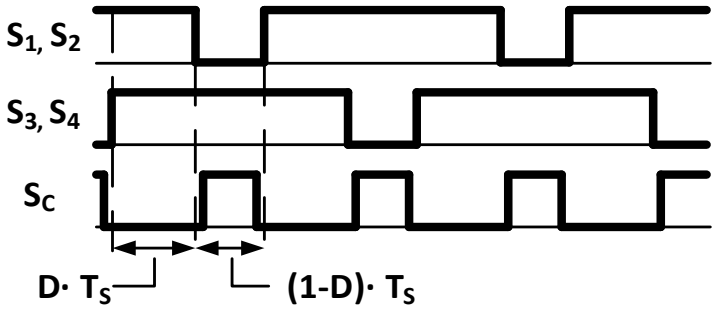

Figure 66: Gate Signal Pattern for Bi-Directional DC/DC Converter for Boost Mode [25]

When all the switches on the current-fed bridge are turned on, the inductor is charging and its voltage is equal to that of the battery. The voltage across the transformer is zero, though some current will flow as a result of leakage inductance in a real transformer. In this phase, the high voltage output capacitor C_2 discharges to supply the current to the load. When an opposing pair of switches is turned off and ignoring the active-clamp temporarily, the energy stored in the inductor is discharged through the transformer. The burst of current supplies the load current and recharges the output capacitor C_2. Current flows through the diodes on the voltage-fed bridge devices. The pattern is then repeated by alternating switch pairs.

Assuming that the converter is operating in boost mode at quasi-steady state, the application of KVL using average value analysis yields the following equation,

$$L\frac{d\langle i_L\rangle}{dt} \approx \frac{1}{T_S}\left[\left(\langle v_{batt}\rangle - \frac{1}{n}\langle v_{dc}\rangle\right)(1-D)T_s - \langle v_{batt}\rangle DT_s\right] \quad \textbf{(5-2)}$$

Which simplifies to,

$$L\frac{d\langle i_L\rangle}{dt} \approx \langle v_{batt}\rangle - \frac{1}{n}\langle v_{dc}\rangle(1-D) \quad \textbf{(5-3)}$$

Note the variable *n* represents the number of turns on the transformer secondary side. Application of KCL on the high voltage (output) side gives the expression,

$$C_2\frac{d\langle v_{dc}\rangle}{dt} \approx \frac{1}{T_S}\left[\left(\frac{1}{n}\langle i_L\rangle - \frac{\langle v_{dc}\rangle}{R_2}\right)(1-D)T_s + \left(-\frac{\langle v_{batt}\rangle}{R_2}\right)DT_s\right] \quad \textbf{(5-4)}$$

Which simplifies to,

$$C_2\frac{d\langle v_{dc}\rangle}{dt} \approx \frac{1}{n}\langle i_L\rangle(1-D) - \frac{\langle v_{dc}\rangle}{R_2} \quad \textbf{(5-5)}$$

Similarly, input current is calculated with KCL as,

$$C_1\frac{d\langle v_{batt}\rangle}{dt} \approx \langle i_{batt}\rangle - \langle i_L\rangle \quad \textbf{(5-6)}$$

For buck mode, the gating sequence for the voltage-fed converter is shown in Figure 67. The opposing switches on the voltage-fed converter produce a reversing voltage on the transformer winding. For a duration of *DTs*, power flows through the transformer and the converter-fed bridge diodes to be stored in the inductor. When both switch pairs are turned off, the inductor discharges stored energy to the low voltage side charging the battery.

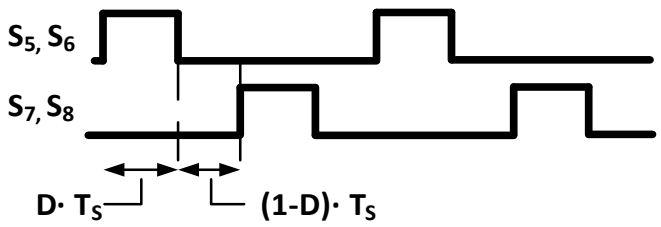

Figure 67: Gate Signal Pattern for Bi-Directional DC/DC Converter for Buck Mode

Now assuming operation in buck mode at quasi-steady state, application of KVL using average values analysis yields the following equation,

$$L\frac{d\langle i_L\rangle}{dt} \approx \frac{1}{T_S}\left[\left(\frac{1}{n}\langle v_{dc}\rangle - \langle v_{batt}\rangle\right)DT_s - \langle v_{batt}\rangle(1-D)T_s\right] \quad \textbf{(5-7)}$$

This simplifies to,

$$L\frac{d\langle i_L\rangle}{dt} \approx \frac{1}{n}\langle v_{dc}\rangle D - \langle v_{batt}\rangle \quad \textbf{(5-8)}$$

Application of KCL on the low voltage side (output) gives the expression,

$$C_1\frac{d\langle v_{batt}\rangle}{dt} \approx \langle i_L\rangle(1-D) - \frac{\langle v_{batt}\rangle}{R_1} \quad \textbf{(5-9)}$$

The input equation is described by,

$$C_2\frac{d\hat{v}_{dc}}{dt} \approx \langle i_{dc}\rangle - \langle i_L\rangle nD \quad \textbf{(5-10)}$$

The average current drawn from the high voltage source is then given by,

$$\langle i_{DC}\rangle \approx \frac{1}{T_s}\left[\langle i_{p,HV}\rangle DT_s + 0(1-D)T_s\right] = \langle i_{p,HV}\rangle D \quad \textbf{(5-11)}$$

Chung et al. [25] develop the small-signal average models for these equations by applying Taylor series and gathering first order terms. The mean values are denoted with capital letters, and perturbations off the mean are denoted with the ˆ identifier. The

resulting equations from [25] are summarized in Table 21 below with DC terms removed. Note here that,

$$D' = (1 - D) \quad \textbf{(5-12)}$$

Table 21: Small-signal Approximation Equations for Controller Development

	Buck Mode	Boost Mode
Inductor Balance	$L\frac{d\hat{\imath}_L}{dt} = \frac{1}{n}D\hat{v}_{dc} + \frac{1}{n}V_{DC}\hat{d} - \hat{v}_{batt}$	$L\frac{d\hat{\imath}_L}{dt} = \hat{v}_{batt} - \frac{D'}{n}\hat{v}_{dc} + \frac{1}{n}V_{DC}\hat{d}$
Output Current	$C_1\frac{d\hat{v}_{batt}}{dt} = \hat{\imath}_L - \frac{\hat{v}_{batt}}{R_1}$	$C_2\frac{d\hat{v}_{dc}}{dt} = \frac{D'}{n}\hat{\imath}_L - \frac{1}{n}I_L\hat{d} - \frac{\hat{v}_{dc}}{R_2}$
Input Current	$C_2\frac{d\hat{v}_{dc}}{dt} \approx \hat{\imath}_{dc} - nI_L\hat{d} - nD\hat{\imath}_L$	$C_1\frac{d\hat{v}_{batt}}{dt} \approx \hat{\imath}_{batt} - \hat{\imath}_L$
Transformer Current	$\hat{\imath}_s = \frac{1}{n}\hat{\imath}_L$	$\hat{\imath}_s = \frac{1}{n}\hat{\imath}_L D'$

Using these equation, we can develop transfer functions that can be developed based on the desired control law. This is done in Appendix B, along with a verification of controllability using numerical values from the converters studied in [25] and [26]. The transfer functions for bus voltage regulation in both buck and boost modes are presented in Table 22.

Table 22: HVDC Control Transfer Function for Buck and Boost Mode

Transfer Function	Buck Mode	Boost Mode
$G_{v_{dc}d}(s)$	$\frac{-(snLI_L + DV_{DC})}{s^2LC_2 + D^2}$	$\frac{R_2(D'V_{DC} - nI_LsL)}{\left(s^2Ln^2C_2R_2 + sLn^2 + R_2D'^2\right)}$

Design of the converter and development of the controller will constitute future work. For now, the task is to develop a reasonable efficiency map for the converter for our

simulation studies. Obtaining product information on these types of converters is often difficult, primarily because large-scale units are often custom designed to the application; however, some insight can be gleaned into the converter's efficiency map as a function of power output by looking at literature discussing converter implementations.

In the work of Park and Choi [99], a 5kW converter of similar topology is design and implemented. The authors provide efficiency data of the converter at varying output levels. It was shown that the converter should be operating at greater than 40% to achieve the best efficiency. Converter efficiency generally gets better as size increases. A commercially available bi-directional buck-boost converter with a 200kW output at similar voltage levels to our case study can achieve >97% efficiency when operating above a 15% capacity factor [98]. The published efficiency map for this converter is shown in Figure 68.

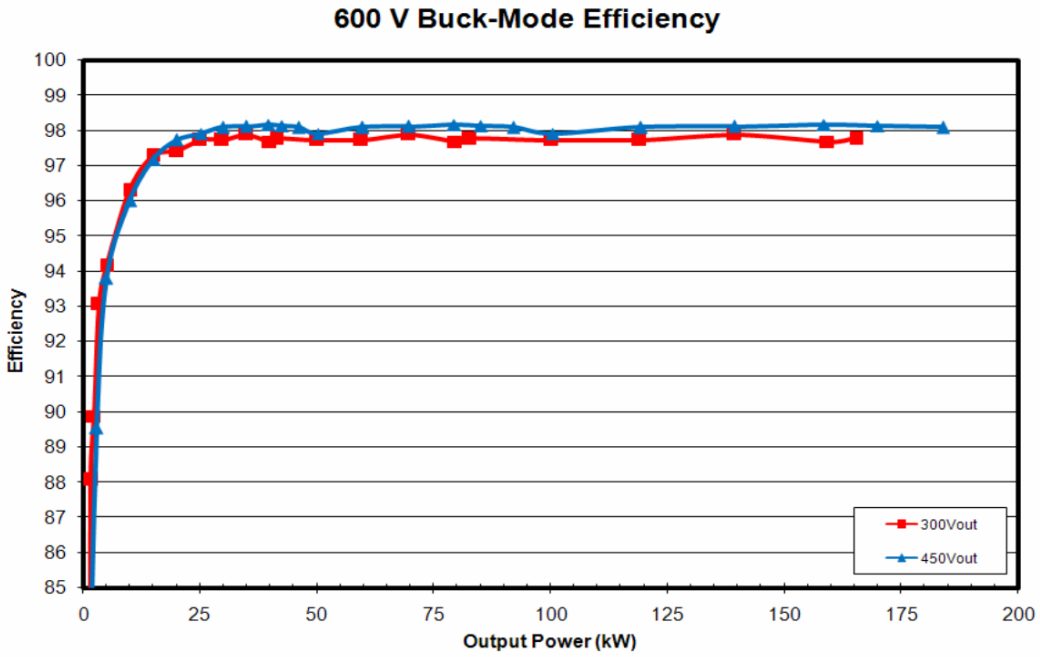

Figure 68: Efficiency Curve of Commercially Available 200kW Bi-Directional Buck/Boost Converter [98]

Because the ship's operational profile has significant swings in power output, it is essential that the capacity factor of the converter be investigated to ensure maximum efficiency over the entire load profile. In berth, the ship's battery will be connected to the charging infrastructure; however, the converter will still supply the main propulsive and hotel loads. Based on observations from the data acquisition study, a high output and low output scenario were developed to investigate capacity factor during both transit and while in berth. Table 23 and Table 24 show a comparison between use of a single 600kW converter, and the use of two 300kW converters assuming the same efficiency map as presented in Figure 68. With a single converter operating while in berth, the low capacity factor will lead to a reduction in overall system efficiency. In contrast, the use of two converters enables a higher potential for maximizing system efficiency at low loads by boosting the capacity factor.

Table 23: Low and High Load Comparison for M.V. Klitsa with Single Converter

Low Operating Condition - In Transit			**High Operating Condition - In Transit**		
Converter Rating	600	kW	Converter Rating	600	kW
Engine 1 Low Output (40%)	100	kW	Engine 1 High Output (80%)	200	kW
Engine 2 Low Output (40%)	100	kW	Engine 2 High Output (80%)	200	kW
Low Hotel Load	10	kW	High Hotel Load	35	kW
Low Load Operational	**210**	**kW**	**High Load Operational**	**435**	**kW**
Capacity Factor	**0.35**		**Capacity Factor**	**0.73**	

Low Operating Condition - In Berth			**High Operating Condition - In Berth**		
Converter Rating	600	kW	Converter Rating	600	kW
Engine 1 Low Output (10%)	25	kW	Engine 1 High Output (15%)	38	kW
Engine 2 Low Output (10%)	25	kW	Engine 2 High Output (15%)	38	kW
Low Hotel Load	10	kW	High Hotel Load	35	kW
Low Load Operational	**60**	**kW**	**Low Load Operational**	**110**	**kW**
Capacity Factor	**0.1**		**Capacity Factor**	**0.183**	

Table 24: Low and High Load Comparison of M.V. Klitsa with Two Converters

Low Operating Condition - In Transit			High Operating Condition - In Transit		
Converter Rating	300	kW	Converter Rating	300	kW
Number of Converters	2		Number of Converters	2	
Total Capacity	600	kW	Total Capacity	600	
Engine 1 Low Output (40%)	100	kW	Engine 1 High Output (80%)	200	kW
Engine 2 Low Output (40%)	100	kW	Engine 2 High Output (80%)	200	kW
Low Constant Hotel Load	10	kW	High Hotel Load	35	kW
Low Load Operational	**210**	**kW**	**High Load Operational**	**435**	**kW**
Converter 1 Output	**210**	**kW**	**Converter 1 Output**	**217.5**	
Capacity Factor - Converter 1	**0.70**		**Capacity Factor - Converter 1**	**0.73**	
Converter 2 Output	**0**	**kW**	**Converter 2 Output**	**217.5**	**kW**
Capacity Factor - Converter 2	**0**		**Capacity Factor – Converter 2**	**0.73**	

Low Operating Condition - In Berth			High Operating Condition - In Berth		
Converter Rating	300	kW	Converter Rating	300	kW
Number of Converters	2		Number of Converters	2	
Total Capacity	600	kW	Total Capacity	600	
Engine 1 Low Output (10%)	25	kW	Engine 1 High Output (15%)	38	kW
Engine 2 Low Output (10%)	25	kW	Engine 2 High Output (15%)	38	kW
Low Hotel Load	10	kW	High Hotel Load	35	kW
Low Load Operational	**60**	**kW**	**High Load Operational**	**110**	**kW**
Converter 1 Output	**60**	**kW**	**Converter 1 Output**	**110**	**kW**
Capacity Factor - Converter 1	**0.20**		**Capacity Factor - Converter 1**	**0.367**	
Converter 2 Output	**0**	**kW**	**Converter 2 Output**	**0**	**kW**
Capacity Factor - Converter 2	**0**		**Capacity Factor – Converter 2**	**0**	

The addition of a second converter also offers some redundancy in the event of a failure, allowing for a “limp home” mode in the event of a fault. The efficiency map of the above system shall provide the basis for the power loss model. Based on these operational characteristics, two parallel converters with 300kW capacity will maintain high operational efficiency at low output conditions for the ship. A rule-based controller using Simulink “State Machine” was developed to load share between the two converters when the demand is above 270kW, or 90% output, otherwise, only a single converter is

used. Once a second converter is brought online, a 20kW hysteresis loop prevents the second converter from switching on-and-off around the cut-in threshold.

The model implementation is shown below in Figure 69. The bus voltage level is set using a constant that is representative of the control law. The state machine senses the power output and determines how many converter are brought online. A negative power output reverses the power flow to charge the batteries. Note that the output of the battery model is the terminal voltage, making this a signal input to the DC/DC converter model. The amount of power transferred is computed using a lookup table that contains the efficiency lookup data provided in [98].

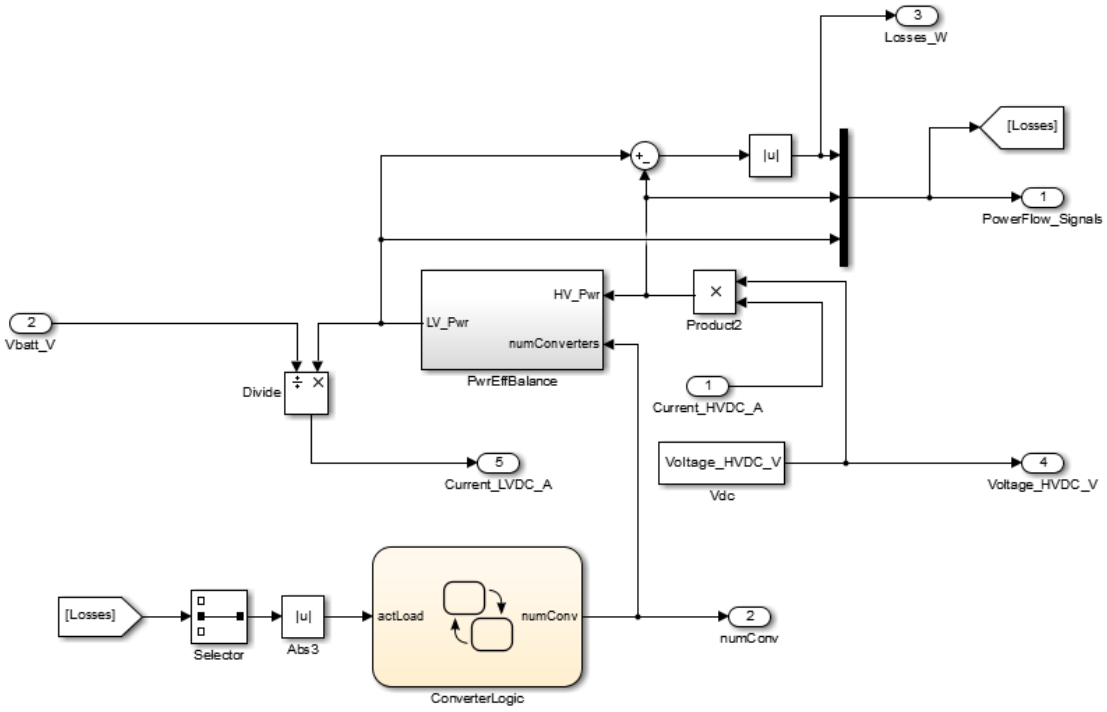

Figure 69: Implementation of Power Loss Model in Using Simscape

Figure 70 and Figure 71 show the DC-DC converter model behaviour output while operating in both buck and boost modes. The first image shows the converter operating boost mode. The low voltage power supplied by the battery is show with cyan line. The

power delivered to the high voltage DC bus is slightly less than the power delivered to the converter, shown by the magenta line. The red and green lines represent the turn-on/turn-off thresholds for the hysteresis loop for activating the second converter. The number of active converters is illustrated in the lower plot. The hysteresis algorithm holds the second converter until it drops below the lower threshold value (green line). The absolute value of the power losses are shown by the yellow line.

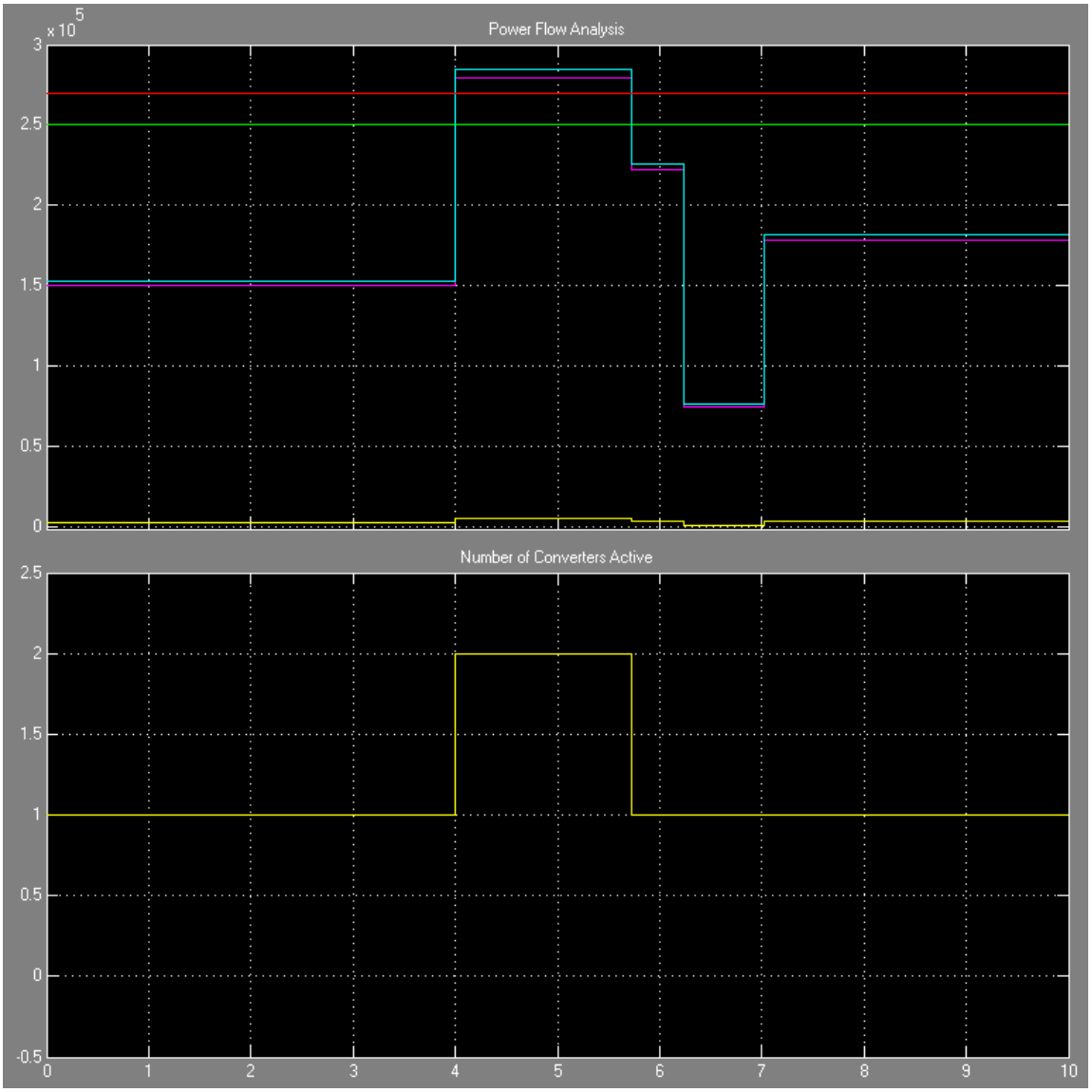

Figure 70: DC-DC Converter Model Operating in Boost Mode

Similarly, Figure 71 shows the converter operating in buck mode where power flow is reversed. The power delivered to the battery, shown again in cyan, is less than that provided by the bus side as expected. The efficiency map has been assumed to be the same for both directions. The number of controllers is coordinated by the same state machine, and based on the same threshold values as in the case of positive power flow.

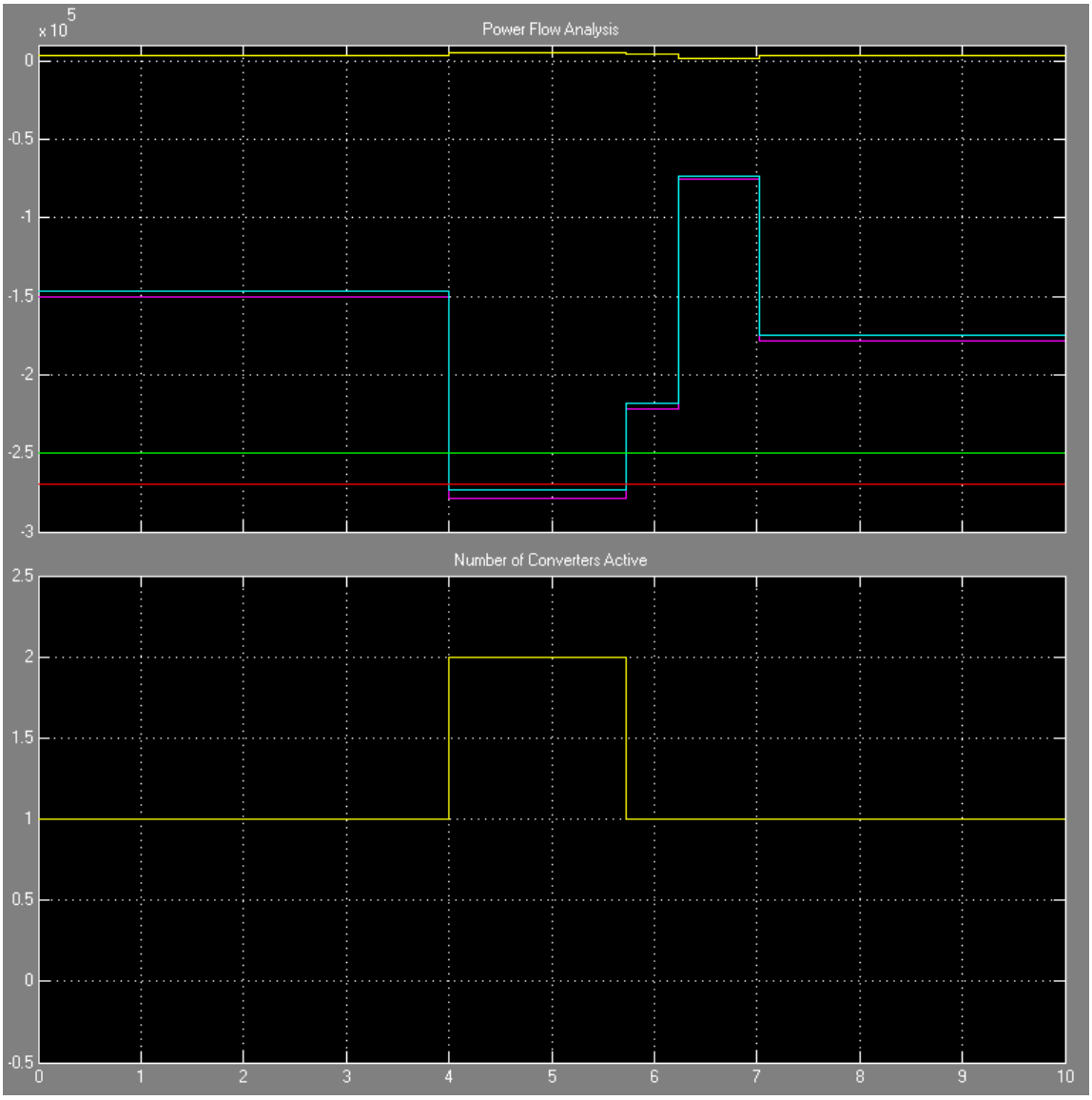

Figure 71: DC-DC Converter Model Operating in Buck Mode

5.2.3 Permanent Magnet Synchronous Machine Electric Drive System

For the purposes of an EV conversion case study, a commercially available high efficiency electric drive system has been selected as a potential candidate for the replacing the existing diesel engine. This particular electric drive system has similar power output and speed characteristics to that of the diesel as shown in Table 25, making it ideal for this particular ship.

Table 25: Comparison of Diesel Engine Output with PMSM Electric Drive

	Electric Drive	Existing Diesel Engine
Operating Speed	0 – 2250 rpm	600 – 1800 rpm
Maximum Torque	3400 Nm	2100 Nm
Rated Power	250kW	261kW

The theoretical background for modeling of PMSMs and VSI drives was presented in Chapter 2. This section now implements the average value simulation model to represent this commercial electric drive system. The manufacturer publishes an efficiency contour map as function of motor output torque and speed. This efficiency map will be used for comparison with a dynamic loss model that is based on analytical derivations. Furthermore, the electric drive manufacturer has also provided the basic machine parameters which allows for an accurate parametrization of the motor equations.

The implementation of the drive system model requires synthesis of a controller for closed-loop speed control. It also requires that the averaging technique be compared to a detailed switching model to confirm its accuracy. Therefore, the proceeding sub-sections will present the implementation and validation methodology including,

a) Parameterization of the fundamental equations
b) Development of an MTPA-based speed controller
c) Analysis of the dynamic loss model

d) Performance comparison of AVM versus detailed model

5.2.3.1 Implementation and Parameterization

The implementation of the average value model is based on the equations developed in Chapter 2. The Simscape language does offer pre-built blocks for PMSM motors; however, they are not conducive to the average value modeling approach developed in this work. The basic block diagram of the electric drive system model is described below in Figure 72.

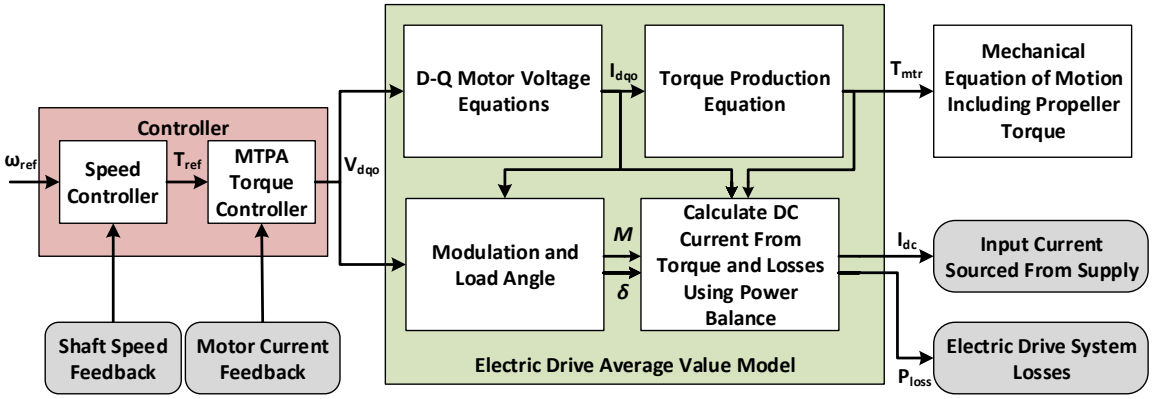

Figure 72: Average Value Model Implementation for Electric Drive System

The plant is manipulated using a speed controller, where the reference signal is to be fed by time series data from the engine speed profiles collected in the data acquisition study. The commercial system is tightly integrated to achieve high efficiency; therefore, the current control loop is likely governed using the Maximum Torque Per Ampere (MTPA) control algorithm. There are several implementation strategies for MTPA, and this work will implement the MTPA reference generator using lookup tables from offline global optimization.

The VSI acts as a voltage source to the motor; therefore, the inputs to the electric machine model are the *d-q* voltages from the inverter referenced to the rotor frame. The motor current is computed using the stator voltage differential equations. Finally, the

calculated *d-q* current outputs are fed into the torque subsystem to determine the instantaneous torque developed by the machine. The machine's electro-magnetic properties are listed in Table 26.

Table 26: Motor Parameters for Simulation Model

Parameter	Value
D-Axis Inductance (L_d)	241.4μH
Q-Axis Inductance (L_q)	409.6 μH
Pole Pairs (P_n)	12
Magnet Flux Linkage (λ_m)	0.18 Wb
Coil Resistance (R_c)	52.7mΩ

The electric drive system efficiency map is provided in Figure 73. The image illustrates the regions of constant torque and constant power for both peak and continuous operating conditions. This efficiency map can be used to extract the nameplate data from the machine, which will serve as the boundary conditions for the MTPA optimization algorithm.

By selecting the SVPWM switching strategy, the maximum achievable AC voltage for the fundamental AC waveform is constrained [32]. The maximum RMS line-to-line AC voltage is given by $V_{dc}/\sqrt{2}$. The maximum line current is not specifically stated in the motor documentation, but can be estimated with an assumption on power factor. A power factor of 0.9 is typical for synchronous machines, and has been assumed in order to establish the MTPA maximum current boundary. The calculated motor nameplate data is presented in Table 27.

Table 27: Estimated Motor Nameplate Data

Motor Ratings		
DC Voltage	750.0	VDC
L-N Peak AC Voltage with SVPWM (Amplitude)	433.0	VAC
L-L Peak AC Voltage with SVPWM (Amplitude)	750.0	VAC
L-N Peak AC Voltage (RMS)	306.2	VAC
L-L AC Voltage (RMS)	530.3	VAC
Maximum Power	250.0	kW
Assumed Power Factor	0.9	
Maximum Line Current (Amplitude)	427.7	AAC
Maximum Line Current (RMS)	302.4	AAC
Maximum Continuous Torque	1500	Nm
Maximum Peak Torque	3500	Nm
Rated Speed for Maximum Power @ Torque (Peak)	600	rpm
Rated Speed for Maximum Power @ Torque (Continuous)	1500	rpm

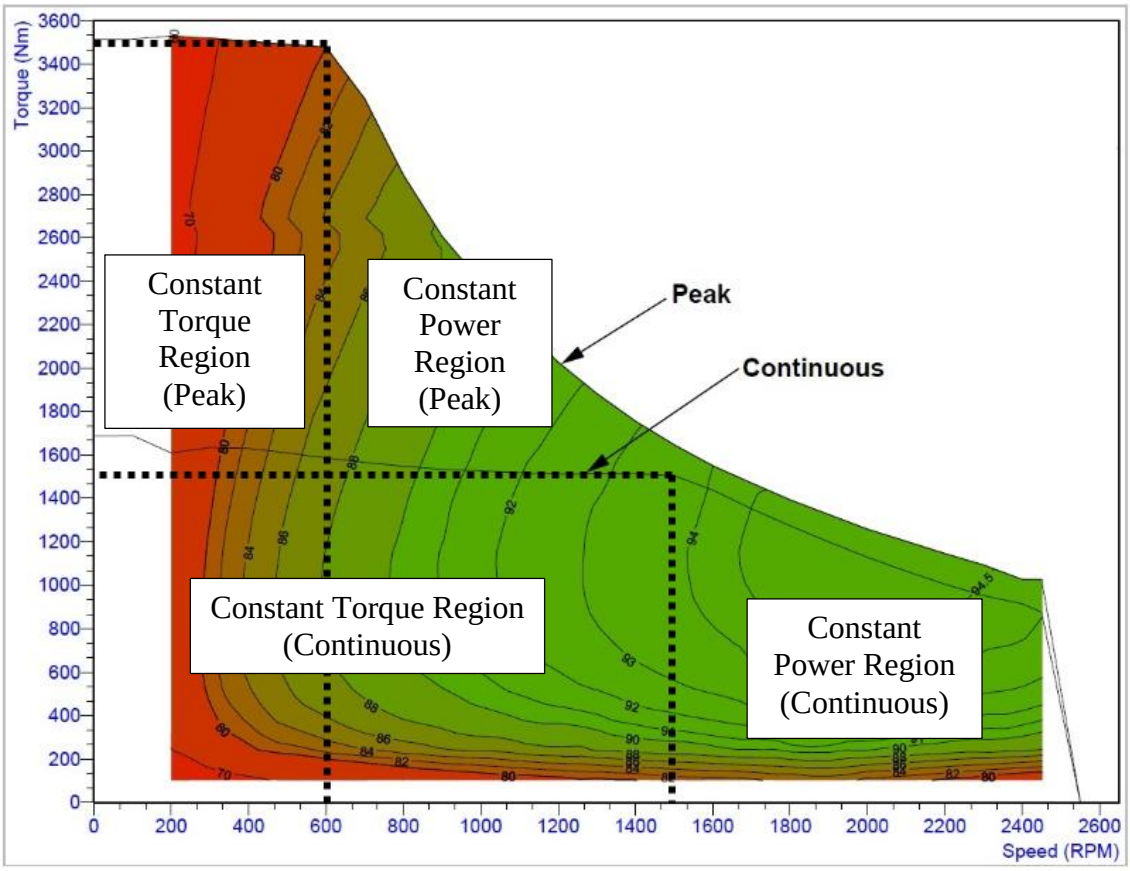

Figure 73: Peak and Continuous Power Outputs for the Electric Drive System

Details relating to the VSI's switching devices and their switching frequency are unknown, as they were not divulged by the manufacturer. The switching carrier frequency has been assumed to be constant at 10kHz. To properly parameterize the semiconductor loss model for the inverter, several pieces of information are required from the device datasheets. Without the exact model number for the true semiconductor devices, parameters have been taken from datasheets of another IGBT device with similar power ratings. The Infineon FZ600R12KE4 IGBT has suitable power ratings for the application, and a copy of the datasheet can be found in Appendix C. The relevant parameters for the semiconductor loss model are summarized in Table 28. It will be shown later that these parameters provide reasonable results in comparison to the published efficiency map.

Table 28: IGBT Parameters for Loss Estimation

IGBT Datasheet Parameters		
V_{ref}	1200	V
I_{ref}	600	A
f_s	10	kHz
V_{DC}	750	V
I_L	427.7	A
$E_{on,I}$	50	mJ
$E_{\mathrm{off},I}$	75	mJ
$E_{\mathrm{off},D}$	42	mJ
$V_{CE,0}$	2	V
R_{CE}	0.003	Ω
$V_{F,0}$	0.6	V
R_F	0.003	Ω

The electric drive system has nine output phases, where each phase is split across three semiconductor devices to reduce the current seen by switching devices and the stator coils as illustrated in Figure 74. This produces higher efficiency power conversion at the expense of increased complexity and manufacturing cost.

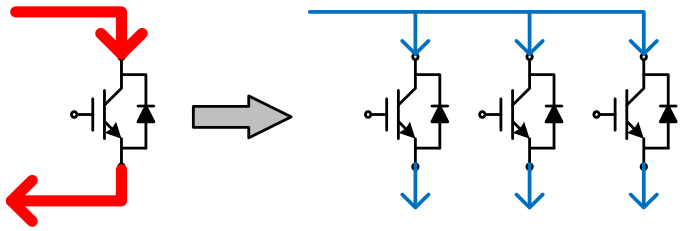

Figure 74: Current Splitting using Multiple Parallel Switching Devices

The semiconductor loss model presented in Chapter 2 has been updated to reflect this change in topology. The top-level semiconductor loss model implementation in Simulink is shown in Figure 75.

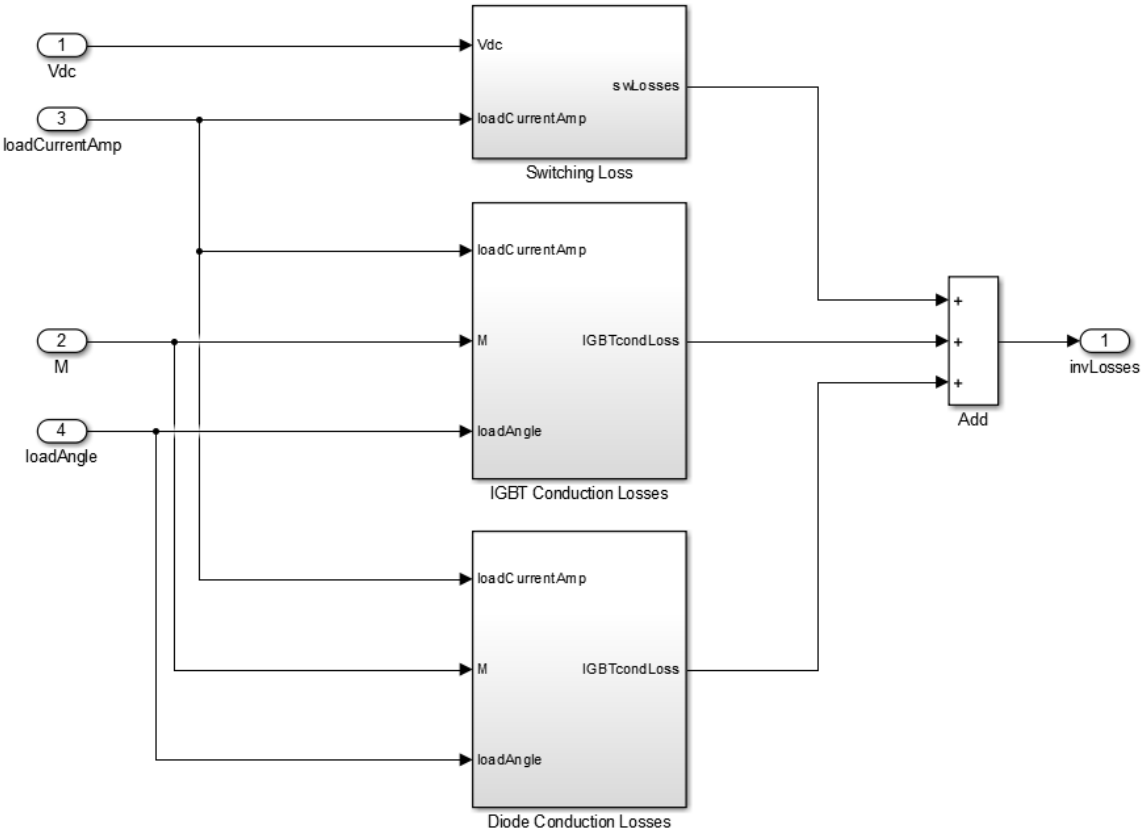

Figure 75: Implementation of Analytical Semiconductor Dynamic Loss Model for VSI

5.2.3.2 Controller Development and the MTPA Control Strategy Implementation

The previous section presented the parameter values needed to characterize the machine and inverter model to match the commercial system. The PMSM/VSI model now requires development of a speed controller for the system-level simulation. The controller model can easily be adapted in future to perform power control, as would be a more effective strategy for power stability in real vessels.

The torque production as a function current is given by Equation (2-64). The torque is dependent on the *d-q* components of the stator currents. The MTPA control strategy delivers the maximum possible amount of torque per unit of current delivered to the machine. There are several methodologies for implementation of this algorithm. In this work, the simplest possible implementation will be adopted by creating lookup tables parameterized from offline optimization.

A nested PI current control loop is included in the model to implement the MTPA reference generator. A block diagram of the speed and nested current controller is presented in Figure 76.

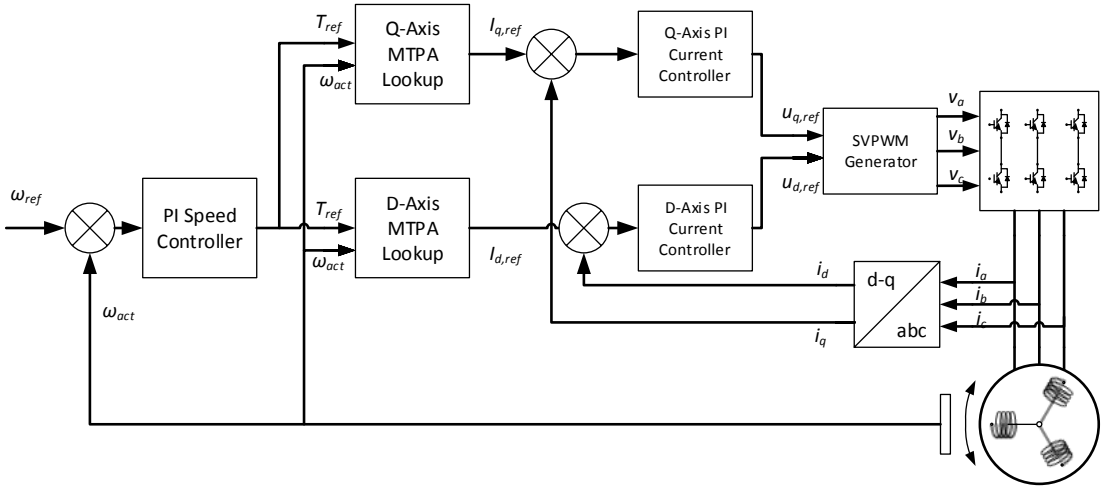

Figure 76: Control System Block Diagram

Generation of the MTPA lookup table data requires formulation of an optimization problem that can be solved in discrete intervals over the motor's operating range. The optimization problem is configured as a constrained minimization problem to compute minimum current for a given torque reference. It should be noted that the motor speed must also be fed into the lookup table to account for EMF induced by the magnets as function of rotor speed. The optimization problem is stated as follows:

$$\min_{i_{od}^r, i_{oq}^r} i_{s,r}\left(i_{od}^r, i_{oq}^r\right) = \sqrt{\left(i_{od,r} - \frac{\omega_r L_q i_{oq,r}}{R_i}\right)^2 + \left(i_{oq,r} + \frac{\omega_r\left(\lambda_m + L_d i_{od,r}\right)}{R_i}\right)^2} \quad \textbf{(5-13)}$$

Subject to,

$$\frac{3}{2} p_n\left(\lambda_m' i_{oq}^r + \left(L_d - L_q\right) i_{oq}^r i_{od}^r\right) - T_{ref,} = 0 \quad \textbf{(5-14)}$$

$$i_{od}^r \leq 0 \quad \textbf{(5-15)}$$

$$i_{oq}^r \geq 0 \quad \textbf{(5-16)}$$

$$i_{s,ref}^2 - {I_{max}}^2 \leq 0 \quad \textbf{(5-17)}$$

$$\left[R_c i_{od,r} + \left(1 + \frac{R_c}{R_i}\right)\left(-\omega_e L_q i_{oq,r}\right)\right]^2 + \left[R_c i_{oq,r} + \left(1 + \frac{R_c}{R_i}\right)\left(\omega_e L_d i_{od,r} + \omega_e \lambda_m\right)\right]^2 - {V_{max}}^2 \leq 0 \quad \textbf{(5-18)}$$

Note that this equation is based on the PMSM's stator equations which account for both copper and iron losses as performed in Chao et al. [34] The iron resistance value R_i was estimated using a parameter sweep with Matlab's optimization toolbox, and the best fit value was approximately at 100Ω. The MTPA optimization problem is well suited to the sequential quadratic programming (SQP) algorithm, where the gradient function can be computed numerically. An SQP algorithm is available within Matlab's *fmincon* function. This function was then systematically executed in a looping routine to solve for

the MPTA at a prescribed set of torque-speed operating points. The routine is described by the flowchart illustrated in Figure 77. With the correct constraints, the procedure should not produce any NaN entries but this diagnostic method provides was included for verification. This approach was validated using the two examples provided in Chao et al. [34].

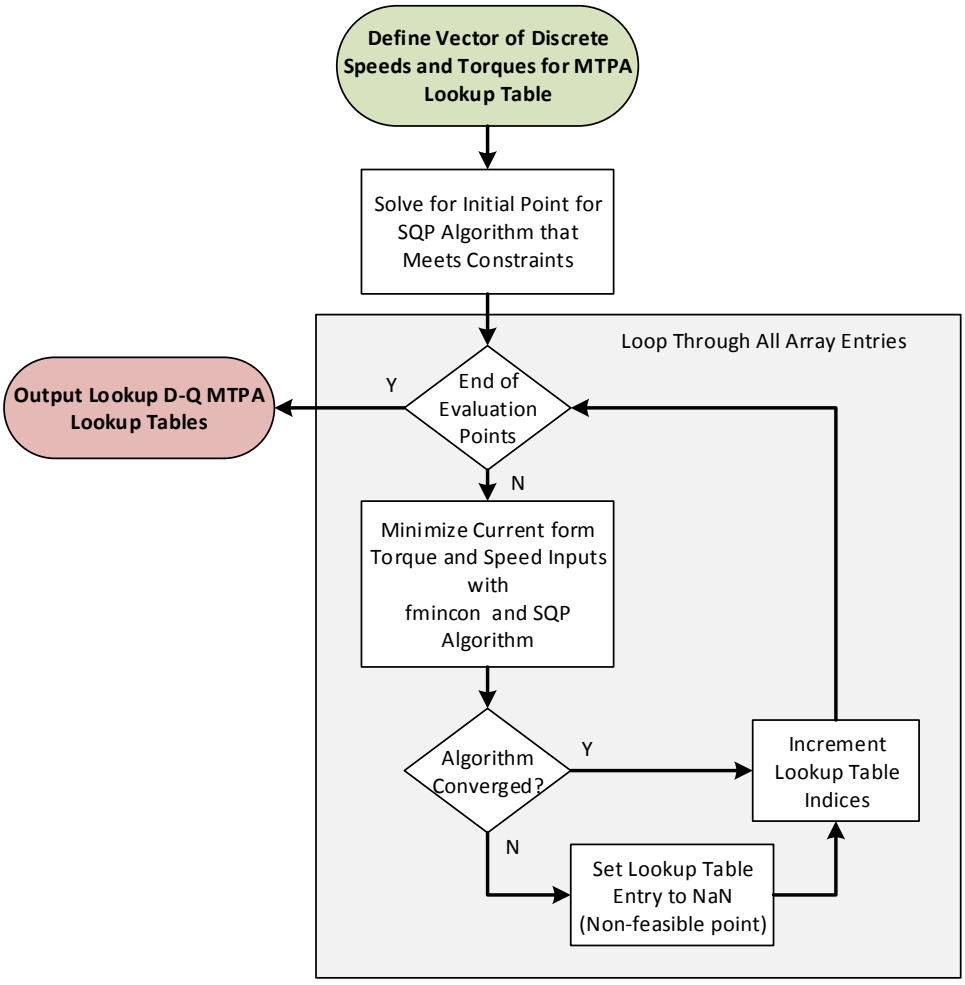

Figure 77: Procedure for Generating MTPA Lookup Tables

Using the machine parameters in Table 26, and assuming the nameplate data in Table 27, the optimization routine was carried out to develop the MTPA reference generators for the *d*-*q* current components as a function of commanded torque. A surface plot of the I_d and I_q lookup data are presented in Figure 78 and Figure 79, respectively.

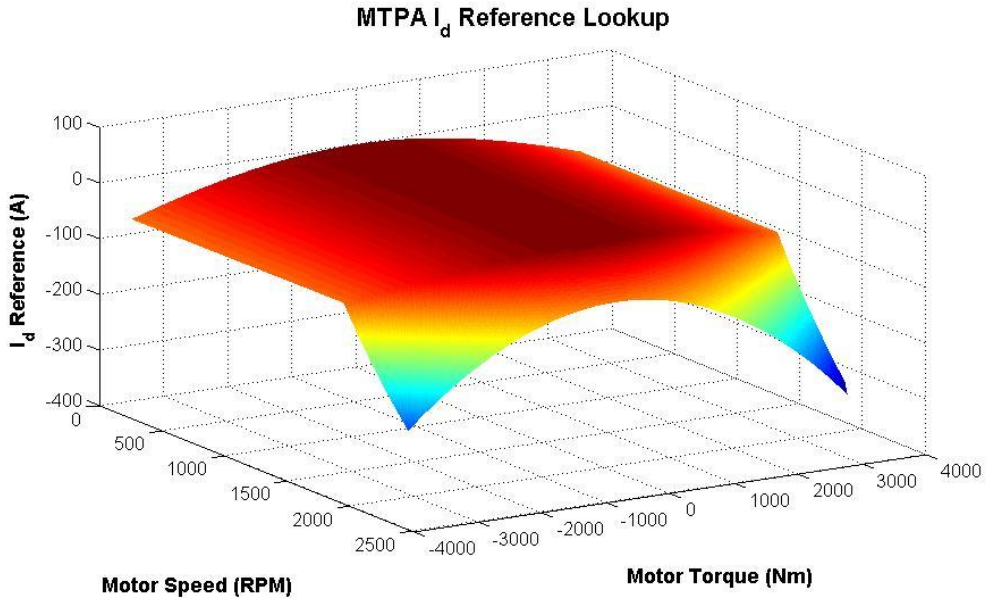

Figure 78: Plot of MTPA I_d Reference Lookup Data

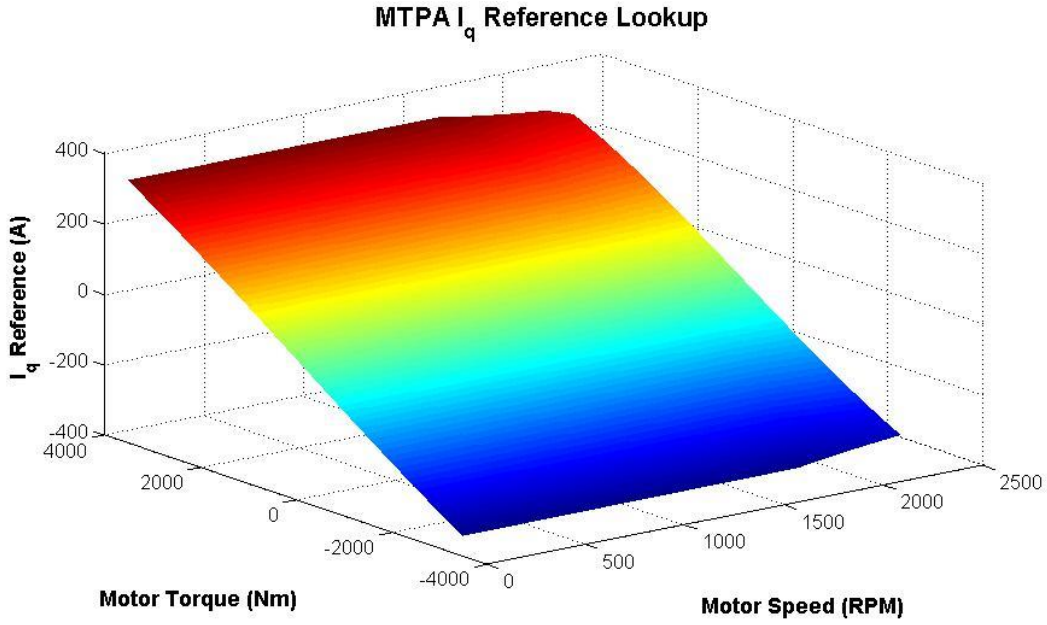

Figure 79: Plot of MTPA I_q Reference Lookup Data

The inner current loop, and outer speed loop PI controllers were then tuned to produce an appropriate dynamic response. The closed-loop response of the electric drive model in response to a step input in commanded speed is illustrated in Figure 80.

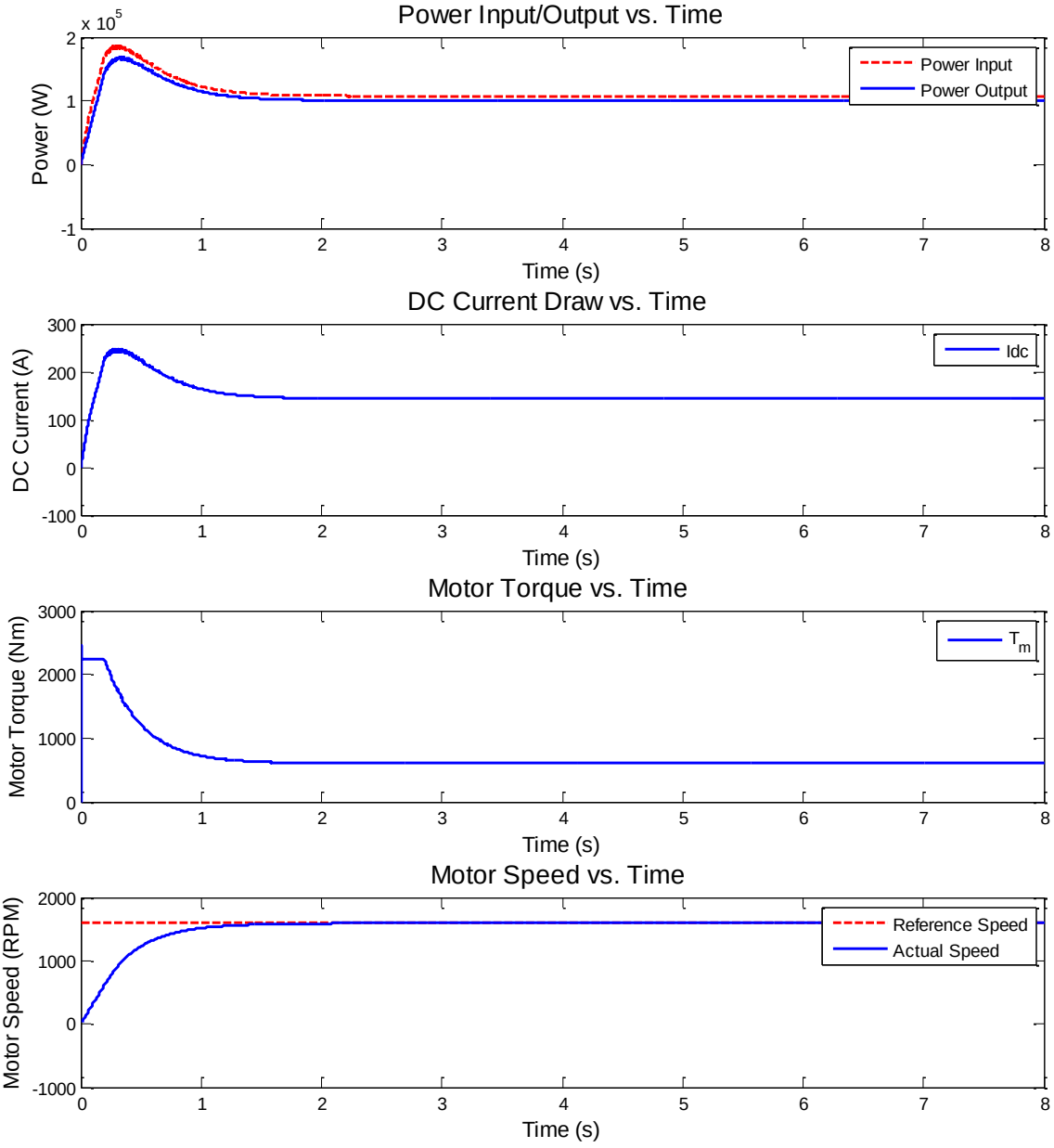

Figure 80: Step Response of Electric Drive System with Speed Control

5.2.3.3 Model Implementation and Loss Model Validation

Though a significant amount of information was acquired from the manufacturer to construct the electric drive system from first principles, the model still carries some underlying assumptions that likely differ from the real drive system. The steady state efficiency map provides a good means of comparison for the analytically derived dynamic loss model, which is computed by summing all the losses,

$$\dot{E}_{loss} = \dot{E}_{Mtr,copper} + \dot{E}_{Mtr,iron} + \dot{E}_{Mtr,stored} + \dot{E}_{Inv,loss} \quad \textbf{(5-19)}$$

An electronic image file of the efficiency contour map was the primary source of efficiency data. In order to make use of this information, the contours were digitally traced to construct an interpolating surface for use as a lookup table in Simulink. The resulting 3D surface of the efficiency map is shown in Figure 81. The digitization of data will have introduced some error into the solution, especially where the efficiency gradient is high; however, this error can be conservatively be bounded at 2% simply based on the process used.

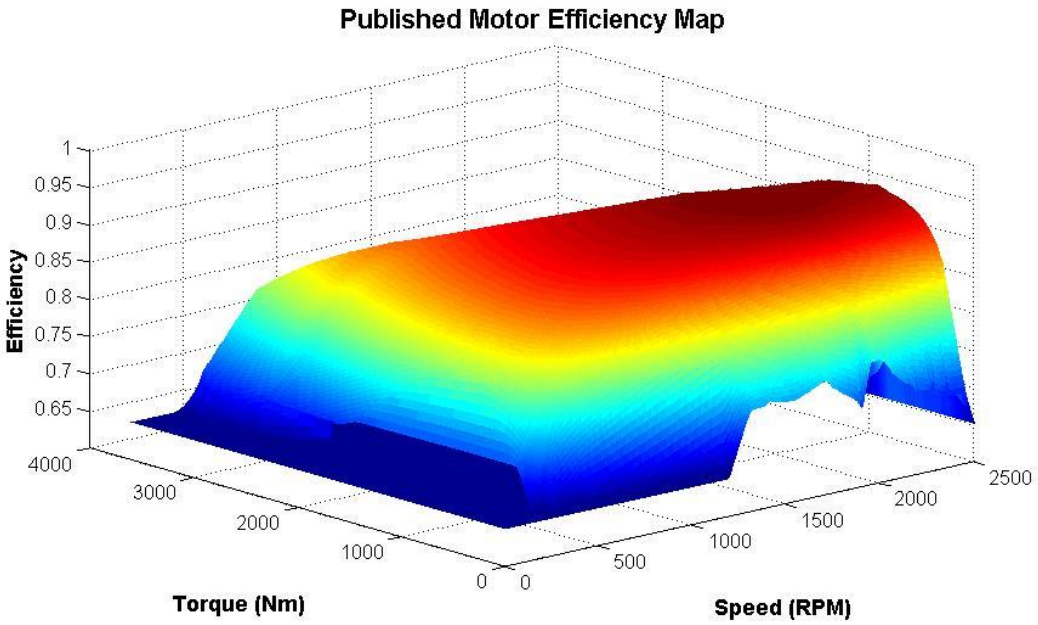

Figure 81: Published Motor Efficiency Map

The electric drive system model including the MTPA-based speed controller was implemented in Simulink such that simulations could be executed programmatically with an automated test script. The total energy loss is computed using Equation (5-19).

A steady state comparison between the published drive efficiency and the analytical loss model is presented in Figure 82. This plot recreates the efficiency contour map, and overlays the results from each test point denoted with an asterix. The different colours represent varying degrees of accuracy as described by the legend. Even with the large number assumptions, it can be seen that the loss model based on first principles provides reasonable results for high level studies if detailed information is not available. Some significant discrepancies do occur, primarily in areas exhibiting a high gradient. The model is also observed to be quite accurate in the high efficiency range of the motor.

The main motivation for implementing a dynamic loss model was to capture the aggregate transient losses that may not be well represented by a steady state loss model. Though the first principles model will likely provide a better estimate for transient losses, it will be seen in Chapter 6 that the load cycles have long stretches during transit where the operating point is quasi-static. Therefore, the published efficiency data is probably more suitable for assessing overall energy consumption. As such, the implementation of the electric drive model allows for two model options, one using steady state data, and the other with the analytical loss model based on first principles.

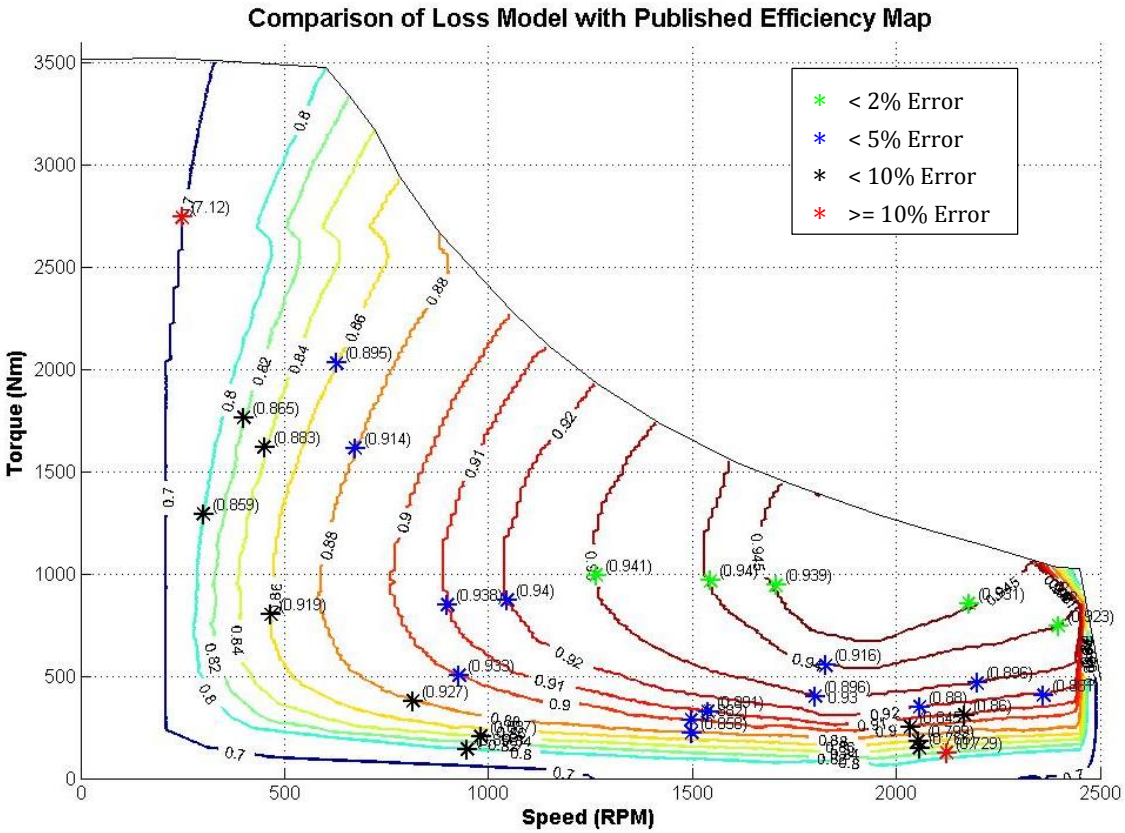

Figure 82: Comparison of First Principles Loss Model with Published Data

The AVM Simulink model for the electric drive system is implemented using the *d-q* referenced equations. The implementation was completed using fundamental Simulink library blocks. The top level of the model of the electric drive model is provided below in Figure 83. The model requires a speed reference signal and mechanical rotational speed feedback signal. Note that the DC voltage is actually a constant and is not a dynamic input.

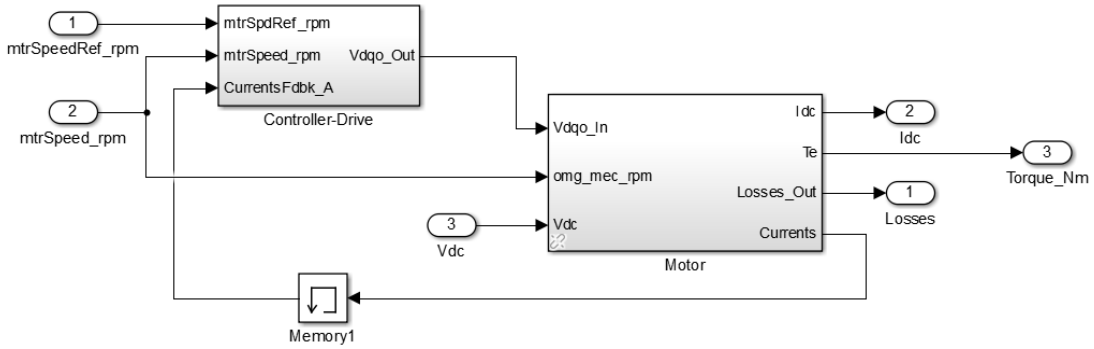

Figure 83: Top-Level Electric Drive System AVM Model Implementation in Simulink

The top-level motor model implementation is shown in Figure 84. Note that the motor sub-system includes the entire dynamic loss model, including the semiconductor losses for convenience. The motor's rotational velocity is fed into the stator voltage equation for computation of the back EMF induced by the rotor's magnets. This signal is also used to compute conversion efficiency from the contour map. Finally, the outputs of the model are the DC current requested from the electrical distribution network, as well as the instantaneous power loss for aggregating the load cycle efficiency.

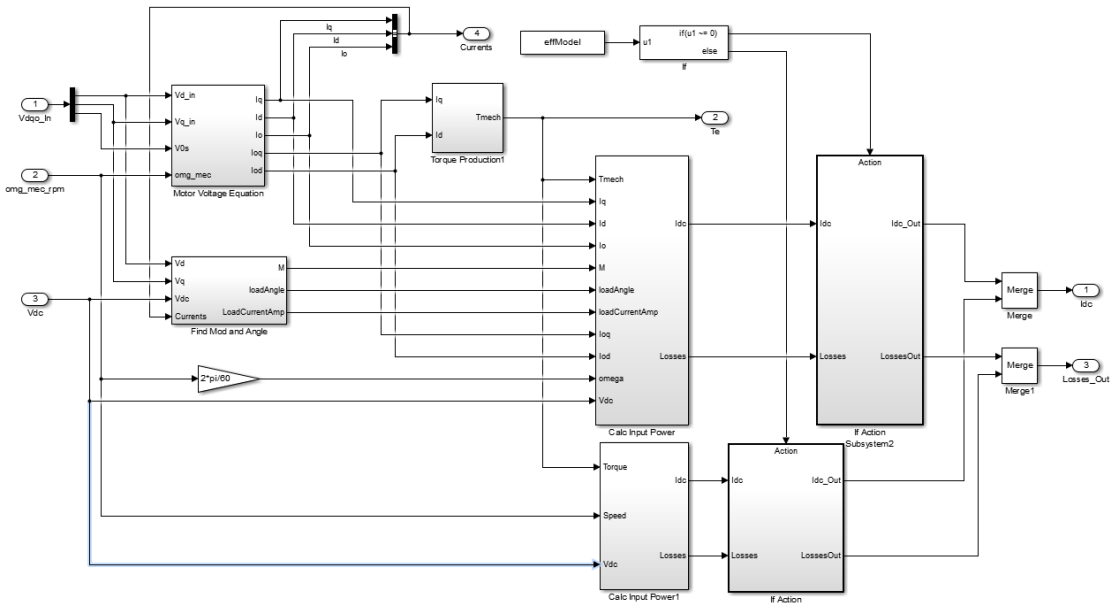

Figure 84: Top-Level Simulation Model for Motor Model

5.2.3.4 Comparison of AVM to Detailed Simulation Model

In order to validate the AVM developed, a detailed simulation model was also created in SimPowerSystems to resolve the switching behaviour of the inverter/motor system. The SVPWM block was used to generate the gate timing signals, while the drive was assembled using IGBT blocks configured into three separate bridge circuits to represent the 9-phase output of the electric drive system. The PMSM Simscape motor block only allows for a three-phase input; therefore, three motor blocks were used to represent the torque production from all nine phases, and the rotationally conserving ports were connected together such that the net torque output was summed from each motor block.

The controller developed for the AVM was used directly in the detailed model for validation; however, the PID controllers were transformed into discrete time. The AVM and detailed model were then co-simulated with the same step inputs for direct comparison. Starting from rest initially, Figure 85 shows a comparison between both models when a step input of 1000rpm is commanded.

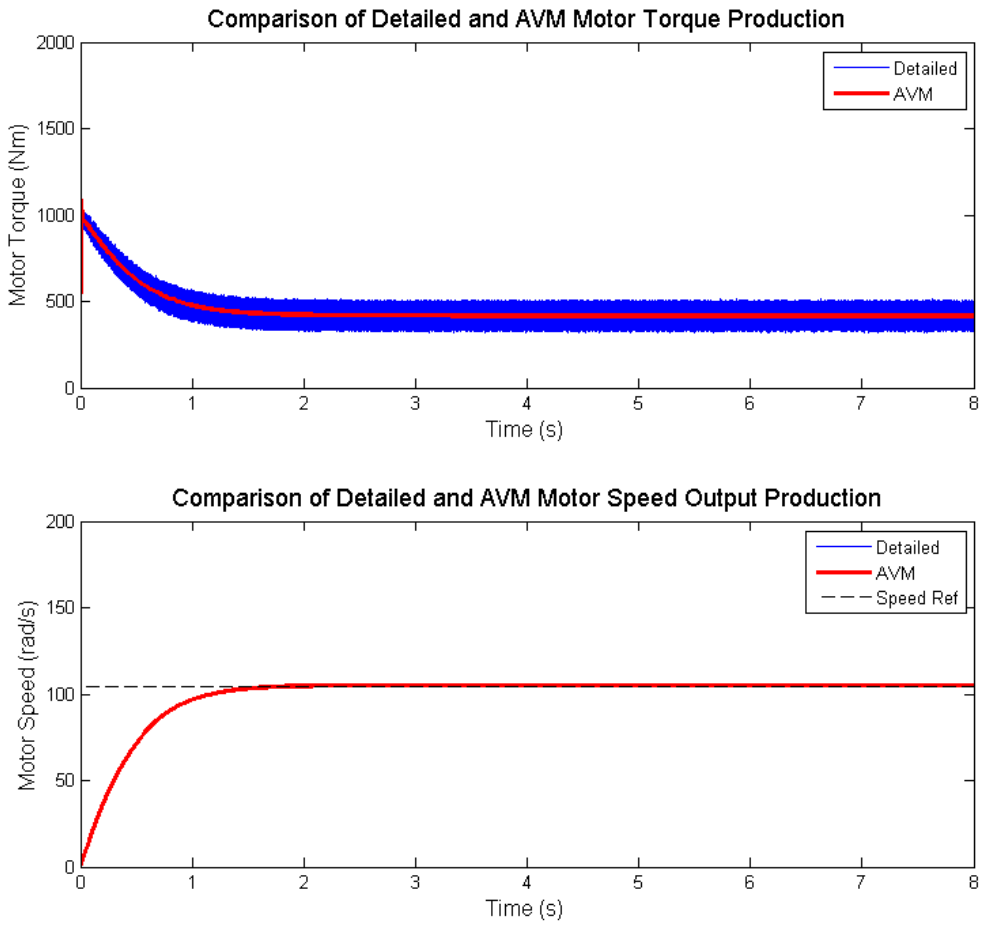

Figure 85: Response Comparison of PMSM/Drive AVM versus Detailed Simulation Model

Here it is observed that the AVM follows the mean value of detailed model which has significant ripple as a results of the inverter switching. The velocity response of both models coincide very well, as illustrated in the lower plot. Similarly, the *d*-*q* axis currents can be investigated to observe the MTPA lookup algorithm in action. Again, it can be seen that the mean of the high frequency signal produced by the detailed model is averaged appropriately by the AVM simulation model for both *d*, and *q* current components.

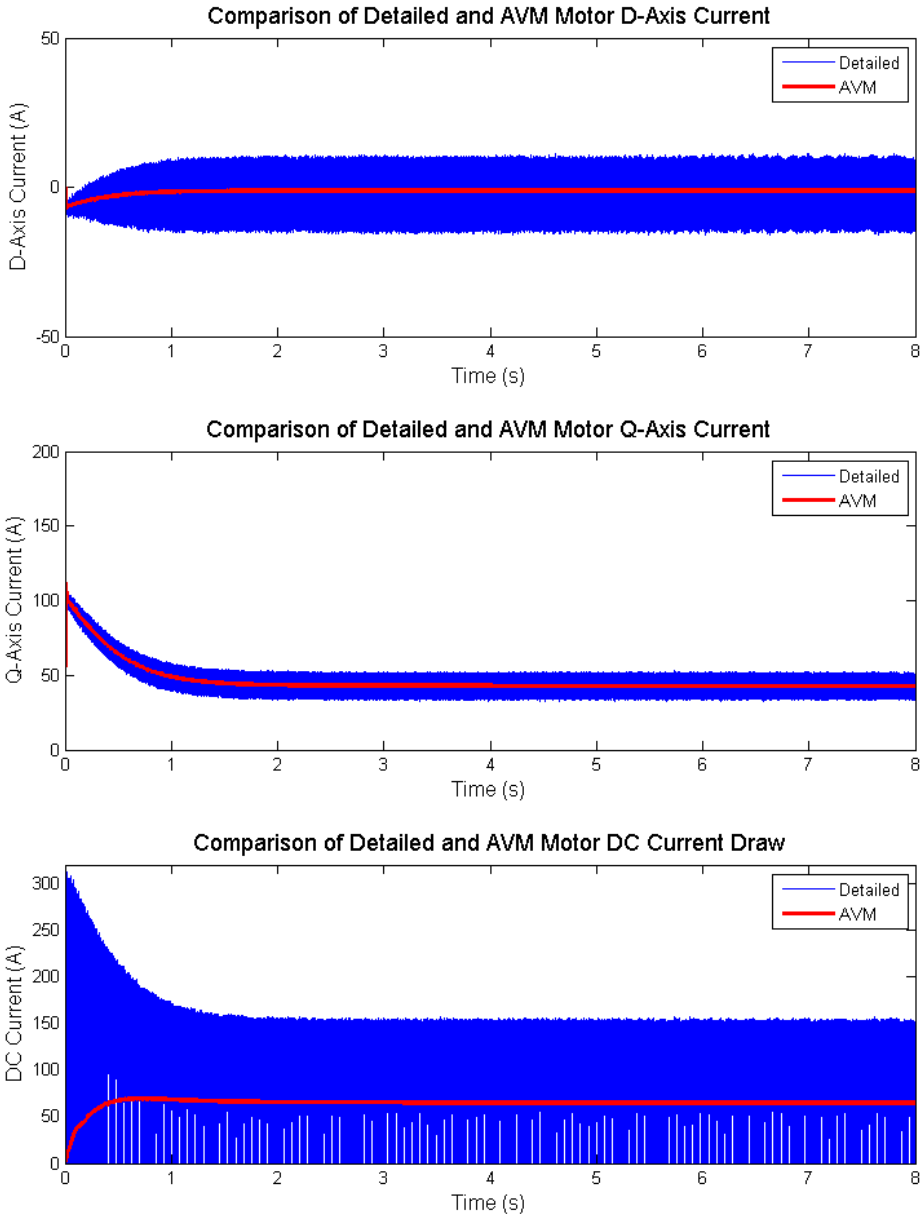

Figure 86: Comparison of D-Q, DC Currents for PMSM/Drive AVM versus Detailed Model

The lower plot in the figure shows a comparison of the DC input current draw. At time zero, there is a clear discrepancy between the AVM and the detailed model. Initially, there will be a large DC current to build the torque required to accelerate the system; however, the initial AVM shows zero input current then builds to the correct averaged value. This comes as a consequence of the quasi power loss-based implementation of the DC current model. As result, a small error in DC current draw will occur around zero

speed for the electric machines; however, this can be considered insignificant for the present study where the machine will not drop below 600rpm. When we zoom into the lower plot at steady state output in Figure 87, it can be seen that the AVM produces the mean value of the DC input current.

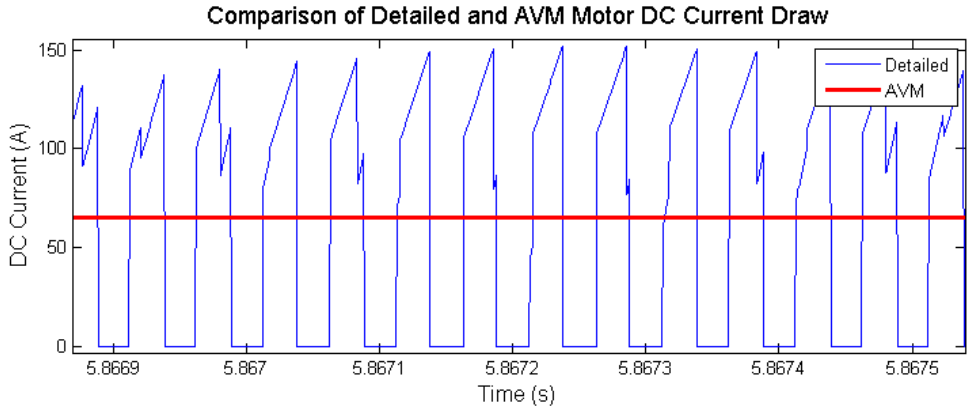

Figure 87: Comparison of DC Current for PMSM/Drive AVM and Detailed Model

5.2.4 Rapid-Charge Infrastructure

The energy storage system has been designed with sufficient capacity to complete a return trip under worst case loading conditions. This case study sought to investigate the use of rapid-charge infrastructure onshore that delivers DC current to charge the battery during loading/unloading cycles at either terminal. The schedule allows for approximately 10 minutes of charging between sailings, though often times the operational data showed that this charge availability was even less. The LTO chemistry was selected because of its fast charging characteristics and high cycle life. With sufficient cooling, LTO cells can achieve charge rates up to 7C. This type of rapid charge infrastructure has already been deployed successfully in a commercial transit application with Proterra's 450kW charger system for their EV bus.

Lithium batteries are charged using a constant current – constant voltage (CC-CV) charge profile. The battery management system, vehicle supervisor controller, and charge controller communicate using standard protocols to regulate the charge process to ensure that the maximum voltage and current ratings of the battery are not exceeded. If we recall from Chapter 2, charging begins at a constant current and the cell voltage gradually climbs until the maximum allowable voltage is achieved. The charger then switches to maintain constant voltage, then the amount of current drawn by the battery reduces exponentially until the system is fully charged. Rapid-charge systems are often designed to execute the CC portion of the charge then disconnect when the maximum voltage is achieved.

The model must provide the functionality for both CC and CV operation. The capacity requirements for the onshore charging system for single-ended charging is given below in Table 29.

Table 29: Charging System Capacity Sizing

Charging System Capacity		
Available Charge Time	0.17	h
Desired Charge Rate	5.00	C
Desired Charge Rate (A)	5000.00	A_{DC}
Voltage @ Cutoff	630.00	VDC
Energy Delivered	833.33	Ah
Energy Delivered (kWh)	460.00	kWh
Capacity Percentage	83.3%	%
DC Charger Power Output	2.76	MW

While the charging system is connected to the ship, the shore power provides both the constant battery charge current in addition to the hotel and propulsion demand; therefore, two PI controllers are required to maintain the CC-CV charge processes. The charger system implementation is illustrated in Figure 88. The charge logic is governed using a

state machine which uses the battery voltage as the feedback variable to select between CC and CV modes. A set of output switches are manipulated by the state machine to simulate opening/closing of contactors in a real system. An external PI reset logic system was also configured to eliminate integrator wind-up when switching between modes. The state machine logic is shown in Figure 89.

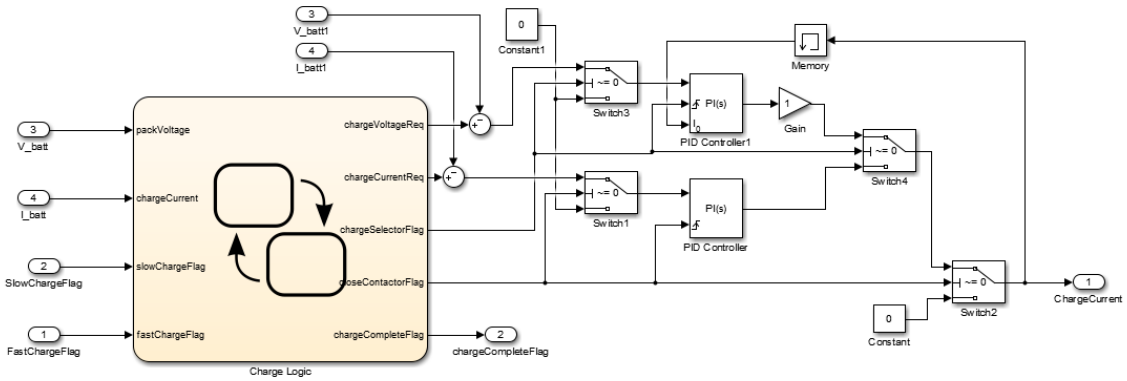

Figure 88: Charger Model Implementation in Simulink

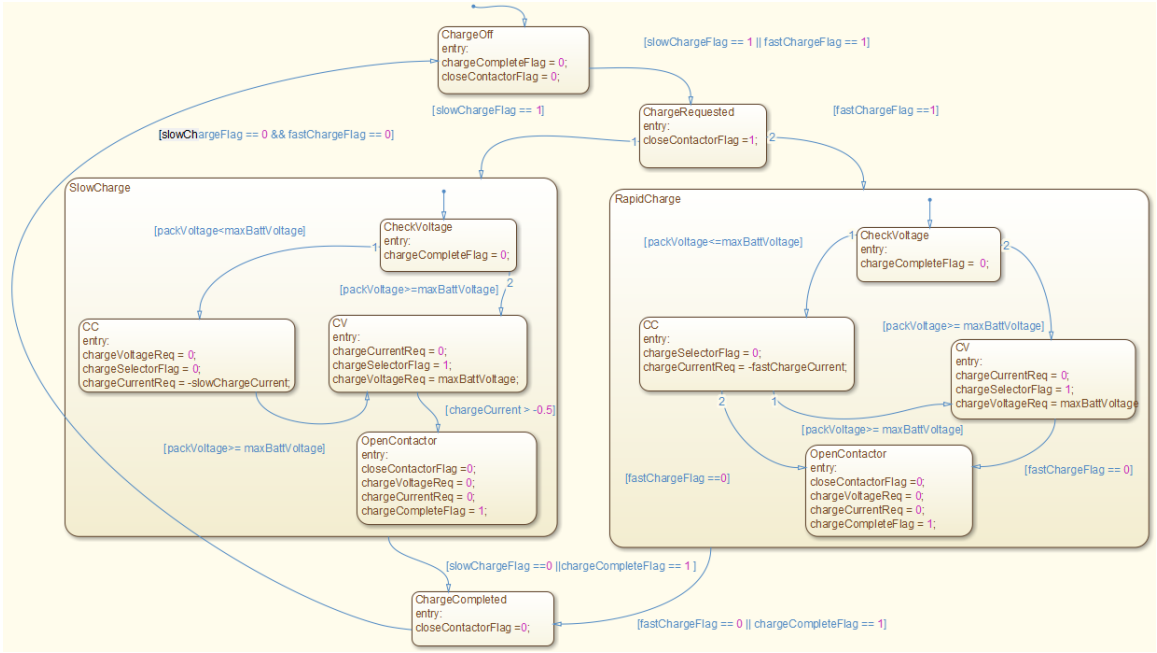

Figure 89: Rapid Charger State Machine Logic

The system is configured to deliver 5C charge during rapid charging with a cut-out voltage of 630VDC. The charging system then disconnects by opening the main contactors. A complete 1C-discharge/5C-charge cycle simulation of the energy storage system is illustrated below in Figure 90. This battery begins at 100% SOC, then is discharged at 1C for 3000s after which it sits at 17% SOC. The charger is then engaged at time 3200 seconds and delivers the 5C charge. The pack voltage climbs quickly until it achieves the maximum rating, at which point the charging is cut-off and the main contactors are opened. For a 5C charge rate, the battery reached 92% SOC and is ready for another crossing. With this simulation, 75% of the pack's energy has been restored over the course of approximately 8 minutes.

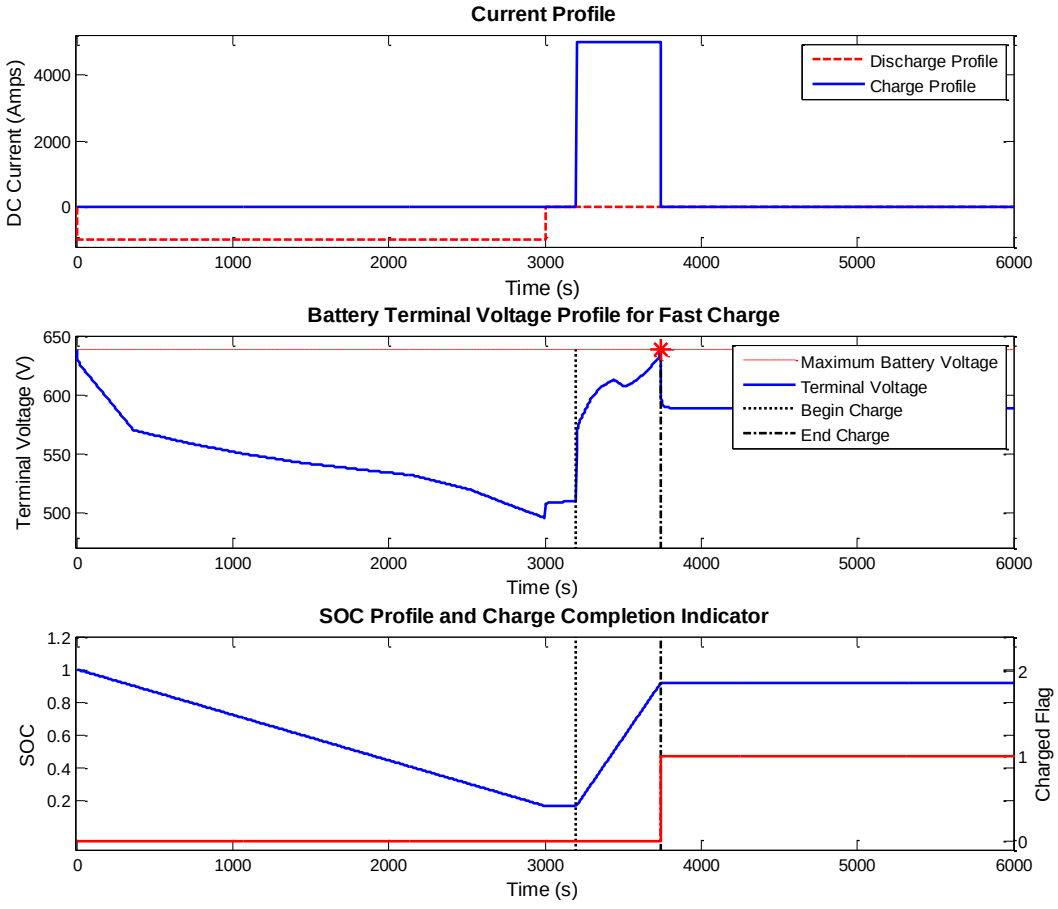

Figure 90: Fast Charging Performance of the Battery and Charger at 5C

Similarly, the full charge algorithm with CC-CV operation can be simulated. For practical reasons, the CV cut-off current has been set to 0.5A to avoid the lengthy exponential decay of the charge current as the SOC approaches 100%. The battery is discharged from 100% at 1C for 3000 seconds. The charger is engaged at 3200 seconds with a 1C constant current charge rate. This charge rate continues until the maximum battery voltage is reached, at which point the charging system applies a constant voltage. As expected, current then decays to approximately zero and the charge complete flag is issued as shown in Figure 91.

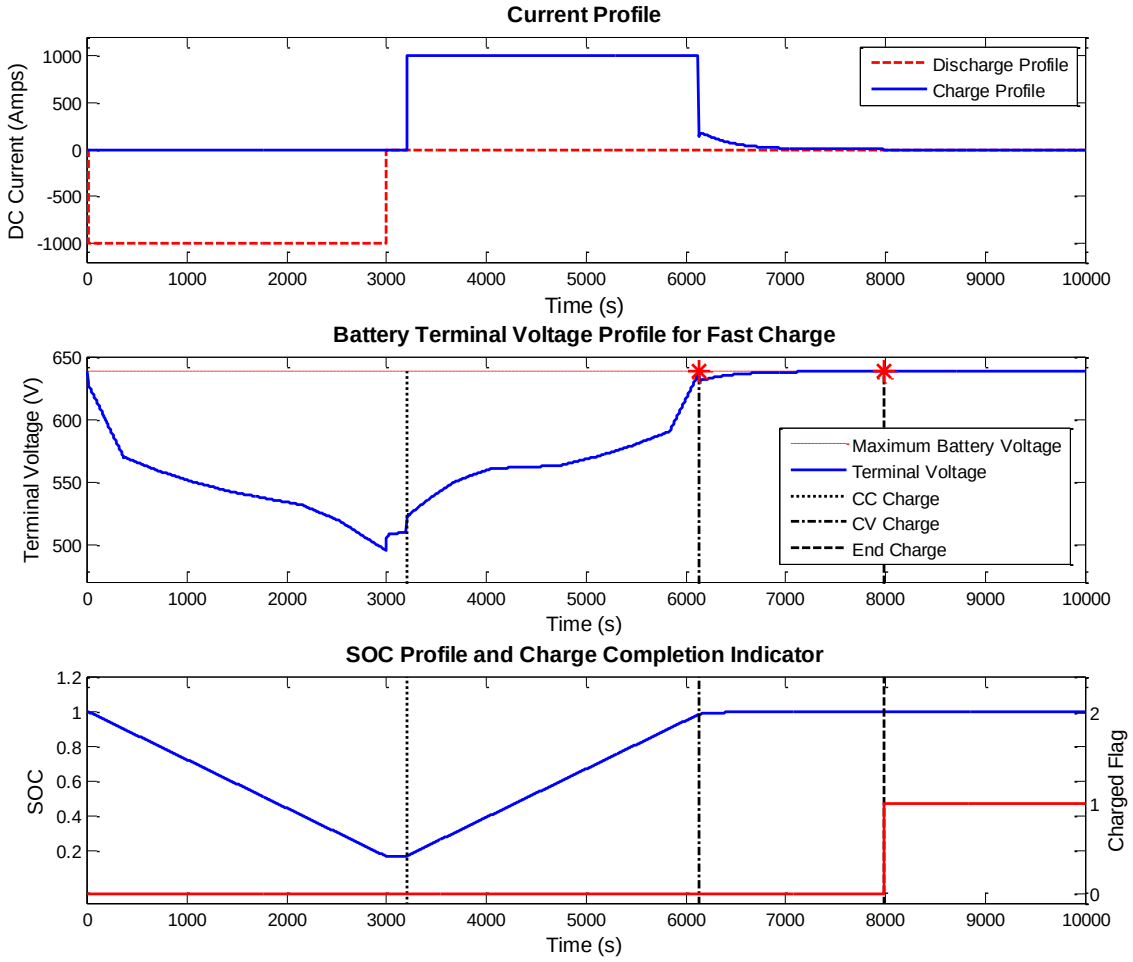

Figure 91: Regular Charging Performance of the Battery and Charger at 1C

5.2.5 Islanding Converter for Hotel Loads

In the modern DC grid shipboard integrated power system, islanding converters are often used to service the AC hotel loads of the ship. One of the major benefits of the DC grid is its enabling of variable-speed generation for increased conversion efficiency from the fuel source to electrical energy. The wild AC output of the machine cannot be used directly for servicing hotel loads because the frequency is unregulated. Hotel loads require a fixed 50/60Hz signal; consequently, DC/AC islanding converters coupled with heavy sine filters were designed to provide the sinusoidal AC voltage source for servicing hotel loads in AES ships equipped with a DC grid. They are referred to as islanding converters because they are capable of driving the AC grid system without the need to synchronize to a voltage waveform.

The detailed topology, analysis, and control of this type of converter is well beyond the scope of this document; however, a model is required to account for electrical load demand on the M.V. Klitsa. The hotel loads for this ship are an order of magnitude less than the propulsive loads, and won't be dominant. As a first approximation, the converter will be assumed to have a constant conversion efficiency of 93% as is typical in converters in the 50kW range. This power loss model will compute the distribution side DC current demand using the hotel load profile collected in the data acquisition study. The model of the converter approximation is shown below in Figure 92.

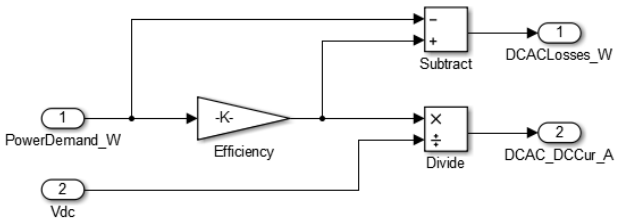

Figure 92: DC/AC Converter Approximation Model Implementation

Chapter 6 Summary of M.V. Klitsa Data Acquisition Experiment and Load Profile Generation

6.1 Introduction to Data Acquisition Experiment

One of the key factors to designing an effective hybrid propulsion systems lies in having *a priori* knowledge of the ship's expected operational profiles. With advanced knowledge of the mission cycles and their statistical distribution, the system can be optimized to deliver the best possible performance while minimizing energy consumption. The MIL platform under development seeks to provide a predictive tool for extracting the load profile based on defined mission cycles. When real operational data is available, it can also facilitate with more detailed design, validation analysis, and control system development.

The short-cross ferry application was selected as the case study partially because of its consistent, and well-defined operating profile. In order to validate the integrated time-domain modeling framework, it was imperative to obtain operational data for the Klitsa as a means of direct comparison. The data acquisition study provided insight into the expected propulsive and hotel load variation, and, as will be seen in this chapter, has also enabled the creation of standardized load cases the can be used as metrics for evaluating different architectures.

Though the ship has been upgraded to include a monitoring and control system, the individual signals to be acquired were not conveniently accessed on a single communication bus; consequently, an independent CAN communication network was installed onboard the ship to enable a single collection point for all signals with time-synchronization. Separate sensors and instrumentation were installed for systems that did not offer a convenient signal source. The full design of the experiment and installation

details are provided in Appendix A. In this chapter, we will limit the discussion to the key features of, and results produced by, the data acquisition study. The master signal list, along with the signal source is summarized in Table 30.

Table 30: Summary of Acquired Parameters in Data Acquisition Study

Description	Physical Parameter	Transducer Signal Source
GPS Data	Position (NED)	Cross Chasm GPS Logger
	Vessel Speed	Cross Chasm GPS Logger
Engine 1 Data	Engine Load	J1587/J1708 Serial Bus
	Engine Speed	J1587/J1708 Serial Bus
	Engine Torque	J1587/J1708 Serial Bus
	Throttle Demand	J1587/J1708 Serial Bus
Engine 2 Data	Engine Load	J1587/J1708 Serial Bus
	Engine Speed	J1587/J1708 Serial Bus
	Engine Torque	J1587/J1708 Serial Bus
	Throttle Demand	J1587/J1708 Serial Bus
Azimuth Propeller 1	Azimuth Angle Position	HRP NMEA0183 Serial Bus
	Thruster Position Reference	HRP NMEA0183 Serial Bus
Azimuth Propeller 2	Azimuth Angle Position	HRP NMEA0183 Serial Bus
	Thruster Position Reference	HRP NMEA0183 Serial Bus
Generator Output	3-Phase Power	Veris H8043-0300-2 Power Sensor
Wind Data	Wind Speed	Campbell Scientific 05103LK Wind Monitor
	Direction	Campbell Scientific 05103LK Wind Monitor
Heading/Attitude	Heading Direction	Maretron SSC200 Fluxgate Gyrocompass
	Pitch Angle	Maretron SSC200 Fluxgate Gyrocompass
	Roll Angle	Maretron SSC200 Fluxgate Gyrocompass
	Turn Rate	Maretron SSC200 Fluxgate Gyrocompass

The data acquisition system made use of the onboard J1587/J1708 serial communication bus for the engines, and the NMEA183 serial bus from the azimuth angle thruster systems. Custom serial converters were developed to read from the onboard serial buses to broadcast the data over the CAN network. CAN traffic was logged using the Cross-Chasm data logger, which also contains an integrated GPS system that was used for tracking vessel position and speed. The system was designed to operate autonomously using an enable message to trigger all nodes to begin broadcasting. The enable was trigger by sensing Engine 1's serial communication bus activity. A schematic of the instrumentation and communication network layout is provided in Figure 93.

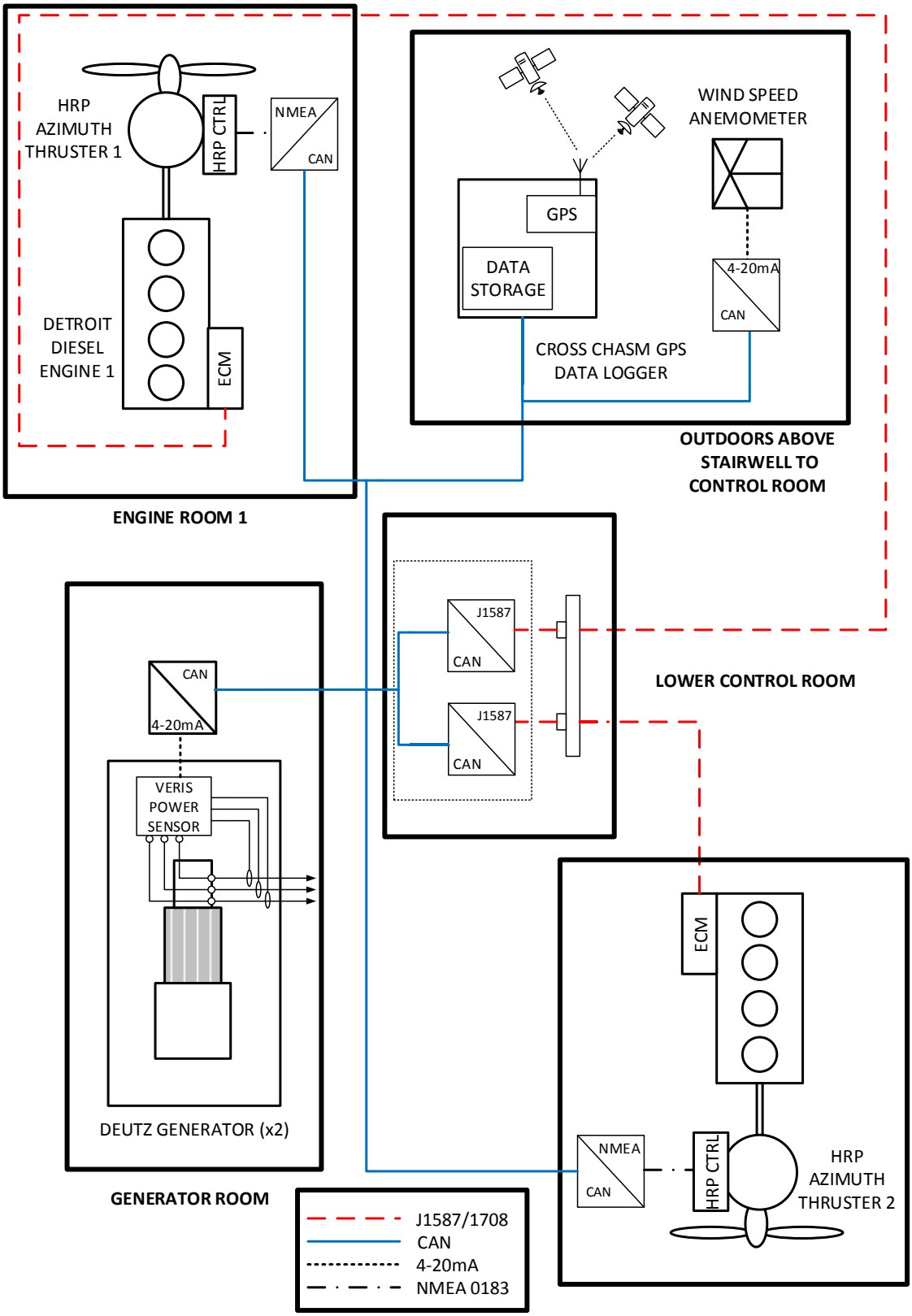

Figure 93: CAN Network Schematic and General Arrangement for DAQ Study

6.2 Development of Load Profiles from Operational Data

Approximately two months' worth of data was collected onboard the ship; however, many technical issues arose with various components which often led to incomplete data. The engine signals were consistently noisy and the system was pulled offline several times in attempt to resolve the issue. The original installation seemed to provide the cleanest signals, and were therefore used in the development of the standard load profiles. The Cross Chasm GPS logger was also found to have a manufacturers' defect in the firmware which would randomly scale the velocity of the ship to the point where the signal was no longer usable.

Despite these problems, several well-conditioned and complete datasets were extracted and developed into a set of representative load profiles of differing power outputs. The primary parameters required for validation of the model are as follows:

1. Propulsion System Load: Torque/Speed vs. Time
2. Hotel Loads: Electrical Power vs. Time
3. Propeller Position: Azimuth Angle vs. Time
4. Vessel Speed vs. Time

The two main diesel engines and the auxiliary generator supply all of the energy required for the ship, and are thus the most important for computing energy demands for the BEIPS. The load information from the engines was captured from the ECM units, which are not-known to have very high precision. The measured engine load can be compared against the published propeller data in the first quadrant as a sanity check. The

azimuth angle time series position data will serve as a model input to simulate the actions of the operator in the system-level simulation.

The present objective is to develop a set of standard drivecycles that represent the variability of the ship's operation described by low, medium, and high output conditions. The data was surveyed to assess the variability in the load profiles observed over the two months of data collected. A maximum operational speed of just over 9 knots was observed in some instances, but normal operating speed typically hovered around 7.5 knots when the ship was on-schedule. Based on these observations, three representative mission profiles were identified as being good representations for use as standardized cases. The time series data for the three velocity profiles are presented in Figure 94.

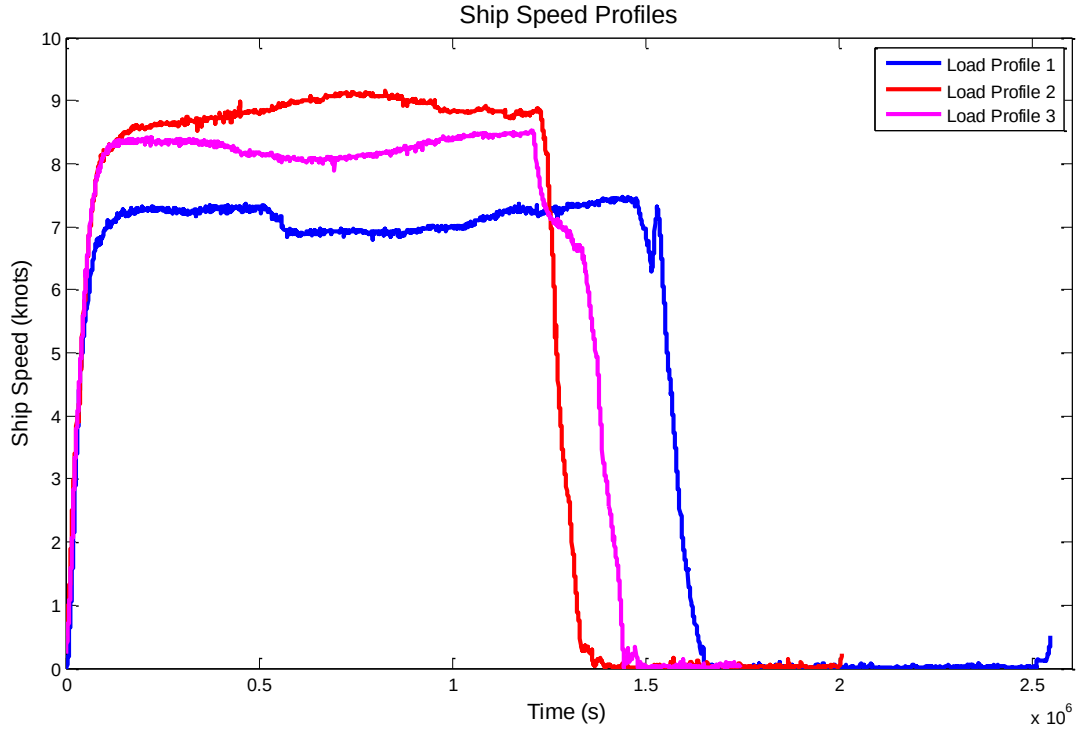

Figure 94: Plot of Ship Speed vs. Time for 3 Load Profiles

The crossing can be considered a fixed distance, though there will be minor variability depending on the course taken. As expected, the higher speed is shown to reduce travel

time; however, this comes at the expense of additional energy consumption when we recall that power output is approximately proportional to the velocity cubed.

The primary input to the MIL model will be the time series data collected for the engine speed profiles. The engine speed sensors offered the cleanest, most stable, and most accurate signals from the ECM. Speed profiles from the three datasets selected are shown in Figure 95.

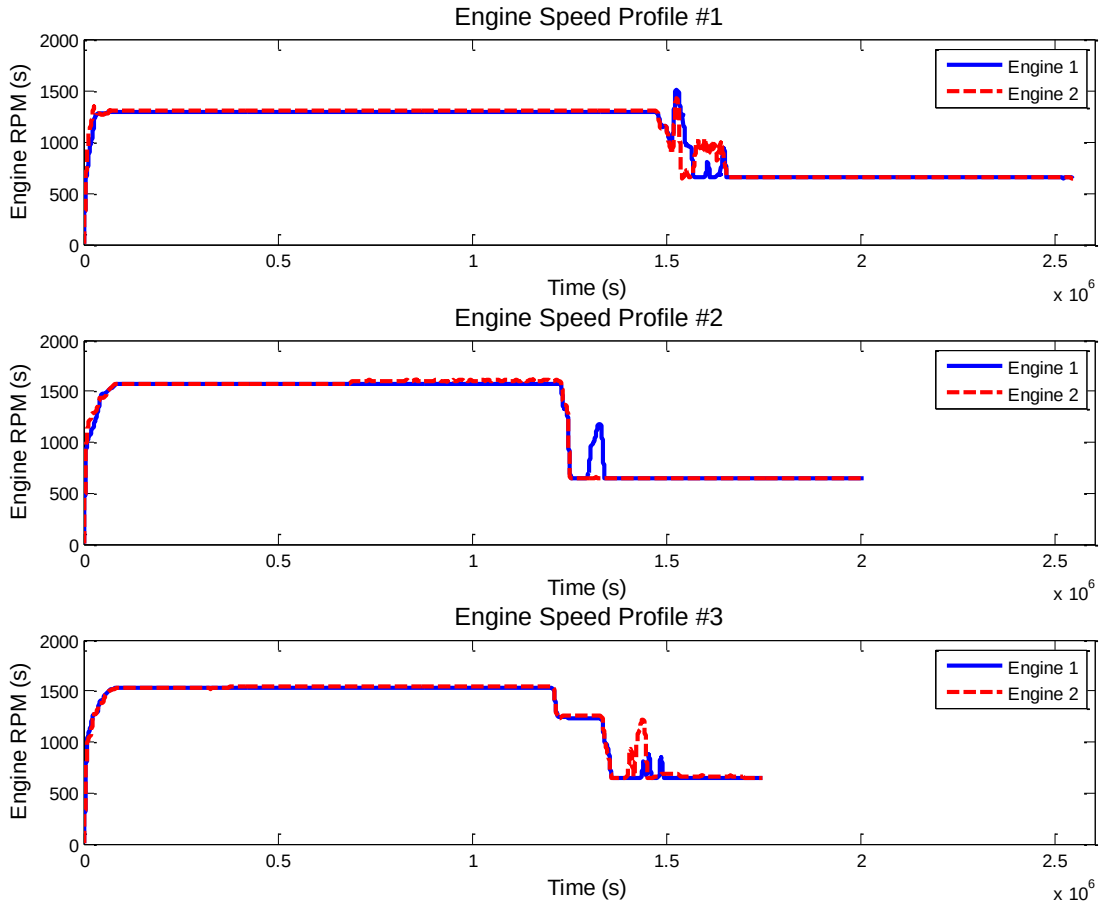

Figure 95: Engine Speed Profiles

Engine speed pulses are observed as the ship is nearing berth. These represent short bursts of thrust required to maneuver the ship into alignment with the berth and control the impact speed with the marine structures. Once the ship is safely resting on the marine

structures, the engines remain clutched-in, operating just above idle speed. The ship lightly powers into the dock for safety when loading and offloading; therefore, propulsive energy is still being expended in-berth. The engine power output profiles are shown in Figure 96.

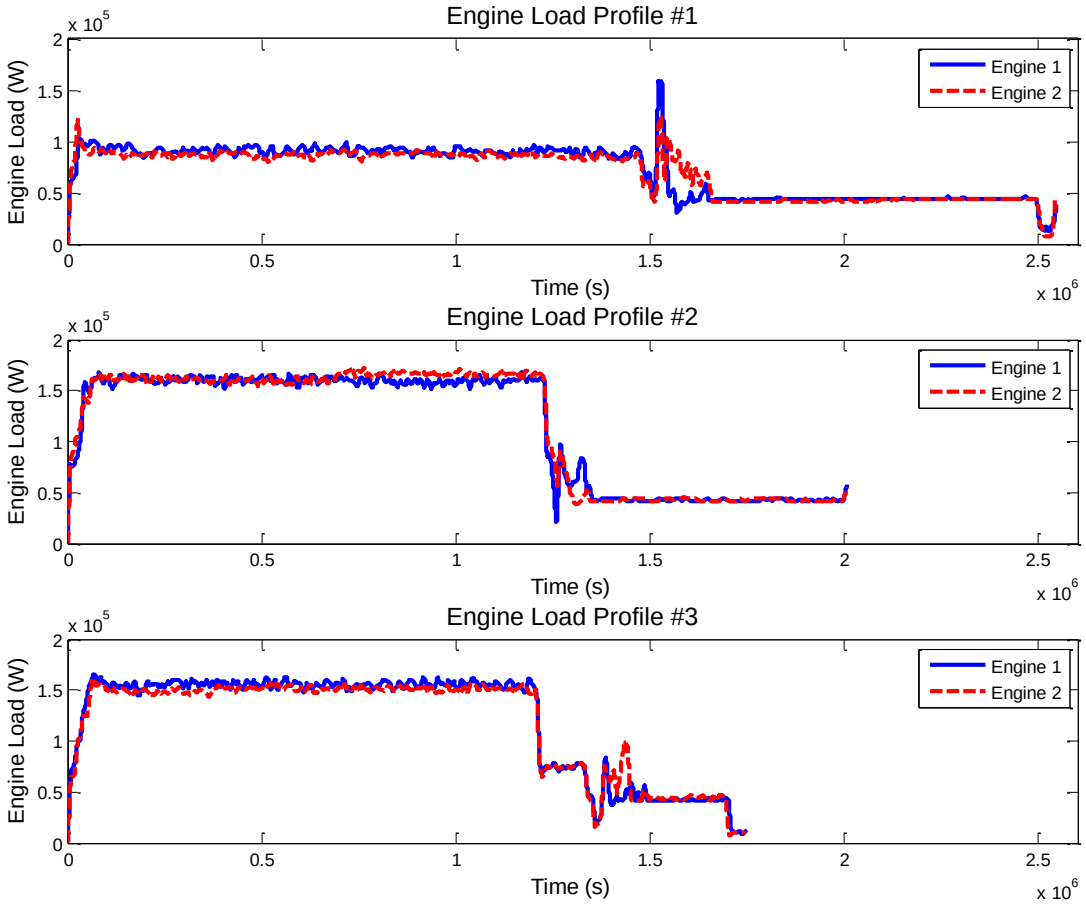

Figure 96: Engine Load Profiles

The power output for both engines is approximately balanced during transit; however, this trend diverges once the ship approaches berth and propellers are operated independently. It should be noted that a large torque transient develops on the input shaft when thrusters are rotated while the ship at forward speed. Interestingly, this event is of significance as it often requires oversizing of the engine to accommodate the transient torque peak at low engine speed. This is one major advantage of electric drive technology

where short-term overload conditions at high torque are permissible. This torque transient is observable in the data as shown in Figure 97.

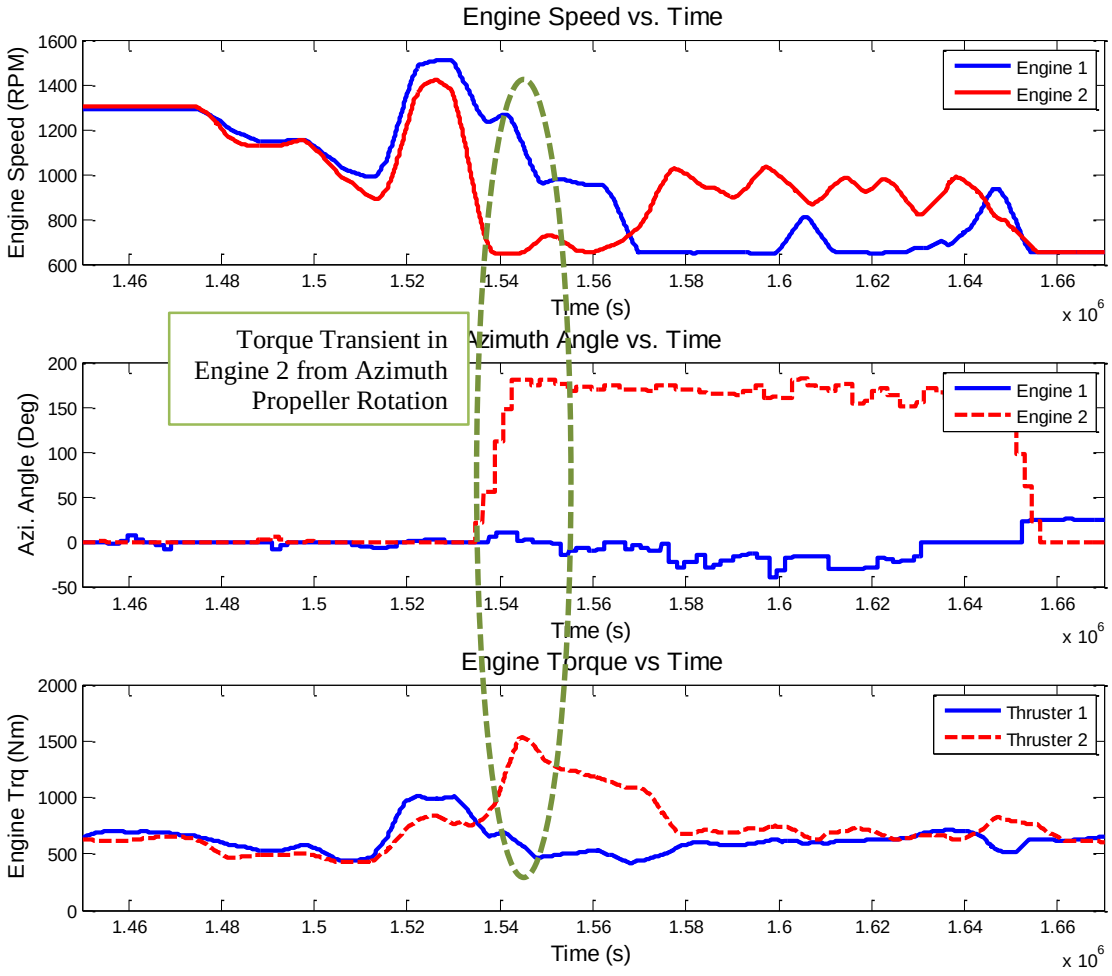

Figure 97: Example of Torque Transient during Azimuth Thruster Rotation

The azimuth angle profiles collected for the three load cycles are presented in Figure 98. When the ship is in transit, both thrusters are aligned. Note that the raw data has an angular definition that differs from the coordinate system used in this work. The axis will be reversed, and the datum rotated by 180° to correct for the system model. When the ship approaches the berth, the fore thruster is rotated to brake the ship and direct the bow as needed. While in berth, the aft thruster is rotated to provide a holding force against the marine structures, while the fore thruster powers into the dock.

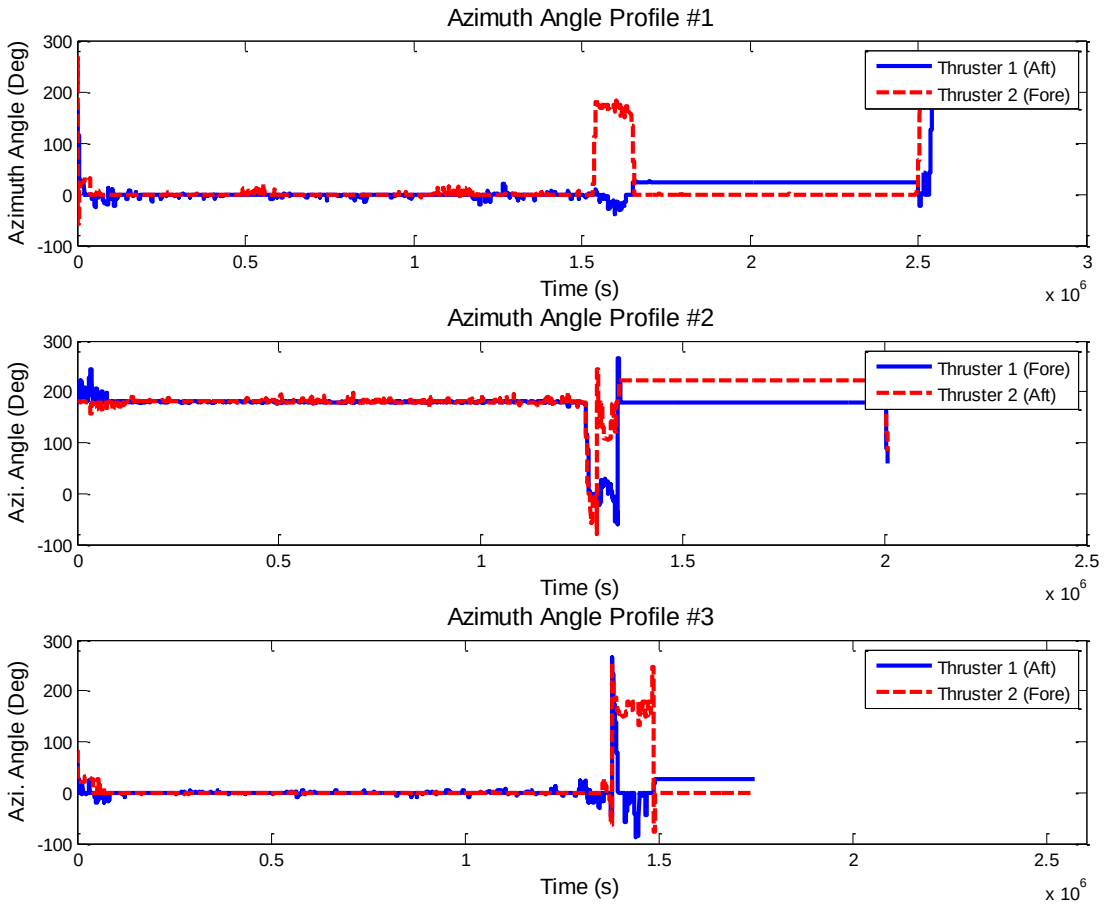

Figure 98: Azimuth Angle Profiles

The remaining component of the energy profile is the electrical generation, or hotel loads. The data acquisition study was conducted in the summer when the electrical loads are typically reduced. During the winter, electrical heaters for cabin spaces will increase the power demand. The electrical profile exhibits temporary peaks from shipboard industrial equipment being activated. In order to develop a representative range of load profiles, the entire set of data collected was overlaid onto a single plot and the mean value, shown in red, was computed to be approximately 11.6kW.

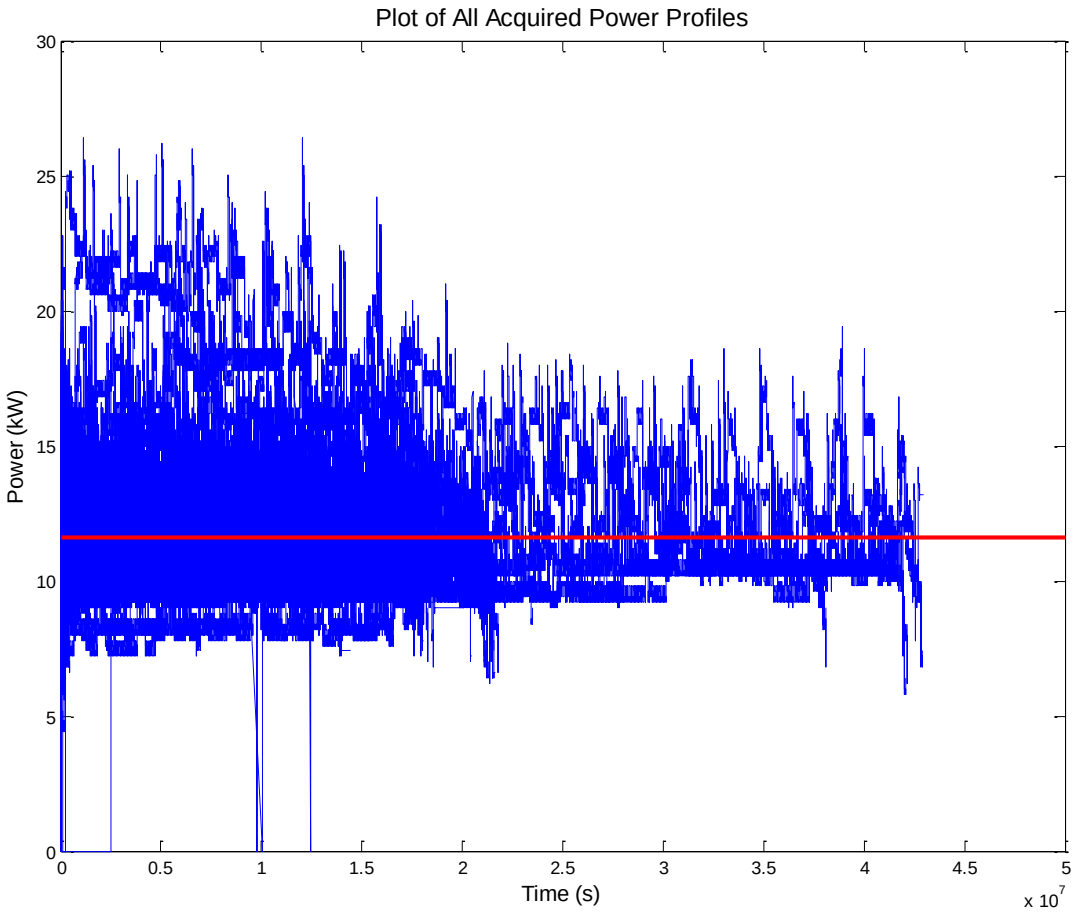

Figure 99: Plot of All Electrical Load Data Collected for Computation of the Mean

The electrical generation profile has been assumed to be independent of the main propulsive loads. It is quite feasible to encounter situations with high propulsive demand and high electrical load simultaneously. This needs to be accounted for appropriately in the battery system design. Based on observation of the data, three electrical load profiles representing high, medium, and low demands were extracted from various datasets. These are plotted in Figure 100. In all three profiles, the temporary peaks from electrically driven equipment are visible. Interestingly, the highest demand is still only approximately 50% of the rated generator load. This is a fairly low efficiency operating point for a typical marine genset.

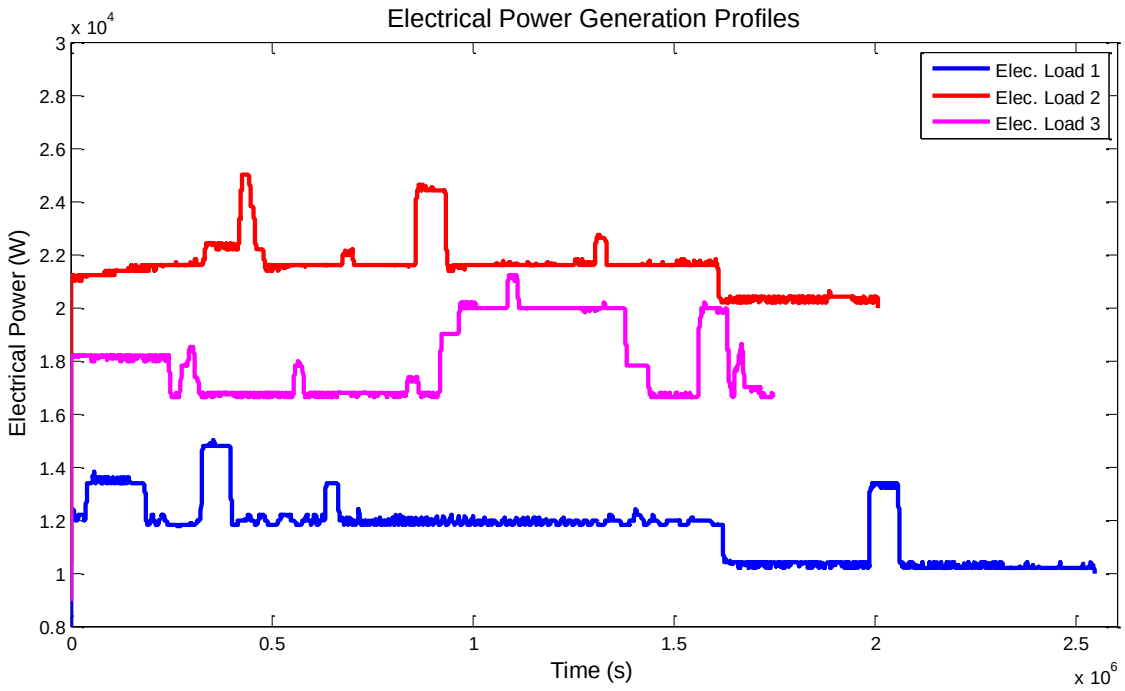

Figure 100: Plot of Representative Electrical Loads for High, Medium, and Low Conditions

6.3 Comparison of Vessel Course for Validation of Dynamics Model

The data acquisition study also included provisions for tracking the vessel's position, heading, and attitude. By collecting this information, an auto-pilot based driver model that employs course/waypoint tracking algorithms can be developed in future work. If the vessel's motion output follows a course that resembles that of the data, then the propulsive forces and maneuvering coefficients are well represented by the system-level model.

The three navigational trajectories taken by the ship for each respective load profile are shown in Figure 101. Two of the three load profiles run from Mill Bay to Brentwood Bay, illustrated with red and green arrows respectively. The third profile runs in the reverse direction with its course plotted with blue arrows. The direction of the arrows has been aligned with the heading data produced by the magnetic gyrocompass sensor.

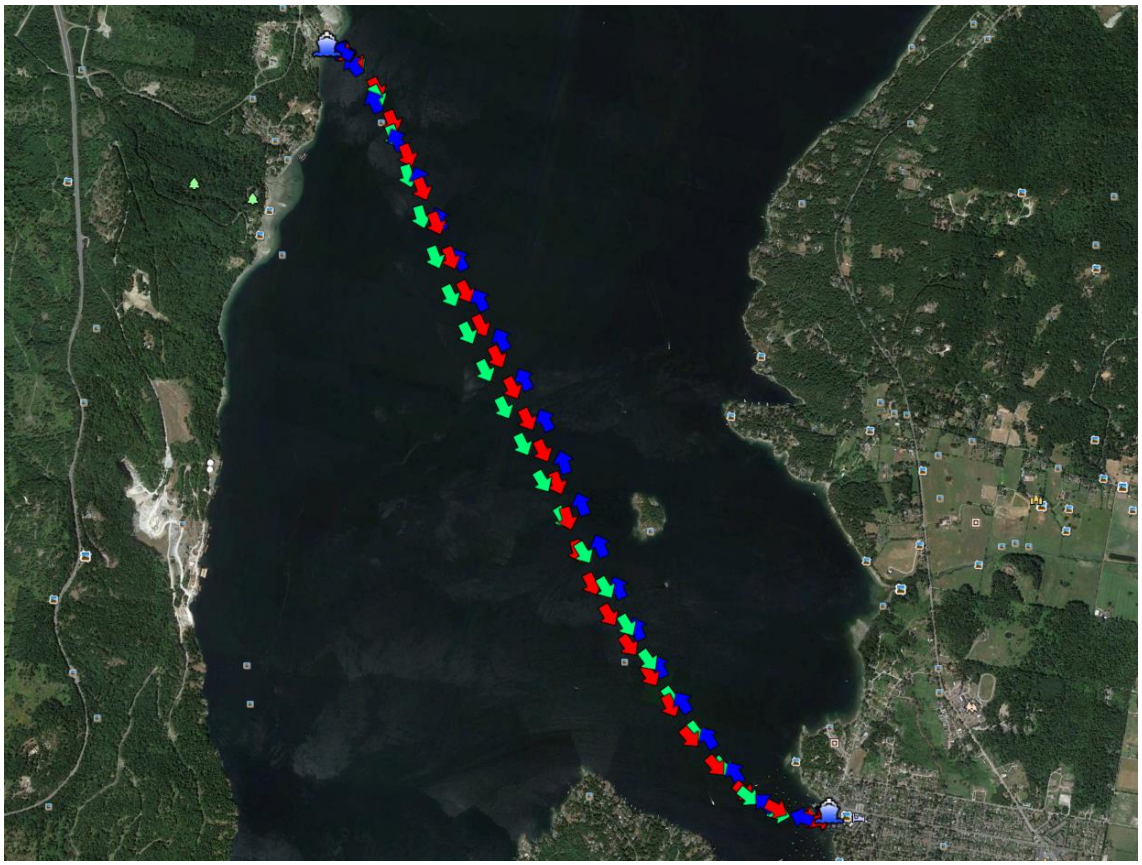

Figure 101: Plot of Course and Heading Data for the Three Load Profiles

It is important to pause here to discuss the coordinate systems used in the development of the ship model and their relation to these load profiles. Recall the ship coordinate definitions shown in Figure 34. When moored in Brentwood Bay, the $+x$ direction is shoreward and the ship is preparing for travel in the $-x$ direction on route to Mill Bay. During transit to Mill Bay, the thrusters are predominately positioned at 0° according to the coordinate system definitions.

Conversely, when the ship is moored at Mill Bay, the $-x$ direction is shoreward and the ship is preparing for travel in the $+x$ direction on route to Brentwood Bay. During transit to Brentwood Bay, the thrusters are predominately positioned at 180° according to the model's definition.

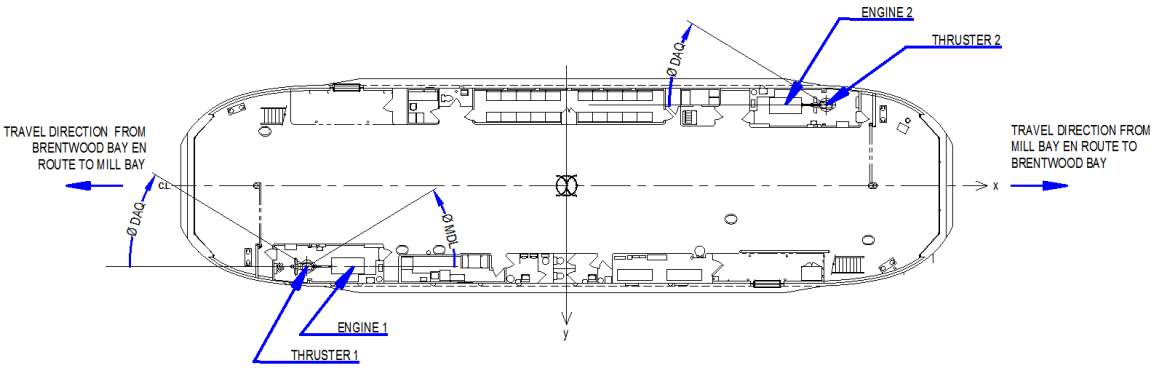

Figure 102: Travel Direction Definitions

6.4 Experimental Uncertainties

Before using the data collected as a validation tool for the system level simulation model, it is important to first comment on the sources of uncertainty in the data. Many of the items have already been identified in the preceding sections; however, it is imperative to elaborate on this topic to help account for any discrepancies between the model and the real ship. It is difficult to perform qualitative analysis on these uncertainties, primarily because of the numerous sources of potential error that arise from experimentation in an uncontrolled environment. The limited experimental freedom and restricted access to the vessel while in-service also rendered it difficult to pinpoint the dominant sources of error.

The data collection experiment began immediately after the ship returned to service following a major dry-dock and refit. The hull was thoroughly cleaned and repainted with a slippery coating to reduce resistance; therefore, the smooth wall condition assumed for the CFD analyses should be a valid assumption. Similarly the propellers were thoroughly overhauled, cleaned, and repainted. This implies that thrust/torque characteristics should be very similar to the original manufacturer data, and discrepancies that result from bio-fouling and natural degradation should be minimal. The engines were rebuilt and

dynamometer tested as part of the refit; therefore, the rated output and ECM calibrations would have been factory reset and verified with the test bench.

With this information, the major sources of experimental error that remain surround the following items:

1. Environmental conditions
2. ECM measurements and torque computation
3. Hydraulic PTO loading
4. Signal noise in engine data

6.4.1 Environmental Errors

There is clear evidence that environmental factors had some influence on the performance of the vessel. For example, the spread of the data points observed in section 4.1.5 in formulation of the thrust deduction factor highlights the discrepancies between similar operating points, mainly engine speed versus vessel speed. This naturally points to environmental factors which are concurrently influencing the loading of the ship. Based on the survey of historic wave data in the Saanich Inlet conducted in Chapter 4, and cross-referencing with the actual weather on the date of the data collected, it is highly unlikely that wave loading was a dominant factor. This leaves current and wind as the potential influencing factors.

An anemometer was configured as part of the data collection study. The anemometer was able to capture relative speed and heading of the wind with respect to the ship. Because the air resistance coefficient wasn't analyzed as part of this work, this forcing factor was not fully accounted for in the analysis. The method by which the load profiles in section 6.2 were selected was largely based on investigation of the wind profile.

Crossings where the ship was exposed to significant wind speeds were disregarded to support the assumption that wind forces were negligible. The load profiles established exhibited relatively low wind speeds, but the data suggests that this force was not negligible.

Ocean Network Canada has conducted an experimental study of tidal currents in the Saanich Inlet as shown in Figure 103. Data was not available for the exact time period when the study was conducted, but a plot of historic data between 2011-2013 is illustrated. Between late June and early September, the highest peak is found to be about 0.25m/s. Taking the nominal ship speed to be 7.5 knots (3.86m/s), this translates to approximately 6.5% of the ship velocity at worst case.

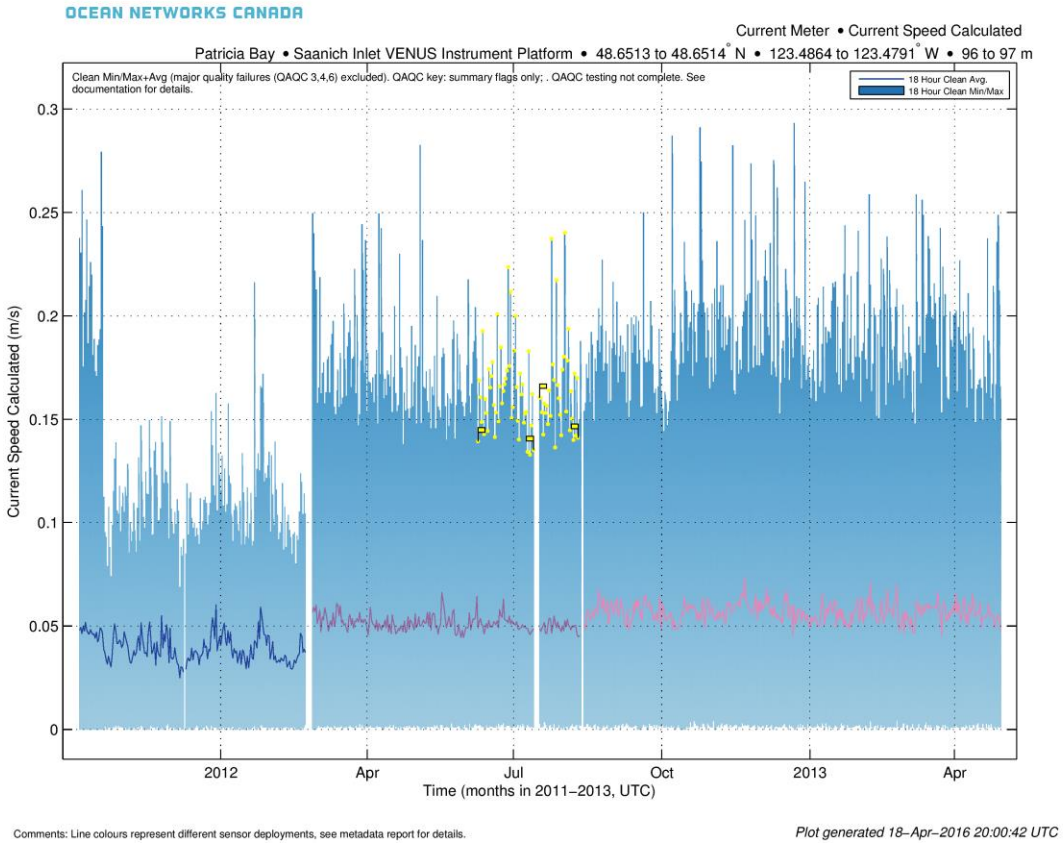

Figure 103: Historic Data for Computed Ocean Current Magnitude in Saanich Inlet [100]

The approximate heading for the measured current about 140° for the May – September time period. The direction is shown relative to the Brentwood Bay – Mill Bay crossing in Figure 104. It can be seen that the current direction could have potentially assisted with the ship in its travel from Mill Bay, and added additional resistance when traveling from Brentwood Bay.

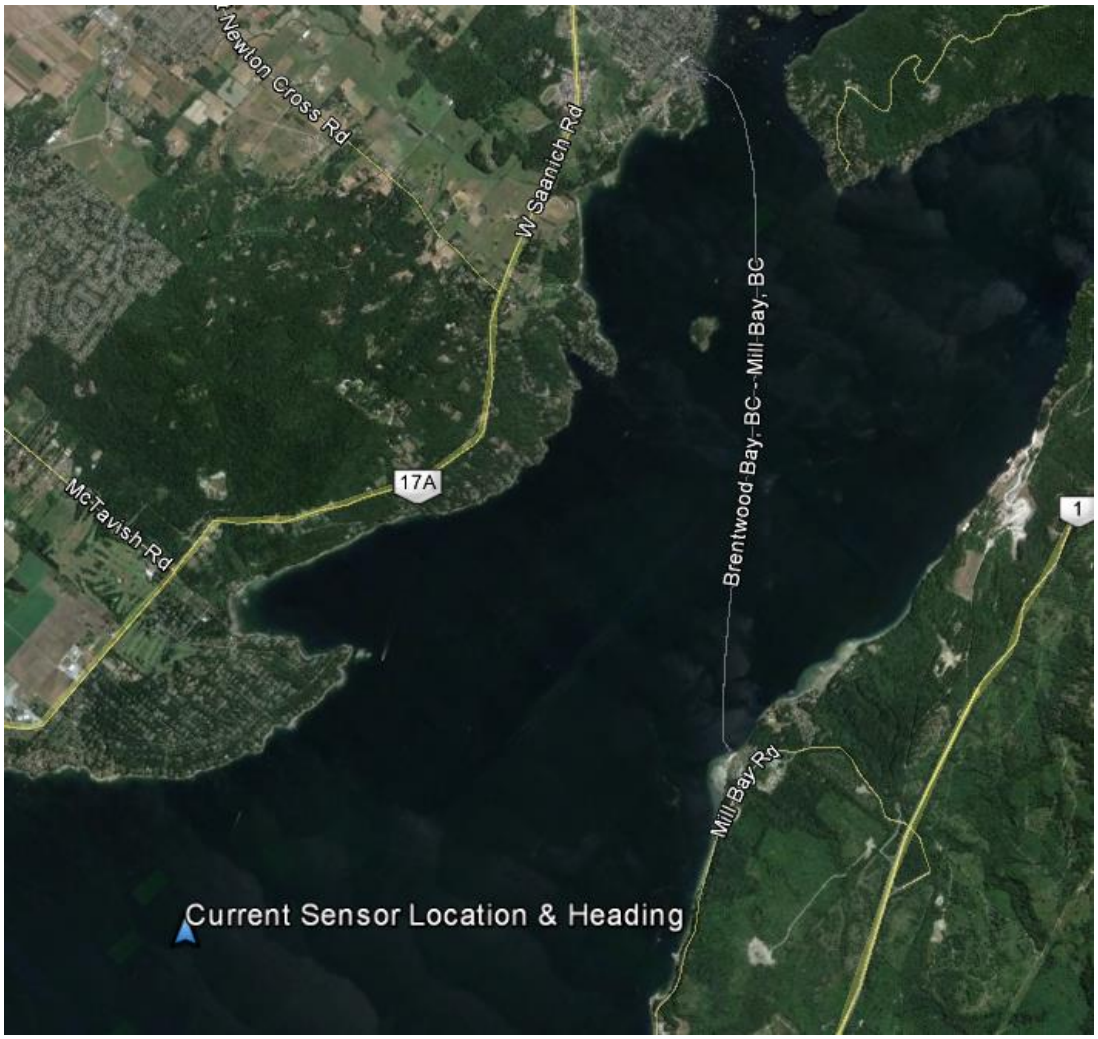

Figure 104: Approximate Current Heading from Ocean Networks Canada versus Brentwood Bay – Mill Bay Crossing [101]

6.4.2 ECM Measurement Errors

The diesel engine ECM output for engine load is not a direct power measurement, but rather a computation based on fuel rates, engine speed, and measurements of the air fuel mixture. If calibrations are correct this signal should provide reasonably accurate results for power output estimation when the engine is operating at quasi-steady state, likely within ±5%. However during transient conditions, especially at low loads, the computed load may diverge from the real value. A literature search was conducted in an attempt to quantify this error during transient conditions. Unfortunately, the search did not yield direct any good comparative data between power computation and direct measurement for similar scale diesel engines.

6.4.3 Signal Noise in Engine Signals

The engine signals were converted from the J1587/1708 onboard engine communication bus to CAN message through custom-built gateway controllers. The intermediate signal conversion process from J1587 to RS232 exhibited a significant amount of high frequency noise and erroneous data that propagated into the dataset. Multiple filtering techniques were attempted to clean up the signal, but a significant post-processing effort was required recreate a realistic load profile. Out of range values were eliminated, and a moving average filter was applied to the data to smooth out erroneous data points. As a result, the post processed load profiles may have damped out higher frequency transients during the maneuvering section that may have account for discrepancies in the model results.

Chapter 7 System Model Validation and Simulation Results

The previous chapters have established the mathematical formulation and Simulink implementation that make-up the BEIPS propulsion architecture, the thruster system, and the hull performance. In this chapter, these components are assembled into a system-level model to validate the simulation framework against real-world operational data. The system-level model allows for component interactions and dependencies to be studied in greater detail. The behaviour can then be compared against results from the real system.

Though the full 6-DOF equations of motion for the vessel have been implemented in the vessel dynamics model, the simulations here are constrained to a single DOF that considers only surge. This simplification was required in this initial body of work because the asymmetric thruster configuration and skeg forces combine to produce a numerically unbalanced yaw moment. Without an auto-pilot algorithm with path tracking, the numerical imbalance caused the ship to turn slightly and go off course. Development of a control algorithm to manage the azimuthing thrusters in this particular configuration is a non-trivial task, so this has been left as future work.

Using the 1-DOF assumption, the model can be systematically tested using the experimental data to validate different sub-systems of the simulation model. The most significant factor that directly affects the powertrain load is the ship velocity. When the ship velocity is under-predicted given the same propeller speed, the advance ratio is decreased thereby increasing propeller torque to produce an over-prediction of energy consumption. Conversely, over-prediction of velocity will produce an under-prediction of energy consumption. The thruster model and wake fraction estimator are also sensitive to changes in velocity. Both of these sub-systems also influence the powertrain load.

In order to isolate these sub-systems for validation, the first set of simulations disabled the vessel dynamics model and imposed the experimental velocity profile collected by the GPS unit in the DAQ experiment. The model's performance was then computed by feeding time series data for engine speed, and azimuth angle data as inputs. This approach provided a direct means of comparison for the powertrain load predictions against the engine load data collected from the ECM.

The second set of simulations included the vessel dynamics model to investigate the full model performance. With the 1-DOF motion constraint, the propeller forces were limited to the x-direction to consider only forces in the surge sub-system. This set of simulations assessed the model's ability to capture dynamic actuation forces for maneuvering and cruise conditions, and how these actuation forces propagate to the IPS.

Before presenting the simulation results for both test cases, this chapter will begin by illustrating the system-level model implementation and configuration in Simulink. This is followed by a presentation of the simulation results, and lastly, a comprehensive discussion of the results and the level of success achieved using this methodology.

7.1 System Model Implementation

Due to the large number of sub-systems, the model will be presented in sections for clarity. The overall propulsion system of the model is shown in Figure 105. This model is divided by two coloured boxes, including an overlap section around the propeller models. The blue box illustrates the information flow between the electrical power system models and the propeller models, with further detail shown in Figure 106. The red box illustrates the actuation forces and the vessel dynamics model, with further detail shown in Figure 107.

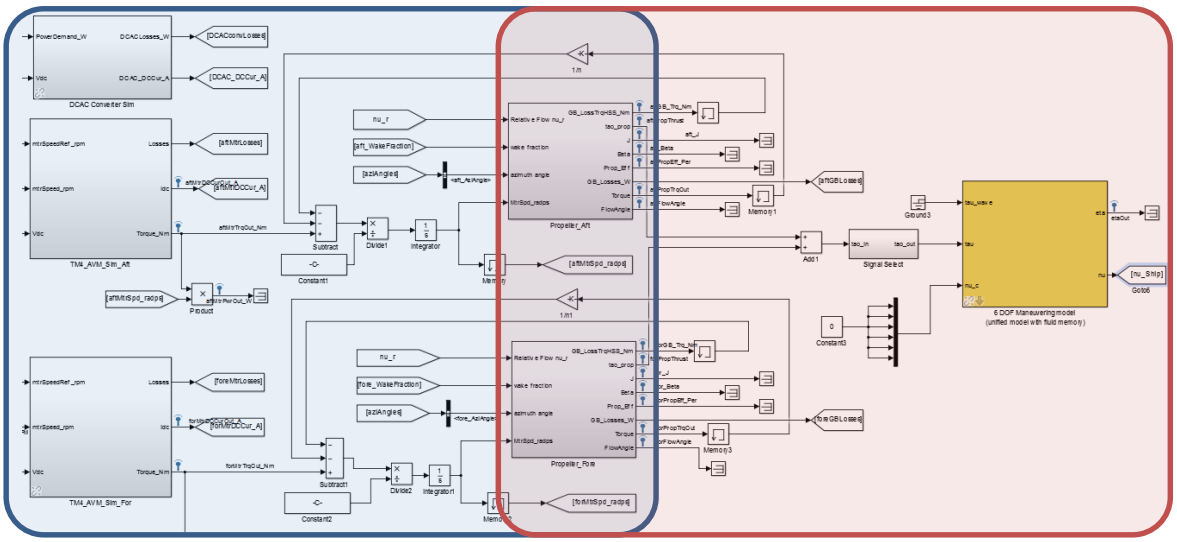

Figure 105: Propulsion System Model Implementation

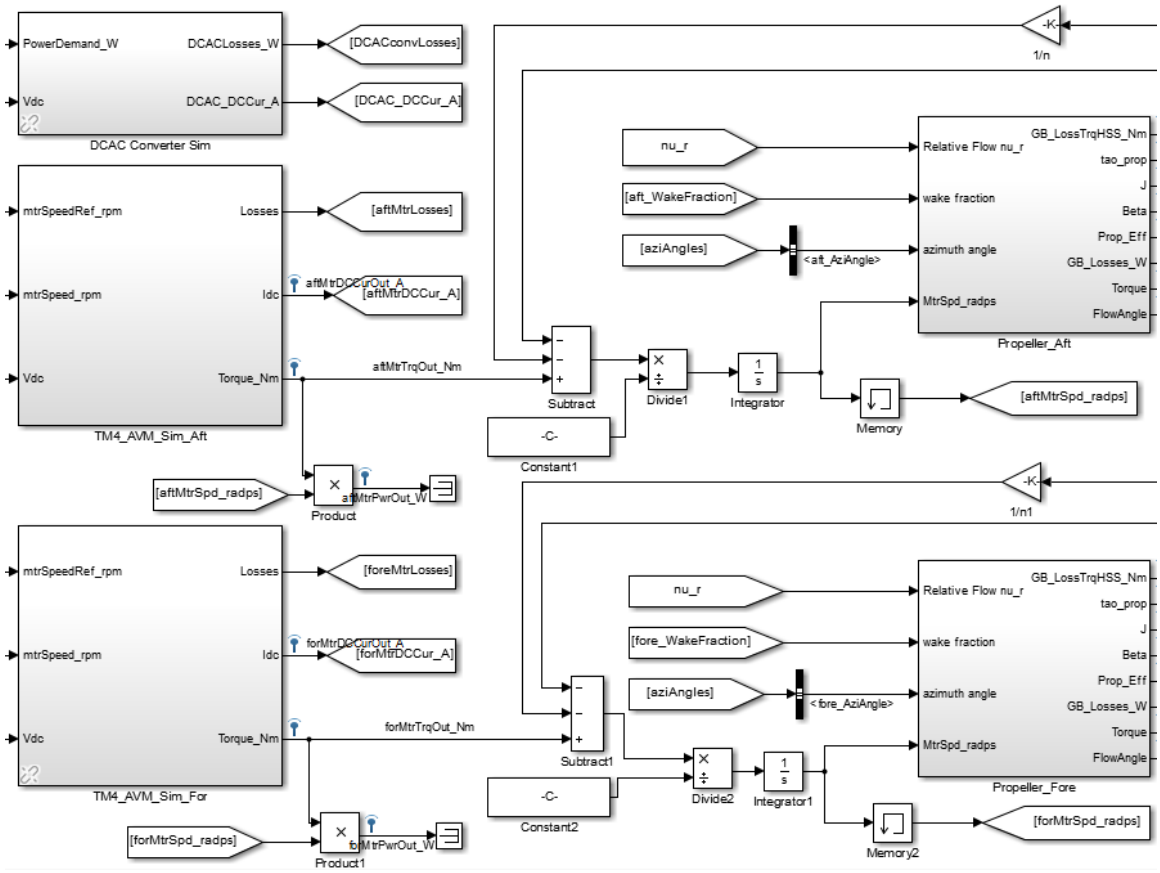

Figure 106: Electric Motor and Thruster Model Connections and Information Flow

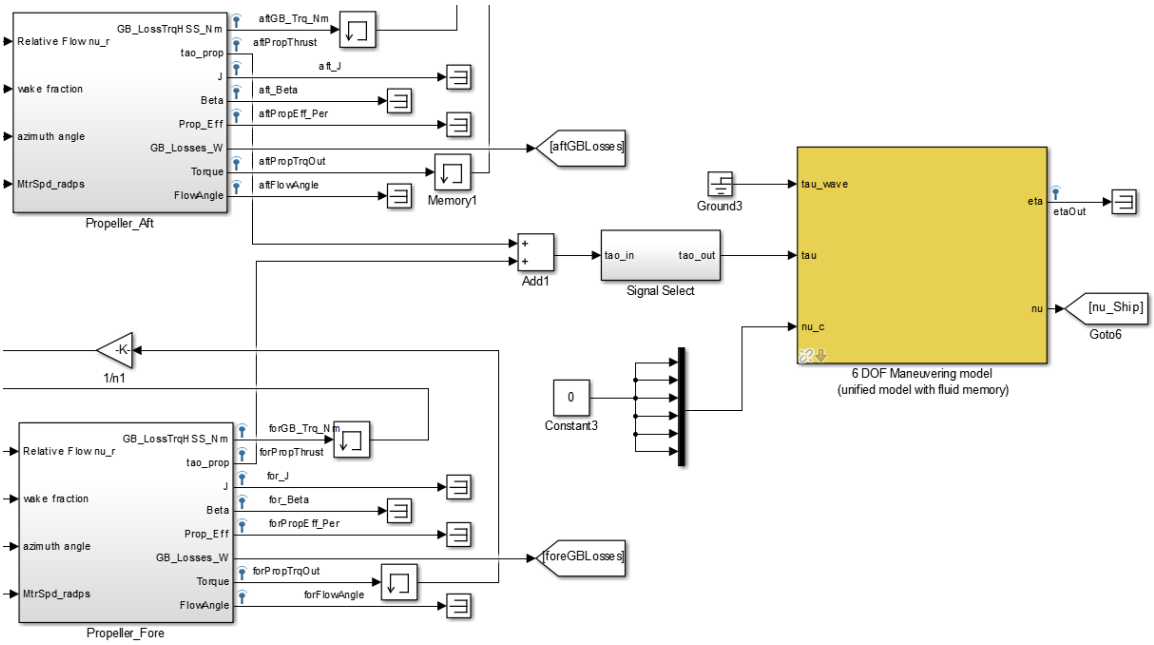

Figure 107: Propeller and Vessel Dynamics Model Information Flow

The IPS model and its connection to the electric propulsion motor models is presented in Figure 108. This image also shows the input signals representing the driver inputs which have been implemented using the "Signal Builder" block in Simulink.

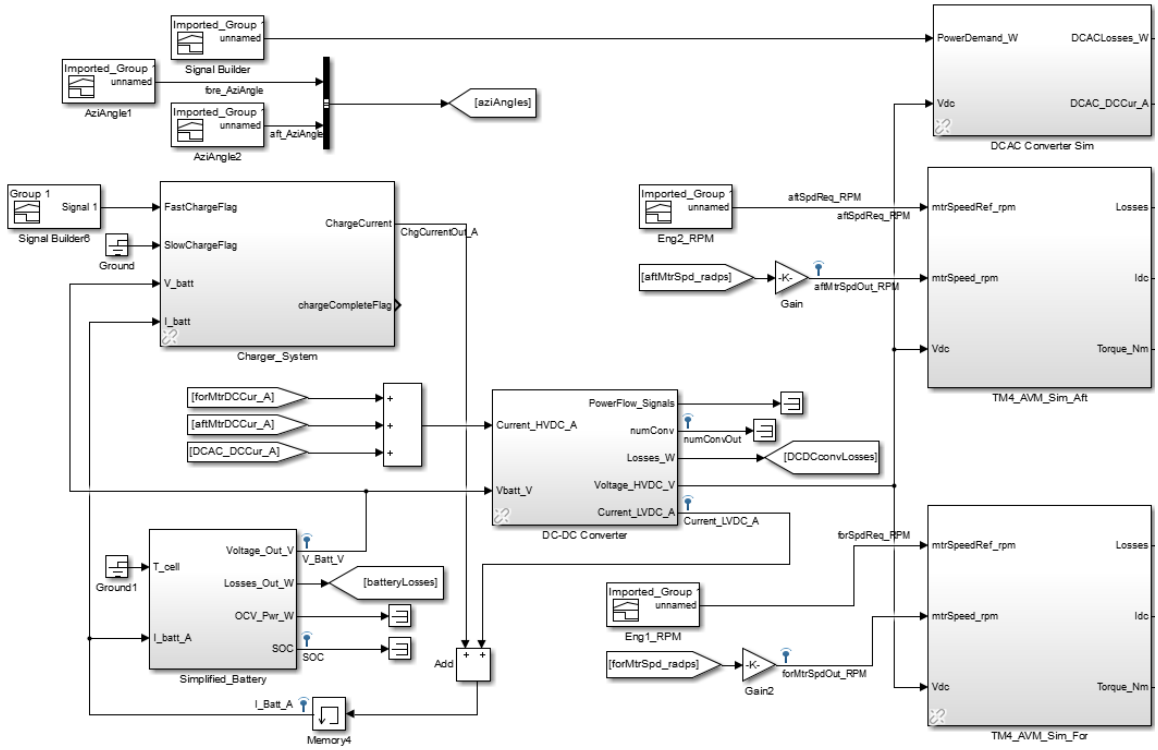

Figure 108: Integrated Power System Model Implementation and Information Flow

The effects of the fore and aft wake fraction are computed based on the surge velocity of the vessel. Because the vessel is double-ended and operates in both directions, the wake fractions are adjusted based on the direction of travel.

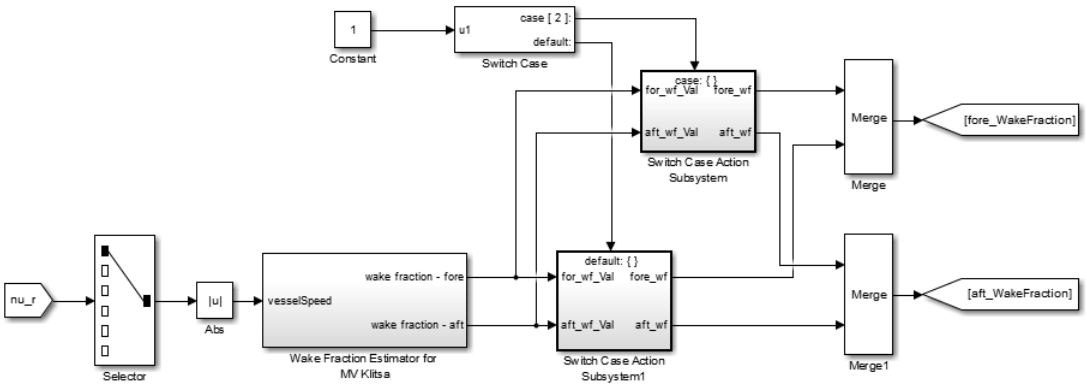

Figure 109: Wake Fraction Generator Sub-System

Finally, the two simulation cases require a method for switching between the vessel dynamics model output and the time series velocity profile from the DAQ data. This is implemented with a simple "Switch" block as shown in Figure 110.

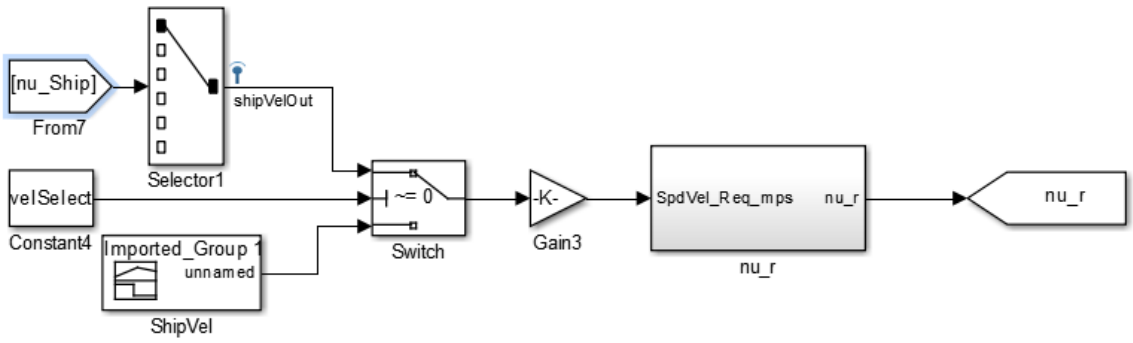

Figure 110: Implementation of Velocity Source Selector

7.2 Powertrain Load Prediction and Verification

7.2.1 Simulation Results for Different Load Profiles

The first set of simulations disabled the vessel dynamics model from the analysis, and instead, applied the experimental velocity data for the three load profiles directly. The GPS velocity profile data was loaded into a "*Signal Builder*" block, and the model was configured to disable the vessel dynamics output as a feedback variable, see Figure 110. The azimuth angle commanded was also directly specified using experimental data to assess the thruster model's effectiveness of capturing transient off-design performance during maneuvers.

The motor speed time-series data collected in the DAQ experiments was also configured as a model input; however, this was used as reference signal to the PI speed controller in the motor drive. The controller was tuned to closely track the signal, thereby minimizing any engine/motor speed discrepancies between model and data. The simulation was performed for the three load profiles, and the results are shown in Figure 111 through Figure 113.

Each cycle begins the instant that the ferry pushes back from the dock and ramps up engines to begin the crossing. The ramp-up period is followed by relatively steady state operation while in transit. As the ferry approaches its destination, the engines are ramped down and the vessel is dynamically braked by the driver. Pulses of thrust are delivered to maneuver the ship into berth and gently touch the marine structures. Once in place, the ship powers into berth at a constant low power output while vehicles are offloaded and then subsequently reloaded. The cycle concludes just before the ship pushes back for its next crossing.

The results are generally in good agreement; however, one blatant discrepancy across all three simulations is the significant under-prediction of propulsive load when the ship is in berth. The propeller torque produced by the thruster model was confirmed to be correct when cross-referenced by the manufacturer's datasheet. It was found that the hydraulic actuation system for the azimuthing thruster is driven off the output shaft of the engine as a PTO. The loading is relatively small compared to the rated output of the engine; however, it is the dominant source of load while in berth.

In addition to the hydraulic system, the right angled gearbox arrangement is not likely well represented by linear damping alone. Coulomb friction and other factors are likely present, but experimental characterization of the damping model was not feasible with the ship in service. The analysis performed by the manufacturer in the original propulsion system design for the Klitsa assumed a constant 15% loss for the propeller system, including hydraulic system PTO. This assumption was initially dismissed as being overly conservative, but the operational data suggests that these systems are reasonably approximated by a constant damping load combined with a speed-dependent damping term.

As a simple revision to the damping model, the linear damping torque was numerically backed out of the simulation results. A revised damping model was numerically inserted to maintain a constant 28kW of damping load to coincide with experimental observation, but also accounting for speed dependent linear damping in the gearbox. The new model was implemented as linear function whose output is fed into a "*Saturation"* block with lower limit of 28kW. This value is about 10.7% of rated load, and is well below the

estimate offered by the manufacturer. The revised model is plotted alongside both the initial model and experimental data for each simulation.

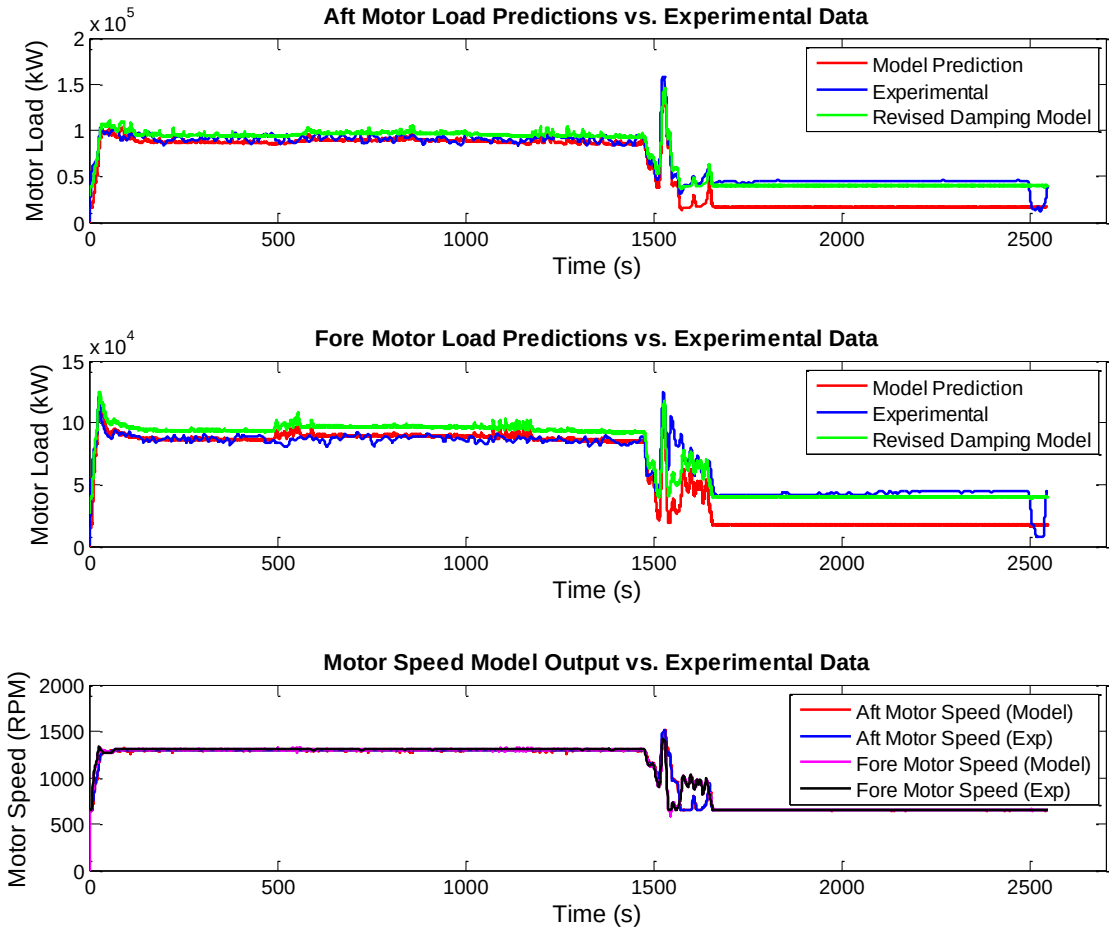

Figure 111: Simulation Results for Load Profile 1 with Vessel Speed Specified

The results for the first load profile show that the engine load prediction from propeller and linear damping alone are in good agreement while the ship is in transit. The revised damping model slightly over-predicts the load during transit, but significantly improves on the low speed problematic areas. The aft motor model tracks well with the thrust pulses during maneuvering, whereas, the fore motor model did not capture all the peaks. This can be explained by observing the motor speed profiles. The experimental data shows some high frequency variation in the engine speed signal that are attenuated by the PI speed controller driving the motor model. Despite the lost resolution from the actual

engine speed, the motor model tracks well with the engine speed data providing an excellent comparative test.

The results from the second load profile simulation are presented in Figure 112. Here, it can be seen that the model is under predicting the load in transit, especially on the aft propeller. The fore propeller is significantly more accurate during transit, also exhibiting a much smoother profile interestingly.

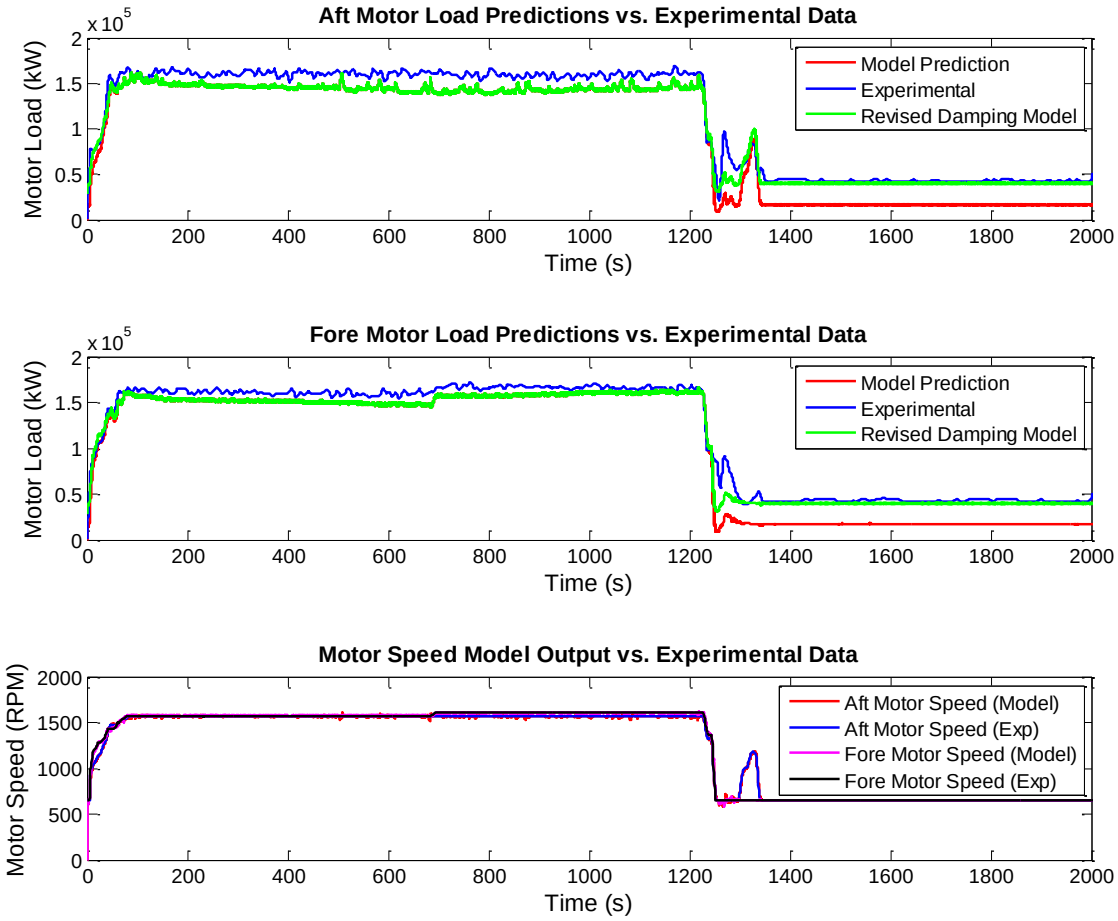

Figure 112: Simulation Results for Load Profile 2 with Vessel Speed Specified

Like the first case, the maneuvering portion of the crossing exhibits lost resolution as a result of the attenuation of the engine speed signal. The location of the peaks are generally well preserved, and the predicted amplitude of the pulses are reasonably accurate when the thrust pulse event in not attenuated by the PI motor speed controller.

The revised damping model provides a much better load prediction at low motor speed, and the higher motor speed overlaps with the original linear damping. This indicates that the linear damping term has exceeded the 28kW lower saturation limit, which was not observed in the results of the first load profile.

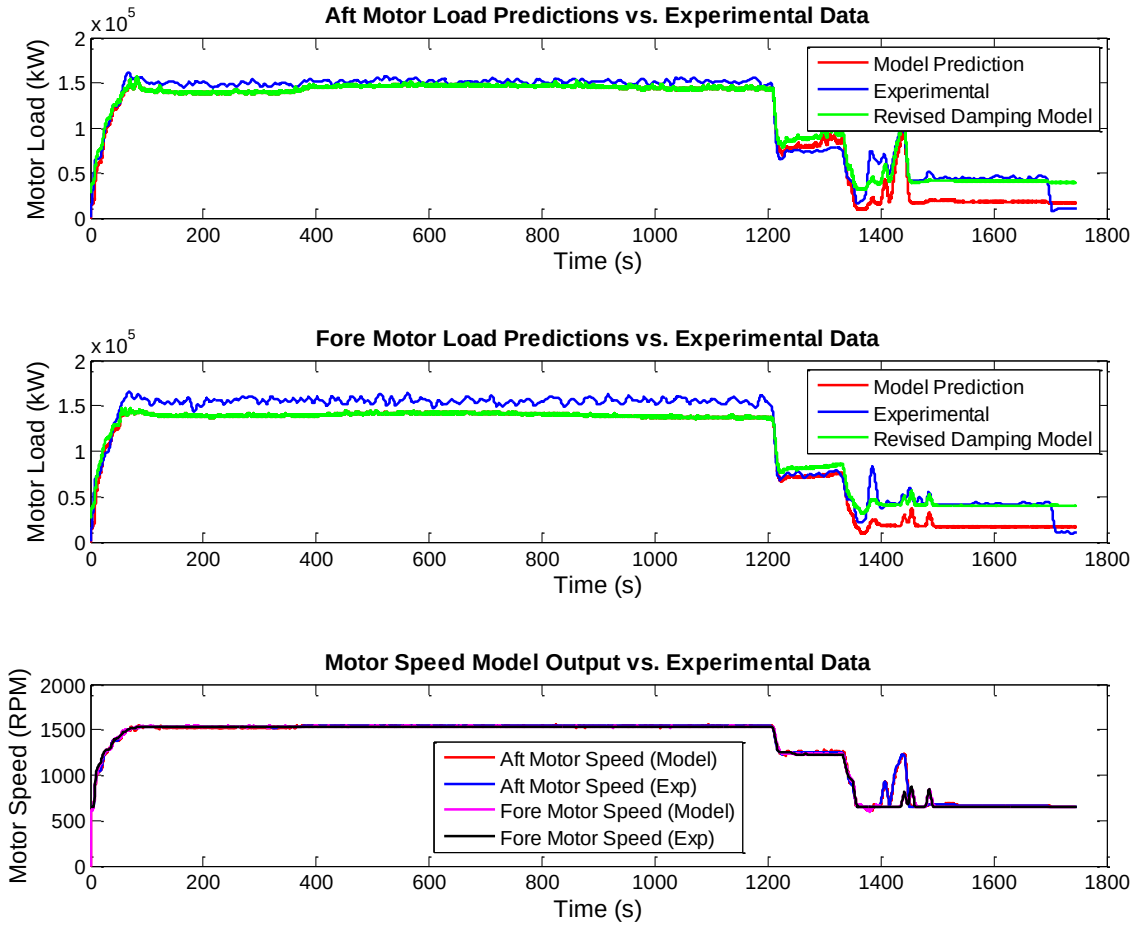

Figure 113: Simulation Results for Load Profile 3 with Vessel Speed Specified

The results of the final load profile are presented in Figure 113. The results show another higher output crossing in comparison to load profile 1. The aft motor prediction is quite good during transit with some lost resolution during maneuvering. The location of thrust pulse peaks for both thrusters are preserved, but higher frequency pulses are attenuated. The mean error produced between the fore thruster and its corresponding data

is the largest of any of the simulation. Interestingly, the experimental data collected for one engine seems to consistently produce larger error regardless of whether it lies in the fore or aft position. The data collected from the other engine consistently produces better results regardless of vessel direction.

By investigating the load profile, it can clearly be observed that a significant amount of energy is needlessly dissipated while the ferry is in berth with the existing diesel architecture. Diesel engines have a prescribed idle speed and the thruster system must maintain a minimum shaft load to keep the clutches engaged. The integrated gearbox/hydraulic systems are the dominant sources of energy dissipation while the engines idle in berth. Furthermore, an unnecessarily high level of propeller load is generated as a consequence of the idle speed constraint. By converting to an electric propulsion system, the propeller can be reduced to zero speed to achieve energy savings, provided that the ship is adequately restrained by the marine structures. The energy savings from zero speed operation in berth, including the contribution from a linear damping approximation for gearbox losses are tabulated in Table 31. Note that load profile 3 is significantly smaller, as this was the end-of-day crossing with only the offload cycle represented.

Table 31: Potential Energy Savings from Zero-Speed Propeller Operation In-Berth

Load Profile	In-Berth Duration (s)	Estimated Energy Savings (kWh)
1	894	8.44
2	647	5.99
3	246	2.44

A more detailed decomposition of the gearbox and hydraulic system load/loss characteristics would provide a more accurate estimate for additional savings. As an aside, a mechanically-driven PTO hydraulic system powered by engine's output shaft is

typically oversized such that pressure and flowrate specifications can be maintained at engine idle speed. At idle speed, the hydraulic system typically operating at a very low-efficiency point. An AES conversion would likely replace this PTO system with a variable-speed electrically driven system. This type of arrangement has the clear benefit of decoupling the hydraulic pump's input speed from the engine speed, allowing the hydraulic pump to operate at its most efficient operation point.

7.2.2 BEIPS Performance Results

The performance of the energy storage system and the charge depletion on all three journeys are plotted in Figure 114. Load profile 2 is the most energy intensive as expected due to the higher transit speed. The quasi-steady power draw of the propulsion engines while in transit produces a linear SOC drop with time. A knee is overserved in each of the datasets that marks the beginning of the ramp-down as the ship nears the berth. Subsequently, the linear trend flattens out to indicate a reduced rate of energy consumption.

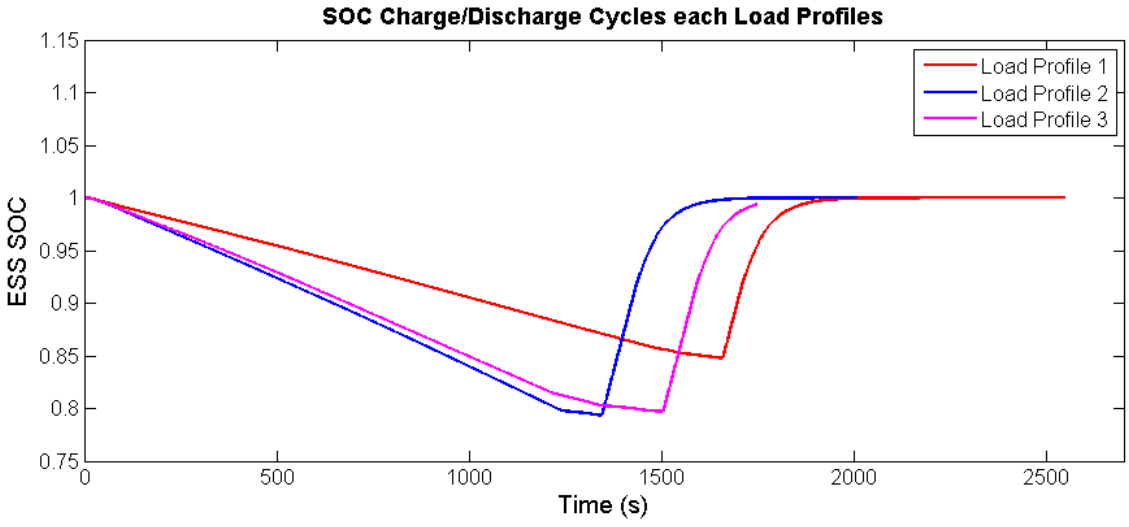

Figure 114: SOC Discharge/Charge Profile for Rapid-Charge System

Once the ship is in berth, the charging system is engaged with a 5C continuous current fast-charge and the SOC increases approximately linearly at first until the maximum voltage is achieved. The charge then exponentially tapers to zero, but at a rate that seems unfeasibly high. The battery parameters were verified in the model, and no error could be identified; however, the equivalent circuit parameter data from Cleary et al. [43] did not provide good resolution for circuit parameters at high SOC which could help explain the results. Regardless, the CC and CV algorithms function as intended and the results show a 20% DoD in the most energy intensive cycle.

Lastly, the modeling results allow for investigation of component efficiencies throughout the cycle. The individual component efficiencies for each load profile are plotted versus time in Figure 115. During transit the motors, battery system, and converters are all operating in excess of 92% across all three cycles. The motor efficiencies drop below 90% as the ship begins its ramp-down, but maintain >80% efficiency throughout the entire cycle with exception to short-term transient events.

During loading/offloading, the motors maintain an efficiency above 83% using the same operational profiles as the diesel engines, though the motors could be reduced to zero speed for energy savings.

The relatively small current draw from the battery while in transit produces little ohmic loss dissipation in the battery model, leading to a high efficiency. Once a rapid charge cycle is engaged, a sharp decline in efficiency is observed as more energy is being dissipated within the battery's internals and electrochemical reactions. Despite the increased ohmic losses during charging, the efficiency remains above 90%.

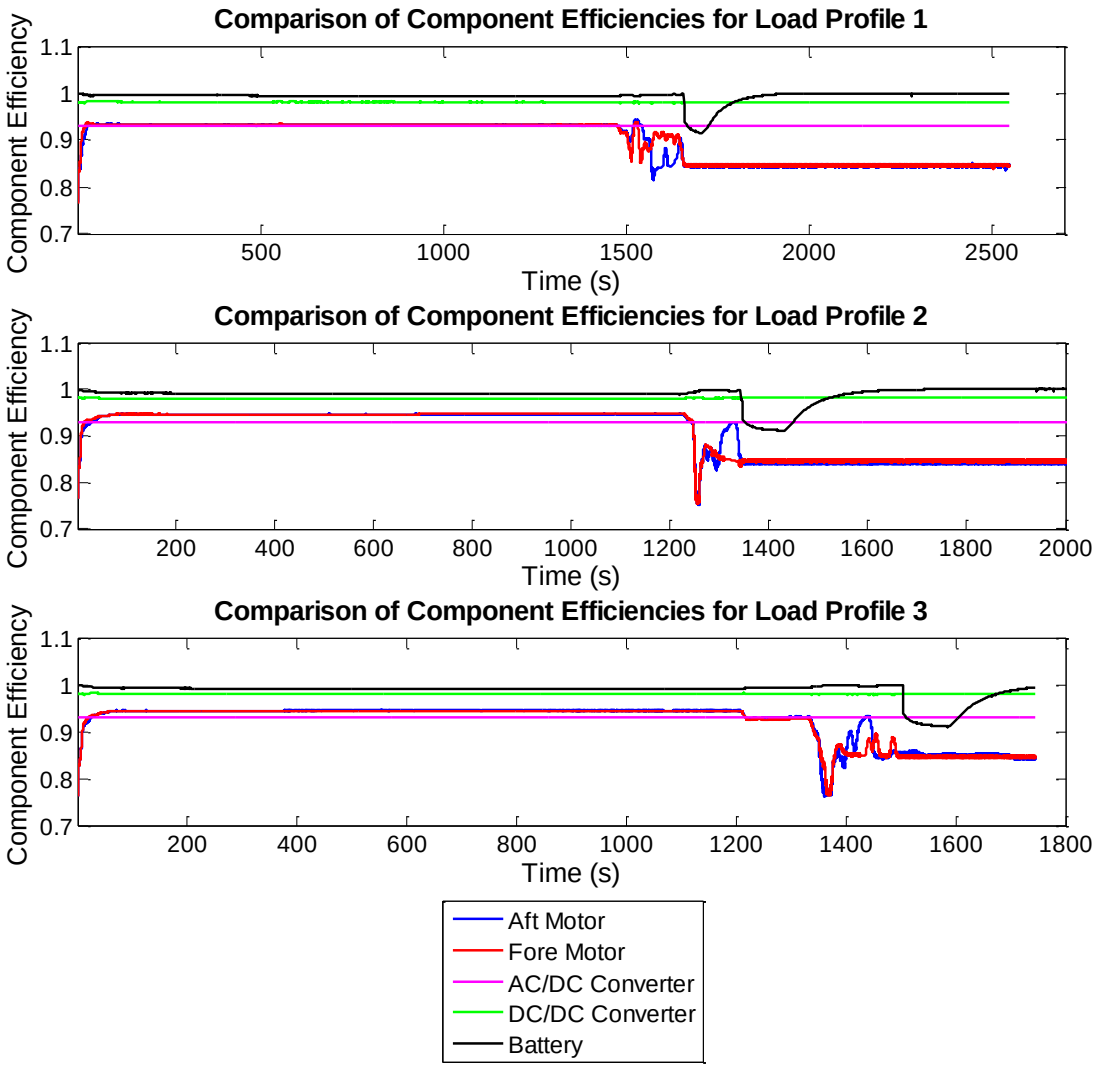

Figure 115: Plot of Component Efficiencies during Load Profiles

The AC/DC is set at a constant 93%, as was discussed in Chapter 5, and is observed to be a flat line as expected. The DC/DC converter model fluctuates slightly based on load, but achieves >97% accuracy throughout the each cycle.

7.3 Simulation Results Including Vessel Dynamics

The second set of simulations deployed the entire system-level model including the vessel dynamics sub-system. As was discussed previously, the vessel dynamics model was limited to a single DOF in surge. In the absence of an intelligent driver model, these simulations are essentially operating in open loop. As was done in the previous

simulations, the azimuth angle and motor speed reference signals were provided as inputs based on the experimental data. The signal output from the vessel dynamics model was connected to complete the feedback loop for the propeller thrust and torque predictions.

A comparison of the model's predicted results against experimental data for engine load, engine speed, and vessel speed are presented for each load profile in Figure 116, Figure 117, and Figure 118, respectively.

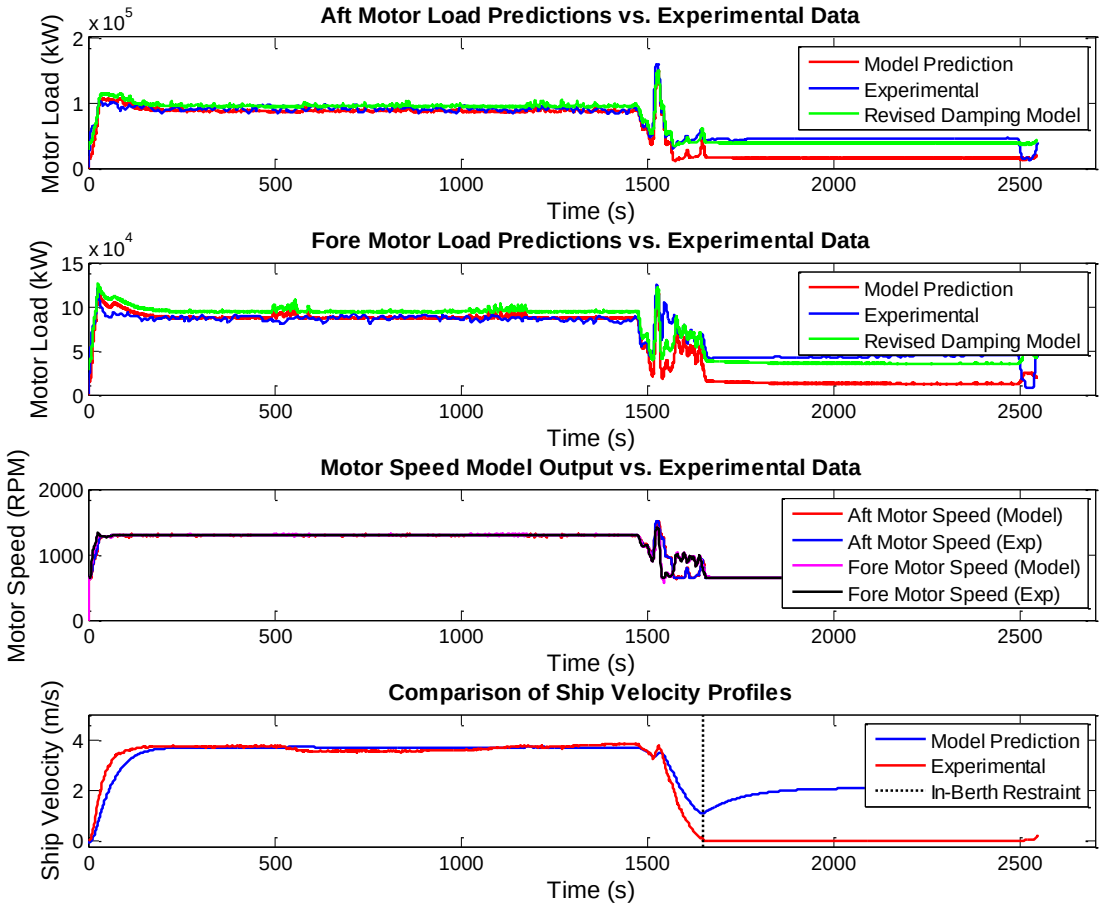

Figure 116: Simulation Results for Load Profile 1 including Vessel Dynamics

Referring to the ship velocity profiles for each of these simulations, a problem can immediately be observed during the in-berth portion of each simulation. The dotted vertical line on each of these plots indicate the point where the ship would otherwise be restrained by the marine structures. In its present form, the model does not account for

this restraining force, and the ship appears to accelerate while in berth; consequently, the results beyond the dotted line are neglected.

Beginning with load profile 1, the predicted powertrain loads with 1-DOF motion are very similar to those observed in the previous sections. The velocity profile predicted by the model shows a slower acceleration during ramp-up which leads to an increased load on the propulsion motors during the acceleration. The increased load is intuitive because propeller thrust and torque production increases as advance ratio decreases in the first quadrant.

The reduced acceleration and deceleration rates naturally point to an inertial discrepancy, especially since the velocity in transit is relatively accurate. There is uncertainty in the inertial properties because the variation in vessel loading could not been easily accounted for in the analysis. If we recall from Chapter 4, the inertial properties were taken from a set operating condition outlined in the ship's stability book. The dynamic braking that occurs as the ship approaches the berth is not well represented, partially because the model inertia will likely be higher than was present during the experiment. The normal departure condition identified in the stability book can conclusively be determined as an over-estimate, because the loading condition specified is not typically encountered in normal operation.

The dynamic braking performed by the driver on the real ship is executed to achieve a near-zero forward speed to gently make contact with the marine structures. Here, the model predicts an approximate 1 m/s forward speed as the ship enters berth. After experimenting with the simulations with reduced inertia, it was concluded that not all of this discrepancy can be attributed to the inertial parameters. Other problematic areas

might include insufficient surge damping, under-prediction of propeller thrust in the anti-/equi-directional states, or from the 1DOF assumption.

The problem is exacerbated when investigating the model results from load profiles 2 and 3. Again, the steady state transit velocity is reasonably well represented, though the experimental data wanders slightly without any changes to motor speed. This indicates the presence of additional environmental factors. The ramp-down/maneuvering portion of cycle clearly illustrates a problem with the model's velocity response and/or dynamic braking thrust production. A closer inspection of the results from load profile 3 suggests that the combination of braking/damping force on the vessel speed is not well represented.

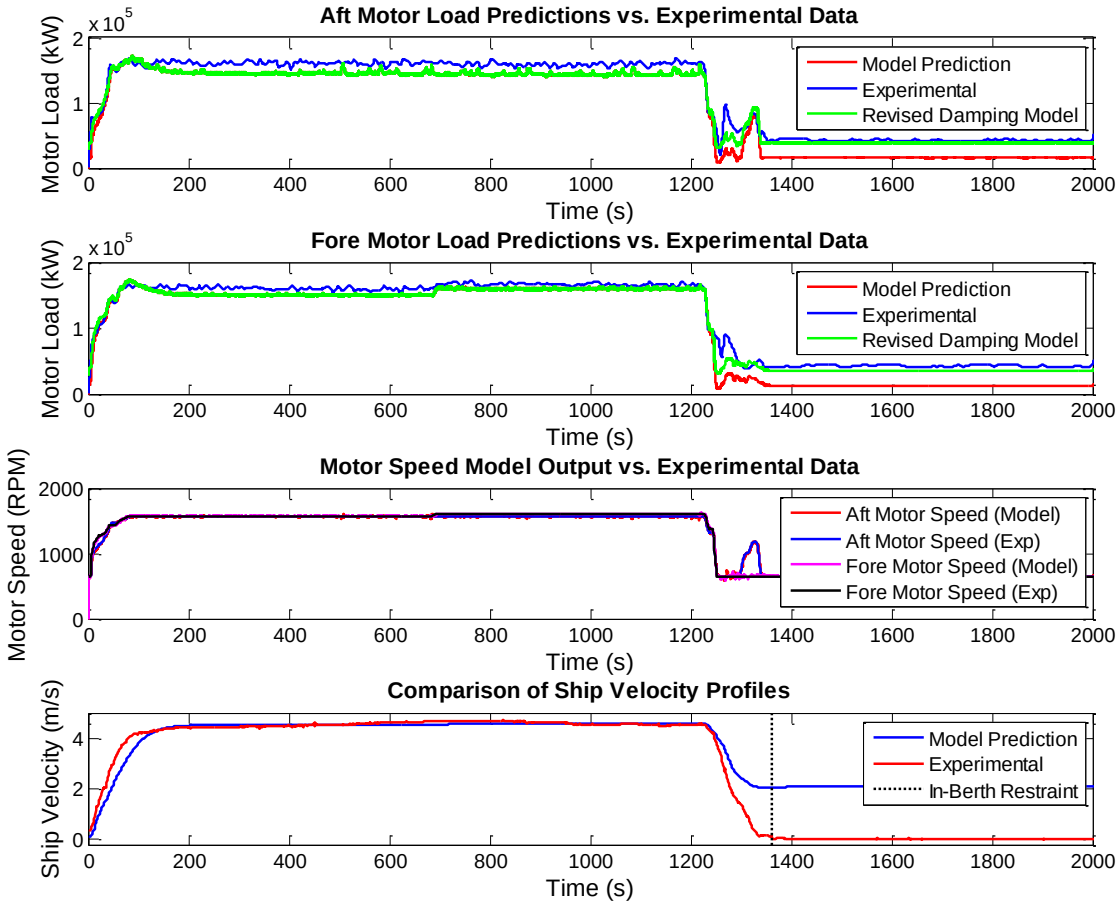

Figure 117: Simulation Results for Load Profile 2 including Vessel Dynamics

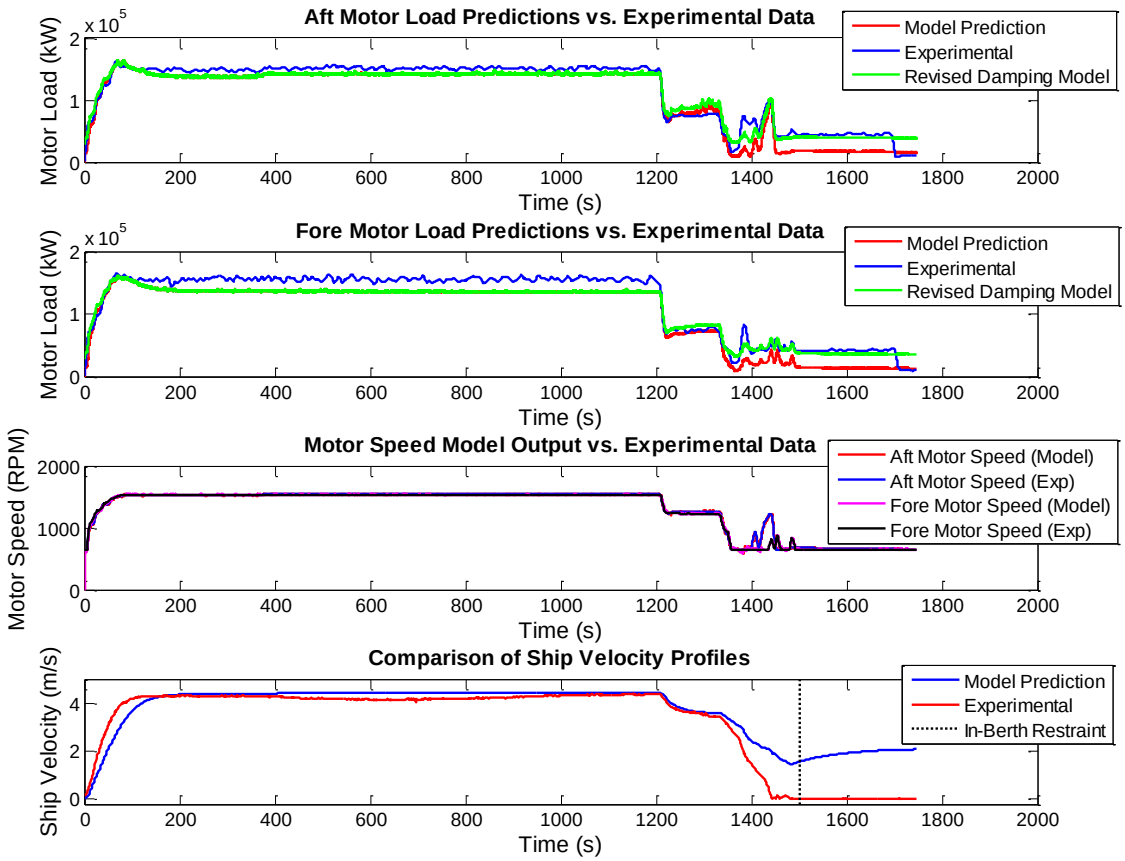

Figure 118: Simulation Results for Load Profile 3 including Vessel Dynamics

The hard braking thrust pulse from the aft motor doesn't produce a sharp decline in ship velocity as is seen in the experimental data. The surge damping should be significantly less in magnitude in comparison to the thrust force, so it is likely that the thruster's off-design performance requires further investigation.

There are additional contributing factors that would account for some of the error observed in the model. These are influencing factors are discussed in the following section, and comparative numerical error analysis is performed to quantitatively judge the results.

7.4 Analysis and Discussion of Results

7.4.1 Model vs. Experimental Direct Comparison

The results from all six simulation studies show relatively good correlation with the experimental data collected, especially during steady in-transit operation. The original linear damping assumption for the mechanical power transmission system did not capture the PTO effects of the hydraulic system, leading to poor results while the ship was at low output. The revised damping model, which maintained a minimum mechanical base load, provided a more accurate representation during low power output conditions but has no physical basis. The revised damping model combined with the propeller torque is still under-predicting engine load at higher output; therefore, the PTO damping model really needs to be examined in further technical detail to pinpoint the source of error. The wake fraction sub-system will also influence propeller load, so it could also be a contributing factor.

The dynamics of the PTO system are likely a contributor to the increased error seen in the maneuvering portion of the cycle. High frequency fluctuations are observed in the experimental engine speed data which also correlates to observable load peaks that are not likely produced by the propeller. These observations naturally point to variations in the PTO hydraulic system during dynamic conditions. The hydraulic system provides the actuation force for rotating the azimuthing thrusters during maneuvers. The PTO model should be linked to azimuthing thruster model to give a more physical interpretation of the dynamic load, but little information was available from the manufacturer to develop a suitable mathematical relationship.

A summary of the mean and maximum instantaneous relative error observed for each cycle, decomposed by load profile and operating regime, is presented in Table 32. The

experimental values were assumed to be correct, and the relative error was computed using the equation,

$$\frac{abs\left(P_{exp} - P_{model}\right)}{P_{exp}} \quad \textbf{(7-1)}$$

Initial start-up conditions for the model and erroneous data points have been omitted in the error analysis. With both simulation configurations, the in-transit is well represented by the model generally yielding results less than 10% mean relative error between predicted load and actual load. As discussed previously, the maneuvering portion is definitely more problematic. The mean relative error diverges with the generally around 20% even with the revised damping model. At constant output in berth, revised damping model produces good results with mean relative error less than 7%.

Table 32: Instantaneous Relative Error Analysis of Simulation Results

Instantaneous Relative Error Analysis												
Load Profile	Aft Motor Model Data (Linear Damping)						For Motor Model Data (Linear Damping)					
	In-Transit		Ramp-Down/Man.		In-Berth		In-Transit		Ramp-Down/Man.		In-Berth	
	Mean	Max	Mean	Max	Mean	Max	Mean	Max	Mean	Max	Mean	Max
LP1 (No Vessel Dynamics)	3.8%	16.0%	33.7%	62.5%	61.8%	64.8%	3.0%	16.1%	35.7%	79.7%	60.1%	62.6%
LP1 (Vessel Dynamics)	4.1%	21.0%	35.8%	69.0%	-	-	3.5%	16.9%	33.8%	79.7%	-	-
LP2 (No Vessel Dynamics)	9.4%	18.9%	41.3%	81.0%	61.0%	73.1%	5.1%	11.2%	54.8%	90.1%	60.0%	71.6%
LP2 (Vessel Dynamics)	8.9%	15.9%	42.3%	81.8%	-	-	4.8%	10.4%	50.8%	90.5%	-	-
LP3 (No Vessel Dynamics)	4.3%	11.5%	29.1%	77.7%	59.1%	63.4%	9.9%	15.9%	29.1%	74.2%	59.4%	62.6%
LP3 (Vessel Dynamics)	5.8%	11.6%	30.0%	84.7%	-	-	11.4%	17.2%	28.2%	74.4%	-	-
Load Profile	Aft Model Data Revised Damping)						For Motor Model Data Revised Damping)					
	In-Transit		Ramp-Down/Man.		In-Berth		In-Transit		Ramp-Down/Man.		In-Berth	
	Mean	Max	Mean	Max	Mean	Max	Mean	Max	Mean	Max	Mean	Max
LP1 (No Vessel Dynamics)	6.0%	24.7%	10.6%	35.2%	10.3%	15.8%	10.2%	25.0%	16.0%	54.0%	7.1%	11.0%
LP1 (Vessel Dynamics)	6.1%	29.6%	10.1%	30.0%	-	-	10.5%	26.0%	16.0%	54.1%	-	-
LP2 (No Vessel Dynamics)	9.2%	17.4%	21.2%	57.7%	7.6%	33.7%	5.1%	11.2%	20.8%	63.5%	6.7%	30.0%
LP2 (Vessel Dynamics)	8.9%	15.9%	20.9%	57.3%	-	-	4.9%	11.3%	20.8%	63.8%	-	-
LP3 (No Vessel Dynamics)	4.3%	11.8%	21.5%	115.5%	8.3%	15.2%	10.0%	17.0%	13.0%	74.6%	5.2%	11.1%
LP3 (Vessel Dynamics)	6.0%	14.2%	21.5%	113.7%	-	-	11.5%	17.8%	11.6%	74.2%	-	-

It should be noted that the data collected for Engine 1 consistently provided the highest discrepancy across each simulation. Recalling that load profiles 1 and 3 have this engine in the fore position, and load profile 2 has this in aft position, this pattern can be observed regardless of position. Engine 2 provided much better results by comparison. It is possible that the ECM computations of engine load contain some error due to improper or

unrepresentative calibration. The engines had just been serviced and dynamometer tested before the data acquisition system was installed, so it's unlikely this error can fully be placed on improper calibration. Future validation will require direct measurement the output shaft to the engine using strain gaging and rotational speed sensors.

The objective of this work was to establish an integrated propulsion modeling tool that was suitable for architectural design studies to assess overall system performance. The simulation framework generally achieves <20% mean error, which can likely be improved upon with minor adjustments to the model. The model has been parameterized, for the most part, using only numerical analysis techniques and manufacturer datasheets. This implies that the approach can be applied during the design stage when operational data is not available.

In general, the correlation between the experimental data and model predictions was fairly good, especially when the velocity profile constrained to known operational profile; however, prediction of load pulses and dynamic actuation forces during maneuvers approach berth were a bit problematic due to attenuation by the electric drive's PI controller.

7.4.2 Model and Sub-System Uncertainties

The model implementation and parameterization has been performed using a combination of computational analysis, empirical coefficients, experimental data, and educated assumptions. Section 6.4 described the sources of uncertainty in the experimental data, some of which will have propagated into the modeling results. Due to the experimental limitations imposed by testing a ship while in-service, there are few opportunities to run prescribed and targeted tests that could quantify uncertainties and

errors in the individual subsystems. A more extensive set of parameterization data for the ship hull could also be developed using additional CFD experiments. Though CFD is a powerful design tool, the time required to generate the full spectrum of data is almost unfeasible, even with a super computing cluster like Westgrid.

In order to highlight the relative degrees of accuracy/uncertainty in the sub-components, Table 33 provides a qualitative ranking of each sub-system to the most significant areas that will improve the model's performance. The relative degree of confidence has been assessed based on the results presented in section 7.3, and the parameterization process/assumptions that went into the model's construction. The PTO/damping model, vessel dynamics model, and thrust deduction factor sub-models carry the most uncertainty. The following sections will provide specific details on the problematic areas within the model and how they can be addressed in future work.

Table 33: Relative Modeling Uncertainty and Degree of Confidence

Sub-Model	Relative Level of Confidence	Description
Thrust/Torque Coefficients	High/Medium	• High confidence in 1st quadrant, medium confidence in angular/opposing flow conditions
Thrust Deduction Factor	Low	• Incomplete dataset *t(u)* • Large scatter in experimental data used to compute *t*
Wake Fraction	High/Medium	• Based on high resolution CFD results, though results differ from original model test data
Battery System	High	• Validated using published experimental data
Electric Drive Systems	High	• Validated using component data
PTO Model	Medium/Low	• Estimated from experimental data, no dynamics associated • Does not consider physical loading factors during actuation of the thruster tower
GB Torque Damping Model	Medium	• Estimated using manufacturer information
Vessel Dynamics Model	Medium	• Surge CFD results under-predicts versus original ship design data • Over-estimate of mass and inertial parameters

		• Hydrodynamic coefficient errors in some of 6DOF matrix entries • Excellent results for in-transit on approximate constant course with unified seakeeping/maneuvering model • Errors developing during maneuvering and large course and speed deviation with vessel dynamics equation

7.4.2.1 Rotational Damping Characteristics and PTO

The rotational damping characteristics of the gearbox system were simplified to a linearly proportional model relative to rotational speed. Coulomb damping and other frictional components are often introduced into the equation as well, for example see Pivano [79], provided that experimental data can be secured. Detailed experimentation was not possible with the full-scale thruster, and such an experiment would require a relatively involved instrumentation setup making it somewhat unfeasible. This remains one of the major areas from improvement. The best course of action for firming up this model would be to engage the manufacturer for any testing results that they may have.

Further to the gearbox, the dynamics and loss characteristics of the hydraulic PTO system was unaccounted for in the original simulation model. With the revised damping model, the 28-30kW discrepancy between model results and experimental data was attributed to the hydraulic system, but this requires further investigation to be conclusive. The performance characteristics of the hydraulic pump at various input shaft speeds, pressures, and flow rates would allow for a preliminary physics-based model to be constructed. The loading characteristics would then need to be mapped to the azimuthing thruster actuation system to relate the physical load back to the IPS.

7.4.2.2 Inertial Discrepancies

The inertial properties of the ship were assumed constant across all load profiles. This assumption was based on a prescribed operating condition in the stability book. The exact

vessel loading data, including passenger/vehicle count, could be retrieved with BC Ferries' historic logs to improve the inertial parameterization. This effort would likely assist in quantifying the upper bound for error in the inertial properties, but will still carry some uncertainty because logs only capture the number of vehicles and not mass explicitly. The assumed mass and inertial specifications can be conclusively deemed as over-estimates simply because the loading condition portrayed in the stability book is rarely achieved during operation.

7.4.2.3 Low Speed Surge Damping Model

It has been commonly documented in related work that the linear/non-linear matrix decomposition can under-predict surge damping characteristics at lower vessel speed, see for example Fossen [63]. Dynamic positioning control systems often use different damping models for low-speed, and in-transit operation. This would be consistent with the result seen in this study. Under-prediction of damping would account for the slower deceleration seen during ramp-down. A transient CFD analysis replicating the ramp-down, or a vessel coasting experiment might provide more insight into the true damping characteristics of the ship.

7.4.2.4 Thrust Deduction Factor

The thrust deduction factor is definitely the sub-system that carries the most uncertainty. The original intent was to conduct a series of self-propelled CFD studies to quantify this additional hull resistance term as a function of forward speed. Unfortunately the configuration of these analyses proved to be somewhat problematic and the results could not be generated within the time period needed. As a result, this term was computed using experimental data and the bare hull CFD results. This produced an

incomplete set of data points which exhibited a large degree of scatter. The results were averaged and fit to a parabolic model which may or may not be appropriate.

This subsystem could account for some of the issues observed in the vessel dynamics model. A more comprehensive treatment of the thrust deduction factor is required to improve the results, and should be one the immediate areas of focus in future work. This can be done either through additional CFD studies or from scale model tow tank testing.

7.4.2.5 1-DOF Surge System Assumption

The 1-DOF assumption used in this work would have accounted for some of the discrepancies seen in the model, especially during the ramp-down/maneuvering portion of the cycle. The GPS data collected is purely a measurement of velocity magnitude and does not factor vector components of the body's motion. Referring back to Figure 101, it can be seen that the ship actually drifts laterally as it comes into berth for both terminals. During this maneuver, the sway component of velocity will be significant. With the 1-DOF assumption, the GPS velocity magnitude was assumed to be entirely in surge. In actual fact, the velocity is split between surge and sway. Inclusion of the additional DOF would likely reconcile some of the dynamic braking issues observed.

In order to investigate the hull model's performance more thoroughly, an intelligent driver/auto-pilot model will need to be developed along with a course tracking algorithm. The trajectories collected in the data acquisition study can be used to produce the desired path. This will allow for a more direct comparison of the vessel dynamics model with the dynamics of the real ship in a closed loop form. This is not a trivial task, mainly because of the Klitsa's thruster configuration. The manipulation of azimuthing thrusters is an optimal control problem, because there are an infinite number of solutions for achieving

the same result. The development of a driver model will require a significant development effort, but provides an excellent academic project moving forward.

7.4.2.6 Signal Attenuation and Lost Resolution in Data

The data collected as part of DAQ experiment contained a fair amount of noise which was digitally filtered using post-processing. The resulting output signal exhibited some lost resolution, though the mean value tracked well with the raw data. The higher frequency engine speed fluctuations observed in the experimental data during maneuvering contained some high frequency fluctuations that were attenuated by the motor drive's PI controller. The combined signal error and attenuation of higher frequency dynamics drastically under-predicted some of thrust peaks observed in the load cycles. The combined effect of these two factors accounts for a portion of the model's error, though this is likely to be negligible in comparison to the error contained in the PTO/damping model.

Chapter 8 Conclusions and Recommendations

8.1 General Summary and Conclusions

This thesis has systematically developed a methodology for creating parametric time-domain ship models for the study of hybrid and electric propulsion systems. As an illustrative example, this work modeled a BEIPS architecture as a case study to predict the performance of this architecture with the hull and thruster system of BC Ferries' M.V. Klitsa. The power system was modeled using a blended modeling approach that utilized both power loss and AVM models to balance accuracy with computational efficiency.

The methodology and model development process outlined in this work relied heavily on the use of computational fluid dynamics for parameterization. CFD was deployed for analysis of the bare hull resistance at a prescribed set of forward speeds that spanned the operating range of the vessel. Furthermore, a design of experiment was devised to generate the necessary data to parameterize a lookup surface of thrust and torque coefficients to quantifying thruster performance under all potential operating conditions.

The BEIPS component models were based off commercially available components, with parameterization primarily from equipment datasheets and manufacturer information. The energy storage system was modeled off experimental data published by Cleary et al. [43]. The components were individually validated against manufacturer or published data to ensure proper implementation.

Performance comparison and validation of the ship model was achieved using experimental data collected from the Klitsa while in operation. A data acquisition system was installed onboard the ship to record the energy demands and typical load/velocity operating profiles. Using this data, three representative load profiles were created to simulate low, medium, and high output crossings. The engine speed and propeller

azimuth angle signals collected as part of the experiment, served as an open loop driver inputs for the model to recreate the real vessel crossing and actuation.

The performance comparison and model validation was done in two parts. The first set of simulations disabled the vessel dynamics model, and applied the experimental time series data for the ship velocity profile as a time-synchronized input. This allowed for a direct comparison of the model's performance in predicting propulsive loads, along with the other influencing subsystems.

In comparison to the experimental operational data, the simulation results were satisfactory but definitely requires some improvement to increase the fidelity. The PTO and linear damping characteristics of the mechanical power transmission system definitely require additional investigation to better define the dynamic loading characteristics, especially during transient conditions while maneuvering. It was found that when the ship's velocity profile was well represented, the propulsive loads were sufficiently accurate for high-level architectural design studies.

Upon incorporating the vessel dynamics into the simulation, each simulation exhibited a reduced acceleration and deceleration rate in comparison to the actual ship. This discrepancy immediately points to an over-estimate of the ship's inertial properties, though the surge damping characteristics, thrust deduction factor, and the 1-DOF motion may have also been contributing factors to the discrepancy.

The primary objective of this entire effort was to develop a simulation platform that can assess the performance of different propulsion system architectures in the context of energy consumption, and system efficiency. This study illustrated the effectiveness of this modeling and simulation process by investigating the power system conversion

efficiency associated with a battery-electric propulsion system. The energy consumption estimates and their relative error in comparison to experimental data are provided in Table 34. The experimentally determined consumption has been taken to be the correct value, and the relative error in energy consumption is expressed as,

$$\frac{abs(E_{exp} - E_{model})}{E_{exp}} \quad \textbf{(8-1)}$$

Using the revised damping model, the estimated energy consumption is within good agreement with the experimentally calculated values. This despite several simplifying assumptions, thereby proving the effectiveness of this approach for high level architectural analysis.

Table 34: Energy Consumption Results and Relative Error Against Experimental

Load Profile	Total Propulsive Motor Energy Consumption (kWh)								
	Experimental Data			Model Data (Linear Rotational Damping)			Model (Revised Damping)		
	In Transit	Man.	In Berth	In Transit	Man.	In Berth	In Transit	Man.	In Berth
LP1 (No Vessel Dyn.)	72.5	7.1	20.6	71.8	4.8	8.3	78.1	6.6	19.4
LP1 (Vessel Dyn.)	72.5	7.1	20.6	72.0	4.8	-	78.3	6.7	-
LP2 (No Vessel Dyn.)	108.4	4.6	15.6	100.5	2.6	6.2	100.8	3.9	14.5
LP2 (Vessel Dyn.)	108.4	4.6	15.6	101.1	2.6	-	101.5	3.9	-
LP3 (No Vessel Dyn.)	100.8	10.1	5.1	93.5	8.1	2.4	93.9	10.6	5.5
LP3 (Vessel Dyn.)	100.8	10.1	5.1	92.2	8.0	-	92.5	10.5	-

Load Profile	Relative Error - Energy Consumption					
	Model Data (Linear Rotational Damping)			Model (Revised Damping)		
	In Transit	Man.	In Berth	In Transit	Man.	In Berth
LP1 (No Vessel Dyn.)	0.9%	32.4%	59.7%	7.7%	6.5%	5.7%
LP1 (Vessel Dyn.)	0.6%	31.7%	-	8.0%	5.9%	-
LP2 (No Vessel Dyn.)	7.3%	43.3%	60.5%	7.0%	16.1%	7.2%
LP2 (Vessel Dyn.)	6.7%	43.0%	-	6.4%	15.8%	-
LP3 (No Vessel Dyn.)	7.3%	19.5%	53.1%	6.9%	5.6%	7.8%
LP3 (Vessel Dyn.)	8.6%	21.2%	-	8.2%	4.0%	-

The model results from the BEIPS simulation were plausible and provided an excellent illustration how this platform can be deployed. The battery system model, which was based on pack-level experimental data, performed very well; however, its performance above 90% SOC has some uncertainty because of the limited dataset provided by Cleary et al. [43]. Combined with the rapid-charge model, the results demonstrate that a battery-electric ship is technologically feasible for this application, though cost factors have not been considered in the analysis. With the ESS design assumptions, the longevity of the battery pack, with the deepest DoD of 20%, would likely exceed 30,000 cycles. This corresponds to approximately 5 years of operation at 18 crossing per day. More advanced degradation models can be incorporated in the future.

8.2 Summary of Recommendations

The modeling and validation approach presented in this work was an ambitious effort to assess the applicability of using model based design for advanced marine propulsion systems, in a manner that is similar to the development process used in the automotive industry. Though the initial results produced in this work have shown that this approach can be effective even with simplifying assumptions, there are numerous sources of error that need to be further investigation to determine what level of fidelity can actually be achieved with this framework.

The major limitation of this work is that the experimental results used for validation carry a significant amount of uncertainty due to the uncontrolled environment. Section 6.4 presented a detailed discussion of the experimental uncertainties, and highlighted the difficulty in quantifying the error found in the data. Without conducting an extensive set of experiments and sea trials with the ship, it is difficult to categorically validate the

simulation framework. The level of experimentation required to produce high quality validation data is unfeasible when the ship is in service, and is very difficult to arrange.

With that said, the data collected does provide some insight into problematic areas within the model. This section summarizes major areas for improvement and future study that will help reconcile the discrepancies observed in the simulation results. Given the tightly coupled interaction between sub-components, the process of increasing the model's fidelity might benefit from a sensitivity analysis. Further experimentation with the vessel is definitely recommended, as this would provide the most effective mechanism to identify the dominant sources of error. The following sub-sections present the immediate recommendations for increasing the model fidelity.

8.2.1 Additional Experimentation

Performing an additional set of more detailed experiments would provide the best means for confirming the model's parameterization and assumptions. The experimental setup developed in this work could mostly be reused; however, the ECM's computation of load should be replaced by a direct power measurement from strain gages and a rotational speed sensor. Similarly, the input shaft to the hydraulic pump should also be equipped to with a direct mechanical power measurement system to quantify the PTO's dynamic load characteristics. Ideally, a run-up/coast-down experiment would be conducted on the azimuthing propeller gearbox in dry-dock would help study the damping characteristics of the gearbox in detail, but this test is likely unfeasible.

A series of sea trials tests at a prescribed displacement would help parameterize the vessel dynamics model and the inertia model. A straight-line coast down experiment in calm seas would provide a meaningful set of data for investigating the surge damping

model. Similarly, pure-sway and pure-yaw experiments would provide a dataset for validating the maneuvering coefficients/model.

8.2.2 PTO and Rotational Damping model

A more accurate representation of the PTO hydraulic system is the first logical step in attempting to reconcile the load discrepancies seen in the simulation results. The PTO's loading characteristics and representative dynamics need to correlate to the physical system that it is driving, in this case it is the actuation of the azimuthing thrusters. Information on this system was requested of the manufacturer, but the pump characteristics and azimuth tower loading details could not be obtained. The power required to rotate the azimuthing tower at forward speed could be approximated using simple drag assumptions based on projected area of the tower/propeller as a function of azimuth angle. Equivalently, CFD could be utilized to provide more accurate results.

The rotational damping model developed in this work lumped the gearbox damping characteristics and the PTO into a single model. These effects need to be separated and studied individually. The lumped model assumed a constant 28kW loss as a minimum for the combined load, and a linear speed-dependent damping function was assumed when the linear loss relationship exceeded 28kW. This lumped model produced an under-estimate of damping at higher output, and an over-estimate at lower output indicating the real relationship is not well suited to the linear assumption.

The best course of action for quantifying gearbox losses and establishing an appropriate mathematical relationship is to first develop a good representation for the PTO system. Once this is established, the PTO and propeller loads can be subtracted from the experimental data collected to produce an estimate for the gearbox damping loads.

This residual dataset can then be used to investigate the mathematical relationship for gearbox damping. A survey of literature can perhaps provide additional insight into the expected behaviour and losses of right-angle drive gearboxes.

8.2.3 Refinement of Inertial Properties

The mass properties assumed for the ship can be conclusively deemed as over-estimates. A preliminary mass sensitivity study was performed to determine the impact of increased mass on the acceleration/deceleration rates from the model. This initial investigation showed that a more realistic estimate of mass did have a positive impact on reducing the simulation error, it will definitely not account for the entire discrepancy.

The interplay between the thrust deduction factor, wake fraction, propeller model, surge damping, and ship mass will simultaneously influence the simulation results. Wherever possible, these sub-components needs to be isolated and refined as best as possible to pinpoint the major source of error. Revising the mass properties is relatively low hanging fruit in that it's a simple parameter change that can be better estimated using historical passenger/vehicle logs from BC Ferries, provided that they can be obtained.

8.2.4 Vector Decomposition of GPS Speed Data

The raw GPS speed data was assumed to be entirely directed in the surge direction. This assumption is valid for in-transit operation, but may have introduced significant error when the ship is maneuvering into berth. The output from the heading sensor and GPS waypoints provide a method to decompose the reported ship velocity into surge, sway, and yaw components. This was not done initially because of problems with the signal output from the Maretron gyrocompass. The raw data is still available, and the issue can be resolved by accessing the Maretron configuration software then exporting

the data to a convenient format. This will process will also be very useful in the development of the auto-pilot model for full 6-DOF simulation.

8.2.5 Thrust Deduction Factor Parameterization

The thrust deduction factor model was a rather crude assumption based on experimental data and a simple parabolic mathematical relationship to account for its speed dependency. The parabolic assumption could be a major contributing factor to the slower acceleration and deceleration with the vessel dynamics model. Self-propelled CFD analysis would provide a means of resolving the actual thrust deduction factor as a function of forward speed. The initial efforts attempted were too ambition as they sought to resolve the rotating propeller along with motion of the ship using overset meshing. The number of cells produced by this approach was computationally unfeasible, and the analyses were abandoned. Instead, the self-propelled model should use an actuator disk to represent the propeller in order to simplify the analysis.

8.3 Concluding Remarks

The methodology for ship model development outlined in this work, and its illustration through a case study of the M.V. Klitsa, has proven to be an effective strategy for predicting high-level performance of the vessel in the design stage. The model developed definitely requires more development and refinement to improve accuracy before it could be used for detailed energy management control system development, or rigorous power system analysis. The ship model developed for the Klitsa can serve as an excellent starting point for future studies, and has laid the foundation for additional functionality including:

- Expansion to 6-DOF vessel motion to allow for free maneuvering
- Introduction of environmental forces
- Development of auto-pilot algorithms or course tracking routines

The implementation using the MSS toolbox allows for a great deal of additional functionality with its pre-built blocks to facilitate future development. This platform also has the ability to be linked to ProteusDS through a direct API software connection for in-depth integrated analysis of vessel motion with integrated propulsion system dynamics. As part of this work, the interfacing MEX code required to link Simulink and ProteusDS has already been developed. This co-simulation platform would be ideal for dynamic positioning, and low-speed maneuvering studies.

With further development and validation, this simulation platform will provide a high impact design tool for naval architects and marine system integrators to help reduce emissions, increase overall system efficiency, reduce OpEx, and enable intelligent propulsion system design.

Bibliography

1. *Diesel-Electric Power Plants*. MAN.
2. Hansen, J.F. and F. Wendt, *History and State of the Art in Commercial Electric Ship Propulsion, Integrated Power Systems, and Future Trends.* Proceedings of the IEEE, 2015. **103**(12): p. 2229-2242.
3. *Setting a Course for Carbon-Free Shipping*. 2015.
4. Woud, H.K. and D. Stapersma, *Design of Propulsion and Electric Power Generation Systems*. 2002: IMarEST, Institute of Marine Engineering, Science and Technology.
5. *Dynamometer Drive Schedules*. December 2, 2015]; Available from: http://www3.epa.gov/nvfel/testing/dynamometer.htm#vehcycles.
6. *Systems Engineering for Intelligent Transportation Systems*. Available from: http://ops.fhwa.dot.gov/publications/seitsguide/section3.htm.
7. Thongam, J.S., et al. *All-electric ships—A review of the present state of the art*. in *Ecological Vehicles and Renewable Energies (EVER), 2013 8th International Conference and Exhibition on*. 2013.
8. McCoy, T.J. and J.V. Amy. *The state-of-the-art of integrated electric power and propulsion systems and technologies on ships*. in *Electric Ship Technologies Symposium, 2009. ESTS 2009. IEEE*. 2009.
9. Tessarolo, A., et al. *Electric generation technologies for all-electric ships with Medium-Voltage DC power distribution systems*. in *Electric Ship Technologies Symposium (ESTS), 2013 IEEE*. 2013.
10. Zahedi, B., O.C. Nebb, and L.E. Norum. *An isolated bidirectional converter modeling for hybrid electric ship simulations*. in *Transportation Electrification Conference and Expo (ITEC), 2012 IEEE*. 2012.
11. Zahedi, B. and L.E. Norum, *Modeling and Simulation of All-Electric Ships With Low-Voltage DC Hybrid Power Systems.* Power Electronics, IEEE Transactions on, 2013. **28**(10): p. 4525-4537.
12. Zahedi, B., L.E. Norum, and K.B. Ludvigsen, *Optimized efficiency of all-electric ships by dc hybrid power systems.* Journal of power sources. **255**: p. 341-354.
13. Prempraneerach, P., et al., *Design of the All-Electric Ship: Focus on Integrated Power System Coupled to Hydrodynamics*. 2008, Massachusetts Institute of Technology. Sea Grant College Program.
14. Apsley, J.M., et al., *Propulsion Drive Models for Full Electric Marine Propulsion Systems.* Industry Applications, IEEE Transactions on, 2009. **45**(2): p. 676-684.
15. Ouroua, A., et al., *Modeling and simulation of electric ships' power system components and their interaction*, in *Proceedings of the 2007 Summer Computer Simulation Conference*. 2007, Society for Computer Simulation International: San Diego, California. p. 250-257.
16. Wei, J., et al. *Performance Prediction and Dynamic Simulation of Electric Ship Hybrid Power System*. in *Electric Ship Technologies Symposium, 2007. ESTS '07. IEEE*. 2007.
17. Jaster, T., *Modeling and Simulation of a Hybrid Electric Vessel*, in *Department of Mechanical Engineering*. 2013, University of Victoria.

18. Hansen, J.F., A.K. ådnanes, and T.I. Fossen, *Mathematical Modelling of Diesel-Electric Propulsion Systems for Marine Vessels.* Mathematical and Computer Modelling of Dynamical Systems, 2001. **7**(3): p. 323-355.
19. Ahmadi, R., H. Behjati, and M. Ferdowsi. *Dynamic modeling and stability analysis of an experimental test bench for electric-ship propulsion*. in *Electric Ship Technologies Symposium (ESTS), 2013 IEEE*. 2013.
20. Seenumani, G., *Real-time Power Management of Hybrid Power Systems in All Electric Ship Applications*, in *Mechanical Engineering*. 2010, University of Michigan.
21. Radan, D., *Integrated Control of Marine Electrical Power Systems*, in *Department of Marine Technology*. 2008, Norwegian University of Science and Technology.
22. Wei, W., et al. *Optimal Power Generation Scheduling of a Shipboard Power System*. in *Electric Ship Technologies Symposium, 2007. ESTS '07. IEEE*. 2007.
23. Husain, I., *Electric and Hybrid Vehicles: Design Fundamentals*. 2nd ed. 2011: CRC Press Taylor & Francis Group.
24. *Handbook of Automotive Power Electronics and Motor Drives*, ed. A. Emadi. 2005, Boca Raton: CRC Press Taylor & Francis Group.
25. Chung, I.-Y., et al., *Integration of a bi-directional DC–DC converter model into a real-time system simulation of a shipboard medium voltage DC system.* Electric Power Systems Research, 2011. **81**(4): p. 1051-1059.
26. Zahedi, B. and L.E. Norum. *Modeling, analysis and control of an isolated boost converter for system level studies*. in *Electrical Machines and Power Electronics and 2011 Electromotion Joint Conference (ACEMP), 2011 International Aegean Conference on*. 2011.
27. Yakushev, V., V. Meleshin, and S. Fraidlin. *Full-bridge isolated current fed converter with active clamp*. in *Applied Power Electronics Conference and Exposition, 1999. APEC '99. Fourteenth Annual*. 1999.
28. Prasanna, U.R. and A.K. Rathore, *Extended Range ZVS Active-Clamped Current-Fed Full-Bridge Isolated DC/DC Converter for Fuel Cell Applications: Analysis, Design, and Experimental Results.* Industrial Electronics, IEEE Transactions on, 2013. **60**(7): p. 2661-2672.
29. Chiniforoosh, S., et al., *Definitions and Applications of Dynamic Average Models for Analysis of Power Systems.* Power Delivery, IEEE Transactions on, 2010. **25**(4): p. 2655-2669.
30. Erickson, R.W., *Fundamentals of Power Electronics*. 1997: Chapman & Hall.
31. Rashid, M.H., *Power Electronics Handbook - Devices, Circuits, and Applications (3rd Edition)*. Elsevier.
32. Krause, P.C., et al., *Analysis of Electric Machinery and Drive Systems*. 3rd ed, ed. I.o.E.a.E.E. Inc. 2013, New Jersey: John Wiley & Sons Inc.
33. Krishnan, R., *Electric Motor Drives: Modeling, Analysis, and Control*. 2001: Prentice Hall Inc.
34. Chao, C., M. Mohr, and F. Diwoky, *Modeling of the System Levle Electric drive using Efficiency Maps Obtained by Simulation Methods.* SAE International, 2014.

35. Hassan, W. and W. Bingsen. *Efficiency optimization of PMSM based drive system*. in *Power Electronics and Motion Control Conference (IPEMC), 2012 7th International*. 2012.
36. Ahmed, A., *Maxium Torque Per Ampere (MTPA) Control for Permanent Magnet Synchronous Machine Drive System*. 2013, University of Akron.
37. Zheng, L. and L. Hongmei. *MTPA control of PMSM system considering saturation and cross-coupling*. in *Electrical Machines and Systems (ICEMS), 2012 15th International Conference on*. 2012.
38. Bierhoff, M.H. and F.W. Fuchs. *Semiconductor losses in voltage source and current source IGBT converters based on analytical derivation*. in *Power Electronics Specialists Conference, 2004. PESC 04. 2004 IEEE 35th Annual*. 2004.
39. Trzynadlowski, A.M. and S. Legowski, *Minimum-loss vector PWM strategy for three-phase inverters.* Power Electronics, IEEE Transactions on, 1994. **9**(1): p. 26-34.
40. Keliang, Z. and W. Danwei, *Relationship between space-vector modulation and three-phase carrier-based PWM: a comprehensive analysis [three-phase inverters]*. Industrial Electronics, IEEE Transactions on, 2002. **49**(1): p. 186-196.
41. Rahn, C.D. and C.-Y. Wang. 2012: Wiley.
42. Chen, M. and G.A. Rincon-Mora, *Accurate electrical battery model capable of predicting runtime and I-V performance.* IEEE transactions on energy conversion, 2006. **21**(2): p. 504-511.
43. Cleary, T., H. Kunte, and J. Kreibick, *Electrical and Thermal Modeling of a Large-Format Lithium Titanate Oxide Battery System*. 2015, Mineta Transportation Institute.
44. Stroe, D.I., et al. *Performance-degradation model for Li4Ti5O12-based battery cells used in wind power applications*. in *7th International Renewable Energy Storage Conference and Exhibition, IRES 2012*. 2012. Germany: EUROSOLAR.
45. Erdinc, O., B. Vural, and M. Uzunoglu. *A dynamic lithium-ion battery model considering the effects of temperature and capacity fading*. in *Clean Electrical Power, 2009 International Conference on*. 2009.
46. Huria, T., et al. *High fidelity electrical model with thermal dependence for characterization and simulation of high power lithium battery cells*. in *Electric Vehicle Conference (IEVC), 2012 IEEE International*. 2012.
47. Ahmed, R., et al., *Reduced-Order Electrochemical Model Parameters Identification and State of Charge Estimation for Healthy and Aged Li-Ion Batteries—Part II: Aged Battery Model and State of Charge Estimation.* Emerging and Selected Topics in Power Electronics, IEEE Journal of, 2014. **2**(3): p. 678-690.
48. Ahmed, R., et al., *Reduced-Order Electrochemical Model Parameters Identification and SOC Estimation for Healthy and Aged Li-Ion Batteries Part I: Parameterization Model Development for Healthy Batteries.* IEEE journal of emerging and selected topics in power electronics. **2**(3): p. 659-677.
49. Lin, S., H. Zhao, and A. Burke, *A First-Order Transient Response Model for Lithium-ion Batteries of Various Chemistries: Test Data and Model Validation* 2012, Institute of Transportation Studies.

50. Burke, A., M. Miller, and H. Zhao, *Fast Charging Tests (up to 6C) of Lithium Titanate Cells and Modules: Electrical and Thermal Response* 2012, Instititute of Transporation Studies.
51. Carlton, J., *Marine Propellers and Propulsion (3rd Edition)*. Elsevier.
52. Kerwin, J.E. and J.B. Hadler, *Principles of Naval Architecture Series - Propulsion*. Society of Naval Architects and Marine Engineers (SNAME).
53. Breslin, J.P. and P.A. Anderson, *Hydrodynamics of Ship Propellers* 1996: Cambridge University Press.
54. Epps, B.P., *OpenProp v2.4 Theory Document*. 2010, MIT Department of Mechanical Engineering.
55. Epps, B.P. and R.W. Kimball, *Unified Rotor Lifting Line Theory.* Journal of Ship Research, 2013. **57**(4): p. 1-21.
56. Yoerger, D.R., J.G. Cooke, and J.J.E. Slotine, *The influence of thruster dynamics on underwater vehicle behavior and their incorporation into control system design.* Oceanic Engineering, IEEE Journal of, 1990. **15**(3): p. 167-178.
57. Healey, A.J., et al., *Toward an improved understanding of thruster dynamics for underwater vehicles.* IEEE journal of oceanic engineering. **20**(4): p. 354-361.
58. Blanke, M., K.-P. Lindegaard, and T.I. Fossen, *Dynamic Model for Thrust Generation of Marine Propellers*. 2000.
59. Bachmayer, R., L.L. Whitcomb, and M.A. Grosenbaugh, *An accurate four-quadrant nonlinear dynamical model for marine thrusters: theory and experimental validation.* Oceanic Engineering, IEEE Journal of, 2000. **25**(1): p. 146-159.
60. Kim, J. and W.K. Chung, *Accurate and practical thruster modeling for underwater vehicles.* Ocean Engineering, 2006. **33**(5–6): p. 566-586.
61. Cummins, W.E., *The Impulse Response and Ship Motions*. 1962, David Taylor Model Basin.
62. Faltinsen, O.M., *Sea loads on ships and offshore structures*. Vol. 1. 1990, Cambridge;New York;: Cambridge University Press.
63. Fossen, T.I., *Handbook of marine craft hydrodynamics and motion control*. 2011: John Wiley & Sons, Ltd.
64. McTaggart, K., *Efficient Predictions of Wave-Induced Ship Motions for Ship Defence Models*. 2004, Defence Research and Development Canada - Atlantic.
65. McTaggart, K., *Hydrodynamic Forces and Motions in the Time Domain for an Unappended Ship Hull*. 2003, Defence Research and Development Canada.
66. Newman, J.N., *Marine hydrodynamics*. 1977, Cambridge, MA;London;: MIT Press.
67. McTaggart, K., *Three Dimensional Ship Hydrodynamic Coefficients Using the Zero Forward Speed Green Function*. 2002, Defence Research and Development - Atlantic.
68. Bertram, V., *Practical Ship Hyrdodynamics*, ed. V. Bertram. 2012, Oxford: Butterworth-Heinemann. 241-298.
69. Abkowitz, M.A., *Lectures on Ship Hyrdodynamics - Steering and Maneuverability*. 1964, Hydro- and Aerodynamic's Laboratory: Lyngby, Denmark.

70. Simonsen, C.D., et al., *Maneuvering Predicitions in the Early Design Phase using CFD Generated PMM Data*, in *29th Symposium on Naval Hydrodynamics*. 2012: Gothenburg, Sweden. p. 26-31.
71. Ross, A., *Nonlinear Manoeuvering Models for Ships: a Lagrangian Approach*, in *Department of Engineering Cybernetics*. 2008, Norwegian University of Science and Technology
72. McTaggart, K., *Simulation of Hydrodynamic Forces and Motions for a Freely Maneuvering Ship in a Seaway*. 2005, Defence Research and Development - Atlantic.
73. McTaggart, K., *Appendage and Viscous Forces for Ship Motions in Waves*. 2004, Defence Research and Development Canada - Atlantic.
74. Ikeda, Y., Y. Himeno, and N. Tanaka, *Ship Roll Damping - Frictional Component and Normal Pressure on Bilge Keel.* Journal of Kansai Society of Naval Architects, 1976. **161**.
75. Ikeda, Y., Y. Himeno, and N. Tanaka, *Components of Roll Damping of Ship at Foward Speed*. 1978, University of Osaka Prefecture.
76. Kato, H., *On the Frictional Resistance to the Roll of Ships.* Journal of the Society of Naval Architects of Japan, 1958. **102**.
77. Kato, H., *Effects of Bige Keels on the Roll Damping of Ships*. 1966, Memories of the Defence Academy, Japan.
78. Perez, T. and T.I. Fossen, *A Matlab Tool for Frequency-Domain Identification of Radiation-Force Models for Ships and Offshore Structures*. 2009, ARC Centre of Excellence for Complex Dynaimc Systems and Control. p. 1-22.
79. Pivano, L., *Thrust Estimation and Control of Marine Propellers in Four-Quadrant Operations*, in *Department of Engineering Cybernetics*. 2008, Norwegian University of Science and Technology: Trondheim.
80. Buchanan, A., *Characterization and Control of a Saab Seaeye Thruster*, in *Department of Mechanical Engineering*. 2015, University of Victoria.
81. Adnanes, A.K., *Maritime Electrical Installations and Diesel Electric Propulsion*. 2003, ABB AS Marine: Oslo.
82. Perez, T. and T.I. Fossen, *Time vs. Frequency-domain Indentification of Parametric Radiation Force Models for Marine Structures at Zero Speed.* Modeling, Identification, and Control, 2008. **29**(1): p. 1-19.
83. Nomoto, K., et al., *On the Steering Qualities of Ships.* Journal of Zosen Kiokai, 1956. **1956**(99): p. 75-82.
84. Fedyaevsky, K.K. and G.V. Sobolev, *Control and Stability in Ship Design*. 1963, State Union Shipbuildng House.
85. Norrbin, N.H. *Theory and Observation of on the Use of a Mathematical Model fo rShip Maneuvering in Deep and Confined Waters*. in *8th Symposium on Naval Hydrodynamics*. 1970. Pasadena, CA.
86. Larsson, L. and H.C. Raven, *Principles of Naval Architecture Series - Ship Resistance and Flow*. Society of Naval Architects and Marine Engineers (SNAME).
87. *Performance, Propulsion: 1978 ITTC Performance Prediction Method*. in *Iternational Towing Tank Conference*. 1978.
88. Hoerner, S.F., *Fluid Dynamic Drag*. 1965, Hartford House.

89. Taghipour, R., T. Perez, and T. Moan, *Hybrid frequency–time domain models for dynamic response analysis of marine structures.* Ocean Engineering, 2008. **35**(7): p. 685-705.
90. Damaren, C.J., *Time-domain Floating Body Dynamics by Rational Approximation* Ocean Engineering 2000. **27**: p. 687-705.
91. Kaasen, K.E. and K. Mo, *Efficient Time-Domain Model for Frequency-Dependent Added Mass and Damping*, in *ASME 2004 23rd International Conference on Offshore Mechanics and Arctic Engineering*. 2004, ASME: Vancouver. p. 885-891.
92. Rahimpour, M. and K. Andersen, *HRP CFD Simulation Results Spreadsheet*. 2015, University of Victoria.
93. Hu, Y., et al., *Electro-thermal battery model identification for automotive applications.* Journal of Power Sources, 2011. **196**(1): p. 449-457.
94. *MV Klitsa Trim and Stability Booklet*. 2011, STX Canada Marine.
95. [cited 2015; Available from: http://www.meds-sdmm.dfo-mpo.gc.ca/isdm-gdsi/waves-vagues/search-recherche/list-liste/data-donnees-eng.asp?medsid=C46134.
96. Rahimpour, M., *Klitsa Resistance CFD Results Spreadsheet*. 2015, University of Victoria.
97. Prescott, D., *Development and Implementation of Control System for an Advanced Multi-Regime Series-Parallel Plug-in Hybrid Electric Vehicle*, in *Department of Mechanical Engineering*. 2015, University of Victoria: Victoria, BC.
98. *EV Bi-Directional DC-DC Datasheet*. Advanced Power Electronics Corporation.
99. Park, E.-S., et al. *A soft-switching active-clamp scheme for isolated full-bridge boost converter*. IEEE.
100. *PatriciaBay_SaanichInletVENUSInstrumentPlatform_CurrentMeter_CurrentSpeedCalculated*. 2016, Ocean Networks Canada Data Archive.
101. *PatriciaBay_SaanichInletVENUSInstrumentPlatform_CurrentMeter_CurrentDirectionCalculated*, O.N.C.D. Archive, Editor. 2016.

Appendix A - Data Acquisition Experiment

This appendix presents the original design of experiment report and installation photos for the data acquisition study whose data was used to analyze and validate the modeling platform developed in this work. The data acquisition system was installed onboard the M.V. Klitsa during its refit in May 2015, and the full system was fully commissioned on June 27. Some minor changes were performed while the system was active in an attempt to improve performance and mitigate noise in the data. Data was collected from June 27, 2015 to September 8, 2015.

University of Victoria
Hybrid Marine Power Systems Research

Design of Data Acquisition Experiment

November 10th, 2014

Prepared By

Kevin Andersen EIT, B.Eng
Graduate Research Assistant
University of Victoria

Revision	D
Issued To	BC Ferries Services Inc.
Description	Issued for Review

Executive Summary

This document presents a comprehensive description and detailed integration plan for UVic's data acquisition (DAQ) system to be installed on the M.V. Klitsa. The DAQ will extract engines signals from the two J1587/J1708 communication buses that transmit information from the main diesel engines. Thruster position and status signals will be extracted from the HRP VDR serial bus, which uses the NMEA 0183 protocol. An electrical power sensor will be installed in the generator room to measure unbalanced three phase power on the AC bus. An external anemometer will provide a wind measurement for determination of wind loading, and finally, a GPS unit will provide position and velocity feedback.

The DAQ system will introduce an external and independent CAN communication bus that will be used for centralized data collection. This system is completely isolated from the shipboard systems and will operate autonomously from the onboard systems. The system has been designed such that UVic researchers do not need to be onsite, and in a manner that will not impact the crew's daily operations.

The integration plan comes as result of multiple collaborative discussions with the Klitsa's crew members, BCFS technicians, as well as technical representatives from Cullen Diesel, and ZF Marine. This document presents a thorough documentation of the proposed installation including the following,

- Specific tie-in points for the new instrumentation with reference to schematics
- Proposed locations for equipment
- Proposed cable routing plans
- Circuit diagrams and schematics

Deployment of the system will require the presence of a ticketed electrician for the power sensor installation. Connections to the HRP system serial bus will require supervision from one of BCFS's electrical system technician or a representative from ZF Marine. Commissioning of the individual system components shall be done on the M.V. Kuper at Deas Dock while the ship is out of service in November 2014. The Kuper has similar powertrain components to those onboard the Klitsa; therefore, this platform will provide a convenient test bench to validate the sensors in a low-risk environment.

UVic researchers ask for BCF to review this document to provide comments, feedback, as well as any suggestions for improvement of the system design.

Table of Contents

List of Tables and Figures

Introduction

UVic's Marine Hybrid Power Systems Research group is currently under contract with Transport Canada under the Clean Transportation Initiative to develop a set of modeling tools for the analysis of advanced marine propulsion systems. The objective of this project is to develop a time-domain modeling and simulation platform that is capable of accurately representing the ship motion, propulsion system, and integrated power system dynamics. This model-based approach to propulsion system development has seen wide success in hybrid and electric vehicles in the automotive industry. Despite its advantages in achieving true design optimization, model based design has not been as well established in the marine industry.

Traditionally, naval architects would design a ship based on a set of design requirements including specification of contract speed, seakeeping metrics, environmental conditions, etc. Designers would then seek to meet all these requirements through hull, powerplant, and propulsor selection. However, studies have shown that many ships don't operate at their original design point, often leading to poorer system efficiency. As a result, there is a growing need for a "mission cycle" oriented approach to propulsion analysis that can provide a true measure of system performance.

The present challenge is to develop a modeling tool that is capable of accurately predicting propulsive load for the hybrid power system. In order to create a relatively simple case to test the effectiveness of the tool for a ship both transit and maneuvering, a detailed data acquisition study of the BC Ferries M.V. Klitsa will be conducted and compared to the results of the modeling platform. The data acquisition (DAQ) will collect essential information from all power producing components on the ship including main propulsive loads and electrical generation. In addition, the DAQ system attempts to capture the oceanographic and environmental conditions for quantifying these external forces.

In order to validate the model, the DAQ will record the actuator position information from the azimuth propellers to assess the effectiveness of the model in predicting maneuvering behaviour. Lastly, GPS data will provide vessel speed and position data for validating output.

This document presents the integration and implementation details for the DAQ system to be installed on the M.V. Klitsa. Prior to deploying the full system, the individual interfacing components will be tested onboard the Kuper over the course of November 2014 while the ship is out of service. . The Kuper has a similar propulsion system components, so the DAQ equipment will be compatible with both vessels.

The plan outlined in this document comes as a result of collaboration with BC Ferries technicians and the Senior Engineer of the Klitsa. This document serves as UVic's proposed arrangement, but our group remains open to suggestions or alternate configurations that will meet the study requirements.

Objectives

The objective of this data acquisition study is to provide a validation test case for the hydrodynamic ship dynamics modeling platform being developed at UVic. One of the major challenges in naval architecture is developing an accurate representation of the variable propulsive loads that will be encountered on a vessel throughout its lifecycle. A plant model of a ship must be able to accurately quantify the time-domain loads for a given mission cycle and architecture. One of the core functionalities of this modeling platform is to generate a mechanism by which propulsive system loads can be extracted using vessel position and velocity data as inputs, as would be the case during the design phase.

Conversely, the tool can be deployed to evaluate performance through simulation of a specific propulsion architecture. One can then evaluate different propulsors, engines, and generators under various operating profiles and environmental conditions.

Given the functionality requirements of the hybrid propulsion modeling platform, this study seeks to collect the necessary data to validate the core functionalities of the tool. BC Ferries has provided the hull CAD file, design data, propeller performance curves, and sea trial that can be used to support the validation process through all stages. The objective of the data acquisition study is to collect a complete set of data which can serve as both the inputs and outputs for the ship model validation.

Using GPS information and the existing vessel architecture as inputs, the tool will be used to estimate the propulsive system load at the propeller shaft. This will then be compared to the output of the main diesel engines and will form the first validation check. Using the actuator thrust information as inputs (includes propeller speed, torque, and azimuth angle), the position, heading, vessel speed can be compared to that measured in the study. This will provide a measure of accuracy for the maneuvering model.

Data Acquisition System Overview

Conducting a data acquisition system on an operational vessel without a fully integrated communication bus network is extraordinarily challenging. The system must be non-invasive and take all necessary measures to ensure that the integrity of the onboard systems is maintained. Another complication arises in planning the routing of cables between sensors. The hull is divided into four watertight sealed compartments for safety. This implies that cable routing must be planned carefully to minimize, or ideally eliminate the need for compartment cable pass-throughs.

The physical parameters of interest for the data acquisition study are presented in Table 1. To minimize the amount of new equipment required, the goal is to access the existing serial buses wherever feasible. These buses broadcast many of the physical measurements needed for the study; however, it requires careful execution so as not to compromise the existing network. In some cases, new sensors have been installed for practicality. Information on the sensors can be found in the electronic folder included with this document.

The collection of all signals is done over a centralized CAN network that operates independently from the other serial buses. Data is collected and stored on the Cross Chasm C5 GPS data logger which has a removable flash storage card. To convert the serial bus data from the J1587/1708 and NMEA 0183

onboard communication buses, UVic's system will incorporate microprocessor based converter units to read the necessary signals and broadcast them over CAN. The schematic of the proposed system is illustrated in Figure 1.

Table 1: Required Measurements/Signals from Vessels

Description	Physical Parameter	Transducer Signal Source
GPS Data	Position (NED)	Cross Chasm GPS Logger
	Vessel Speed	Cross Chasm GPS Logger
Engine 1 Data	Engine Load	J1587/J1708 Serial Bus
	Engine Speed	J1587/J1708 Serial Bus
	Engine Torque	J1587/J1708 Serial Bus
	Throttle Demand	J1587/J1708 Serial Bus
Engine 2 Data	Engine Load	J1587/J1708 Serial Bus
	Engine Speed	J1587/J1708 Serial Bus
	Engine Torque	J1587/J1708 Serial Bus
	Throttle Demand	J1587/J1708 Serial Bus
Azimuth Propeller 1	Azimuth Angle Position	HRP VDR Serial Bus
	Thruster Position Reference	HRP VDR Serial Bus
Azimuth Propeller 2	Azimuth Angle Position	HRP VDR Serial Bus
	Thruster Position Reference	HRP VDR Serial Bus
Electrical Generator Output	Voltage 3-Phases	Veris H8043-0300-2 Power Sensor
	Current 3-Phases	Veris H8043-0300-2 Power Sensor
Wind Data	Wind Speed	Campbell Scientific 05103LK Wind Monitor
	Direction	Campbell Scientific 05103LK Wind Monitor

Two additional sensors will be introduced to the system for wind and electrical power sensing. A wind anemometer vane-style unit shall be mounted above deck in a suitable location with restricted access. This sensor will provide a measurement of wind and incident direction to allow for quantification of wind resistance. The Campbell Scientific 05103LK anemometer will be used which provides two 4-20mA signals for wind speed and direction, respectively, which are converted to a CAN message.

An external electrical power sensor will be introduced to provide a measure of the electrical load demand over time. This sensor uses a 3-phase measurement with 3 split-core current transformers and 3 voltage leads. Like the anemometer, its output is a 4-20mA analog signal. Because there are two onboard generators, the CT's and potential leads need to be installed on the AC bus rather than on a specific generator.

The DAQ system is to be configured to run autonomously such that it will not require any user input for initialization or terminating. The goal is to set the system to operate over 2-3 weeks to obtain a varied set of data which includes different driver patterns, and environmental conditions. UVic researchers may need to checkup on the system every couple days, which will arranged in advance with the engineer on shift. The general schematic for the data acquisition system showing the tie-in points to the onboard systems is provided in the proceeding sections. Though the initial testing and verification of the system will be conducted on the Kuper while it is out of service, this document will present integration details specific to the M.V. Klitsa.

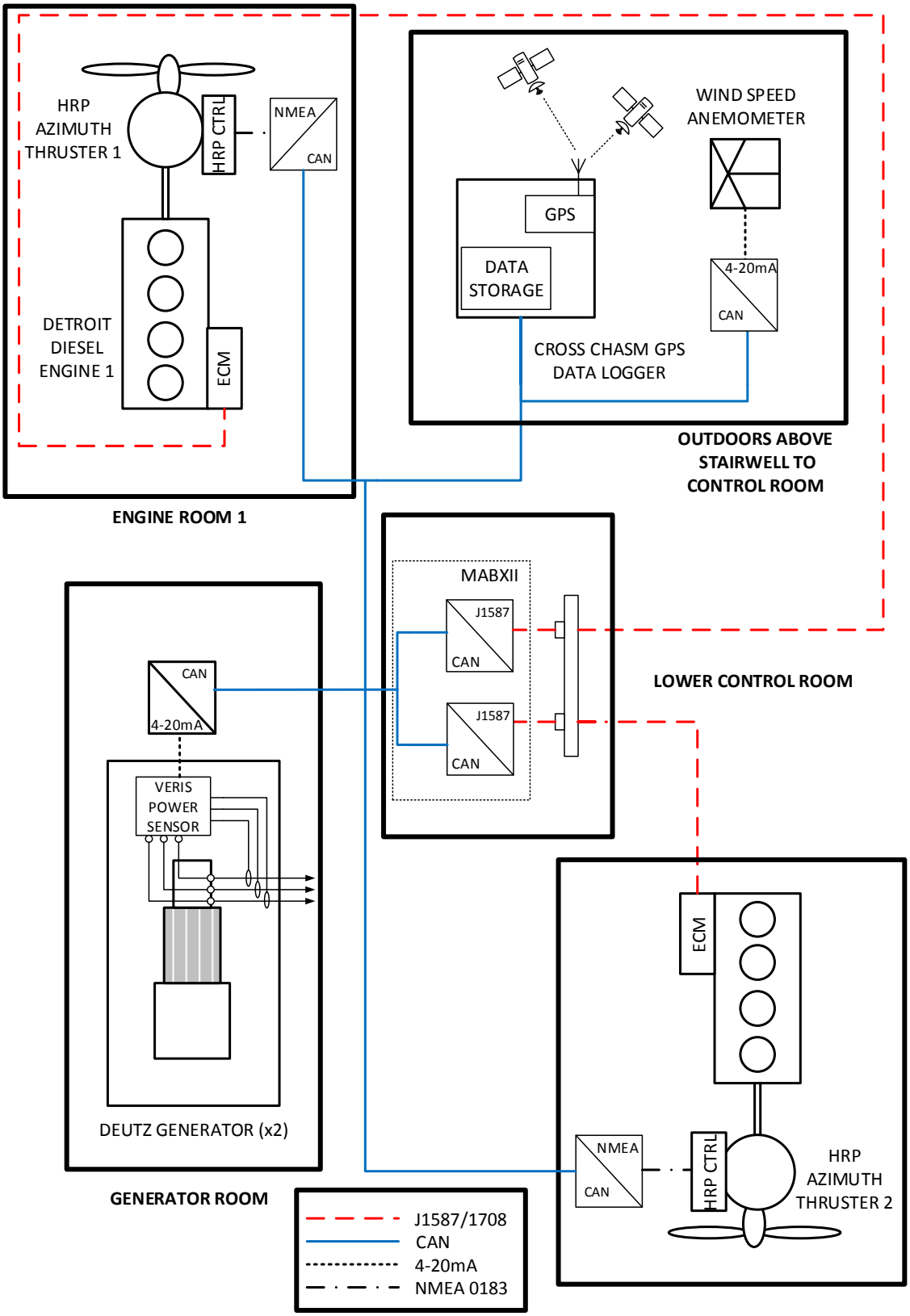

Figure 1: Schematic of the CAN Data Acquisition Network

Signal Collection and System Design

CAN Network Specifications

Because the locations of the sensors are separated by a fair distance, a CAN network was selected as the communication protocol for broadcasting measurements to enable centralized data collection. The CAN network has remarkable noise immunity and is conducive to long runs between nodes. The basic configuration parameters for the CAN network are shown below in Table 2. With 500kbps baud rate, the maximum cable length between nodes is 100m.

Table 2: CAN Configuration Parameters

Network	Baud Rate	Identifiers	Voltage Level
CAN_DAQ	500k	Standard	12V

Engine Signals

The engine signals are broadcast over a J1587/1708 communication bus throughout the vessel. This protocol consists of an identifier, referred to as a PID, which tells the listener what parameter is being reported. Information on PID signals can be found in the Detroit Diesel user's manual. For our purposes, we are interested in collecting four signals from this communication bus. This information is presented in Table 3. It also presents the signal mapping to a CAN message that will be collected.

Each engine will broadcast a single CAN message with the multiplexed sub-signals. The conversion from J1587/1708 to CAN is done in two stages. First, incoming message are converter to RS232 using an HDV100A3 serial converter by B&B Electronics. This information is then translated to CAN using the dSPACE MABXII controller.

Table 3: PID to CAN Message Mapping Specifications

Description	Physical Parameter	Source	J1587/1708 Signal Info				CAN Mapping				Signal Name
			PID	Rate (Hz)	Num. Bytes	Scaling	Msg. ID	Start Bit	Num. Bytes	Scaling	
Engine 1 Data	Engine Speed	J1587/J1708 Serial Bus	190	10	2	0.25 rpm/ Bit	0x100	0	2	0.25 rpm/Bit	Eng1_Speed
	Engine Load	J1587/J1708 Serial Bus	92	10	1	0.5%/ Bit	0x100	16	1	0.5%/ Bit	Eng1_Load
	Engine Torque	J1587/J1708 Serial Bus	93	1	1	20 ft-lb/ Bit	0x100	24	1	20 ft-lb/Bit	Eng1_Trq
	Percent Throttle	J1587/J1708 Serial Bus	91	10	1	0.4%/Bit	0x100	32	1	0.4%/Bit	Eng1_ Throt

Description	Physical Parameter	Source	J1587/1708 Signal Info				CAN Mapping				Signal Name
			PID	Rate (Hz)	Num. Bytes	Scaling	Msg. ID	Start Bit	Num. Bytes	Scaling	
Engine 2 Data	Engine Speed	J1587/J1708 Serial Bus	190	10	2	0.25 rpm/ Bit	0x101	0	2	0.25 rpm/ Bit	Eng2_Speed
	Engine Load	J1587/J1708 Serial Bus	92	10	1	0.5%/ Bit	0x101	16	1	0.5%/ Bit	Eng2_Load
	Engine Torque	J1587/J1708 Serial Bus	93	1	1	20 ft-lb/ Bit	0x101	24	1	20 ft-lb/ Bit	Eng2_Trq
	Percent Throttle	J1587/J1708 Serial Bus	91	10	1	0.4%/ Bit	0x101	32	1	0.4%/ Bit	Eng2_ Throt

HRP Thruster Signals

Though the primary purpose of the data acquisition study is to investigate the energy consumption, we also want to collect actuator data to be used for validation of the model. This information includes the reference and the actual thruster angle position signals, as well as the clutch status signal for determining periods of idling.

The HRP system has a VDR adapter which broadcasts real-time information about the thrusters over an NMEA 0183 serial bus. The configuration properties of this protocol are shown below in Table 4. This protocol allows for a single talker and multiple listeners on the bus. Our device will be a passive listener and will be physically incapable of transmitting information to the bus.

Care must be taken when tapping into the bus to avoid creating ground loops. The NMEA 0183 standard provides recommendations for isolation and protection circuitry to mitigate this risk. The VDR adapter appears to be located in the main HRP controller panel inside each engine room; therefore, this will be the location of the tie-in point. Our experimental apparatus has followed the standard's recommendations and incorporated full opto-isolation as will be seen later in this document.

Table 4: NMEA 0183 Serial Bus Specifications

Network	Baud Rate	Num. Data Bits	Stop Bits	Parity	Handshake	Physical Layer Voltage
HRP NMEA 0183	4800	8	1	None	None	+/- 15V

The thruster information is broadcast in a pseudo-sentence format whose structure is presented in Figure 2. Information is broadcast in ASCII format with sentences always beginning with '$' or 0x3F in hexadecimal. The data sets are delimited by ASCII commas ',' (0x2C). Once all the information is received a checksum is included for verification purposes.

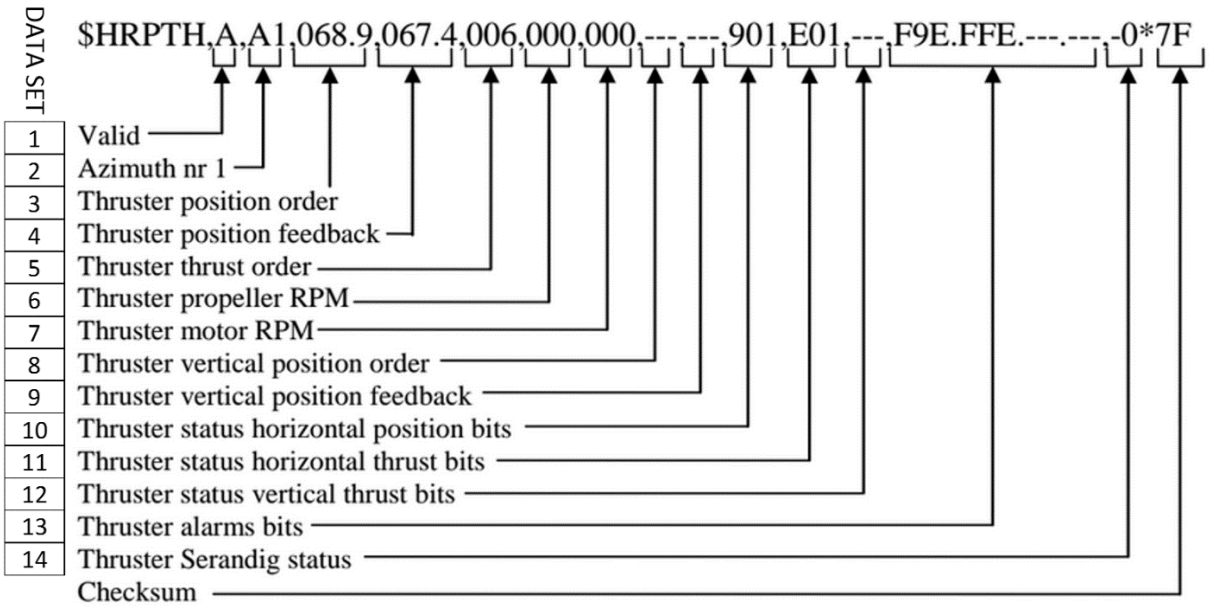

Figure 2: HRP Thruster Serial Sentence Format

This information needs to be read from the serial bus then converted to CAN as was done with the engine signals. Table 5 provides the CAN mapping and scaling properties for the thruster measurements. Because the HRP reports to the tenth decimal place, the angular measurement is multiplied by 10 for scaling to give a bitwise scaling of 0.1° per bit.

Table 5: HRP Thruster Signal Mapping Specifications

Description	Physical Parameter	Source	NMEA Message			CAN Mapping				Signal Name
			Data Field Position	Bytes	Bits	Msg. ID	Start Bit	Num. Bytes	Scaling	
Thruster 1 Data	Thruster Position Reference	HRP VDR NMEA 0183 Adapter	3	5	N/A	0x200	0	2	0.1°/ Bit	Thrst_Pos_Ref
	Thruster Position Actual	HRP VDR NMEA 0183 Adapter	4	5	N/A	0x200	16	2	0.1°/ Bit	Thrst_Pos_Act
	Thrust Order	HRP VDR NMEA 0183 Adapter	5	3	N/A	0x200	24	1	1%/ Bit	Thrst_Per
	Propeller RPM	HRP VDR NMEA 0183 Adapter	6	3	N/A	0x200	32	1	1%/ Bit	Prop_Spd
	Clutch Enabled	HRP VDR NMEA 0183 Adapter	11	1		0x200	40	1 Bit	Bool	Clutch_Ena

Description	Physical Parameter	Source	NMEA Msg			CAN Mapping				Signal Name
			Data Field Position	Bytes	Bits	Msg. ID	Start Bit	Num. Bytes	Scaling	
Thruster 2 Data	Thruster Position Reference	HRP VDR NMEA 0183 Adapter	3	5	N/A	0x201	0	2	0.1°/ Bit	Thrst_Pos_Ref
	Thruster Position Actual	HRP VDR NMEA 0183 Adapter	4	5	N/A	0x201	16	2	0.1°/ Bit	Thrst_Pos_Act
	Thrust Order	HRP VDR NMEA 0183 Adapter	5	3	N/A	0x201	24	1	1%/ Bit	Thrst_Per
	Propeller RPM	HRP VDR NMEA 0183 Adapter	6	3	N/A	0x201	32	1	1%/ Bit	Prop_Spd
	Clutch Enabled	HRP VDR NMEA 0183 Adapter	11	1		0x201	40	1 Bit	Bool	Clutch_Ena

Electrical Generation Signals

The 3-phase power measurement provides a 4-20mA output signal that needs to be mapped to CAN. The actual power output is given by the equation,

$$kW = 108.1 \times (mA_{out} - 4mA)/16$$

An Arduino microcontroller will be used to read this analog signal using a voltage measurement from an external load resistor. The Arduino is capable of reading a 0-5VDC analog input; therefore, the load resistor is chosen to provide 5V at 20mA. Therefore, $R_{Load,\ PS}$ is selected to be the closest value to 250 ohms.

The maximum and minimum measurements with respect to the input voltage are given by,

$$Maximum\ Measurement = \ 20mA \times \frac{5V}{20mA} = 5V$$

$$Minimum\ Measurement\ @4mA = \frac{0km}{h} \Rightarrow 4mA \times \frac{5V}{20mA} = 1V$$

The net scaling is,

$$Scale = \left(\frac{16mA}{5V - 1V} \times \frac{108.1kW}{16mA}\right) = 27.025\frac{kW}{V}$$

The measurement of power with respect to the input voltage then becomes,

$$Power\ Output = \left({}^{27.025\ km/h}/_{V} \times V_{in}\right) - 27.025 km/h$$

The Arduino platform uses a 10bit ADC converter which provides 1024 discretized values for the analog input signal which is good to 5V. Therefore, the resolution of the signal is given by,

$$ADC\ Resolution = \frac{5V}{1024} = 0.00488 \frac{V}{Bit}$$

$$Signal\ Resolution = \ 0.00488 \frac{V}{Bit} \times 27.025 \frac{kW}{V} = 132 \frac{W}{Bit}$$

The CAN scaling will reflect the resolution of the ADC on the Arduino. These scaling variable will be finalized once the circuit has been constructed; however, the CAN signal mapping is summarized below in Table 6.

Table 6: Power Sensor Signal Mapping Specifications

Description	Source	Tx Output		CAN Mapping				Signal Name
		Output Type	Output Scaling	CAN Msg. ID	Start Bit	Num. Bytes	CAN Msg. Scaling	
3-ϕ Unbalanced Measurement	Veris Transducer	Analog	4-20mA	0x300	0	10 bit	132 W/ Bit	Elec_Pwr_Act

Wind Anemometer Signals

Similar to the power sensor, the wind anemometer provides two 4-20mA outputs for the physical parameters representing wind speed and wind direction. Beginning with the wind speed measurement system, the wind speed is calculated using the following equation:

$$Wind\ Speed = \left(12.5\ {}^{km/h}/_{mA} \times mA_{out}\right) - 50 km/h$$

Here the scaling is 12.5km/h per milliamp of current. Again we want to structure the system such that the maximum sensor output reflects the full voltage of the analog input. The maximum and minimum measurement are then given by,

$$Maximum\ Measurement = \ 20mA \times \frac{5V}{20mA} = 5V$$

$$Minimum\ Measurement = 4mA \times \frac{5V}{20mA} = 1V$$

The physical measurement with respective to voltage is given by the scaling,

$$Scale = \left(\frac{16mA}{5V - 1V} \times \frac{12.5km/h}{mA}\right) = 50\frac{km/h}{V}$$

Therefore, the measurement with respect to ADC input voltage becomes,

$$Wind\ Speed = \left({}^{50\ km/h}/_{V} \times V_{in}\right) - 50km/h$$

The resolution of the ADC converter is the same as was presented in the power sensor; therefore, the total signal resolution for wind speed is,

$$Wind\ Speed\ Resolution = \ 0.00488\frac{V}{Bit} \times 50\frac{km/h}{V} = \frac{0.244km/h}{Bit} = \frac{0.68m/s}{Bit}$$

The wind heading measurement is provided by a rotary weather-vane style system that uses a linear potentiometer to determine angular position. The usable range for potentiometer is from 0° to 355°. There is a five degree direction dead-band where the measurement will be ambiguous, thus this band shall be placed in a direction with the least probable wind orientation. At first guess, the dead-band will sit perpendicular to the length of the ship pointing towards the centre.

The wind direction measurement is given by,

$$Wind\ Direction = \left(22.5\ {}^{degrees}/_{mA} \times mA_{out}\right) - 90\ degrees$$

Again designing the system to provide maximum rated voltage at full sensor output, the maximum and minimum measurements are 5

$$Maximum\ Measurement = \ 20mA \times \frac{5V}{20mA} = 5V$$

$$Minimum\ Measurement = 4mA \times \frac{5V}{20mA} = 1V$$

The physical measurement with respective to voltage is given by the scaling,

$$Scale = \left(\frac{16mA}{5V - 1V} \times \frac{22.5degrees}{mA}\right) = 90\frac{degrees}{V}$$

The wind direction measurement with respect to ADC input voltage is given by,

$$Wind\ Direction = \left(90\ {}^{degrees}/_{V} \times V_{in}\right) - 90\ degrees$$

Finally, the resolution can be determined as was done previously using,

$$Wind\ Speed\ Resolution = \ 0.00488\frac{V}{Bit} \times 90\frac{degrees}{V} = \frac{0.439degrees}{Bit}$$

The CAN message mapping and specification for these signals are provided below in Table 7.

Table 7: Anemometer Signal Mapping Specifications

Description	Source	Tx Output		CAN Mapping				Signal Name
		Output Type	Output Scaling	CAN Msg. ID	Start Bit	Num. Bytes	CAN Msg. Scaling	
Wind Speed Measurement	Anemometer	Analog	4-20mA	0x400	0	10 bit	0.068 ms^{-1} /Bit	Wind_Spd_Act
Wind Direction Measurement	Anemometer	Analog	4-20mA	0x400	10	10 bit	0.44°/ Bit	Wind_Dir_Act

GPS Data Signals

The GPS data is logged automatically by direct configuration of the Cross Chasm unit. The configuration has been set to log the information as presented in Table 8. There is no CAN message associated with the GPS unit as this is computed internally by the Cross Chasm using which also performs the data logging. GPS signal will be validated with output from the ship's GPS system.

Table 8: GPS Configuration Specifications

Description	Source	Logging Frequency (Hz)
Position	Cross Chasm GPS Logger	2
Velocity	Cross Chasm GPS Logger	2

Message Transmission Rates

The data logger is configured to store all of the CAN messages on the bus; therefore, the amount of data transmitted on the bus must be investigated so as not exceed the electronic data storage. The proposed data transmission rates for the CAN messages are shown in Table 9.

Table 9: CAN Message Transmission Frequency and Storage Requirements

Description	Message Name	CAN Msg. ID	Num. Bytes	Rate (Hz)	Identifier Bits	Total Bytes Per Second to Record
Engine 1 Data	Eng1_Signals	0x100	5	10	2	70
Engine 2 Data	Eng2_Signals	0x101	5	10	2	70
Thruster 1 Data	Thrust1_Signals	0x200	7	10	2	90
Thruster 2 Data	Thrust2_Signals	0x201	7	10	2	90
Electrical Data	ElecPower_Signals	0x300	2	10	2	40
Wind Data	Wind_Signals	0x400	3	10	2	50
Total Bytes Per Second for Data Logger						410

The 11bit CAN identifiers will be logged with the data such that it can be deciphered by the dbc file; therefore, an additional 2 bytes worth of data will be stored with each message containing the message ID. The total number of bytes to be recorded per second is 410. Assuming 12 hours of operation per day, the amount of data to be stored, not including the GPS data is given by,

$$12\frac{hr}{day} \times \frac{3600s}{hr} \times 410\frac{Bytes}{s} \times \frac{1GB}{1 \times 10^9 Bytes} = 0.017712\frac{GB}{day}$$

This is a relatively small amount of data that can easily be handled by the logger's internal 500MB flash card. This implies that our group should not have to be onsite every day to extract data. For signals being converted from onboard serial communication buses, the data transmission rates are equivalent to their original broadcast frequency.

CAN System Configuration and Grounding

CAN networks can be configured in star or a chain arrangement. While both systems are acceptable topologies, the chain structure explicitly defines physical ends to the bus making it simple to locate bus termination points. Terminating resistors are required at the physical ends to prevent signal reflections.

The proposed layout of the CAN nodes for this study is also very conducive to the chain arrangement as it will provide opportunities for cable routing efficiency. A schematic of the configuration is provided in Figure 3. The interconnecting cables shall be a 2-conductor, 24AWG shielded twisted pair. The shielding of the CAN cables will be single-end grounded to prevent noise.

Multiple DC power supplies will be used to power the Arduino microcontrollers and the MicroAutoBoxII. To ensure that the CAN voltage levels are all referenced to a common potential, a second grounding cable will connect the negative terminals of each power supply. The same 2-conductor shielded cable used in the CAN network will be used for simplicity, though shielding termination may not be required.

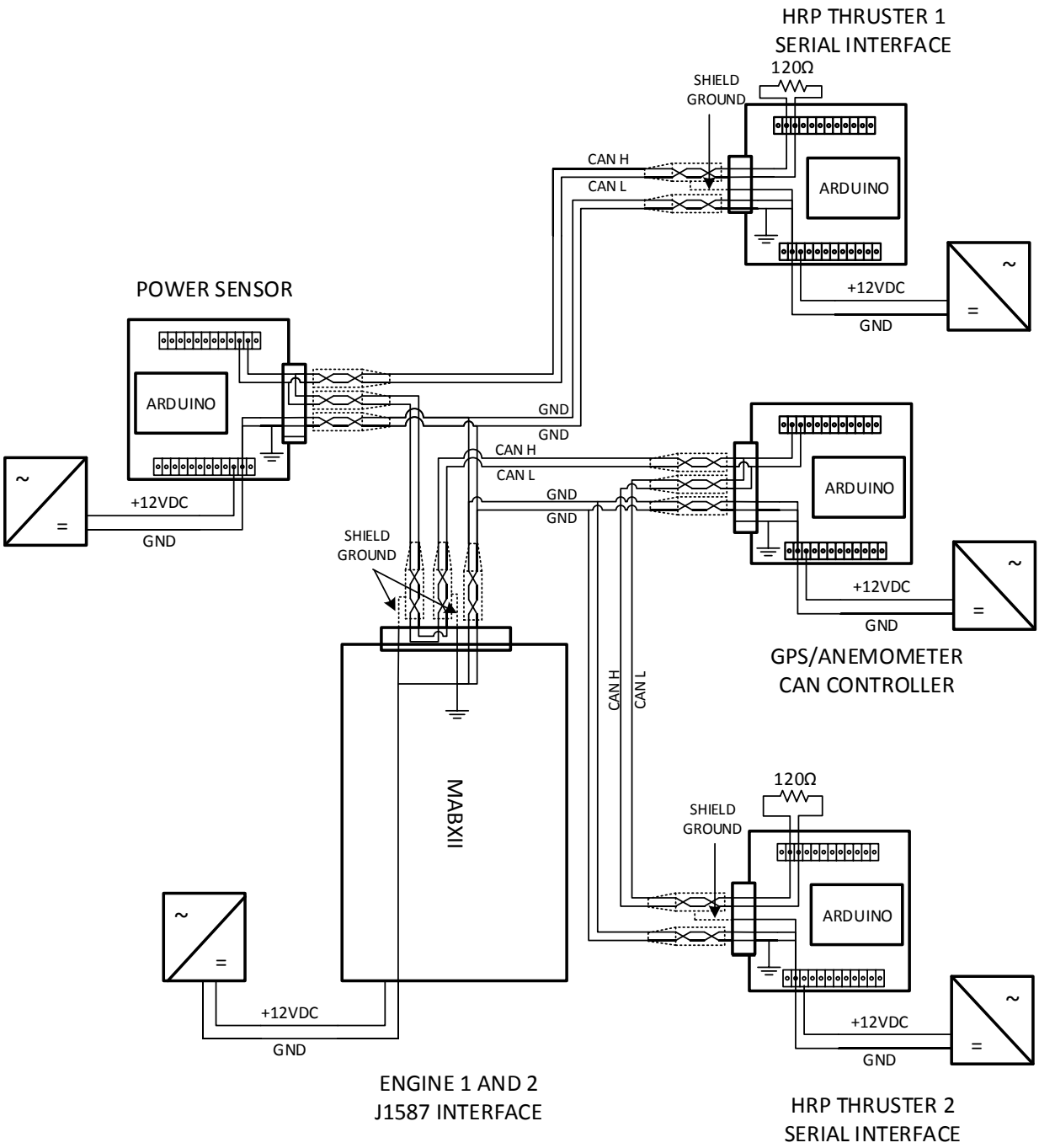

Figure 3: CAN Network Configuration, Schematic and Grounding Diagram

Automated Start/Stop Logging

In order to conserve disk space and capture only the sensor information while the ship is running, it is highly desirable that the data acquisition system have an automated hardware triggering signal. The nodes of the CAN bus can be configured to begin transmitting after a specific message has been received. Therefore, one of the controllers must have provisions to sense a digital hardware pin from either the HRP thruster system or from the engine's ECU.

One possible way to do this is to sense the voltage on the "Start Interlock" contactor provided by the HRP system as shown in Figure 4. When this voltage level is logic high, then the system is stopped and available for starting. When the logic is low, the engine is operating. After reviewing the HRP schematic, we have not been able to determine where this terminal is located inside the main HRP controller unit inside the engine room. This will require guidance from BC Ferries' technicians to locate a suitable hardware pin for this automated start/stop process.

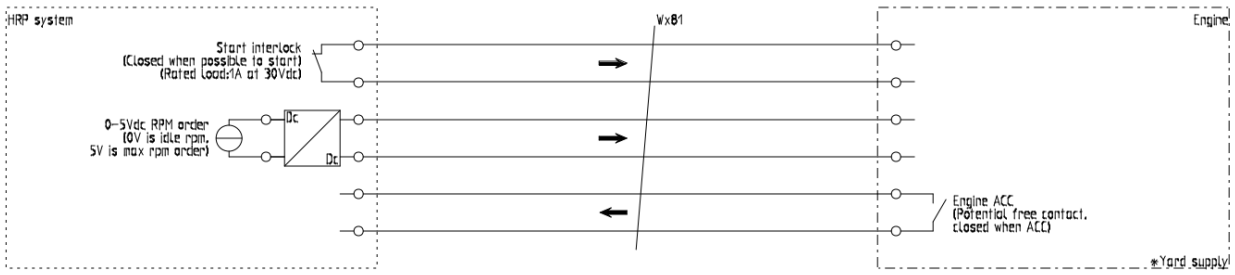

Figure 4: Potential Hardware Tie-In for Automated Start of DAQ System

Integration Plan

Engine Signal Acquisition

The engine signal acquisition will take place in the control room located underneath the main vehicle deck. Signals from engines 1 and 2 are broadcast over J1587/1708 throughout the vessel, and two diagnostics ports provide a convenient place to tap into the serial bus. The location of the two diagnostics ports in the control room are shown in Figure 5.

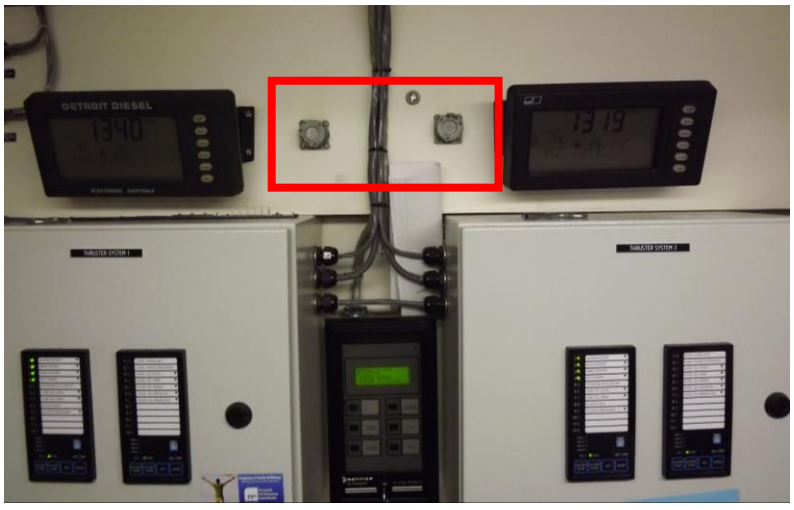

Figure 5: Diagnostics Ports in Underdeck Control Room

The connection to the bus is made via a 6 Pin Deutsch connection converter which interfaces with an HDV100A3 J1587/1708 to RS232 converter. The RS232 stream is then fed into the dSPACE MicroAutoBoxII controller for processing of the data and conversion to CAN. This system as already been verified on the Klitsa and did not cause any problems with ground loops.

The individual system requires an external 12V power supply to operate the MicroAutoBoxII. The HDV100A3 is fully isolated; therefore the incoming RS232 signal ground will be referenced connected to the ground of MABX. A schematic of the system is provided in Figure 6.

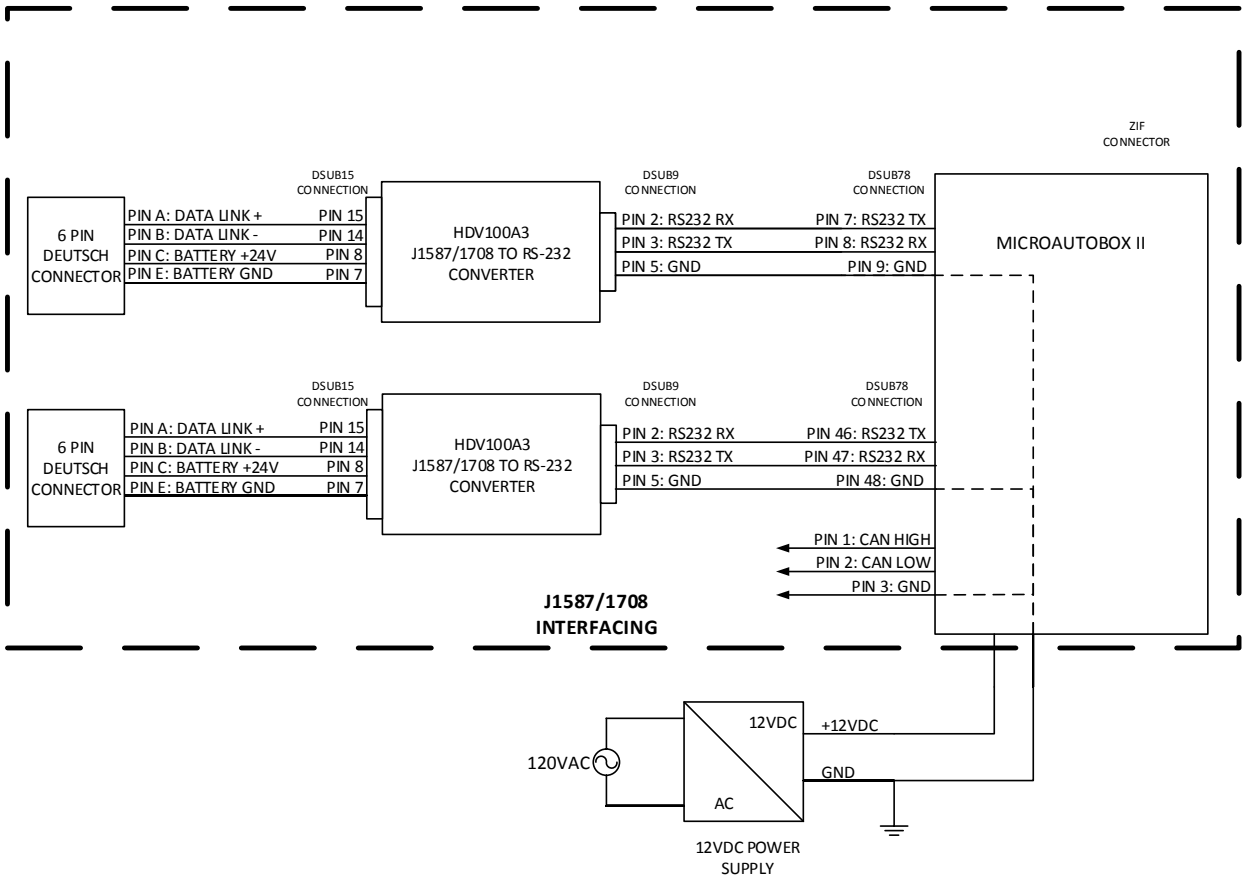

Figure 6: J1587/1708 Tie-In and Converter Schematic

The MABXII and power supply are fairly bulky, and the engineers onboard the Klitsa have asked that it not reside in the control room if at all possible. As such, the system components shall be installed outside of the control room on the adjacent work bench. A plan view of the proposed arrangement is depicted Figure 7. An image of the work area and the proposed location of the measurement equipment are provided in Figure 8. Finally, the routing path for bringing the cable outside of the control room and around to the workbench is shown in Figure 9. The cables supported by small adhesive plastic wiring hangers and zap straps for quick installation and removal.

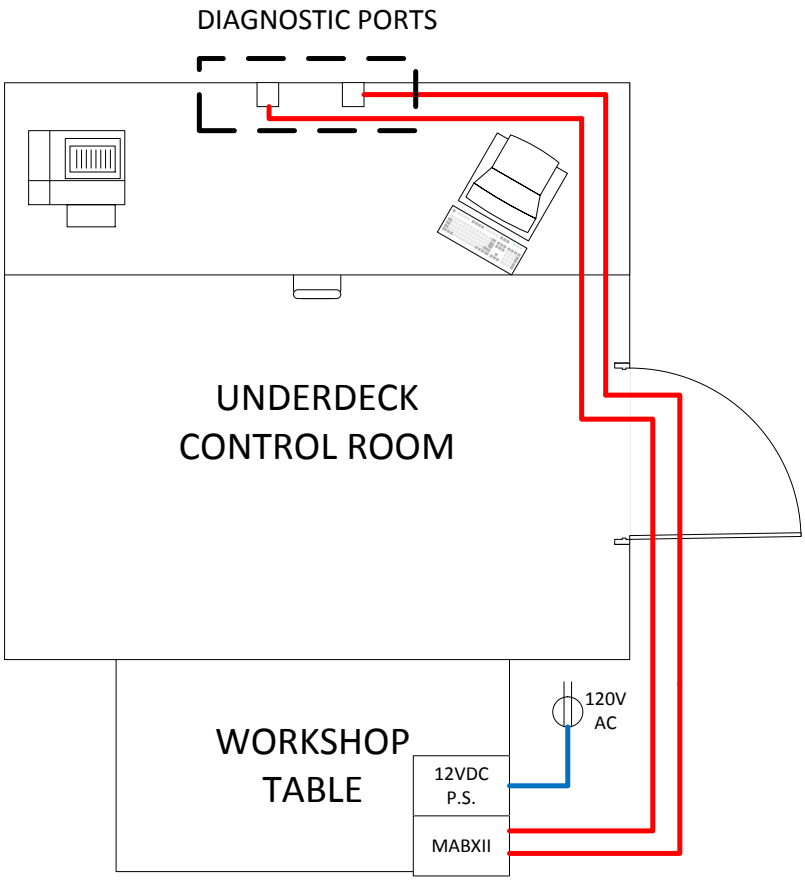

Figure 7: Plan View of Proposed Wire Routing from Diagnostics Ports

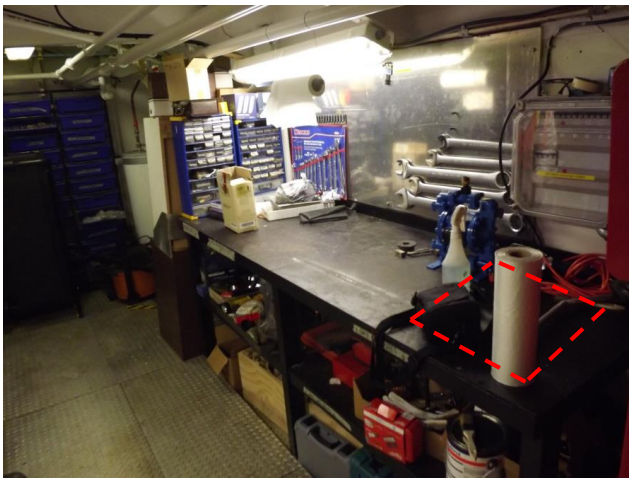

Figure 8: Image of Workbench Showing Proposed Location of MABXII and Power Supply

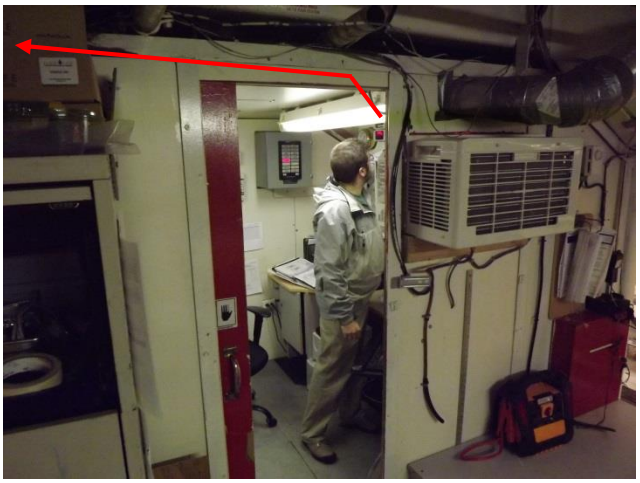

Figure 9: Image Illustrating Cable Routing from Diagnostics Port in Control Room Towards Workbench Area

HRP Signal Acquisition

The HRP signal acquisition will require a convenient tie-in point to the serial bus. The only location that provides relatively simple access to the leads is at the VDR communication modules located inside the main HRP thruster controller residing in the engine rooms. A schematic of the communication wiring is provided below in Figure 10. The NMEA 0183 serial signals are found on pin J2-5 and J2-6 respectively. This will form the tie-in point for the data acquisition system. Shielded twisted pair cable will be used to connect the DAQ microcontroller with the communication unit; therefore, the shielding will be co-terminated at the terminal J2-12. The shielding will be connected using a suitable solder sleeve terminator to ensure a proper 360 degree connection that will minimize the chance of noise leakage.

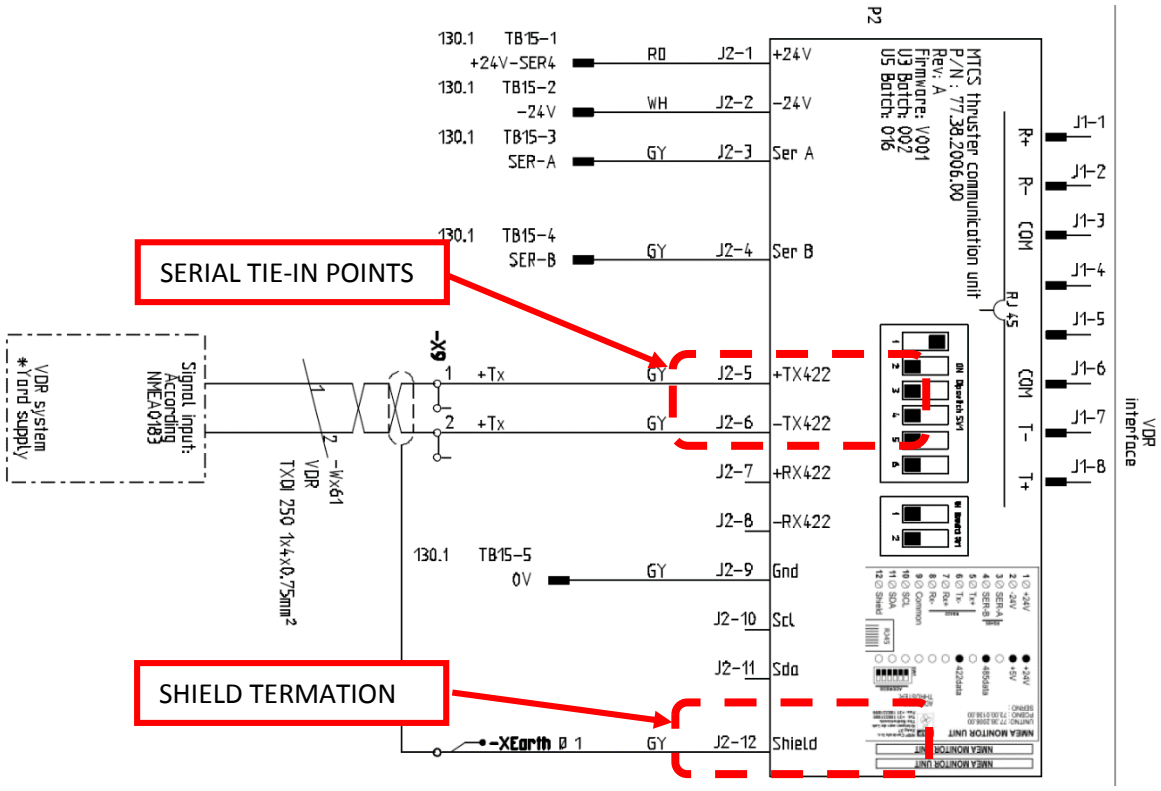

Figure 10: VDR Communication Unit Schematic Showing Tie-In Point

The NMEA 0183 standard provides two example circuits for isolation and protection of the communication bus. It also states that the listener should not draw more than 2mA. These recommendations ensure that the introduction of listeners will not cause ground loops nor cause faults on the bus.

Figure 11 shows the proposed schematic for the NMEA to CAN converter. The circuitry will be constructed on protoboard which will be fully enclosed with the Arduino microcontroller. These hardware enclosures will be mounted within each of the main HRP thruster controllers for thrusters 1 and 2 respectively as illustrated in Figure 12. The microcontroller requires a 12V power supply. To keep the footprint as small as possible, an LM7812 DC/DC converter has been introduced to use the internal 24VDC power supply in the HRP controller rather than introduce an external power supply. This integrated circuit will provide a 12V regulated voltage.

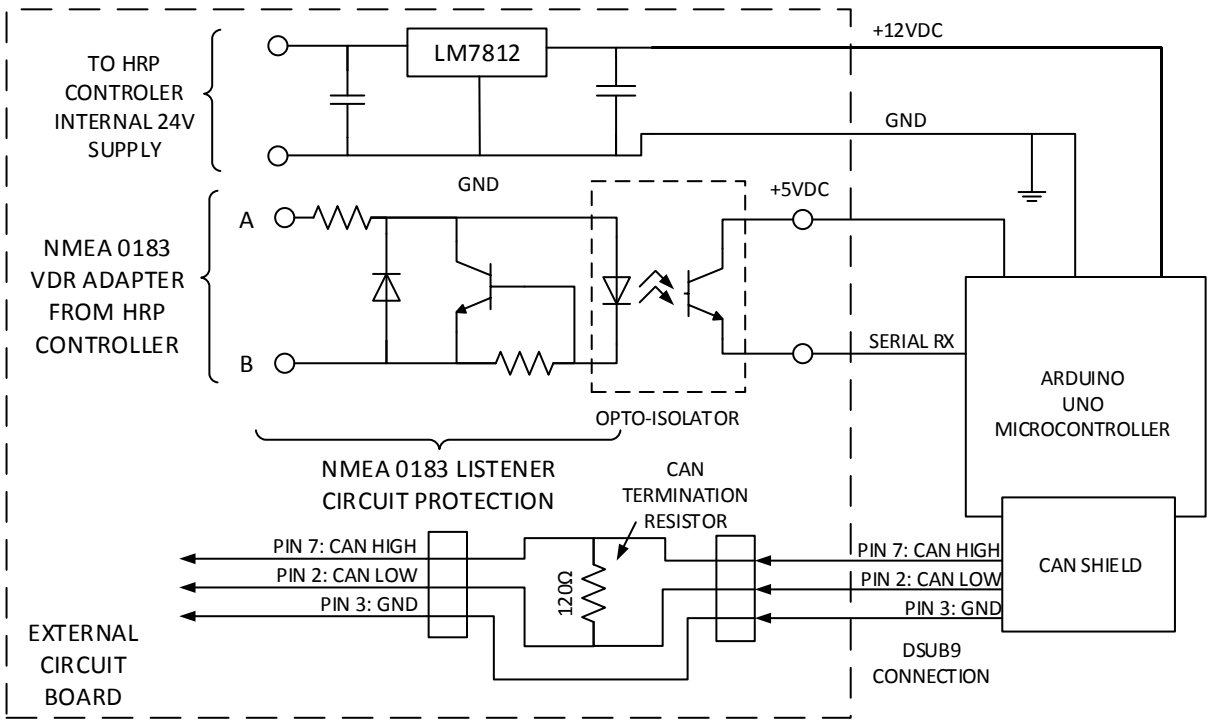

Figure 11: Schematic for DAQ to Read NMEA 0183 and Converter to CAN

Because these controllers will be on the physical ends of the CAN bus, 120ohm terminating resistors will be required at the CAN interface of these converters.

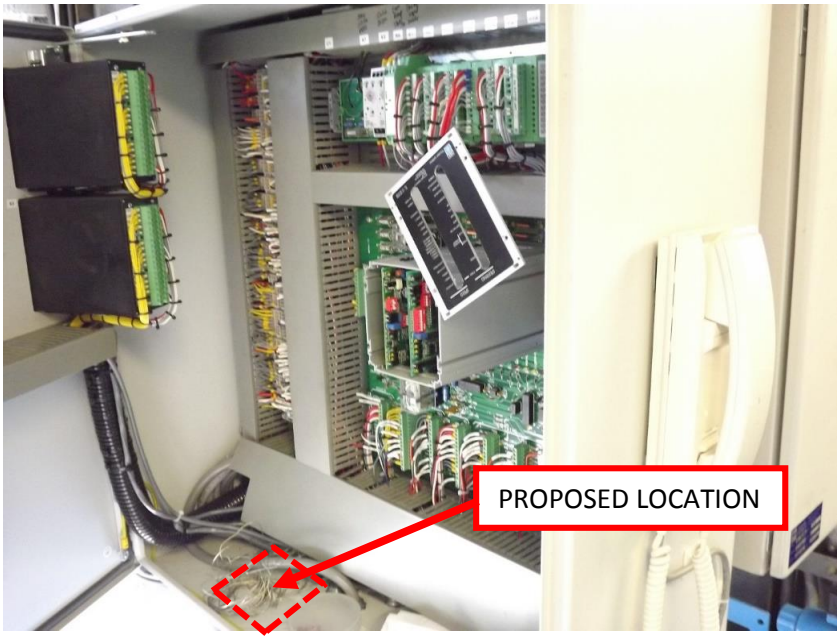

Figure 12: Image Showing the Internals of the HRP Controller and Proposed Mounting Location of DAQ Hardware

Electrical Sensors

The electrical power transducer measures the 3-phase power unbalanced power delivered by the generator. It consists of 3 current transformers (CTs) and 3 terminal voltage leads that need to be installed on the AC bus. An excerpt of the Klitsa's single line electrical diagram is provided in Figure 13 which illustrates the desired insertion point of the power sensor. Since we are only interested in the onboard generation, we don't need to capture the shore power when the vessel is not in operation.

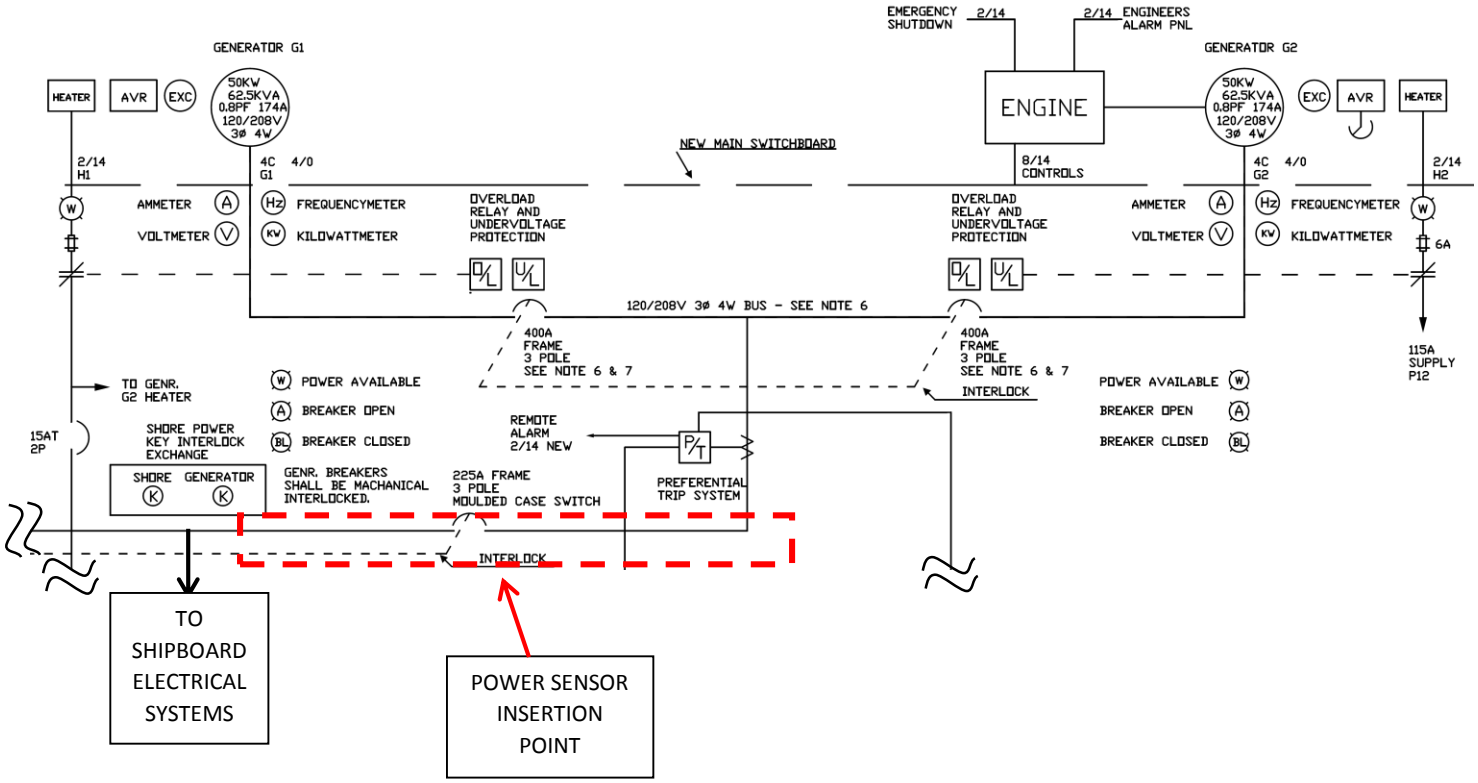

Figure 13: Excerpt from M.V. Klitsa's Electrical Single Line Diagram Showing Insertion Point of Power Sensor

An image of the proposed insertion point for both the CTs and voltage leads is shown in Figure 14. Here, another CT will be added to each of the phase cables that are marked with red, black and blue. Two sets of CTs already exist for each phase cable. The new CTs are split core, and don't require that the cable be removed from the power distribution terminal block; however, the voltage leads will need to a direct connection to the line voltages. This will require the assistance of a certified electrician to perform the installation.

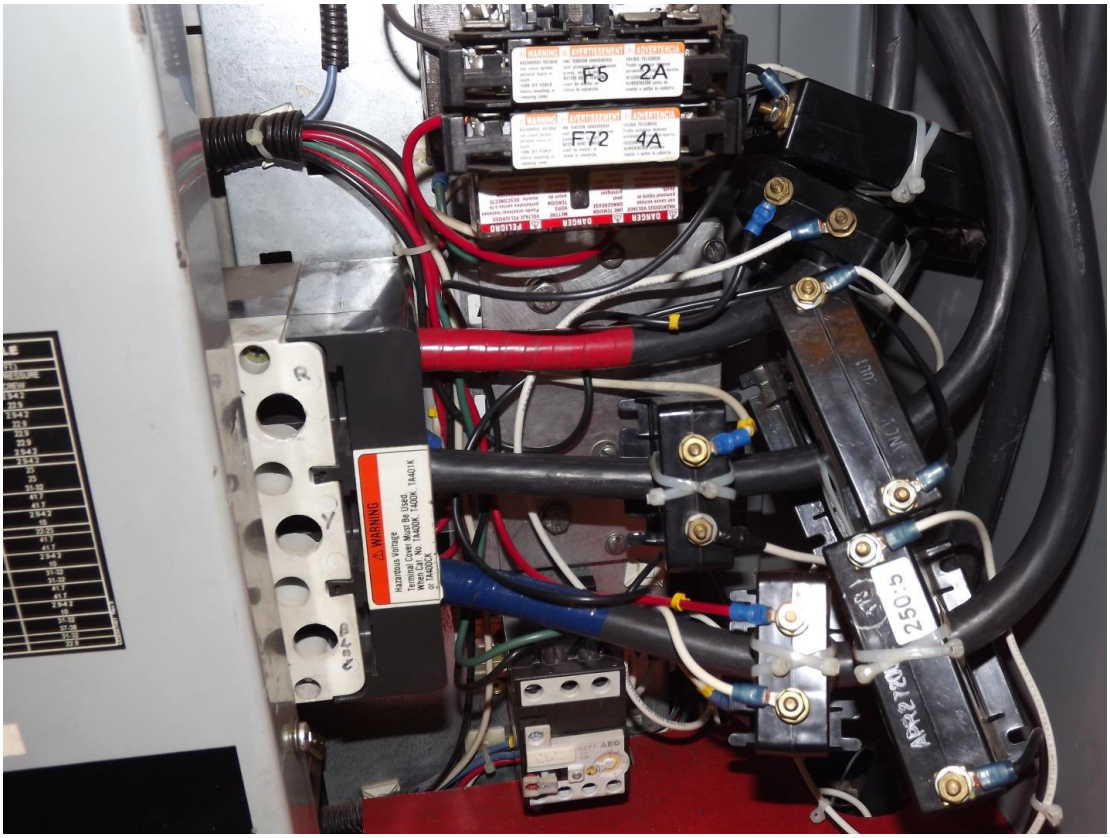

Figure 14: Proposed Insertion Point for the Power Sensor

The power sensor is very compact and doesn't require mounting of a central processing unit. The installation of the sensor is illustrated in Figure 15. However, UVic's analog-to-CAN signal converter will require a small space claim within the electrical panel.

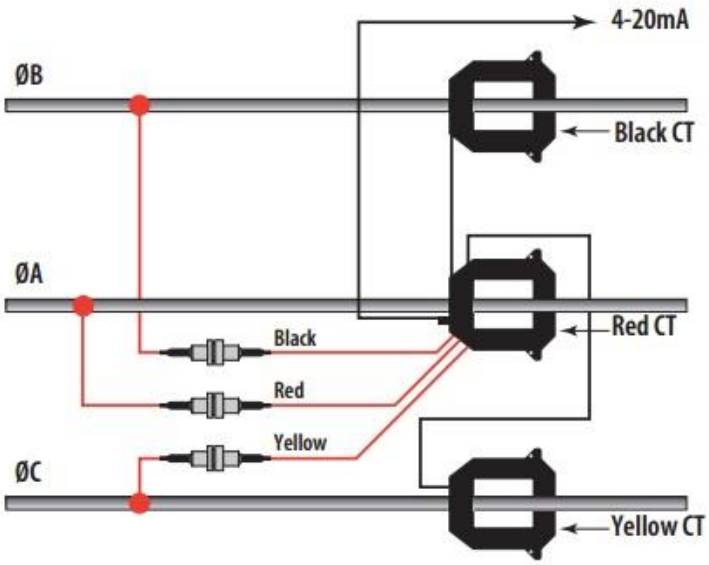

Figure 15: Installation of Veris H8043-300-2 Power Sensor with 4-20mA Output

The microcontroller will be enclosed in a sealed box with an external Delphi 10 pin female connector with the pin-out illustrated in Figure 16. DC power is supplied by an AC/DC DIN Rail mounted power supply that will also require mounting inside the electrical panel. The AC source will be taken from a line-to-line single phase of the generator from the same connection point as the transducer's voltage leads. The overall connection schematic is presented in Figure 16.

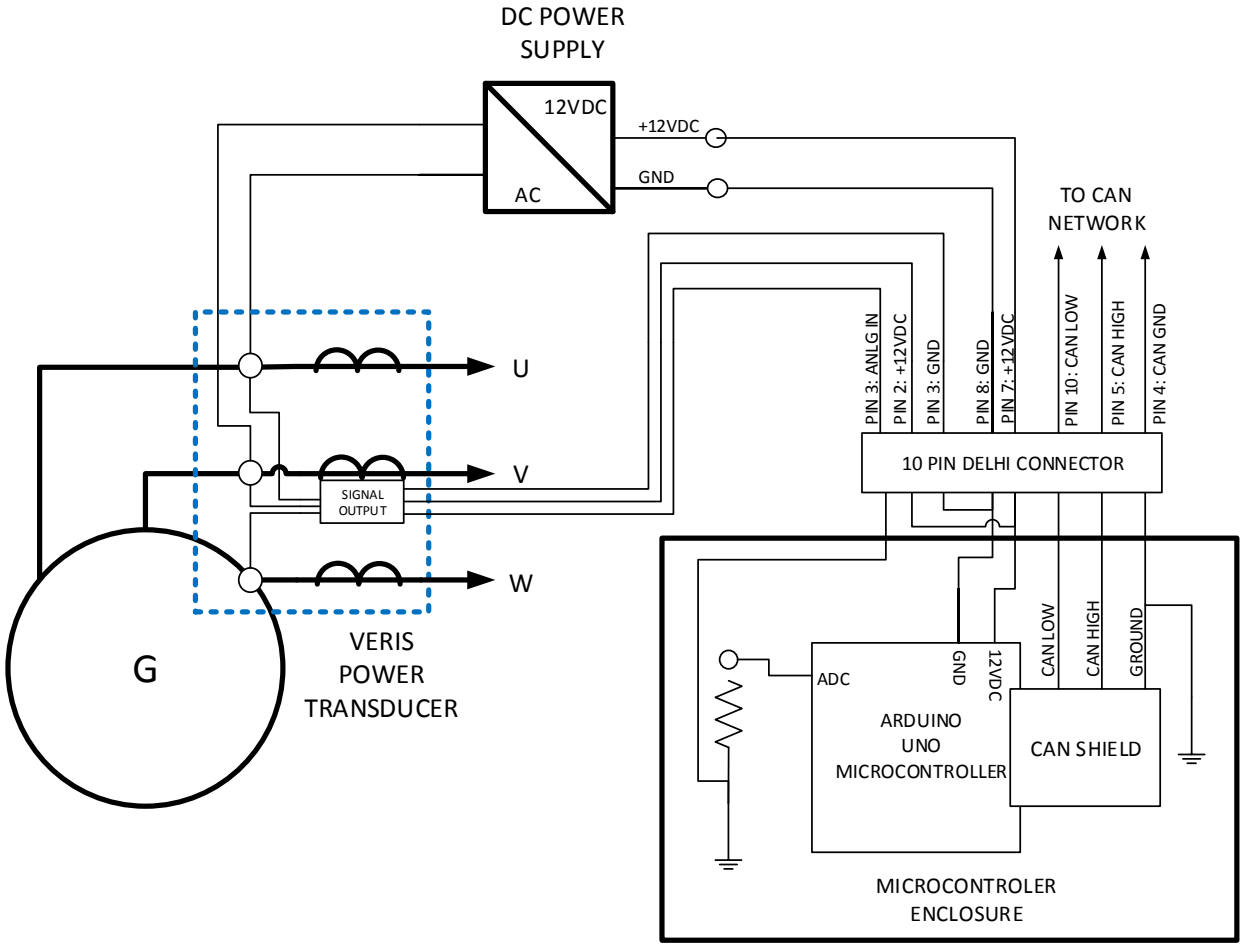

Figure 16: Electrical Power Sensor Integration Schematic

Wind Anemometer and GPS System

The GPS and wind anemometer form the final two components that require integration. For convenience, these two items shall be located in the same outdoor area. This will reduce the amount of equipment required and the number of cable runs on the ship. These two sensors are the only two sensors that don't derive their signals from onboard systems.

The primary challenge in integrating these items is in locating a suitable outdoor location that has access to 120VAC power and has provisions to make a cable indoor/outdoor pass through. Only a single CAN

cable is required for two instruments, and all of their electronics and circuitry shall be fully enclosed within a watertight enclosure to be mounted outdoors.

The GPS system consists of two components: an antenna and a controller. The controller is located insider the enclosure. The antenna is a small puck with an adhesive bonding agent for mounting a structure. The puck is easily removed using a scraper is needed.

The anemometer shall be located on a pole which will be strapped to a structure onboard the ship. A hand rail will provide a suitable mounting point. The proposed location for the anemometer is shown in Figure 17. This area is a restricted access area, which eliminates the possibility of tampering with the instrumentation. It is also tucked away in an area that shouldn't have any impact on the crew's normal activities.

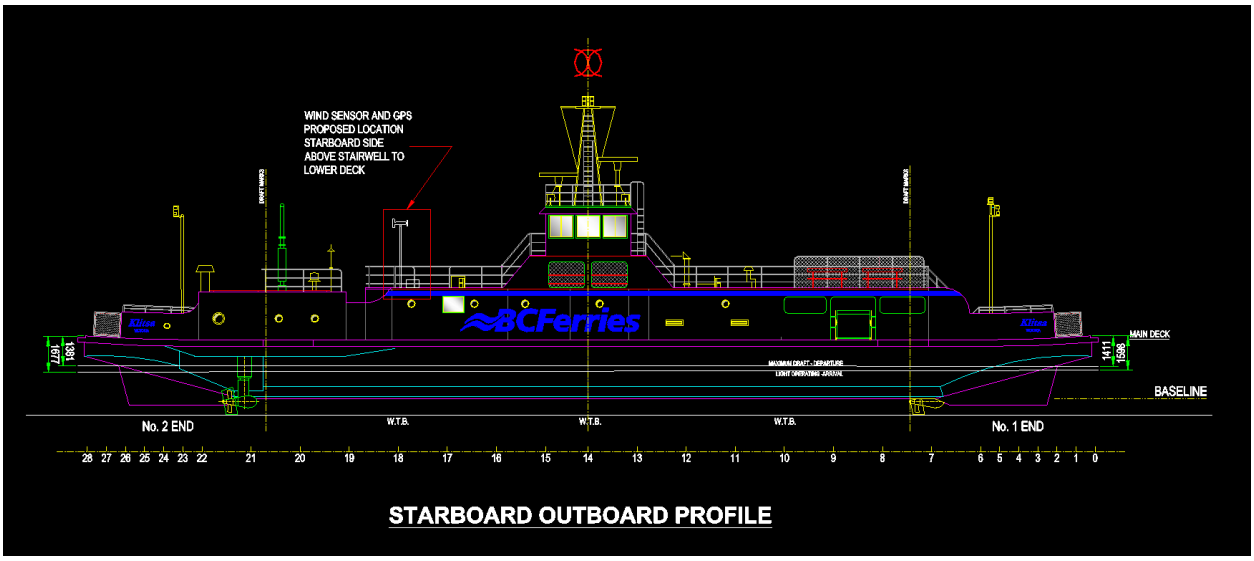

Figure 17: Proposed Locations of Wind Anemometer and GPS System

The combined electrical schematic is given in Figure 18. External load resistors for the two 4-20mA signals shall be contained within the enclosure, as well as a DIN Rail mounted DC power supply.

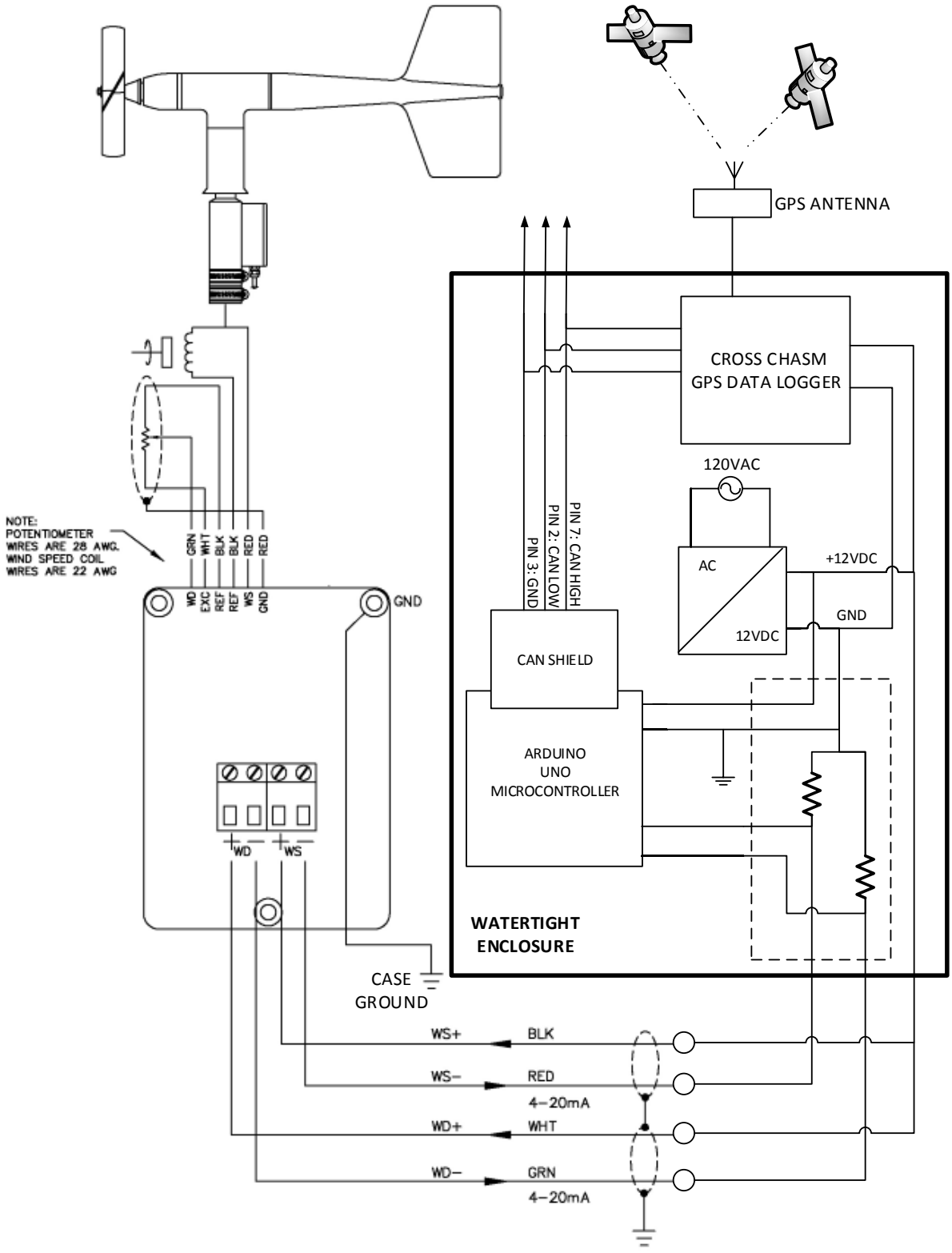

Figure 18: GPS and Wind Sensor Electrical Schematic

CAN Network Cable Routing and Grounding

To physically connect the CAN nodes, it will be necessary to introduce external cables onboard the ship. This is one of the primary challenges that UVic researchers have encountered in developing this plan. The goal is to introduce these cables in such a way that it will not impact crew operations, nor passenger amenities.

The ship's hull is divided into four sealed compartments. Though these compartments do have provisions for cable pass-throughs, utilizing these passage ways would require a re-sealing procedure that is highly undesirable. Therefore, the proposed wire routing herein attempts to avoid crossing sealed compartments underdeck. The design of the data acquisition system attempted to keep as much instrumentation in the compartment containing the underdeck control room. Wherever possible, the wiring is run underdeck to minimize the chance of cable damage.

The preliminary wire routing plan is presented in Figure 19. This illustration shows the desired pass-through locations and provides the most desirable routing from our perspective. To minimize the risk of crushing the cable on the main vehicle deck, UVic researchers would like to route cable outdoors on the upper deck. Outdoor cable routing has been assumed to be the most practical approach whenever the cable must cross sealed hull compartments. The cable can be tucked along the base of handrails and secured so that it does not pose any tripping hazards.

The images of the proposed outdoor wiring are shown in Figure 20 and Figure 21. An image of the proposed cable path to pass through the lower deck to the main vehicle deck is shown in Figure 22. Existing cable pass-throughs for the generator room to the lower deck is presented in Figure 23.

Note it may be more convenient to run the cable underdeck from the GPS/Anemometer to the Engine Room 2; however, it is currently unknown whether that would require a cable pass through across a sealed compartment. Because of the daisy-chain style arrangement of the CAN network combined with the outdoor location of the GPS/Anemometer, it makes more physical sense to make the final run outdoors provided that a suitable pass-through can be supplied into the engine room from the roof.

Our group will require the guidance of the onboard engineers and technicians to provide input on the best possible routing paths. This is probably the most logistically difficult portion of the data acquisition experiment, so we are completely open to alternate wiring configurations provided that they meet our requirements.

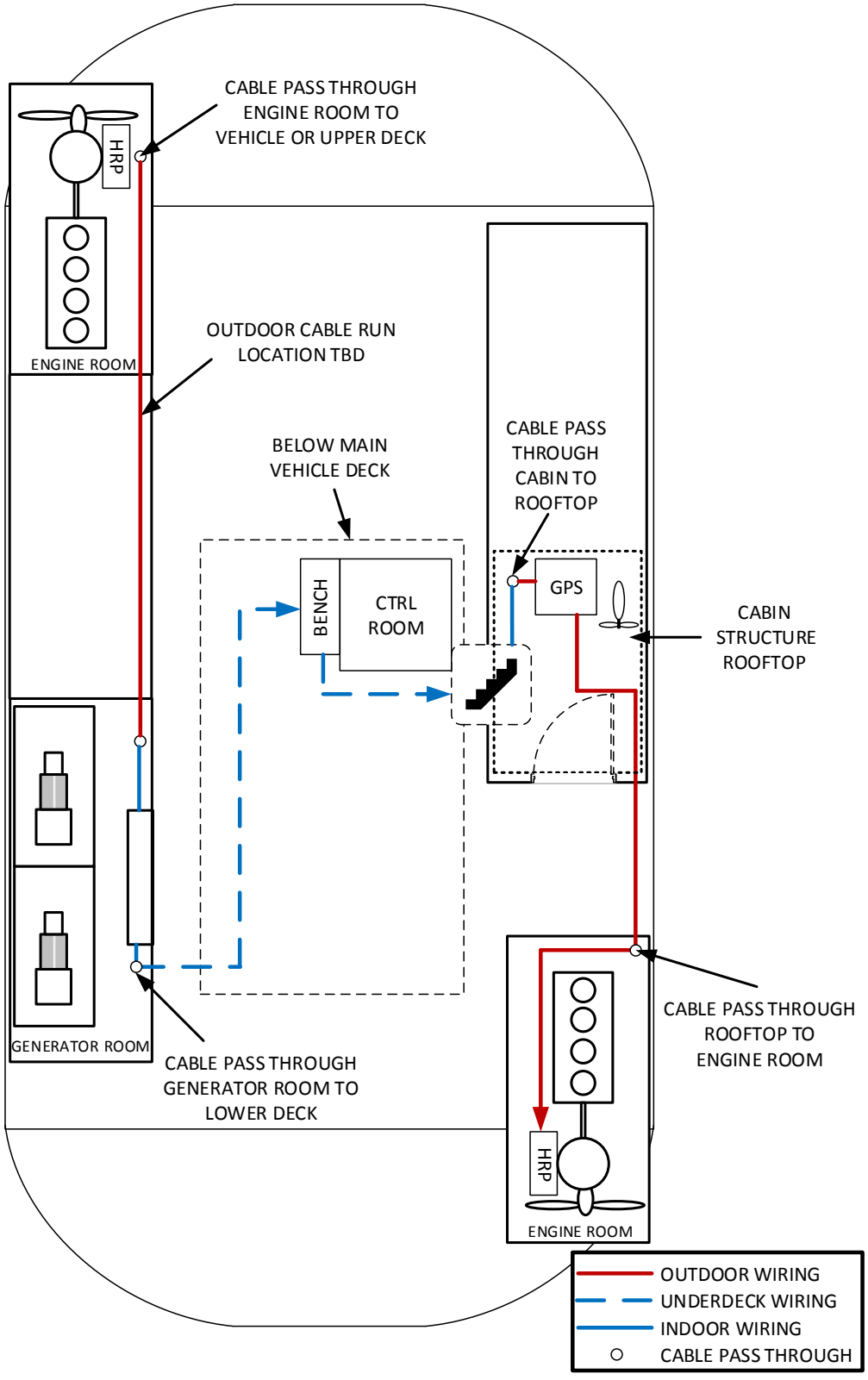

Figure 19: Proposed Wiring Diagram for CAN Network

Figure 20: Proposed Outdoor Wiring Route between Engine Room 1 and Generator Room

Figure 21: Proposed Outdoor Wiring Route between Lower Deck Stairwell, GPS Location, and Engine Room 2

Figure 22: Cable Routing Up Stairwell from Lower Deck Heading Towards Cabin Rooftop

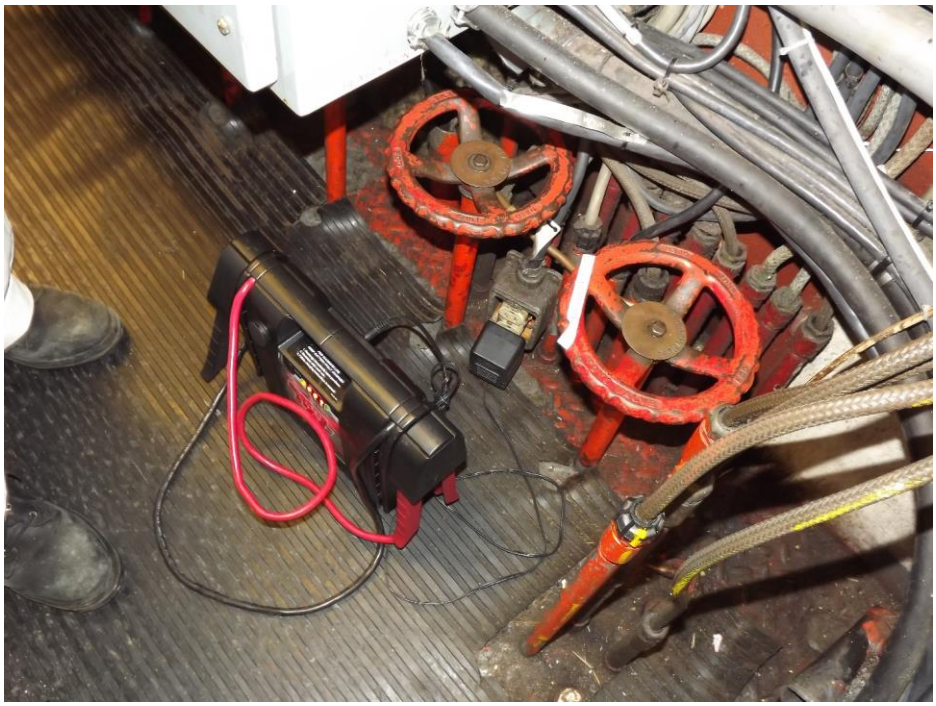

Figure 23: Generator Room to Lower Deck Cable Pass-Throughs

BC Ferries Installation Support

UVic's research group will require various levels of support from BC Ferries throughout the planning and execution of the study. The integration plan presented in the in previous sections sought to resolve the majority of the installation details from studying the schematics; however, there are still some unanswered questions regarding tie-in points and cable routing which will require further consultation with onboard crew as well as the BC Ferries technicians. This will need to be done onsite after this document has been reviewed.

The installation of the entire system shall be performed over the course of two days. The following sections provide a high level description of the activities to be completed on each day. The goal is to perform as much of the installation during normal work hours; however, some afterhours work will be required when the connections to the serial bus are made while the ship is not in operation.

Day 1

On the first day, the team will arrive at first sailing and begin routing of the cables that will connect the CAN nodes. This will be done with the help of the crew's engineer who will provide both guidance and assistance for the cable routing, and identifying suitable pass-throughs. The team will likely need to access restricted areas of the ship, but the goal is to have no impact on the sailing schedule and the crew's daily operations.

The anemometer and the GPS system will be mounted and installed over the course of the day. During the mid-day layover, the team will make the cable pass-throughs from the electrical room down to the lower deck. Furthermore, a certified electrician shall be onsite to perform the installation of a power sensor, which shouldn't take more than 15 minutes. The duration of the day will be spent completing the underdeck wiring. The J1587/1708 connections has already demonstrated that it poses no threat to the integrity of the system, so it will be completed on Day 1.

Day 2

In the morning of Day 2, all remaining wiring shall be finalized, installed, and secured. The team will spend the morning verifying connections, testing the CAN communication, and checking the instrumentation prior to being hooked up. A BC Ferries technician shall arrive onsite after the final sailing is complete. The team will then work with the technician to make all necessary communication bus and electrical connections for the HRP thrusters and hardware enable pin for the automated start. An engineer will also be required on the ship to assist in this process, and verify that the ship's functionality remains intact after the installation. With sufficient planning, this process should be completed within two hours.

System Removal

Once the DAQ system has collected all of the necessary data, the instrumentation will be removed in a single day. An electrician will be required at mid-day layover to remove the power sensor and verify the electrical connections, and a BC Ferries electrical technician will be required afterhours to disconnect the serial bus tie-in lines.

Figure A-1: J1587/1708 Engine Bus Connection in Control Room

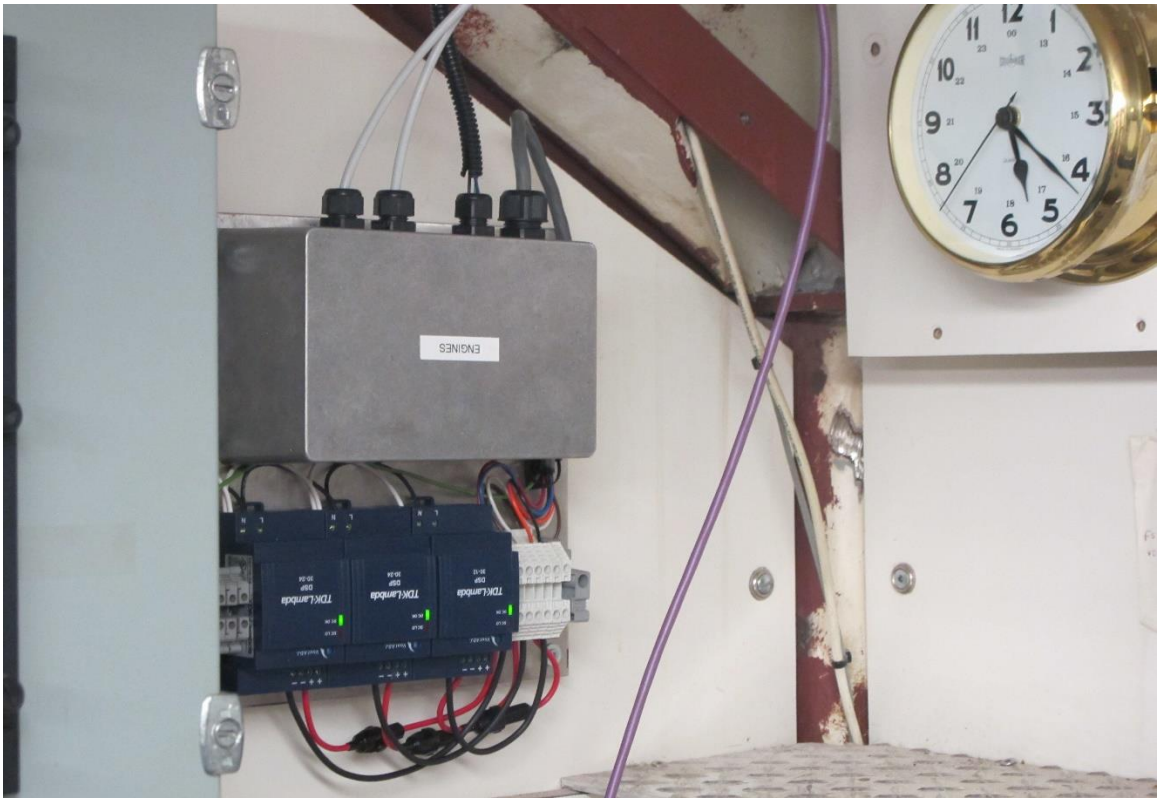

Figure A-2: RS232/CAN Isolated Converter System

Figure A-3: Deutz 6 Pin Connections and HDV100A3 J1587/RS232 Converter

Figure A-4: Electrical Sensor 4-20mA/CAN Converter

Figure A-5: HRP1 NMEA 183/CAN Converter

Figure A-6: HRP2 NMEA 183/CAN Converter

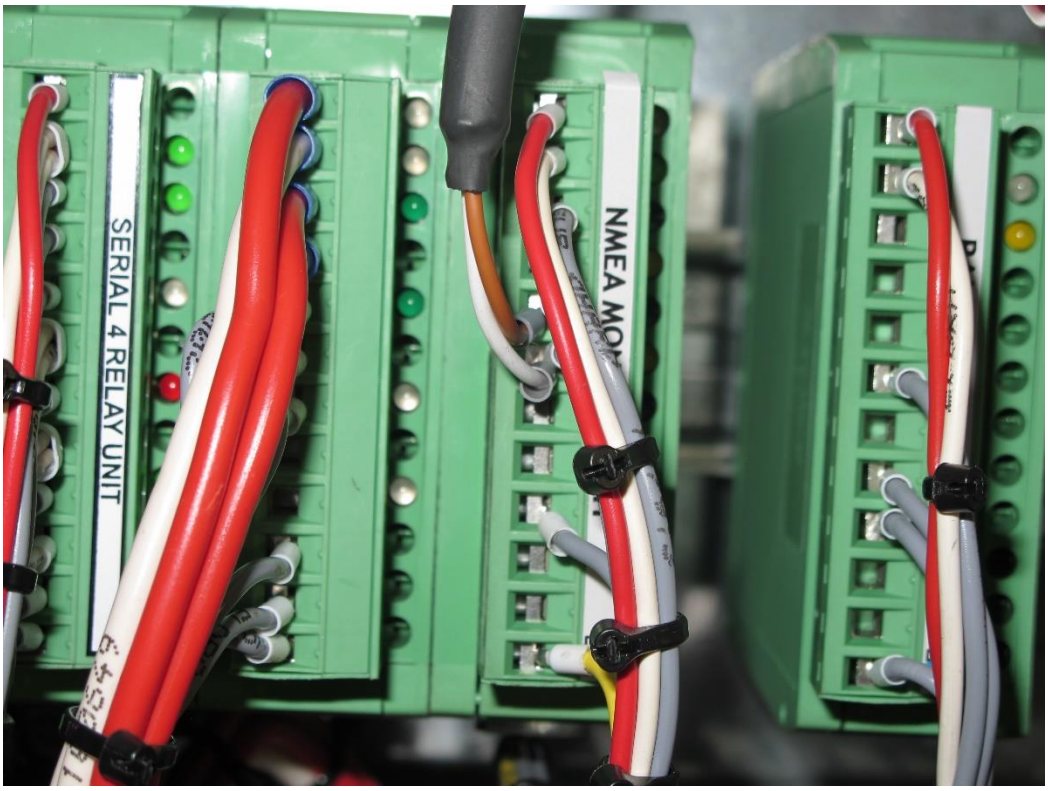

Figure A-7: Connection to HRP NMEA 183 Serial Bus

Figure A-8: GPS Unit and CAN Data Logger Installation

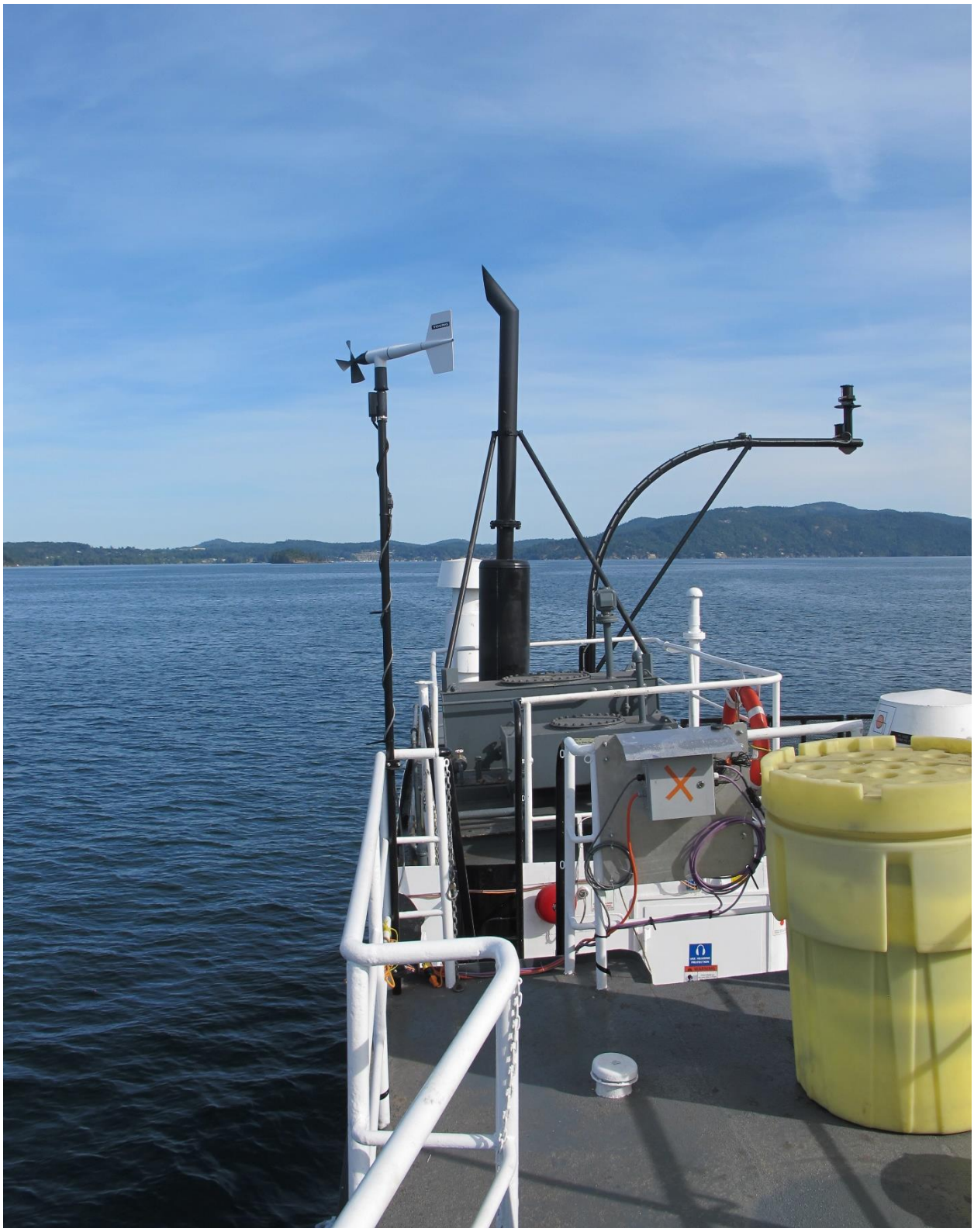

Figure A-9: Anemometer, GPS, and Data Logger Installation

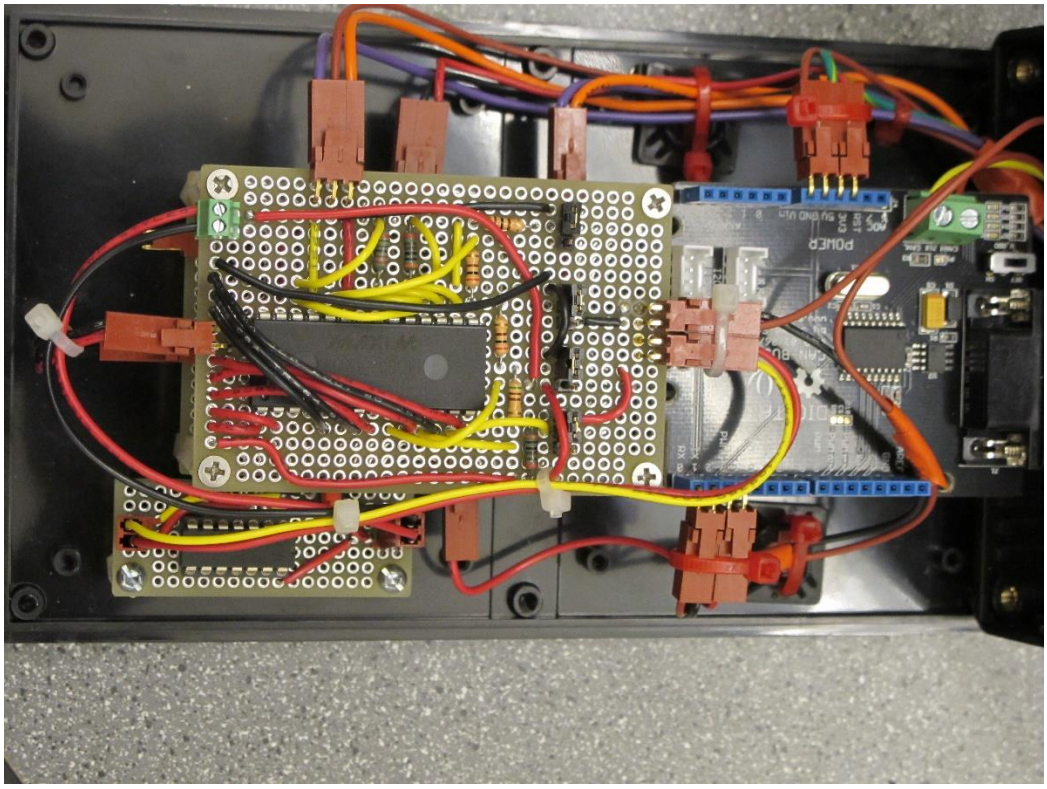

Figure A-10: Arduino Microcontroller and Custom Isolated RS485 Receiver Internals

Figure A-11: Wire Routing through Roxtec Fireproof/Waterproof Bulkhead Pass-Throughs

Appendix B – Derivation of DC/DC Converter Control Law

Beginning with the small-signal approximation equations developed in Chung, this appendix verifies that the desired control law can be implemented. The small signal equations presented in Table 21 are reintroduced here in the table below.

	Buck Mode	Boost Mode
Inductor Balance	$L\frac{d\hat{\imath}_L}{dt} = \frac{1}{n}D\hat{v}_{dc} + \frac{1}{n}V_{DC}\hat{d} - \hat{v}_{batt}$ **(B - 1)**	$L\frac{d\hat{\imath}_L}{dt} = \hat{v}_{batt} - \frac{D'}{n}\hat{v}_{dc} + \frac{1}{n}V_{DC}\hat{d}$ **(B - 2)**
Output Current	$C_1\frac{d\hat{v}_{batt}}{dt} = \hat{\imath}_L - \frac{\hat{v}_{batt}}{R_1}$ **(B - 3)**	$C_2\frac{d\hat{v}_{dc}}{dt} = \frac{D'}{n}\hat{\imath}_L - \frac{1}{n}I_L\hat{d} - \frac{\hat{v}_{dc}}{R_2}$ **(B - 4)**
Input Current	$C_2\frac{d\hat{v}_{dc}}{dt} \approx \hat{\imath}_{dc} - nI_L\hat{d} - nD\hat{\imath}_L$ **(B - 5)**	$C_1\frac{d\hat{v}_{batt}}{dt} \approx \hat{\imath}_{batt} - \hat{\imath}_L$ **(B - 6)**
Transformer Current	$\hat{\imath}_s = \frac{1}{n}\hat{\imath}_L$ **(B - 7)**	$\hat{\imath}_s = \frac{1}{n}\hat{\imath}_L D'$ **(B - 8)**

Considering first buck mode, we need to develop some insight into the physical system behaviour to develop the control equations. In buck mode, the system is absorbing power by charging the ESS. The bus voltage (HV) is still to be regulated by the DC/DC converter, so current can be sourced from the PMSM drive system by commanding regeneration torque. The ESS side voltage (LV) is set by the battery bank; therefore, current must be the control variable on the LV side to balance the power.

We begin by defining the time-domain inputs and outputs of the system. It is convenient to write the system in state space format for checking controllability. The states of the small-signal equations for buck mode are given by,

$$\text{Let,}\quad x_1 = \hat{\imath}_L \qquad \textbf{(B - 9)} \qquad \Rightarrow \qquad \dot{x}_1 = \frac{d\hat{\imath}_L}{dt} \qquad \textbf{(B - 10)}$$

$$x_2 = \hat{v}_{batt} \qquad \textbf{(B - 11)} \qquad \Rightarrow \qquad \dot{x}_2 = \frac{d\hat{v}_{batt}}{dt} \qquad \textbf{(B - 12)}$$

$$x_3 = \hat{v}_{dc} \qquad \textbf{(B - 13)} \qquad \Rightarrow \qquad \dot{x}_3 = \frac{d\hat{v}_{dc}}{dt} \qquad \textbf{(B - 14)}$$

We define the inputs to the system as duty cycle *d* and input current $\hat{\imath}_{dc}$. In state vector form, we can write input and output vectors as

Input Vector		**Output Vector**	
$\boldsymbol{u} = \begin{bmatrix} \hat{d} \\ \hat{\imath}_{dc} \end{bmatrix}$	**(B - 15)**	$y = x_3$	**(B - 16)**

Now, the state space representation for buck mode can be written as,

$$\begin{bmatrix} \dot{x}_1 \\ \dot{x}_2 \\ \dot{x}_3 \end{bmatrix} = \underbrace{\begin{bmatrix} 0 & -1/L & D/Ln \\ 1/C_1 & -1/R_1C_1 & 0 \\ -nD/C_2 & 0 & 0 \end{bmatrix}}_{A} \begin{bmatrix} x_1 \\ x_2 \\ x_3 \end{bmatrix} + \underbrace{\begin{bmatrix} V_{DC}/Ln & 0 \\ 0 & 0 \\ -nD/C_2 & 0 \end{bmatrix}}_{B} \begin{bmatrix} \hat{d} \\ \hat{\imath}_{dc} \end{bmatrix} \qquad \textbf{(B - 17)}$$

$$[y_1] = \underbrace{[0 \quad 0 \quad 1]}_{C} \begin{bmatrix} x_1 \\ x_2 \\ x_3 \end{bmatrix} + \underbrace{[0 \quad 0]}_{D} \begin{bmatrix} \hat{d} \\ \hat{\imath}_{dc} \end{bmatrix} \qquad \textbf{(B - 18)}$$

The controllability matrix is formulated as follows:

$$R = [A \quad AB \quad A^2B \quad \cdots \quad A^{m-1}B] \qquad \textbf{(B - 19)}$$

The system is considered controllable if the matrix *R* is of rank *m*. Matlab's function *ctrb()* builds the controllability matrix from state space system object. The function *rank*

determines the rank of the system; therefore, if *rank(**A**)* and *rank(**R**)* are the equal, then the system is controllable. A Matlab script and its subsequent results for numerical examples provided in Chung et al. [25] and Zahedi et al. [26] are presented after derivation of the boost mode.

We can develop a similar expressions for the converter is boost mode. In this mode of operation, the converter takes voltage input from the battery terminals and manipulates the duty cycle *d* for switches on the current fed side to regulate the DC bus voltage. If we define the states as,

$$\text{Let,}\quad x_1 = \hat{\imath}_L \qquad \textbf{(B - 20)} \qquad \Rightarrow \qquad \dot{x}_1 = \frac{d\hat{\imath}_L}{dt} \qquad \textbf{(B - 21)}$$

$$x_2 = \hat{v}_{dc} \qquad \textbf{(B - 22)} \qquad \Rightarrow \qquad \dot{x}_2 = \frac{d\hat{v}_{dc}}{dt} \qquad \textbf{(B - 23)}$$

We define the inputs to the system as duty cycle *d* and battery's input voltage $\hat{v}_{batt}$. In state vector form,

Input Vector		**Output Vector**	
$\boldsymbol{u} = \begin{bmatrix} \hat{d} \\ \hat{v}_{batt} \end{bmatrix}$	**(B - 24)**	$y = x_2$	**(B - 25)**

Then the state space representation for boost mode can be written as,

$$\begin{bmatrix} \dot{x}_1 \\ \dot{x}_2 \end{bmatrix} = \underbrace{\begin{bmatrix} 0 & -D'/Ln \\ D'/nC_2 & -1/R_2C_2 \end{bmatrix}}_{A} \begin{bmatrix} x_1 \\ x_2 \end{bmatrix} + \underbrace{\begin{bmatrix} V_{dc}/Ln & 1/L \\ -I_L/n\,C_2 & 0 \end{bmatrix}}_{B} \begin{bmatrix} \hat{d} \\ \hat{v}_{batt} \end{bmatrix} \qquad \textbf{(B - 26)}$$

$$[y_1] = \underbrace{[0 \quad 1]}_{C} \begin{bmatrix} x_1 \\ x_2 \end{bmatrix} + \underbrace{[0 \quad 0]}_{D} \begin{bmatrix} \hat{d} \\ \hat{v}_{batt} \end{bmatrix} \qquad \textbf{(B - 27)}$$

Returning back to buck mode, the transfer function governing the voltage regulation in can be developed by taking the Laplace transform of equation (B - 1) for inductor balance to yield the result,

$$sL\hat{\imath}_L(s) = \frac{1}{n}D\hat{v}_{dc}(s) + \frac{1}{n}V_{DC}\hat{d}(s) - \hat{v}_{batt}(s) \qquad \textbf{(B - 28)}$$

The input and output current relationships, Equation (B - 5) and Equation (B - 3), can be transformed, rearranged and substituted into the equation above to develop the control law as shown below.

Input Current (Buck): $$sC_1\hat{v}_{batt}(s) = \hat{\imath}_L(s) - \frac{\hat{v}_{batt}(s)}{R_1} \qquad \textbf{(B - 29)}$$

Output Current (Buck): $$sC_2\hat{v}_{dc}(s) = \hat{\imath}_{dc}(s) - nI_L\hat{d}(s) - nD\hat{\imath}_L(s) \qquad \textbf{(B - 30)}$$

Rearranging Equation (B - 30) to isolate the averaged inductor current we get,

$$\hat{\imath}_L(s) = \frac{1}{nD}\left[\hat{\imath}_{dc}(s) - sC_2\hat{v}_{dc}(s) - nI_L\hat{d}(s)\right] \qquad \textbf{(B - 31)}$$

We will use the above result to substitute into the inductor balance equation to get,

$$\frac{sL}{nD}\left[\hat{\imath}_{dc}(s) - sC_2\hat{v}_{dc}(s) - nI_L\hat{d}(s)\right] = \frac{1}{n}D\hat{v}_{dc}(s) + \frac{1}{n}V_{DC}\hat{d}(s) - \hat{v}_{batt}(s) \qquad \textbf{(B - 32)}$$

Expanding we get,

$$-\frac{s^2LC_2}{nD}\hat{v}_{dc}(s) + \frac{sL}{nD}\hat{\imath}_{dc}(s) - \frac{sLI_L}{D}\hat{d}(s) = \frac{1}{n}D\hat{v}_{dc}(s) + \frac{1}{n}V_{DC}\hat{d}(s) - \hat{v}_{batt}(s) \qquad \textbf{(B - 33)}$$

Grouping like-terms yields,

$$-\left[\frac{sLI_L}{D}+\frac{1}{n}V_{DC}\right]\hat{d}(s) = \left[\frac{s^2LC_2}{nD}+\frac{1}{n}D\right]\hat{v}_{dc}(s) - \underbrace{\hat{v}_{batt}(s)}_{Disturbance} - \underbrace{\frac{sL}{nD}\hat{\imath}_{dc}(s)}_{Disturbance} \quad \textbf{(B - 34)}$$

Finally we arrive at the control transfer function for controlling DC bus voltage using duty cycle manipulation of the voltage-fed converter.

$$G_{v_{dc}\cdot d}(s) = \frac{\hat{v}_{dc}(s)}{\hat{d}(s)} = -\frac{\frac{sLI_L}{D}+\frac{1}{n}V_{DC}}{\frac{s^2LC_2}{nD}+\frac{1}{n}D} = \frac{-(snLI_L+DV_{DC})}{s^2LC_2+D^2} \quad \textbf{(B - 35)}$$

Similarly, the transfer function governing the voltage regulation in boost mode can be developed by taking the Laplace transform of the average value equation for inductor balance, Equation (B - 2), to yield the result,

$$sL\hat{\imath}_L(s) = \hat{v}_{batt}(s) - \frac{D'}{n}\hat{v}_{dc}(s) + \frac{1}{n}V_{DC}\hat{d}(s) \quad \textbf{(B - 36)}$$

Again, we are using the output current balance equation to develop the control transfer function. Taking the Laplace transform of the output current relationship defined by Equation (B - 4), we get

$$sC_2\hat{v}_{dc}(s) = \frac{D'}{n}\hat{\imath}_L(s) - \frac{1}{n}I_L\hat{d}(s) - \frac{\hat{v}_{dc}(s)}{R_2} \quad \textbf{(B - 37)}$$

The equation can be rearranged to isolated averaged inductor current,

$$\hat{\imath}_L(s) = \frac{n}{D'}\left[\left(sC_2+\frac{1}{R_2}\right)\hat{v}_{dc}(s) + \frac{1}{n}I_L\hat{d}(s)\right] \quad \textbf{(B - 38)}$$

Substituting into the inductor balance Equation (B - 36) gives,

$$sL\frac{n}{D'}\left[\left(sC_2+\frac{1}{R_2}\right)\hat{v}_{dc}(\mathrm{s})+\frac{1}{n}I_L\hat{d}(s)\right] = \underbrace{\hat{v}_{batt}(s)}_{Disturbance} - \frac{D'}{n}\hat{v}_{dc}(s)+\frac{1}{n}V_{DC}\hat{d}(s) \qquad \textbf{(B - 39)}$$

Note here that fluctuations in battery voltage will present disturbances to the system. If we neglect the effects of changes in battery voltage, the above result can be rearranged as follows:

$$sL\frac{n}{D'}\left[\left(sC_2+\frac{1}{R_2}\right)\hat{v}_{dc}(\mathrm{s})\right]+\frac{D'}{n}\hat{v}_{dc}(s)=\left(\frac{1}{n}V_{DC}-\frac{I_L}{D'}sL\right)\hat{d}(s) \qquad \textbf{(B - 40)}$$

Gathering like terms,

$$\left(sL\frac{n}{D'}\left[\left(sC_2+\frac{1}{R_2}\right)\right]+\frac{D'}{n}\right)\hat{v}_{dc}(s)=\left(\frac{1}{n}V_{DC}-\frac{I_L}{D'}sL\right)\hat{d}(s) \qquad \textbf{(B - 41)}$$

Finally, we simplify the expression to get the final control transfer function,

$$\begin{aligned} G_{iv}(s)=\frac{\hat{v}_{dc}(s)}{\hat{d}(s)} &= \frac{\left(\frac{1}{n}V_{DC}-\frac{I_L}{D'}sL\right)}{\left(sL\frac{n}{D'}\left[\left(sC_2+\frac{1}{R_2}\right)\right]+\frac{D'}{n}\right)} \\ &= \frac{\left(\frac{1}{n}D'V_{DC}-I_LsL\right)}{\left(sLn\left[\left(sC_2+\frac{1}{R_2}\right)\right]+\frac{D'^2}{n}\right)} \\ &= \frac{(D'V_{DC}-nI_LsL)}{\left(sLn^2\left[\left(sC_2+\frac{1}{R_2}\right)\right]+D'^2\right)} \end{aligned} \qquad \textbf{(B - 42)}$$

The final result is summarized below,

$$G_{iv}(s) = \frac{\hat{v}_{dc}(s)}{\hat{d}(s)} = \frac{R_2(D'V_{DC} - nI_L sL)}{\left(s^2 Ln^2 C_2 R_2 + sLn^2 + R_2 D'^2\right)} \quad \textbf{(B - 43)}$$

The following page provides a numerical verification of the controllability for two converter examples from Chung et al. [25] and Zahedi et al. [26].

****

Matlab Code for Checking Controllability

```
%%{
% From Zahedi
L = 516e-6;
C1 = 267e-6;
C2 = 267e-6;
R1 = 1;
R2 = 19.22;
n = 3;
d = 0.6;
dp = (1-d);
Vdc = 620;
Vbatt = 100;
%}

%{
% From Chung
L = 1e-3;
C1 = 2e-3;
C2 = 2.7e-3;
R1 = 0.2667;
R2 = 10;
n = 3;
d = 0.6;
dp = (1-d);
Vdc = 5000;
Vbatt = 800;
IL = 800;
%}

% Buck Mode
    %x1 = i_L
    %x2 = v_batt
    %x3 = v_dc
    %y1 = x3
A = [0,-1/L,d/(L*n);1/C1,-1/(C1*R1),0;-n*d/C2,0,0];
B = [Vdc/(L*n),0;0,0;-n*d/C2,0];
C = [0 0 1];
D = [];
sys = ss(A,B,C,D);
```

```
co = ctrb(sys);
rankCo1 = rank(co);
rankSys1 = rank(A);

% Boost Mode
    %x1 = i_L
    %x2 = v_batt
    %x3 = v_dc
    %y1 = x3
A = [0,-dp/(n*L);dp/(n*C2),-1/(R2*C2)];
B = [Vdc/(n*L),1/L;-IL/(n*C2),0];
C = [0,1];
D = [];
sys2 = ss(A,B,C,D);
co2 = ctrb(sys2);
rankCo2 = rank(co2);
rankSys2 = rank(A);
disp(strcat('Rank of Buck Controllability Matrix: ',num2str(rankCo1)));
disp(strcat('Rank of Buck Matrix A: ',num2str(rankSys1)));
disp(strcat('Rank of Boost Controllability Matrix:
',num2str(rankCo2)));
disp(strcat('Rank of Boost Matrix A: ',num2str(rankSys2)));
```

Matlab output using parameters from Chung et al.

```
>> CheckControllability
Rank of Buck Controllability Matrix:3
Rank of Buck Matrix A:3
Rank of Boost Controllability Matrix:2
Rank of Boost Matrix A:2
>>
```

Matlab output using parameter from Zahedi et al.

```
>> CheckControllability
Rank of Buck Controllability Matrix:3
Rank of Buck Matrix A:3
Rank of Boost Controllability Matrix:2
Rank of Boost Matrix A:2
```

Appendix C – IGBT Datasheet for Loss Model

This appendix provides the datasheet for the IGBT module that was assumed in the development of the analytical energy loss simulation model. The datasheet contains the parameter values, and provides a reference for future studies.

Technische Information / Technical Information

IGBT-Module
IGBT-modules

FZ600R12KE4

62mm C-Serien Modul mit Trench/Feldstopp IGBT4 und Emitter Controlled 4 Diode
62mm C-Series module with Trench/Fieldstop IGBT4 and Emitter Controlled 4 diode

Vorläufige Daten / Preliminary Data

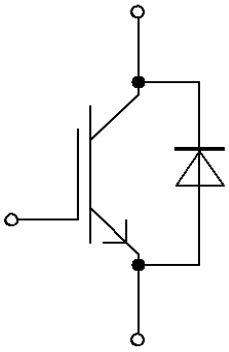

V_{CES} = 1200V
$I_{C\ nom}$ = 600A / I_{CRM} = 1200A

Typische Anwendungen

- Hochleistungsumrichter
- Motorantriebe
- USV-Systeme
- Windgeneratoren

Typical Applications

- High Power Converters
- Motor Drives
- UPS Systems
- Wind Turbines

Elektrische Eigenschaften

- Erweiterte Sperrschichttemperatur $T_{vj\ op}$
- Niedrige Schaltverluste
- Sehr große Robustheit
- V_{CEsat} mit positivem Temperaturkoeffizienten
- Niedriges V_{CEsat}

Electrical Features

- Extended Operation Temperature $T_{vj\ op}$
- Low Switching Losses
- Unbeatable Robustness
- V_{CEsat} with positive Temperature Coefficient
- Low V_{CEsat}

Mechanische Eigenschaften

- 4 kV AC 1min Isolationsfestigkeit
- Gehäuse mit CTI > 400
- Große Luft- und Kriechstrecken
- Isolierte Bodenplatte
- Standardgehäuse

Mechanical Features

- 4 kV AC 1min Insulation
- Package with CTI > 400
- High Creepage and Clearance Distances
- Isolated Base Plate
- Standard Housing

Module Label Code

Barcode Code 128

Sample
00000123456000000000000

DMX - Code

Content of the Code	Digit
Module Serial Number	1 - 5
Module Material Number	6 - 11
Production Order Number	12 - 19
Datecode (Production Year)	20 - 21
Datecode (Production Week)	22 - 23

prepared by: MK	date of publication: 2013-11-04	
approved by: WR	revision: 2.1	UL approved (E83335)

Vorläufige Daten
Preliminary Data

IGBT,Wechselrichter / IGBT,Inverter

Höchstzulässige Werte / Maximum Rated Values

Kollektor-Emitter-Sperrspannung Collector-emitter voltage	T_{vj} = 25°C	V_{CES}	1200		V
Kollektor-Dauergleichstrom Continuous DC collector current	T_C = 100°C, $T_{vj\,max}$ = 175°C	$I_{C\,nom}$	600		A
Periodischer Kollektor-Spitzenstrom Repetitive peak collector current	t_P = 1 ms	I_{CRM}	1200		A
Gesamt-Verlustleistung Total power dissipation	T_C = 25°C, $T_{vj\,max}$ = 175°C	P_{tot}	3000		W
Gate-Emitter-Spitzenspannung Gate-emitter peak voltage		V_{GES}	+/-20		V

Charakteristische Werte / Characteristic Values

			min.	typ.	max.	
Kollektor-Emitter-Sättigungsspannung Collector-emitter saturation voltage	I_C = 600 A, V_{GE} = 15 V I_C = 600 A, V_{GE} = 15 V I_C = 600 A, V_{GE} = 15 V	T_{vj} = 25°C T_{vj} = 125°C T_{vj} = 150°C	$V_{CE\,sat}$		1,75 2,00 2,05	2,10	V V V
Gate-Schwellenspannung Gate threshold voltage	I_C = 23,0 mA, V_{CE} = V_{GE}, T_{vj} = 25°C		V_{GEth}	5,2	5,8	6,4	V
Gateladung Gate charge	V_{GE} = -15 V ... +15 V		Q_G		5,60		µC
Interner Gatewiderstand Internal gate resistor	T_{vj} = 25°C		R_{Gint}		1,3		Ω
Eingangskapazität Input capacitance	f = 1 MHz, T_{vj} = 25°C, V_{CE} = 25 V, V_{GE} = 0 V		C_{ies}		42,0		nF
Rückwirkungskapazität Reverse transfer capacitance	f = 1 MHz, T_{vj} = 25°C, V_{CE} = 25 V, V_{GE} = 0 V		C_{res}		1,70		nF
Kollektor-Emitter-Reststrom Collector-emitter cut-off current	V_{CE} = 1200 V, V_{GE} = 0 V, T_{vj} = 25°C		I_{CES}			5,0	mA
Gate-Emitter-Reststrom Gate-emitter leakage current	V_{CE} = 0 V, V_{GE} = 20 V, T_{vj} = 25°C		I_{GES}			400	nA
Einschaltverzögerungszeit, induktive Last Turn-on delay time, inductive load	I_C = 600 A, V_{CE} = 600 V V_{GE} = ±15 V R_{Gon} = 1,2 Ω	T_{vj} = 25°C T_{vj} = 125°C T_{vj} = 150°C	$t_{d\,on}$		0,24 0,25 0,26		µs µs µs
Anstiegszeit, induktive Last Rise time, inductive load	I_C = 600 A, V_{CE} = 600 V V_{GE} = ±15 V R_{Gon} = 1,2 Ω	T_{vj} = 25°C T_{vj} = 125°C T_{vj} = 150°C	t_r		0,09 0,10 0,11		µs µs µs
Abschaltverzögerungszeit, induktive Last Turn-off delay time, inductive load	I_C = 600 A, V_{CE} = 600 V V_{GE} = ±15 V R_{Goff} = 1,2 Ω	T_{vj} = 25°C T_{vj} = 125°C T_{vj} = 150°C	$t_{d\,off}$		0,61 0,64 0,66		µs µs µs
Fallzeit, induktive Last Fall time, inductive load	I_C = 600 A, V_{CE} = 600 V V_{GE} = ±15 V R_{Goff} = 1,2 Ω	T_{vj} = 25°C T_{vj} = 125°C T_{vj} = 150°C	t_f		0,10 0,14 0,15		µs µs µs
Einschaltverlustenergie pro Puls Turn-on energy loss per pulse	I_C = 600 A, V_{CE} = 600 V, L_S = 60 nH V_{GE} = ±15 V, di/dt = 5500 A/µs (T_{vj} = 150°C) R_{Gon} = 1,2 Ω	T_{vj} = 25°C T_{vj} = 125°C T_{vj} = 150°C	E_{on}		35,0 50,0 55,0		mJ mJ mJ
Abschaltverlustenergie pro Puls Turn-off energy loss per pulse	I_C = 600 A, V_{CE} = 600 V, L_S = 60 nH V_{GE} = ±15 V, du/dt = 3500 V/µs (T_{vj} = 150°C) R_{Goff} = 1,2 Ω	T_{vj} = 25°C T_{vj} = 125°C T_{vj} = 150°C	E_{off}		50,0 75,0 80,0		mJ mJ mJ
Kurzschlußverhalten SC data	$V_{GE} \leq$ 15 V, V_{CC} = 800 V $V_{CEmax} = V_{CES} - L_{sCE} \cdot di/dt$	$t_P \leq$ 10 µs, T_{vj} = 150°C	I_{SC}		2400		A
Wärmewiderstand, Chip bis Gehäuse Thermal resistance, junction to case	pro IGBT / per IGBT		R_{thJC}			0,05	K/W
Wärmewiderstand, Gehäuse bis Kühlkörper Thermal resistance, case to heatsink	pro IGBT / per IGBT λ_{Paste} = 1 W/(m·K) / λ_{grease} = 1 W/(m·K)		R_{thCH}		0,017		K/W
Temperatur im Schaltbetrieb Temperature under switching conditions			$T_{vj\,op}$	-40		150	°C

prepared by: MK	date of publication: 2013-11-04
approved by: WR	revision: 2.1

Vorläufige Daten
Preliminary Data

Diode, Wechselrichter / Diode, Inverter

Höchstzulässige Werte / Maximum Rated Values

Periodische Spitzensperrspannung Repetitive peak reverse voltage	T_{vj} = 25°C	V_{RRM}	1200	V
Dauergleichstrom Continuous DC forward current		I_F	600	A
Periodischer Spitzenstrom Repetitive peak forward current	t_P = 1 ms	I_{FRM}	1200	A
Grenzlastintegral I²t - value	V_R = 0 V, t_P = 10 ms, T_{vj} = 125°C V_R = 0 V, t_P = 10 ms, T_{vj} = 150°C	I²t	51000 49000	A²s A²s

Charakteristische Werte / Characteristic Values

			min.	typ.	max.	
Durchlassspannung Forward voltage	I_F = 600 A, V_{GE} = 0 V I_F = 600 A, V_{GE} = 0 V I_F = 600 A, V_{GE} = 0 V	T_{vj} = 25°C T_{vj} = 125°C T_{vj} = 150°C	V_F		1,80 1,75 1,70	2,35	V V V
Rückstromspitze Peak reverse recovery current	I_F = 600 A, - di_F/dt = 5500 A/µs (T_{vj}=150°C) V_R = 600 V V_{GE} = -15 V	T_{vj} = 25°C T_{vj} = 125°C T_{vj} = 150°C	I_{RM}		440 560 590		A A A
Sperrverzögerungsladung Recovered charge	I_F = 600 A, - di_F/dt = 5500 A/µs (T_{vj}=150°C) V_R = 600 V V_{GE} = -15 V	T_{vj} = 25°C T_{vj} = 125°C T_{vj} = 150°C	Q_r		55,0 100 115		µC µC µC
Abschaltenergie pro Puls Reverse recovery energy	I_F = 600 A, - di_F/dt = 5500 A/µs (T_{vj}=150°C) V_R = 600 V V_{GE} = -15 V	T_{vj} = 25°C T_{vj} = 125°C T_{vj} = 150°C	E_{rec}		27,0 52,0 60,0		mJ mJ mJ
Wärmewiderstand, Chip bis Gehäuse Thermal resistance, junction to case	pro Diode / per diode		R_{thJC}			0,07	K/W
Wärmewiderstand, Gehäuse bis Kühlkörper Thermal resistance, case to heatsink	pro Diode / per diode λ_{Paste} = 1 W/(m·K) / λ_{grease} = 1 W/(m·K)		R_{thCH}		0,024		K/W
Temperatur im Schaltbetrieb Temperature under switching conditions			$T_{vj\,op}$	-40		150	°C

Vorläufige Daten
Preliminary Data

Modul / Module

Isolations-Prüfspannung Isolation test voltage	RMS, f = 50 Hz, t = 1 min.	V_{ISOL}		4,0		kV
Material Modulgrundplatte Material of module baseplate				Cu		
Innere Isolation Internal isolation	Basisisolierung (Schutzklasse 1, EN61140) basic insulation (class 1, IEC 61140)			Al_2O_3		
Kriechstrecke Creepage distance	Kontakt - Kühlkörper / terminal to heatsink Kontakt - Kontakt / terminal to terminal			25,0 19,0		mm
Luftstrecke Clearance	Kontakt - Kühlkörper / terminal to heatsink Kontakt - Kontakt / terminal to terminal			25,0 10,0		mm
Vergleichszahl der Kriechwegbildung Comperative tracking index		CTI		> 400		
			min.	typ.	max.	
Wärmewiderstand, Gehäuse bis Kühlkörper Thermal resistance, case to heatsink	pro Modul / per module λ_{Paste} = 1 W/(m·K) / λ_{grease} = 1 W/(m·K)	R_{thCH}		0,01		K/W
Modulstreuinduktivität Stray inductance module		L_{sCE}		16		nH
Modulleitungswiderstand, Anschlüsse - Chip Module lead resistance, terminals - chip	T_C = 25°C, pro Schalter / per switch	$R_{CC'+EE'}$		0,50		mΩ
Lagertemperatur Storage temperature		T_{stg}	-40		125	°C
Anzugsdrehmoment f. Modulmontage Mounting torque for modul mounting	Schraube M6 - Montage gem. gültiger Applikationsschrift Screw M6 - Mounting according to valid application note	M	3,00	-	6,00	Nm
Anzugsdrehmoment f. elektr. Anschlüsse Terminal connection torque	Schraube M4 - Montage gem. gültiger Applikationsschrift Screw M4 - Mounting according to valid application note Schraube M6 - Montage gem. gültiger Applikationsschrift Screw M6 - Mounting according to valid application note	M	1,1 2,5	- -	2,0 5,0	Nm Nm
Gewicht Weight		G		340		g

Vorläufige Daten
Preliminary Data

Ausgangskennlinie IGBT,Wechselrichter (typisch)
output characteristic IGBT,Inverter (typical)
$I_C = f(V_{CE})$
V_{GE} = 15 V

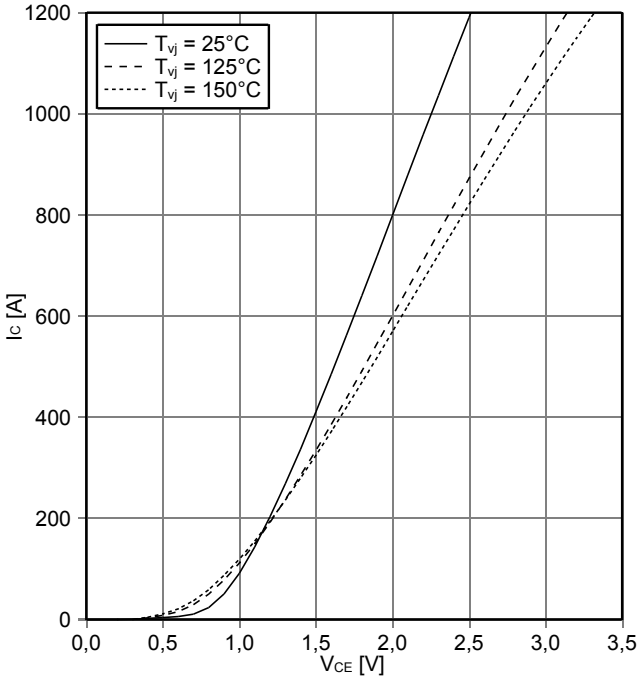

Ausgangskennlinienfeld IGBT,Wechselrichter (typisch)
output characteristic IGBT,Inverter (typical)
$I_C = f(V_{CE})$
T_{vj} = 150°C

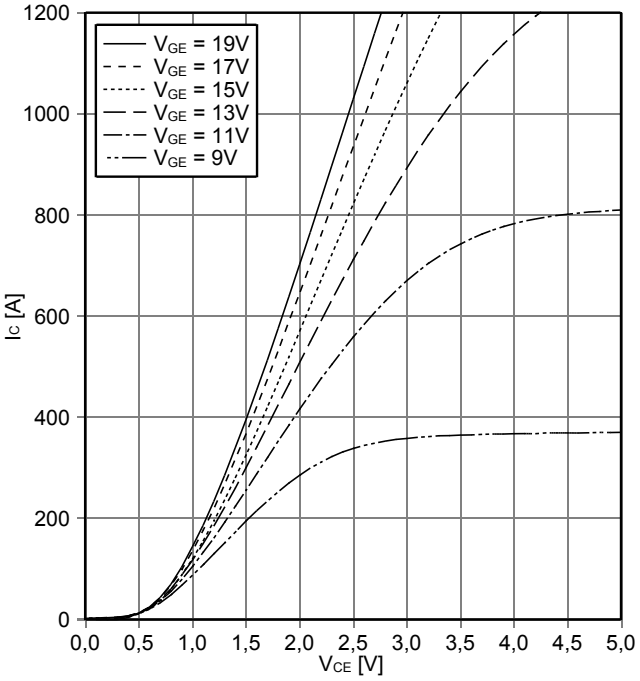

Übertragungscharakteristik IGBT,Wechselrichter (typisch)
transfer characteristic IGBT,Inverter (typical)
$I_C = f(V_{GE})$
V_{CE} = 20 V

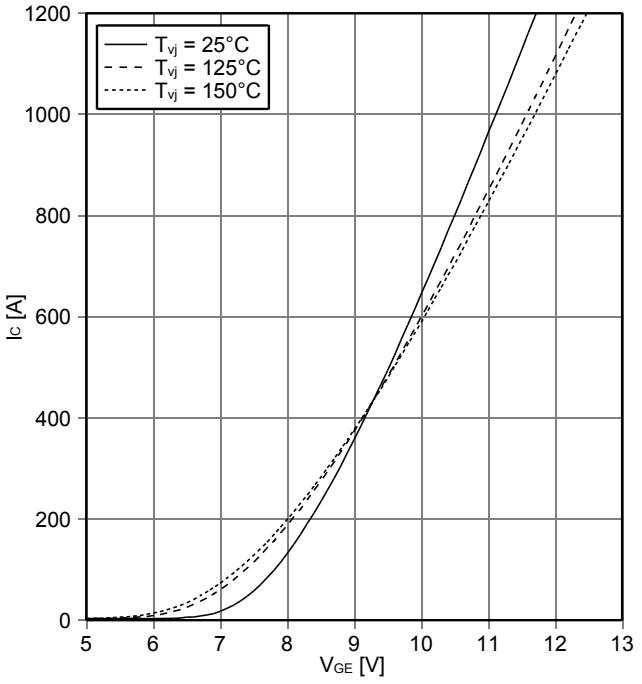

Schaltverluste IGBT,Wechselrichter (typisch)
switching losses IGBT,Inverter (typical)
$E_{on} = f(I_C)$, $E_{off} = f(I_C)$
V_{GE} = ±15 V, R_{Gon} = 1.2 Ω, R_{Goff} = 1.2 Ω, V_{CE} = 600 V

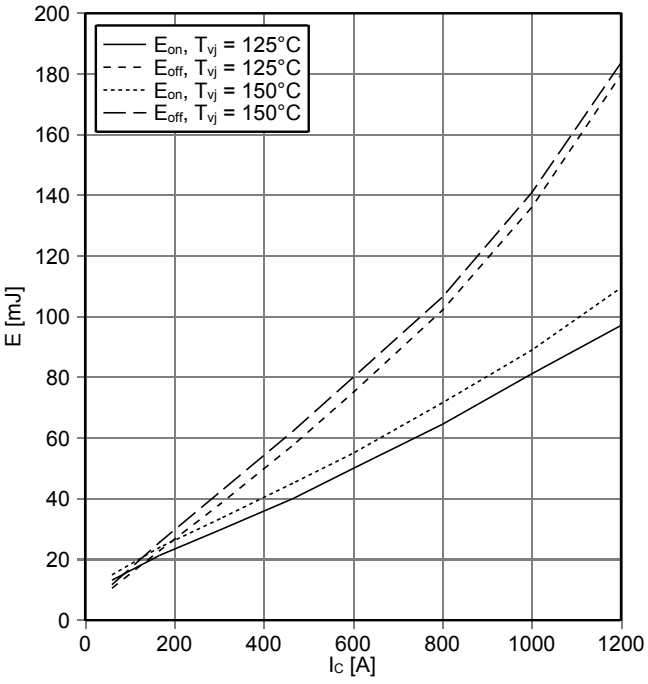

prepared by: MK	date of publication: 2013-11-04
approved by: WR	revision: 2.1

Vorläufige Daten
Preliminary Data

Schaltverluste IGBT,Wechselrichter (typisch)
switching losses IGBT,Inverter (typical)
$E_{on} = f(R_G)$, $E_{off} = f(R_G)$
V_{GE} = ±15 V, I_C = 600 A, V_{CE} = 600 V

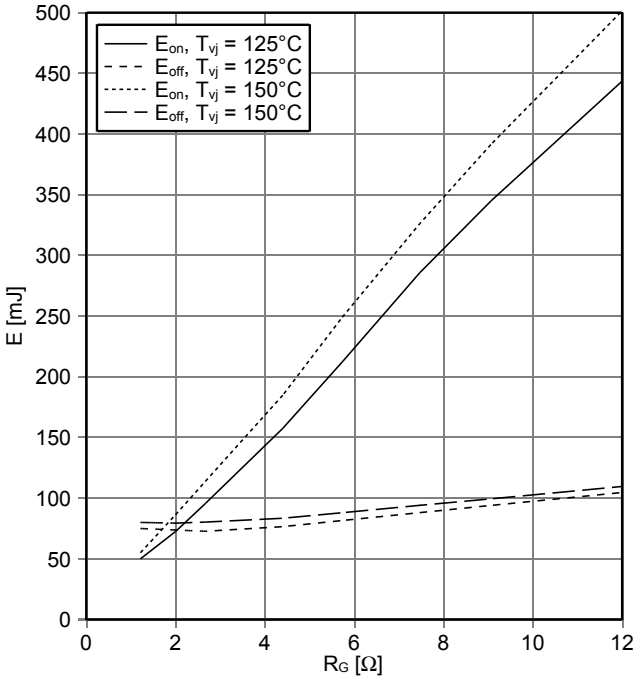

Transienter Wärmewiderstand IGBT,Wechselrichter
transient thermal impedance IGBT,Inverter
$Z_{thJC} = f(t)$

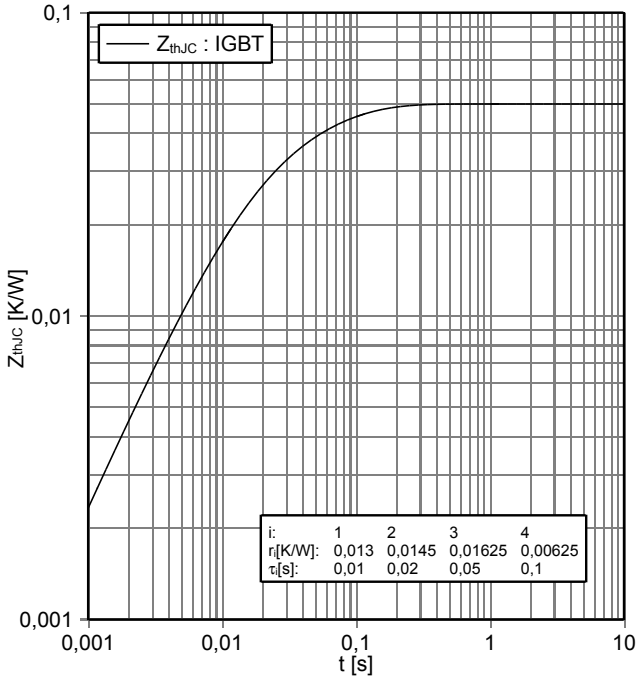

Sicherer Rückwärts-Arbeitsbereich IGBT,Wechselrichter (RBSOA)
reverse bias safe operating area IGBT,Inverter (RBSOA)
$I_C = f(V_{CE})$
V_{GE} = ±15 V, R_{Goff} = 1.2 Ω, T_{vj} = 150°C

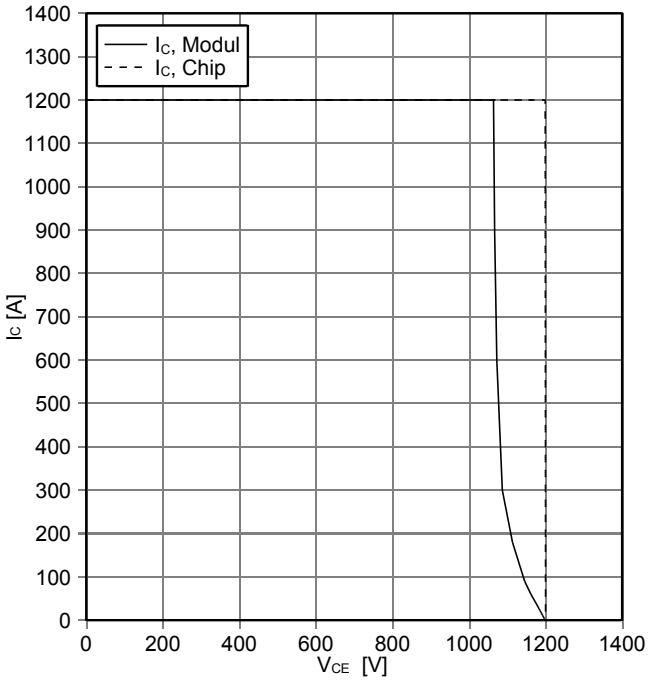

Durchlasskennlinie der Diode, Wechselrichter (typisch)
forward characteristic of Diode, Inverter (typical)
$I_F = f(V_F)$

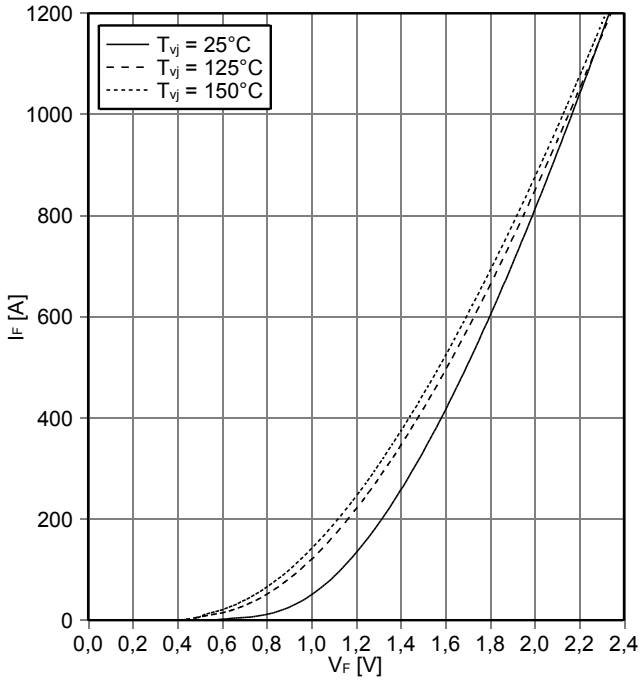

prepared by: MK	date of publication: 2013-11-04
approved by: WR	revision: 2.1

Vorläufige Daten
Preliminary Data

Schaltverluste Diode, Wechselrichter (typisch)
switching losses Diode, Inverter (typical)
$E_{rec} = f(I_F)$
$R_{Gon} = 1.2\ \Omega$, $V_{CE} = 600$ V

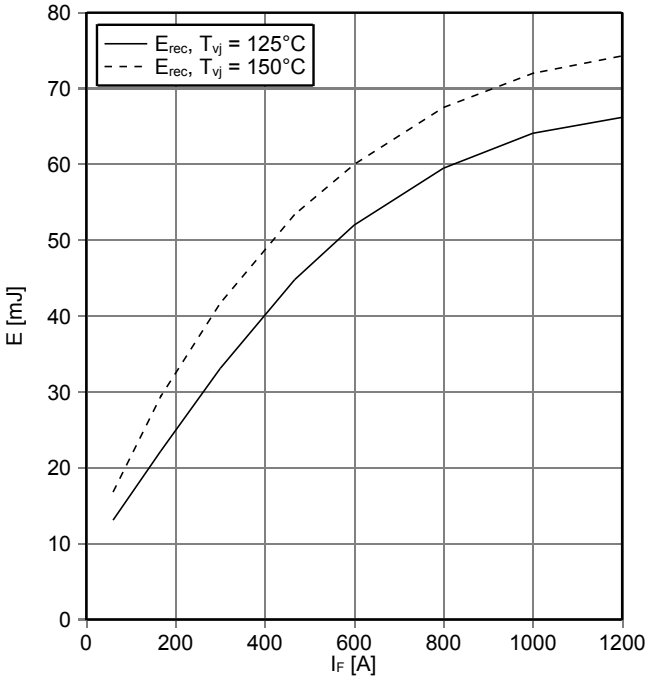

Schaltverluste Diode, Wechselrichter (typisch)
switching losses Diode, Inverter (typical)
$E_{rec} = f(R_G)$
$I_F = 600$ A, $V_{CE} = 600$ V

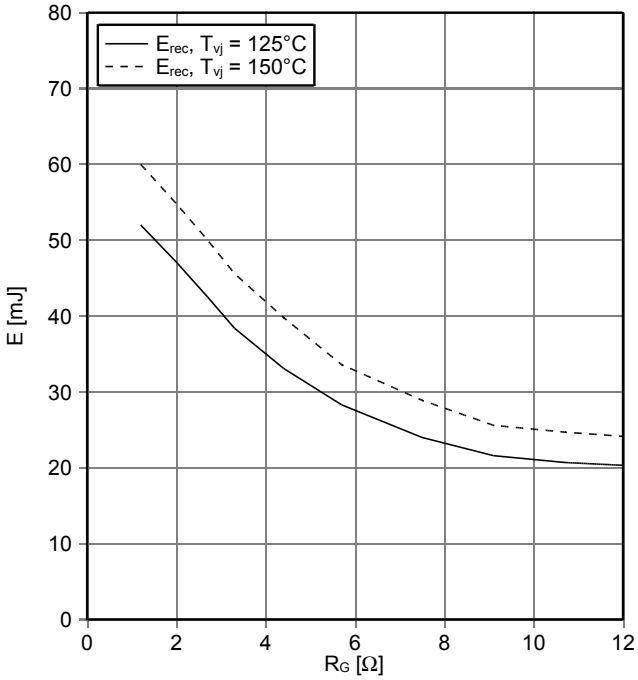

Transienter Wärmewiderstand Diode, Wechselrichter
transient thermal impedance Diode, Inverter
$Z_{thJC} = f(t)$

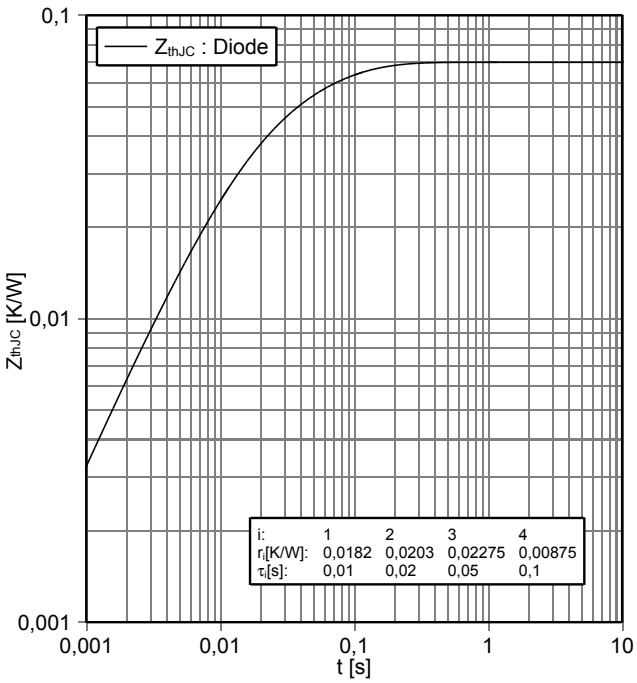

prepared by: MK	date of publication: 2013-11-04
approved by: WR	revision: 2.1

Vorläufige Daten
Preliminary Data

Schaltplan / circuit_diagram_headline

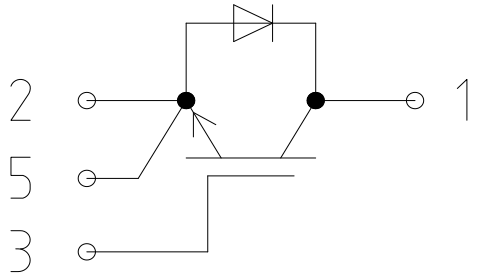

Gehäuseabmessungen / package outlines

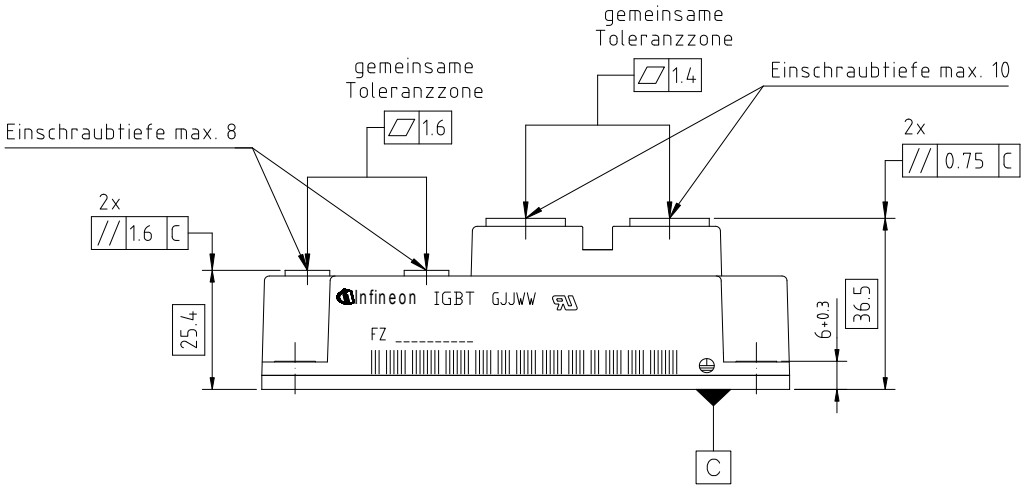

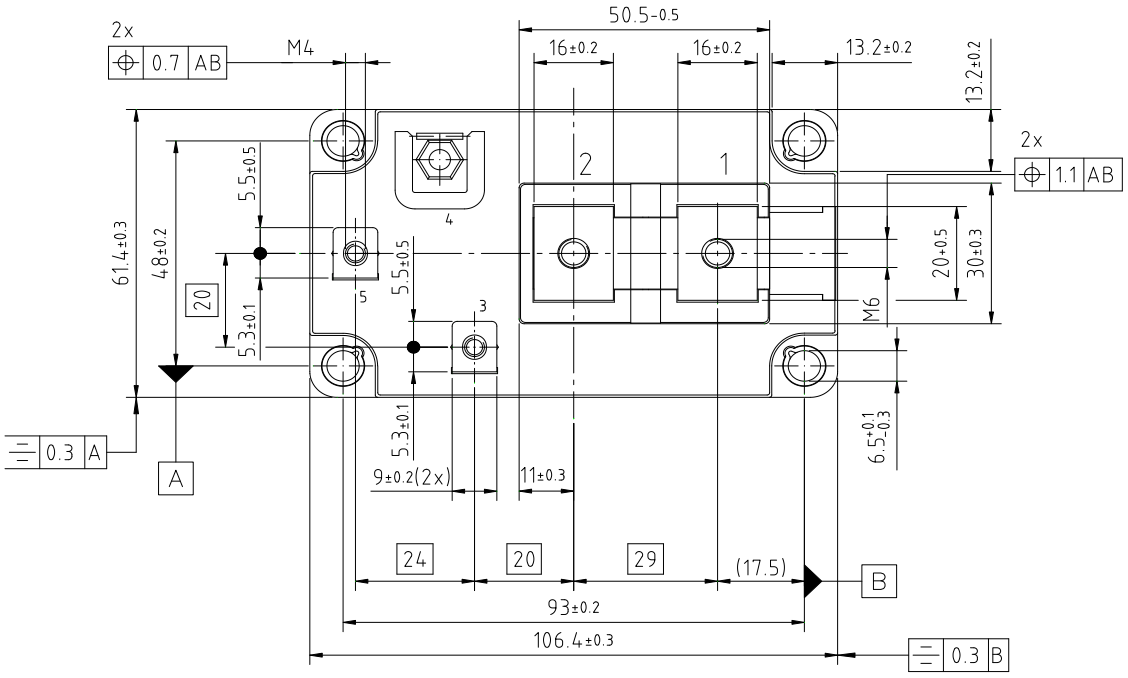

prepared by: MK	date of publication: 2013-11-04
approved by: WR	revision: 2.1

Vorläufige Daten
Preliminary Data

Nutzungsbedingungen

Die in diesem Produktdatenblatt enthaltenen Daten sind ausschließlich für technisch geschultes Fachpersonal bestimmt. Die Beurteilung der Eignung dieses Produktes für Ihre Anwendung sowie die Beurteilung der Vollständigkeit der bereitgestellten Produktdaten für diese Anwendung obliegt Ihnen bzw. Ihren technischen Abteilungen.

In diesem Produktdatenblatt werden diejenigen Merkmale beschrieben, für die wir eine liefervertragliche Gewährleistung übernehmen. Eine solche Gewährleistung richtet sich ausschließlich nach Maßgabe der im jeweiligen Liefervertrag enthaltenen Bestimmungen. Garantien jeglicher Art werden für das Produkt und dessen Eigenschaften keinesfalls übernommen. Die Angaben in den gültigen Anwendungs- und Montagehinweisen des Moduls sind zu beachten.

Sollten Sie von uns Produktinformationen benötigen, die über den Inhalt dieses Produktdatenblatts hinausgehen und insbesondere eine spezifische Verwendung und den Einsatz dieses Produktes betreffen, setzen Sie sich bitte mit dem für Sie zuständigen Vertriebsbüro in Verbindung (siehe www.infineon.com, Vertrieb&Kontakt). Für Interessenten halten wir Application Notes bereit.

Aufgrund der technischen Anforderungen könnte unser Produkt gesundheitsgefährdende Substanzen enthalten. Bei Rückfragen zu den in diesem Produkt jeweils enthaltenen Substanzen setzen Sie sich bitte ebenfalls mit dem für Sie zuständigen Vertriebsbüro in Verbindung.

Sollten Sie beabsichtigen, das Produkt in Anwendungen der Luftfahrt, in gesundheits- oder lebensgefährdenden oder lebenserhaltenden Anwendungsbereichen einzusetzen, bitten wir um Mitteilung. Wir weisen darauf hin, dass wir für diese Fälle
- die gemeinsame Durchführung eines Risiko- und Qualitätsassessments;
- den Abschluss von speziellen Qualitätssicherungsvereinbarungen;
- die gemeinsame Einführung von Maßnahmen zu einer laufenden Produktbeobachtung dringend empfehlen und gegebenenfalls die Belieferung von der Umsetzung solcher Maßnahmen abhängig machen.

Soweit erforderlich, bitten wir Sie, entsprechende Hinweise an Ihre Kunden zu geben.

Inhaltliche Änderungen dieses Produktdatenblatts bleiben vorbehalten.

Terms & Conditions of usage

The data contained in this product data sheet is exclusively intended for technically trained staff. You and your technical departments will have to evaluate the suitability of the product for the intended application and the completeness of the product data with respect to such application.

This product data sheet is describing the characteristics of this product for which a warranty is granted. Any such warranty is granted exclusively pursuant the terms and conditions of the supply agreement. There will be no guarantee of any kind for the product and its characteristics. The information in the valid application- and assembly notes of the module must be considered.

Should you require product information in excess of the data given in this product data sheet or which concerns the specific application of our product, please contact the sales office, which is responsible for you (see www.infineon.com). For those that are specifically interested we may provide application notes.

Due to technical requirements our product may contain dangerous substances. For information on the types in question please contact the sales office, which is responsible for you.

Should you intend to use the Product in aviation applications, in health or live endangering or life support applications, please notify. Please note, that for any such applications we urgently recommend
- to perform joint Risk and Quality Assessments;
- the conclusion of Quality Agreements;
- to establish joint measures of an ongoing product survey, and that we may make delivery depended on the realization of any such measures.

If and to the extent necessary, please forward equivalent notices to your customers.

Changes of this product data sheet are reserved.

prepared by: MK	date of publication: 2013-11-04
approved by: WR	revision: 2.1